NOTE TO USERS

UNIVERSITÉ DE MONTRÉAL

BIAXIAL FATIGUE MECHANISMS AND LIFE PREDICTIONS FOR 1045 STEEL AND 7075 ALUMINUM ALLOY INCLUDING ANISOTROPY AND NOTCH EFFECTS

HUIFANG GUO

GÉNIE MÉTALLURGIQUE

ÉCOLE POLYTECHNIQUE DE MONTRÉAL

THÈSE PRESENTÉE EN VUE DE L'OBTENTION

DU DIPLÔME DE PHILOSOPHIAE DOCTOR (Ph.D.)

(GÉNIE METALLURGIQUE)

AOÛT 2003

Your file Votre référence
ISBN: 0-612-89227-1
Our file Notre référence
ISBN: 0-612-89227-1

UNIVERSITÉ DE MONTRÉAL

ÉCOLE POLYTECHNIQUE DE MONTRÉAL

Cette thèse intitulée:

BIAXIAL FATIGUE MECHANISMS AND LIFE PREDICTIONS FOR 1045 STEEL AND 7075 ALUMINUM ALLOY INCLUDING ANISOTROPY AND NOTCH EFFECTS

Présentée par: GUO Huifang

en vue de l'obtention du diplôme de: Philosophiae Doctor

a été dûment acceptée par le jury d'examen constitué de:

M. DICKSON, J. Ivan, Ph.D., président

M. VERREMAN, Yves, Ph.D., membre et directeur de recherche

Mme. BERNARD, Marie, Ph.D., membre

M. FATEMI, Ali, Ph.D., membre

DÉDICACE

To my parents

To my husband and my son, Xiangyang and Rui

ACKNOWLEDGMENT

I would like to express my sincere appreciation to Professor Yves Verreman, my thesis supervisor, for his guidance and constant encouragement throughout this research. His support and understanding give me a great courage to complete my Ph.D. thesis in École Polytechnique de Montréal.

I wish to thank Professor J. Ivan Dickson for his helpful comments on fracture surface observations during my study of fatigue mechanisms.

Thanks also go to Marius Banu for his consistent help in solving problems on the fatigue machine and other laboratory equipment. I also appreciate the kind help provided by Nathalie Limodin in using FEA software.

During my study and research in École Polytechnique, personnel and friends in Génie Métallurgique gave me enthusiastic support. I would like to express my acknowledgment for all the help I received from many of them. I wish to give special thanks to Carole Massicotte and Josée Laviolette for their help in my experiments.

ABSTRACT

This thesis focuses on biaxial high cycle fatigue mechanisms and fatigue life predictions for metals under constant amplitude axial-torsional loadings. The effects of non-proportional loadings (out-of-phase loading and mean tensile stress), material anisotropy and stress concentration on the axial-torsional fatigue behaviors are studied. Different fatigue life prediction approaches are evaluated or proposed on the basis of detailed observation of fatigue cracking mechanisms.

The available fatigue information in literature on cracking mechanisms and fatigue life prediction parameters is first reviewed. Cracks generally initiate at PSBs oriented close to the maximum shear planes. Stage I crack propagation occurs on the maximum shear plane and stage II crack propagation on the plane of maximum normal stress. In most materials, most of fatigue life is consumed under shear-control (crack initiation and stage I propagation). The maximum shear stress (strain) amplitude on the critical plane is the control parameter for fatigue damage, but the normal stress on the critical plane plays an important secondary role. The authors use different combinations of stresses and/or strains to predict fatigue life. Most of fatigue life parameters can be considered as extensions of Tresca criterion (e.g. McDiarmid and Fatemi-Socie) or of Von-Mises criterion (e.g. Sines and Papadopoulos) by adding a second term to account for the normal stress effect (normal stress on the critical plane or hydrostatic stress). Parameters based on the critical-plane concept are the most prominent.

Stress-controlled high cycle fatigue tests (10^5-10^7 cycles) were carried out on smooth thin-walled tubular specimens made of as-rolled 1045 steel under proportional loadings (axial, torsional and in-phase fatigue) and non-proportional loadings (90^0 out-of-phase fatigue and torsional fatigue with static tension). A replica technique was used for crack monitoring from initiation sites. External surfaces of failed specimens and fracture surfaces were also observed in detail under SEM.

The cracks initiate at PSBs oriented close to maximum shear planes in all loading conditions. Under non-proportional loadings, more cracks initiate on the maximum shear plane where the normal stress (amplitude or mean) is the highest. Crack initiation is a shear-controlled process and tensile normal stress on the maximum shear plane assists this process. The two stages of crack propagation are clearly observed in three loading cases: torsional fatigue, in-phase fatigue and high λ out-of-phase fatigue. The transition from stage I to stage II could correspond to a microstructural barrier in depth. Fatigue life consumed under shear control represents an important part of total life. Shear-based critical-plane parameters can be appropriate for fatigue life prediction. Easier crack initiation (all ferrite grains well oriented) and easier crack propagation (no stage II crack coalescence and crack branching) occur in the special loading case ($\phi=90^0$, $\lambda=0.5$) where the shear stress amplitudes are equal in all plane orientations.

Eight multiaxial fatigue life parameters have been evaluated in their life prediction abilities under different loading conditions (including out-of-phase loading and cyclic torsion with static axial stress). There are four stress-based parameters (Tresca, McDiarmid, Dang-Van, and Papadopoulos), three strain-based parameters (KBM, Wang-Brown, Fatemi-Socie) and one energy-based parameter (GWP) parameter. Two sets of biaxial high cycle fatigue data on ferritic-pearlitic steels (our own data and data from literature) are used for this evaluation.

The maximum shear stress amplitude (Tresca parameter) is not sufficient for biaxial fatigue life prediction. The parameters including a normal stress/strain term can well predict fatigue life under in-phase loading and low λ out-of-phase loading. Fatigue life under high λ out-of-phase loading is often underestimated. The attenuation of normal stress amplitude effect by the phase angle on the critical plane explains this underestimation. However, macroscopic plastic strain can be non-negligible above the fatigue limits, and a parameter using both strain and stress terms can be required to account for different stress-strain response between in-phase and out-of-phase loadings.

The maximum normal stress on the critical plane is more appropriate than the maximum hydrostatic stress to account for both effects of normal mean stress and normal stress amplitude. Fatigue life in the special loading case ($\phi=90^0$; $\lambda=0.5$) is often overestimated. This is attributed to more damaging mechanisms in crack initiation and crack propagation. A modification of McDiarmid parameter, using an extra damage factor (EDF) is proposed to obtain a conservative life prediction for all loading conditions we considered.

Material anisotropy effects on cracking mechanisms and fatigue life were investigated from tests carried out on smooth tubular specimens made of a 7075 aluminum alloy having elongated grains and many inclusions strings in the longitudinal direction. Three loading conditions were employed: axial fatigue, torsional fatigue and torsional fatigue with static tension. The last loading condition introduces a competition between two failure mechanisms: a critical-plane mechanism (transverse shear cracking due to static axial tensile load) and an anisotropy-enhanced mechanism (longitudinal shear cracking on the material weak plane). The material was tested in both underaged and overaged conditions.

No anisotropy effect is observed under axial fatigue. Under torsional fatigue, anisotropy effect is more important in the underaged material than in the overaged material. Mechanical fibering plays a role in both materials, but planar slip and (111) texture in the underaged material enhance the weakness of the longitudinal plane and result in a low torsional fatigue performance (crystallographic fracture). Transverse shear cracking appears only when the static tension is high enough. The underaged material has not the same resistance to the longitudinal shear cracking as to the transverse shear cracking. Two stress-life relations are needed to predict fatigue life when two different failure mechanisms are involved. In the overaged material, anisotropy effect is less important, and McDiarmid parameter can reasonably well correlate fatigue lives obtained in the three loading conditions.

Notch effects on axial and torsional fatigue behaviors were studied using two circumferentially V-notched cylindrical specimens made of as-rolled 1045 steel. The specimens have the same notch angle of 90 degree but have different notch depths. Detailed FEM stress analyses at notch tip for both mode I and mode III loadings have been performed using the Catia V5 code.

Fatigue notch factor and notch size effect are higher in axial fatigue than in torsional fatigue. One explanation is that notch stress concentration in torsional fatigue ($\tau_{z\theta}/\tau_{net}$) is lower than that in axial fatigue (σ_{zz}/σ_{net}). Further, the factory-roof fracture in torsional fatigue results in high resistance to crack propagation. Under both mode I and mode III loadings, the stress fields at V-notch tip are singular. They are uniquely determined by the mode I and mode III notch stress intensity factors. One should obtain the same fatigue performance within the same stress field. A remarkable experimental confirmation has been obtained. Both mode I and mode III notch stress intensity factors well correlate fatigue lives from different notches under axial fatigue and under torsional fatigue, respectively. These correlations open the door for a future study on notch fatigue behavior under combined axial-torsional loadings. Fatigue life is expected to be a function of mode I and mode III notch stress intensity factors.

RÉSUMÉ

Cette thèse a pour sujets principaux l'étude des mécanismes de fatigue à grand nombre de cycles et la prédiction de la durée de vie des métaux sollicités en traction-torsion combinée sous amplitude constante. Les effets des chargements non-proportionnels (chargement hors phase et contrainte moyenne), de l'anisotropie du matériau et des concentrations de contraintes sur le comportement en fatigue en traction-torsion combinée ont été étudiés. Différentes approches de prédiction de la durée de vie ont été évaluées ou proposées en s'appuyant sur une observation détaillée des mécanismes de fissuration en fatigue.

Dans un premier temps, une revue de la littérature a permis de rassembler les informations sur les mécanismes de fatigue et les paramètres de prédiction existants. En général, les fissures s'amorcent sur des bandes de glissement persistantes au voisinage des plans de cisaillement maximal. La propagation des fissures de stade I se produit sur le plan de cisaillement maximal et celle des fissures de stade II sur le plan de contrainte normale maximale. Dans la plupart des matériaux, la majeure partie de la durée de vie est dépensée sous le contrôle du cisaillement (amorçage et stade I de la propagation de fissure). L'amplitude maximale de la cission (déformation) sur le plan critique est le paramètre qui contrôle l'endommagement en fatigue mais la contrainte normale sur le plan critique joue un rôle secondaire non négligeable. Les auteurs utilisent différentes combinaisons des contraintes et/ou déformations pour prédire la durée de vie en fatigue. La plupart des paramètres de durée de vie peuvent être considérés comme des extensions du critère de Tresca (par exemple McDiarmid et Fatemi-Socie) ou du critère de Von-Mises (par exemple Sines et Papadopoulos) où on ajoute un second terme pour prendre en compte l'effet de la contrainte normale (contrainte normale sur le plan critique ou contrainte hydrostatique). Les paramètres basés sur le concept de plan critique sont les plus en vue à l'heure actuelle.

Des essais de fatigue à grand nombre de cycles (10^5-10^7 cycles) en contrainte contrôlée ont été réalisés sur des éprouvettes tubulaires lisses fabriquées dans un acier 1045 brut de laminage. Ces essais ont été effectués pour des chargements proportionnels (traction, torsion et chargement biaxial en phase) et des chargements non proportionnels (chargement biaxial avec déphasage de 90° et torsion cyclique avec une tension statique). La technique des répliques a été utilisée pour suivre la fissure à partir des sites d'amorçage. Les surfaces externes des éprouvettes rompues ainsi que les surfaces de rupture ont été observées en détail au microscope électronique à balayage.

Les fissures s'amorcent sur les bandes de glissement persistantes orientées dans une direction proche des plans de cisaillement maximal pour toutes les conditions de chargement. En chargement non-proportionnel, un plus grand nombre de fissures s'amorce sur le plan de cisaillement maximal où la contrainte normale (amplitude ou contrainte moyenne) est à son maximum. L'amorçage des fissures est un processus contrôlé par le cisaillement et assisté par la contrainte normale de traction qui agit sur le plan de cisaillement maximal. Les deux stades de la propagation sont distinctement observés pour les trois conditions de chargement: torsion cyclique, fatigue en phase et fatigue hors phase avec un rapport λ élevé. La transition du stade I au stade II pourrait correspondre à une barrière microstructurale en profondeur. La durée de vie dépensée sous le contrôle du cisaillement représente une part importante de la durée de vie totale. Les paramètres de plan critique fondés sur le cisaillement sont appropriés pour prédire la durée de vie en fatigue. Dans le cas du chargement spécial (ϕ=90°; λ=0.5) où les amplitudes de cisaillement sont égales quel que soit l'orientation du plan, l'amorçage (tous les grains de ferrite bien orientés) et la propagation (pas de coalescence des fissures en stade II et bifurcation de fissures) sont plus faciles.

Huit paramètres de durée de vie en fatigue multiaxiale ont été évalués quant à leur capacité à prédire la durée de vie dans différentes conditions de chargement (incluant le chargement hors phase et la torsion cyclique avec une contrainte axiale statique). Il y a quatre paramètres basés sur les contraintes (Tresca, McDiarmid, Dang-Van et

Papadopoulos), trois basés sur les déformations (KBM, Wang-Brown, Fatemi-Socie) et un basé sur l'énergie (GWP). Deux séries de données (nos propres données et celles de la littérature) sur la fatigue biaxiale à grand nombre de cycles dans les aciers ferrito-perlitiques ont été utilisées lors de cette évaluation.

L'amplitude de cisaillement maximal (paramètre de Tresca) ne suffit pas à prédire la durée de vie en fatigue biaxiale. Les paramètres qui incluent un terme de contrainte/déformation normale peuvent assez bien prédire la durée de vie en fatigue pour un chargement en phase et pour un chargement hors phase avec un faible λ. La durée de vie en fatigue pour un chargement hors phase avec un λ élevé est souvent sous-estimée. L'atténuation par l'angle de déphasage de l'effet de l'amplitude de la contrainte normale sur le plan critique explique cette sous-estimation. Cependant, une déformation plastique macroscopique non négligeable peut se produire au-dessus de la limite d'endurance. Par conséquent, un paramètre utilisant une combinaison de déformation et de contrainte peut être nécessaire pour prendre en compte les différences de réponse contrainte-déformation entre les chargements en phase et hors phase.

La contrainte maximale sur le plan critique est plus appropriée que la contrainte hydrostatique maximale pour tenir compte des effets de la contrainte moyenne et de l'amplitude de contrainte normale. La durée de vie en fatigue dans le cas du chargement spécial (ϕ=90°; λ=0.5) est souvent surestimée. Cette surestimation est attribuée à des mécanismes plus endommageants dans l'amorçage et la propagation des fissures. Une modification du paramètre de McDiarmid est proposée; un facteur d'endommagement additionnel (" Extra Damage Factor " - EDF) est introduit afin d'obtenir une prédiction conservatrice pour toutes les conditions de chargement étudiées.

Les effets de l'anisotropie du matériau sur les mécanismes de fissuration et sur la durée de vie ont été étudiés à partir d'essais sur des éprouvettes tubulaires lisses réalisées dans un alliage d'aluminium 7075; cet alliage possède des grains allongés et de nombreuses inclusions allongées dans la direction longitudinale. Trois conditions de chargement ont

été utilisées: la fatigue axiale, la torsion cyclique et la torsion cyclique avec une contrainte de traction statique. Le dernier type de chargement introduit une compétition entre deux mécanismes de défaillance: un mécanisme de plan critique (fissuration en cisaillement transversal due à la charge de traction statique) et un mécanisme favorisé par l'anisotropie (fissuration en cisaillement longitudinal sur le plan le plus faible du matériau). Le matériau a été étudié à l'état sous-vieilli et à l'état sur-vieilli.

En fatigue axiale, aucun effet de l'anisotropie n'est observé. En torsion cyclique, l'effet de l'anisotropie est plus important pour le matériau sous-vieilli que pour le matériau sur-vieilli. Le fibrage mécanique joue un rôle dans les deux matériaux mais le glissement planaire et la texture (111) du matériau sous-vieilli augmente la faiblesse du plan longitudinal, ce qui se traduit par une faible performance en torsion cyclique (rupture cristallographique). La fissuration en cisaillement transversal se produit seulement quand la contrainte de traction statique est suffisante. Le matériau sous-vieilli n'a pas la même résistance à la fissuration en cisaillement longitudinal qu'à la fissuration en cisaillement transversal. Deux relations entre la contrainte et la durée de vie sont nécessaires pour prédire la durée de vie en fatigue lorsque deux mécanismes de rupture différents sont impliqués. Dans le matériau sur-vieilli, l'effet de l'anisotropie est moins important et le paramètre de McDiarmid peut corréler relativement bien les durées de vie obtenues pour les trois conditions de chargement.

L'effet d'entaille sur les comportements en fatigue axiale et en torsion cyclique a été étudié sur deux géométries d'éprouvettes cylindriques dotées d'entaille en V fabriquées à partir d'un matériau 1045 brut de laminage. Les éprouvettes ont un même angle d'entaille de 90° mais une profondeur d'entaille différente. Des calculs par éléments finis ont été réalisés à l'aide du logiciel Catia V5 afin d'analyser en détail les contraintes en fond d'entaille tant pour le chargement en mode I que pour celui en mode III.

Le facteur de réduction de la résistance en fatigue et l'effet d'échelle de l'entaille sont plus élevés en fatigue axiale qu'en torsion cyclique. Cela pourrait s'expliquer par un

coefficient théorique de concentration de contraintes plus faible en fatigue-torsion ($\tau_{z\theta}$ / τ_{net}) qu'en fatigue axiale (σ_{zz} / σ_{net}). De plus, la rupture en " toit d'usine " en torsion cyclique s'accompagne d'une résistance accrue à la propagation de fissures. Les champs de contraintes au fond de l'entaille en V sont singuliers tant en mode I qu'en mode III. Ils sont déterminés uniquement par les facteurs d'intensité de contrainte de l'entaille en mode I et en mode III. A un même champ de contraintes devrait correspondre une même performance en fatigue. L'expérience apporte une remarquable confirmation de cette hypothèse. Les facteurs d'intensité de contrainte de l'entaille en mode I et en mode III corrèlent bien les durées de vie obtenues pour différentes entailles sollicitées en fatigue axiale et en torsion cyclique respectivement. Ces corrélations ouvrent la voie à une étude future sur le comportement en fatigue d'éprouvettes entaillées soumises à un chargement en traction et torsion combinées. Dans ces conditions, la durée de vie en fatigue devrait être une fonction des facteurs d'intensité de contrainte de l'entaille en mode I et en mode III.

CONDENSÉ EN FRANÇAIS

Introduction

Cette thèse dans le domaine de la fatigue biaxiale des métaux porte à la fois sur les mécanismes d'amorçage et de propagation des fissures et sur la prédiction de la durée de vie en chargement d'amplitude constante. La recherche est limitée au régime de fatigue à grand nombre de cycles où la déformation cyclique macroscopique est principalement élastique. Les essais de fatigue ont été réalisés à température ambiante en contraintes imposées avec une machine servo-hydraulique biaxiale qui permet de combiner des chargements axiaux et des chargements de torsion sur des éprouvettes cylindriques. La technique des répliques est utilisée pour suivre en surface l'évolution des fissures à partir de leur site d'amorçage. Les surfaces externes et les surfaces de rupture ont été aussi observées directement sous le microscope électronique à balayage.

Quatre principaux objectifs ont été visés:

- L'analyse microscopique des mécanismes de fatigue biaxiale dans l'acier 1045 en chargements proportionnels et non-proportionnels (torsion alternée avec chargement axial alterné et déphasé ou avec tension axiale statique).
- L'évaluation critique de différents paramètres de fatigue multiaxiale, basés sur les contraintes et/ou les déformations, à pouvoir prédire la durée de vie à grand nombre de cycles d'un acier ferrito-perlitique.
- L'étude des effets de l'anisotropie d'un matériau pour des essais de fatigue en torsion alternée, avec différents niveaux de tension statique, d'un alliage d'aluminium 7075 dans les états sous-vieilli et sur-vieilli.
- L'étude des effets d'entaille sur la fatigue axiale et la fatigue en torsion de l'acier 1045, avec une approche de mécanique linéaire élastique de la rupture développée pour le cas d'entailles sévères en forme de V.

Étude bibliographique (chap. I)

L'information disponible dans la littérature est d'abord analysée. Les fissures s'amorcent en général à partir de bandes persistantes de glissement dont l'orientation correspond aux plans d'amplitude de cisaillement maximale. La propagation en stade I continue sur ces plans de cisaillement maximal, puis il y a la propagation en stade II sur les plans où l'amplitude de contrainte normale est maximale. Pour la plupart des matériaux, une grande partie de la durée de vie est contrôlée par le cisaillement (amorçage et propagation en stade I). L'amplitude de cisaillement maximale sur le plan critique est la force motrice de la fatigue, mais la contrainte normale sur le plan critique joue un deuxième rôle important. Les auteurs proposent différents paramètres combinant des contraintes et/ou des déformations pour prédire la durée de vie. La plupart des paramètres sont des extensions du critère de Tresca (ex: McDiarmid, Fatemi-Socie) ou de celui de Von Mises (ex: Sines, Papadopoulos) qui incluent un deuxième terme pour prendre en compte l'effet de la contrainte normale (ex: contrainte normale sur le plan critique ou contrainte hydrostatique). Les paramètres basés sur le concept de plan critique deviennent les plus en vue à l'heure actuelle.

Objectifs du travail (chap. II)

Les objectifs du travail, énoncés en introduction dans ce condensé, sont décrits dans le deuxième chapître.

Mécanismes de fatigue biaxiale dans des échantillons tubulaires faits d'acier 1045 (chap. III)

Des essais de fatigue à grand nombre de cycles (10^5-10^7 cycles) ont été réalisés sur des échantillons tubulaires à paroi mince faits d'acier 1045. Cinq cas de chargement sont considérés: chargement axial alterné, chargement de torsion alternée, chargements

biaxiaux en phase (λ=0,5) et déphasés (ϕ=90^0; λ=2 et λ=0,5), et chargement de torsion alternée avec différents niveaux de tension axiale statique.

Les fissures s'amorcent en surface depuis des bandes persistantes de glissement dans des grains de ferrite bien orientés. Quel que soit le cas de chargement, la plupart des fissures s'amorcent sur les plans d'amplitude de cisaillement maximale. L'amorçage des fissures est contrôlé par le cisaillement mais les contraintes normales de tension assistent le processus. En chargements non-proportionnels, davantage de fissures s'amorcent sur le plan de cisaillement maximal où la contrainte normale (cyclique ou statique) est la plus grande.

La propagation de la fissure fatale continue sur ce plan critique (stade I) puis elle bifurque sur un plan où l'amplitude de contrainte normale est maximale (stade II). Les deux stades de propagation ont été clairement mis en évidence dans trois cas de chargement: torsion pure et chargements biaxiaux en phase (λ=0,5) et déphasés (λ=2; ϕ=90°). La transition stade I / stade II est difficile à discerner en chargement axial où il y un nombre infini de plans critiques. Pour le chargement biaxial déphasé (λ=0,5; ϕ=90°), il n'y a pas de bifurcation en stade II puisque la fissure en stade I se propage déjà sur un plan où l'amplitude de contrainte normale est maximale.

Les durées de vie de propagation en surface et les facteurs de forme des fissures (longueur/profondeur) varient selon les cas de chargement. Cependant, les courbes de croissance des fissures en fonction de la durée de vie relative se rejoignent approximativement quand cette croissance est mesurée par la profondeur des fissures. En d'autres mots, la proportion de durée de vie nécessaire pour amorcer une fissure de profondeur donnée ne dépendrait pas du type de chargement. En particulier, la transition entre le stade I et le stade II a lieu à environ 30%-45% de la durée de vie totale dans la région de 10^5 à 10^6 cycles. Alors que la longueur des fissures en stade I varie de 50 µm à 750 µm selon le cas de chargement, leur profondeur est approximativement la même, de

l'ordre de 20 µm à 40 µm. La transition stade I/stade II pourrait correspondre à une barrière microstructurale en profondeur.

Le chargement biaxial déphasé (λ=0,5; ϕ=90°) est un cas particulier puisque l'amplitude de cisaillement est la même quelle que soit l'orientation du plan. Tous les grains sont bien orientés et l'amorçage des fissures est plus facile. La densité surfacique des fissures est beaucoup plus élevée que celle des autres cas de chargement. La propagation est accélérée par la coalescence des fissures et par l'absence de bifurcation en stade II. Dans ce cas particulier de chargement, des mécanismes plus endommageants agissent à la fois dans l'amorçage et la propagation des fissures.

Une fraction importante de la durée de vie est contrôlée par le cisaillement (amorçage et propagation en stade I). Les paramètres basés sur l'amplitude de cisaillement maximale sont donc bien appropriés pour prédire la durée de vie en fatigue biaxiale de l'acier 1045. Il faudrait cependant prendre en compte les mécanismes plus endommageants qui agissent dans le cas de chargement particulier où l'amplitude de cisaillement est égale sur tous les plans.

Évaluation de la capacité de paramètres de plan critique à prédire la durée de vie en fatigue biaxiale (chap. IV)

Huit paramètres de fatigue multiaxiale ont été évalués quant à leur capacité à prédire la durée de vie à grand nombre de cycles dans différents cas de chargement (notamment les chargements biaxiaux déphasés et la torsion alternée avec tension axiale statique). Il y a quatre paramètres basés sur les contraintes (Tresca, Mc Diarmid, Dang-Van et Papadopoulos), trois paramètres basés sur les déformations (Kandil-Brown-Miller (KBM), Wang-Brown et Fatemi-Socie) et un paramètre basé sur l'énergie (Glinka-Wang-Plumtree (GWP)). Tous exploitent le concept de plan critique (contrainte ou déformation de Tresca) sauf le paramètre de Papadopoulos qui est une extension du critère de Von

Mises. Nous avons utilisé deux jeux de données: les durées de vie obtenues avec notre propre programme d'essais et celles obtenues par un autre auteur sur un acier ferrito-perlitique.

Le paramètre de Tresca ne peut pas corréler les durées de vie de fatigue biaxiale à cause des effets de contrainte normale. La performance en fatigue décroît avec l'accroissement de l'amplitude ou de la valeur statique de la contrainte normale sur le plan critique. Le paramètre de Tresca doit être modifié. Le paramètre GWP, qui prend en compte les effets de contrainte normale, ne permet pas de consolider les durées de vie obtenues en chargement axial et en torsion pure, mais il donne une corrélation globale raisonnable. Les six autres paramètres, qui utilisent une constante k pour ajuster les données en chargement axial et en torsion pure, corrèlent bien les durées de vie obtenues en chargement biaxial en phase et en chargement biaxial déphasé de rapport $\lambda<0,5$. Les durées de vie obtenues dans les autres cas (chargement biaxial déphasé de rapports $\lambda>0,5$ et $\lambda=0,5$, et torsion alternée avec tension axiale statique) sont sous-estimées ou surestimées selon les cas.

En chargement biaxial déphasé de rapport $\lambda>0,5$, les paramètres de McDiarmid, Fatemi-Socie et KBM sous-estiment les durées de vie. Ceci peut s'expliquer par un plus faible effet de la contrainte normale sur la plan critique, puisqu'elle est déphasée à 90° du cisaillement maximal. Le paramètre de Wang-Brown, qui prend en compte ce déphasage, donne une meilleure corrélation. Les paramètres de Dang-Van et de Papadopoulos, dont le deuxième terme est la contrainte hydrostatique, fonctionnent bien aussi dans ce cas.

L'amplitude et la valeur statique de la contrainte normale sur le plan critique ont a priori des effets différents. La première est une force motrice en mode I et la deuxième a un effet d'ouverture. La contrainte normale maximale sur le plan critique rend compte des deux effets. Les paramètres de McDiarmid et de Fatemi-Socie donnent une bonne prédiction de la durée de vie en torsion alternée avec tension axiale statique. Les

paramètres de KBM et de Wang-Brown ne rendent pas compte de l'effet statique de la contrainte normale puisque le deuxième terme de ces paramètres est une amplitude de déformation. Les paramètres de Dang-Van et de Papadopoulos, qui utilisent la contrainte hydrostatique maximale, surestiment la durée de vie en torsion alternée avec tension axiale statique. La partie statique de la contrainte hydrostatique contribue davantage à la fatigue que la partie cyclique.

La plus mauvaise performance obtenue dans le cas particulier du chargement déphasé de rapport λ=0,5 est attribuée à des mécanismes plus endommageants qui agissent à la fois dans l'amorçage et dans la propagation des fissures. Ceci explique pourquoi la plupart des paramètres surestiment la durée de vie dans ce cas de chargement. Pour obtenir une prédiction conservatrice, le paramètre de McDiarmid peut être modifié en introduisant un facteur d'endommagement supplémentaire (EDF=extra damage factor). Ce facteur peut être calibré par le rapport entre la résistance en torsion pure et celle mesurée dans le cas particulier où ϕ=90° et λ=0,5.

L'évaluation précédente des paramètres de fatigue multiaxiale a été faite dans le régime de fatigue à grand nombre de cycles, en supposant que la réponse contrainte-déformation du matériau est totalement élastique. Cependant la déformation plastique peut ne pas être négligeable au-dessus de la limite d'endurance. Dans ces conditions, un paramètre basé sur une combinaison de contrainte et de déformation (ex: le paramètre de Fatemi-Socie) peut être requis pour rendre compte d'une différence de réponse contrainte-déformation entre les chargements en phase et les chargements déphasés (durcissement cyclique plus important en chargement déphasé). De meilleures prédictions de la durée de vie pourraient être obtenues en chargement déphasé de rapport λ>0,5. Toutefois, l'effet néfaste observé dans le cas particulier de chargement déphasé de rapport λ=0,5 ne pourrait pas être pris en compte.

Comportement en fatigue biaxiale d'un alliage d'aluminium 7075 sous-vieilli et sur-vieilli: effets de l'anisotropie du matériau (chap. V)

Des effets d'anisotropie sur les mécanismes de fissuration et les durées de vie ont été étudiés par des essais réalisés sur des échantillons tubulaires à paroi mince faits d'alliage d'aluminium 7075. Cet alliage a des grains allongés et un important fibrage inclusionnaire dans la direction longitudinale. Trois cas de chargement sont considérés: chargement axial alterné, torsion alternée et torsion alternée avec différents niveaux de tension axiale statique. Ce dernier cas de chargement introduit une compétition entre deux mécanismes de rupture: un mécanisme de plan critique (fissuration par cisaillement transversal favorisée par la tension axiale statique) et un mécanisme favorisé par l'anisotropie du matériau (fissuration par cisaillement longitudinal sur le plan faible du matériau). L'alliage 7075 a été éprouvé dans chaque cas dans les états sous-vieilli et sur-vieilli.

En chargement axial, aucun effet d'anisotropie n'apparaît puisque le plan de faiblesse longitudinal n'est pas soumis au cisaillement. En torsion pure, l'anisotropie est mise en évidence car un plan de cisaillement maximal correspond au plan de faiblesse du matériau. On observe une fissuration par cisaillement longitudinal, en particulier à haut niveau de contrainte. Les effets d'anisotropie sont plus importants dans le matériau sous-vieilli que dans le matériau sur-vieillli. En torsion alternée avec tension statique, la fissuration redevient transversale pour une faible tension statique dans le matériau sur-vieilli, tandis qu'elle reste longitudinale dans le matériau sous-vieilli tant que la tension statique n'est pas suffisamment élevée. Le fibrage inclusionnaire joue un rôle dans les deux matériaux, mais la combinaison d'une texture (111) et d'un glissement planaire dans le matériau sous-vieilli accroît sa faiblesse sur le plan longitudinal (rupture cristallographique).

Pour une même amplitude de cisaillement maximal, la durée de vie du matériau sur-vieilli est plus élevée en torsion pure qu'en chargement axial. L'application d'une tension statique fait décroître la durée de vie en torsion. L'inverse se produit pour le matériau sous-vieilli. La durée de vie en torsion pure est plus faible qu'en chargement axial et elle ne décroît pas avec l'application d'une tension statique. Ces différences s'expliquent par le fait que le matériau sous-vieilli n'a pas la même résistance à la fissuration par cisaillement longitudinal qu'à la fissuration par cisaillement transversal.

Pour le matériau sur-vieilli, l'effet d'anisotropie est peu important. Un paramètre tel que celui de McDiarmid peut faire une corrélation raisonnable des durées de vie obtenues dans les trois cas de chargement. Par contre la forte anisotropie du matériau sous-vieilli nécessite deux relations contrainte-durée de vie pour prendre en compte sa différence de résistance à deux mécanismes de fissuration. Chaque relation peut être calibrée par différents cas de chargement pour lesquels le même mécanisme se produit. La prédiction de la durée de vie pour un chargement donné consistera à prendre la plus petite des durées de vie calculées par les deux relations. Ces conclusions sont cependant basées sur un nombre d'essais limité. Elles restent à confirmer par une étude plus approfondie.

Comportement en fatigue axiale et en fatigue par torsion de cylindres entaillés faits d'acier 1045 (chap. VI)

Des effets d'entaille en chargement axial alterné et en torsion alternée ont été étudiés par des essais réalisés sur des échantillons cylindriques faits d'acier 1045 et entaillés en V autour de leur circonférence. Deux géométries d'entaille de même angle mais de profondeur différente sont considérées. Elles ont été usinées pour avoir un rayon d'entaille aussi faible que possible (<0,075mm). Des analyses détaillées des champs de contrainte en fond d'entaille, en mode I et en mode III, ont été effectuées avec le code d'éléments finis Catia V5.

Le facteur d'entaille en fatigue et l'effet d'échelle (taille de l'entaille) sont plus importants en chargement axial qu'en torsion. Une explication vient des champs de contrainte: le profil de concentration de contrainte en torsion ($\tau_{z\theta}$ / τ_{net}) est plus faible que celui en chargement axial (σ_{zz} / σ_{net}). De plus le type de rupture en torsion résulte en une plus grande résistance à la propagation. Même si la rupture a lieu localement en mode I dans les deux cas de chargement, le faciès de rupture est plat en chargement axial tandis qu'il forme un profil en " toit d'usine " en torsion. La résistance en torsion à la propagation des fissures est presque la même que celle à l'amorçage des fissures dans les échantillons lisses tubulaires, si la comparaison est basée sur la contrainte de cisaillement nominale.

L'analyse numérique des contraintes confirme que les champs de contrainte au fond des entailles en V sont singuliers en chargement axial et en torsion. Ces champs de contrainte sont déterminés uniquement par des facteurs d'intensité de contrainte en mode I et en mode III respectivement. Un champ de contrainte donné doit résulter en une même durée de vie en fatigue. Ce principe de similitude est bien confirmé expérimentalement. Les facteurs d'intensité de contrainte de l'entaille en mode I et en mode III corrèlent bien les durées de vie obtenues pour les deux géométries (entailles de profondeur différente), sollicitées en chargement axial et en torsion respectivement. Ces corrélations ouvrent la porte à une future étude sur la fatigue de pièces entaillées en chargement biaxial. Il est logique de s'attendre à ce que la durée de vie soit fonction d'une combinaison des deux facteurs d'intensité de contrainte, en mode I et en mode III.

Conclusion générale

La prédiction de la durée de vie doit se baser sur une bonne connaissance des mécanismes de fatigue. Pour des pièces lisses faites d'un matériau où la fissuration par cisaillement domine la durée de vie (acier 1045, alliage d'aluminium 7075), il est approprié d'utiliser un paramètre de plan critique basé sur le critère de Tresca (ex:

McDiarmid, Fatemi-Socie). Mais, pour faire une prédiction conservatrice de la durée de vie, une modification est nécessaire pour prendre en compte les mécanismes plus endommageants qui ont lieu dans le cas particulier d'un chargement où l'amplitude du cisaillement est la même sur tous les plans. Dans le cas d'une forte anisotropie (alliage d'aluminium 7075 sous-vieilli), la fissuration par cisaillement longitudinal sur le plan faible du matériau devrait aussi être prise en compte dans la prédiction de la durée de vie. Pour les entailles sévères, où la fatigue est contrôlée par la propagation des fissures courtes, il est préférable d'utiliser une approche de type mécanique de la rupture. Les champs de contrainte au fond des entailles en V sont caractérisés par des facteurs d'intensité de contrainte en mode I et en mode III. Ces deux facteurs d'intensité de contrainte en entaille corrèlent bien les durées de vie de deux géométries de profondeur différente, sollicitées respectivement en chargement axial et en torsion.

TABLE OF CONTENTS

DÉDICACE..... iv

ACKNOWLEDGMENT..... v

ABSTRACT..... vi

RÉSUMÉ..... x

CONDENSÉ EN FRANÇAIS..... xv

TABLE OF CONTENTS..... xxv

LIST OF TABLES..... xxxi

LIST OF FIGURES..... xxxii

NOMENCLATURE..... xliii

INTRODUCTION..... 1

CHAPTER I - LITERATURE SURVEY..... 9

1.1 Basic notions..... 9

1.2 Biaxial fatigue mechanisms..... 14

1.2.1 Crack initiation mechanisms..... 14

1.2.1.1 Crack initiation along persistent slip bands (PSBs)..... 14

1.2.1.2 Crack initiation at defects in materials..... 17

1.2.1.3 Intergranular crack initiation..... 18

1.2.1.4 Crack initiation at stress concentrations..... 19

1.2.2 Crack propagation mechanisms..... 19

1.2.2.1 The three modes of crack growth..... 19

1.2.2.2 The three stages of fatigue crack propagation..... 20

1.2.3 The three regions of fatigue behavior..... 23

1.2.4 Case A and Case B cracks..... 26

1.3 Non-proportional loadings 28
1.3.1 Out-of-phase loading 28
1.3.1.1 Out-of-phase loading and fatigue mechanisms 29
1.3.1.2 Effects of out-of-phase loading on fatigue life 30
1.3.2 Mean stress effects 32
1.3.2.1 Normal mean stress effects 33
1.3.2.2 Shear mean stress effects 36
1.3.2.3 Biaxial mean stress effects 37
1.4 Multiaxial fatigue life parameters 40
1.4.1 Stress-based parameters 41
1.4.1.1 Early parameters 41
1.4.1.2 Extensions of the static yield criteria 42
1.4.1.3 Modifications to von Mises criterion 44
1.4.1.4 Modifications to Tresca criterion (critical plane parameters) 46
1.4.2 Strain-based parameters 48
1.4.2.1 Extensions of the static yielding criteria 48
1.4.2.2 Critical-plane parameters (modifications to Tresca criterion) 49
1.4.3 Energy-based parameters 51
1.4.3.1 Parameters involving a critical plane 52
1.4.3.2 Modification to von Mises criterion 53
1.4.4 Remarks on the multiaxial fatigue life parameters 54
1.5 Material anisotropy effects 54
1.5.1 Orientation-dependent fatigue behavior of anisotropic material 55
1.5.2 Anisotropic material versus isotropic material 58
1.6 Characterization of crack growth under multiaxial fatigue 59
1.6.1 Long crack growth under multiaxial fatigue 59
1.6.1.1 Mixed mode I-mode II loading 60
1.6.1.2 Mixed mode I-mode III loading 62
1.6.2 Short crack propagation 65

1.7 Notch effects 69
1.7.1 Local stress/strain approaches 69
1.7.2 Critical distance approaches 71
1.7.3 Fracture mechanics approaches 72
1.7.4 Notch stress intensity factor 77
1.8 Critical summary of literature review 80

CHAPTER II -OBJECTIVES 85

CHAPTER III - BIAXIAL FATIGUE MECHANISMS IN SMOOTH TUBULAR SPECIMENS MADE OF AS-ROLLED 1045 STEEL 88

3.1 Introduction 88
3.2 Experiments 89
3.2.1 Material 89
3.2.2 Specimen geometry and preparation 91
3.2.3 Fatigue tests 94
3.2.4 Fatigue cracking monitoring 97
3.3 Observation on biaxial fatigue cracking mechanisms 99
3.3.1 Crack initiation 99
3.3.2 Crack propagation 105
3.3.3 Crack length and depth versus cycle life 113
3.4 Discussion 125
3.4.1 Factors influencing crack initiation 125
3.4.2 Stage I and stage II crack propagation 126
3.4.3 Relative life consumed under shear control 128
3.4.4 Special loading case (90^0 out-of-phase; λ=0.5) 129

CHAPTER IV - EVALUATION OF CRITICAL-PLANE FATIGUE LIFE PREDICTION PARAMETERS 131

4.1 Introduction 131
4.2 The eight parameters 132

4.3 Fatigue data 134
4.4 Parameter computation and stress analysis 136
4.5 Evaluation results 140
4.5.1 The Tresca and GWP parameters 140
4.5.2 The six other parameters 141
4.5.2.1 90° out-of-phase loading 141
4.5.2.2 Torsional fatigue with mean tensile stress (Data 1 only) 142
4.6 Discussion 147
4.6.1 High λ out-of-phase loading and phase angle effects 147
4.6.2 Tensile mean stress effects (data 1 only) 149
4.6.3 Extra damage in the special loading case (90° out-of-phase; λ= 0.5) 150
4.7 Summary 154

CHAPTER V - BIAXIAL FATIGUE BEHAVIOR OF UNDERAGED AND OVERAGED 7075 ALUMINUM ALLOY: MATERIAL ANISOTROPY EFFECTS 157

5.1 Introduction 157
5.2 Experiments 159
5.2.1 Material 159
5.2.2 Specimen geometry 163
5.2.3 Fatigue tests 164
5.3 Observations of fatigue cracking mechanisms 165
5.3.1 Surface crack evolution 165
5.3.1.1 In overaged material 165
5.3.1.2 In underaged material 170
5.3.2 Surface crack length versus life ratio 173
5.3.3 Fracture surface observations 175
5.3.3.1 Macroscopic observations 175
5.3.3.2 Microscopic observations 177

5.4 Fatigue life 180
5.4.1 Overaged material 180
5.4.2 Underaged material 181
5.4.3 Static tensile stress effects 182
5.5 Discussion and analysis 183
5.5.1 Anisotropy effects and materials 183
5.5.2 Anisotropy effect and stress level 187
5.5.3 Fatigue life prediction parameters 187
5.6 Summary 190

CHAPTER VI - AXIAL AND TORSIONAL FATIGUE BEHAVIOR OF CIRCUMFERENTIALLY V-NOTCHED CYLINDERS MADE OF AS-ROLLED 1045 STEEL 193

6.1 Background of this study 193
6.2 Experiments 195
6.2.1 Material 195
6.2.2 Specimen geometry 196
6.2.3 Fatigue tests 199
6.3 Fatigue life results 200
6.3.1 Axial fatigue 204
6.3.2 Torsional fatigue 207
6.4 Fractography 210
6.4.1 Axial fatigue 210
6.4.2 Torsional fatigue 213
6.5 Correlations between fatigue lives and notch SIFs 218
6.5.1 Finite element analysis and notch stress intensity factors 218
6.5.1.1 Mode I notch stress intensity factors (K_I^{N1} and K_I^{N2}) 218
6.5.1.2 Mode III notch stress intensity factors (K_{III}^{N1} and K_{III}^{N2}) 221
6.5.2 Fatigue life and notch stress intensity factor 224
6.6 Notch effects versus loading conditions 227

6.7 Summary 229

CONCLUSIONS 231

STATEMENT OF ORIGINALITY AND CONTRIBUTIONS TO KNOWLEDGE 238

REFERENCES 239

APPENDIX I - STRESS ANALYSIS OF THE THIN-WALLED TUBULAR SPECIMEN UNDER AXIAL-TORSIONAL LOADING 267

APPENDIX II - STRESS ANALYSIS OF CIRCUMFERENTIALLY V-NOTCHED CYLINDRICAL SPECIMENS UNDER AXIAL AND TORSIONAL LOADINGS 273

LIST OF TABLES

Table 3.1 Chemical composition and tensile properties of as-rolled 1045 steel 90
Table 3.2 Biaxial tests and fatigue lives 96
Table 3.3 Crack aspect ratios for several loading cases. 115

Table 4.1 The eight parameters to be evaluated. 134
Table 4.2 Data 2 from Nishihara and Kawamoto (1942). 136
Table 4.3 Fatigue life parameters computed for different loading cases 137

Table 5.1 Chemical composition of 7075 aluminum alloy (in weight %). 159
Table 5.2 Tensile properties of 7075 aluminum alloy (T7351). 159
Table 5.3 Fatigue tests and life data of underaged and overaged 7075 aluminum alloys 164

Table 6.1 Geometry specifications of the two notched specimens (Figures 6.1 and 6.2). 199
Table 6.2 Axial fatigue tests and life results for N1 and N2 specimens. 199
Table 6.3 Torsional fatigue tests and life results for N1 and N2 specimens. 200

LIST OF FIGURES

Figure 1.1 Typical specimens for biaxial fatigue tests. (a) Thin-walled tubular specimen (Lissenden et al, 1997); (b) Cruciform specimen (Batolotta et al, 1997). (All dimensions are in millimeters) 10

Figure 1.2 Principal stress/strain ratios reached (cross-hatched areas) under different loadings on a thin-walled tubular specimen. 11

Figure 1.3 Correlation of axial and torsional fatigue lives 14

Figure 1.4 Scanning electron micrograph showing extrusions and intrusions on the surface of a Cu crystal fatigued at room temperature for 120000 cycles at γ_p= 0.002 (Ma and Laird, 1989) 15

Figure 1.5 Scanning electron micrograph showing the nucleation of a fatigue crack normal to the tensile axis (vertical direction) at the site of an $MnO\text{-}SiO_2\text{-}Al_2O_3$ inclusion that is partially debonded from the 4340 steel matrix denoted M. (Lankford and Kusenberger, 1973) 18

Figure 1.6 The three basic modes of crack growth. (a) Tensile opening (Mode I). (b) In-plane shear (Mode II). (c) Anti-plane shear (Mode III) (Suresh, 1998). 20

Figure 1.7 Illustration of Stage I and Stage II fatigue crack propagation (Brown, 1988). 21

Figure 1.8 Crack density versus orientation at (a) 25% and (b) 95% of the lifetime. Curves A and B (solid and dashed lines) show the variation of the normal and shear stress amplitudes acting on the crack plane, respectively. These stress amplitudes are normalized with respect to the applied axial or torsional stress amplitude (λ, stress ratio; Φ, phase angle; N/N_f, life ratio). (Ohkawa et al, 1997) 22

Figure 1.9 Cracking behaviors observed in 304 stainless steel 24

Figure 1.10 Cracking behaviors observed in Inconel 718. 25

Figure 1.11 Case A and Case B crack formation, showing the importance of the free surface (cross hatched) orientation in multiaxial fatigue cracking (Brown and Miller, 1973). 27

Figure 1.12 (a) A cylindrical specimen subjected to combined axial and torsional loadings. (b) Strain-time history for proportional loading where the axial and torsional strains are in-phase. (c) Strain-time history for non-proportional loading where the axial and torsional strains are 90^0 out-of-phase. (d) Loading paths for in-phase (straight line) and 90^0 out-of-phase loading (circle) in normalized strain space. 29

Figure 1.13 (a) Maximum shear strain range versus fatigue lives in 1%-Cr-Mo-V steel. (b) Fatigue life as a function of normal strain range on maximum shear planes at the same maximum shear strain range (3%) in 1%-Cr-Mo-V steel (Kanazawa, 1977). 31

Figure 1.14 Characteristics of fatigue crack growth in torsion. 35

Figure 1.15 Loading histories employed by Socie and Shield (1984). 38

Figure 1.16 Crack observed under the loading histories in Figure 1.15 (the specimen axis is vertical in each photo; the scale is shown at the upright of this figure). 39

Figure 1.17 Combined mode I-mode II fatigue fracture envelope for AISI 316 stainless steel showing the locus of onset of fatigue crack growth (solid curve). The dashed curve indicates the mixed loading conditions at which fatigue fracture occurs on a plane normal to the maximum hoop stress, $\sigma_{\theta\theta}$ (Gao et al, 1985) 62

Figure 1.18 Variation of mode I and mode III fatigue crack growth rates with nominal values of $(\Delta CTD)_I$ and $(\Delta CTD)_{III}$, respectively, in 4340 steel (Tschegg, 1983). 63

Figure 1.19 Variation of mode III fatigue crack growth rates as a function of crack depth a. (measured from the tip of the circumferential notch in the cylindrical specimen) in AISI 1018 steel. The numbers shown for

each curve correspond approximately to the fixed values of $(\Delta CTD)_{III}$ in millimeters (Tschegg, 1983). 64

Figure 1.20 Typical fatigue crack-growth behaviors for short and long cracks. 66

Figure 1.21 Measured crack length histories and fitted polynomials for individual crack under torsional fatigue at $\Delta\tau$=500 MPa (Perez Carbonell and Brown, 1986). 67

Figure 1.22 The fatigue limit depends on notch depth, threshold stress intensity factor and stress concentration factor. Note that the fatigue limit is independent of the stress concentration factor at K_T = Z. (Smith and Miller, 1977) 72

Figure 1.23 Crack growth rate from the root of a notch: the driving force is assumed to be the sum of two contributions: one from the notch plasticity, the other from the crack tip plasticity (Smith and Miller, 1978). 74

Figure 1.24 Fatigue crack growth rates in welds. (a) Plotted against ΔK. (b) Plotted against ΔK_{eff}. The curve in (a) indicates the trend of long crack behavior obtained in stress-relieved specimens. 74

Figure 1.25 (a) "Factory-roof" fracture surface at a low torque without static axial load. (b) Flat mode III fracture surface at a high torque without static load. (c) Correlation of mode I crack growth data with "Factory-roof" cracking and "Flat" mode III cracking. (Brown et al, 1985)....76

Figure 1.26 Illustration of V-notch 77

Figure 1.27 Nominal stress vs. "crack initiation life"....78

Figure 1.28 Notch stress intensity factor vs. "crack initiation life"....79

Figure 3.1 **(a)** Microstructure of as-rolled 1045 steel consisting of pearlite colonies (bright) and ferrite grains (dark) (transverse section etched by 2% Nital). (b) Inclusions along the rolling direction (longitudinal section without etching)....90

Figure 3.2 Specimens geometry. (a) Thin-walled tubular specimen for torsional and biaxial fatigue (wall thickness = 2 mm). (b) Hourglass solid specimen for axial fatigue (minimum diameter is 10 mm; $k_t \approx 1.07$). (Unit: mm) 92

Figure 3.3 Instron biaxial test machine (can perform static and cyclic axial-torsional tests including out-of-phase loadings; axial load = ±100kN; torque = ±1130 N.m).....94

Figure 3.4 Loading paths employed in our tests: axial fatigue, torsional fatigue, axial-torsional in-phase fatigue (λ=0.5), 90^0 out-of-phase axial-torsional with λ=0.5, 90^0 out-of-phase axial-torsional with λ=2, and torsional fatigue with static axial tension.....95

Figure 3.5 Illustration of the replica technique. These replicas are taken during an axial fatigue test on an hourglass specimen at different number of cycles (N). The replicas are observed backwards under SEM to trace the fatal crack initiation and propagation process.....98

Figure 3.6 Variations of shear stress amplitude τ_a and normal stress amplitude σ_a (normalized by the applied axial stress amplitude σ_0 or the shear stress amplitude τ_0) with plane orientation for different loading conditions. The plane orientation is defined by the angle between the normal of the plane and the specimen axis. 101

Figure 3.7 Typical slip-bands and grain-sized cracks (see arrows) observed in 1045 steel under SEM for different loading conditions. Specimen axis is horizontal in each photo.....102

Figure 3.8 Frequency of grain-size cracks and slip bands in 1045 steel at different orientations under different loading conditions. 103

Figure 3.9 Crack propagation in 1045 steel under axial fatigue. (a) N/N_f=23.2%; (b) N/N_f=55.8%; (c) N/N_f=74.5%. (The arrow on the top-left of each photo showing the specimen axis).....106

Figure 3.10 Crack propagation in 1045 steel under torsional fatigue. (a) N/N_f=24%. (b) N/N_f=58.2%. (c) N/N_f=92.5%. (Specimen axis is shown by the arrow in each photo) 108

Figure 3.11 Typical fatigue crack in 1045 steel under in-phase axial-torsional fatigue. The specimen axis is shown by the arrow at the top-left of the photo. The solid white lines at the top-right show the maximum shear planes, and the dotted white line shows the maximum normal plane. 109

Figure 3.12 Crack evolution under 90^0 out-of-phase loading (λ=2) observed on replicas taken under SEM at different lifetime. (In each photo, specimen axis is vertical; N/N_f is life ratio; cracks are pointed by arrows; white solid lines represent the critical plane while dashed lines represent the planes of maximum normal stress amplitude, see (a).) 110

Figure 3.13 Normalized shear and normal stress variations with time on the two maximum normal stress planes ($\pm 45^0$). The phase angles between shear and normal stresses on these two planes are different (arrows); the phase angle on the $+45^0$ plane is larger than that on the -45^0 plane. 111

Figure 3.14 Crack evolution in 1045 steel under 90^0 out-of-phase loading (λ=0.5) observed on replicas taken at different lifetimes. In each photo, specimen axis is vertical; cracks are pointed by arrows; white solid line in photo (a) represents the critical plane while dashed line represents the plane of maximum normal stress amplitude. 112

Figure 3.15 Surface crack length versus fatigue life ratio for several loading cases in 1045 steel, with the arrows pointing out the approximate transition from stage I to stage II. No cracks or PSBs are observed until 80% of total life under high cycle fatigue axial loading 114

Figure 3.16 Crack depth versus fatigue life ratio for several loading cases in 1045 steel (arrows pointing out the approximate transition from stage I to stage II). 116

Figure 3.17 Small cracks observed on the fracture surface in 1045 steel. The crack aspect ratio depends on the loading case..... 117

Figure 3.18 Multiple crack initiation in 1045 steel under axial fatigue observed under SEM. (a) On large scale. (b) On microscopic-scale. 118

Figure 3.19 Fracture surface of torsional fatigue in 1045 steel under SEM at low magnification. The globe fracture surface is oriented at 45^0 with respect to the specimen axis. The arrow shows the stage I crack. 119

Figure 3.20 Fracture features at area close to initiation observed in 1045 steel (arrows showing the initiation sites). 120

Figure 3.21 Fatigue fracture features at area away from the crack initiation sites observed in 1045 steel under several loading cases..... 121

Figure 3.22 Multiple slips accommodate cracking paths under different loading cases observed in 1045 steel. 122

Figure 3.23 Rubbing traces on the fracture surface observed in 1045 steel under axial-torsional in-phase and out-of-phase loadings. 123

Figure 3.24 Dimples in the static fracture area observed in 1045 steel in axial loading..... 124

Figure 4.1 Normalized shear and normal stresses on the critical plane during one loading cycle under different loading conditions..... 139

Figure 4.2 Fatigue lives plotted against the eight selected parameters (data 1). Loading conditions and symbols are given in the plot of McDiarmid parameter (b). (Continued on the next page). 143

Figure 4.3 Fatigue lives plotted against the eight parameters (data 2). Loading conditions and symbols are given in the plot of McDiarmid parameter (plot (b)). (Continued on the next page). 145

Figure 4.4 Crack densities for the different loading conditions, plotted against McDiarmid parameter (A: axial fatigue; T: torsional fatigue; In: in-phase loading; Out: out-of-phase loading; TS: torsional fatigue with static tension; the number in the parentheses is the stress ratio λ)..... 151

Figure 4.5 (a) A typical crack in the special loading case. (b) Possibility of coalescence between two cracks with different orientations (see arrow)..... 152

Figure 5.1 Aging curve of 7075 aluminum alloy at 120^0C,..... 160

Figure 5.2 Microstructures of underaged 7075 aluminum alloy in (a) longitudinal section and in (b) transverse section (Etchant: Keller's regent)..... 161

Figure 5.3 Microstructures of overaged 7075 aluminum alloys in (a) longitudinal section and (b) transverse section (Etchant: Keller's regent)..... 162

Figure 5.4 The geometry of thin-walled tubular specimen (units: mm)..... 163

Figure 5.5 Axial fatigue crack evolution in overaged 7075 aluminum alloy observed from replicas under SEM (AL7A4, σ_0=140MPa, N_f=57,449 cycles.). Arrows show two crack initiation sites. Specimen axis is vertical in each photo. (a) N=20,000 cycles. (b) N=30,000 cycles. (c) N=40,000 cycles..... 167

Figure 5.6 Surface crack evolution in overaged 7075 aluminum alloy under torsional fatigue (AL7T2, τ_0=100MPa, N_f=89,240 cycles) observed on replicas under SEM. (a) N=20,000 cycles. (b) N=30,000 cycles. (c) N=60,000 cycles. Specimen axis is vertical in each photo. Crack initiation site is pointed by arrow..... 168

Figure 5.7 Cracks in overaged 7075 aluminum alloy under torsional fatigue at low shear stress level (AL7T5, τ_0=60MPa, N_f=385,431 cycles), observed on a replica taken at 78% of total life. Specimen axis is vertical..... 169

Figure 5.8 Crack evolution in underaged 7075 aluminum alloy under torsional fatigue (ALUT2, τ_0=100MPa, N_f=35,000 cycles), observed on replicas under SEM. (a) N=10,000 cycles. (b) N=15,000 cycles. (c) N=30,000 cycles. Specimen axis is vertical in each photo. Crack initiation site is indicated by arrows. 171

Figure 5.9 Cracking behavior of underaged 7075 aluminum alloy under torsional fatigue with static tensile load, observed on replicas under SEM. (a) τ_0 =100MPa, σ_m=100MPa. (b) τ_0=100MPa, σ_m=165MPa. Specimen axis is vertical in each photo. 172

Figure 5.10 Surface crack length plotted against fatigue life ratio for different loading conditions in underaged and overaged materials (solid symbols for underaged material, and open symbols for overaged material). 174

Figure 5.11 Macro-fractures of underaged and overaged 7075 aluminum alloys under different loadings. (a) Overaged, torsional fatigue, τ_0=100MPa. (b) Underaged, torsional fatigue, τ_0=100MPa. (c) Underaged, torsional fatigue, τ_0=60MPa. (d) Underaged, torsional fatigue with static tensile load, τ_0=100MPa, σ_0=165MPa. 176

Figure 5.12 Fractographic features in 7075 aluminum alloy under axial fatigue. 178

Figure 5.13 Fractographic features in 7075 aluminum alloy under torsional fatigue. 179

Figure 5.14 Fatigue life data of overaged 7075 aluminum alloy plotted against maximum shear stress amplitude. 180

Figure 5.15 Fatigue life data of underaged 7075 aluminum alloy plotted against maximum shear stress amplitude (the values of the static tensile load σ_m refer to Table 5.3). 181

Figure 5.16 Effects of the static tensile stress on the torsional fatigue life of underaged and overaged 7075 aluminum alloys. The applied torsional stress amplitude is τ_0=100MPa for all data points. 182

Figure 5.17 The X-ray diffraction patterns on the longitudinal and the transverse planes in the overaged material (relative strength being the X-ray count normalized by the highest peak count). 185

Figure 5.18 The X-ray diffraction patterns on the longitudinal and the transverse plane in the underaged material (relative strength being the X-ray count normalized by the highest peak count). 186

Figure 5.19 Fatigue life versus McDiarmid parameter in overaged material. 189

Figure 6.1 Geometry of N1 specimen (unit: mm); notch depth is 2.86mm 196

Figure 6.2 Geometry of N2 specimen (unit: mm).; notch depth is 0.635mm 197

Figure 6.3 Normalized SIFs K_I and K_{III} plotted against a/2D for circumferentially cracked round bars. (Stars and circles show K_I and K_{III} for notches N1 and N2.) 198

Figure 6.4 Typical curve of compliance variation, plotted against fatigue lifetime under axial fatigue 202

Figure 6.5 Typical curve of compliance variation plotted against fatigue lifetime under torsional fatigue. 202

Figure 6.6 Illustration of marks, made by intermittent axial fatigue, (indicated by arrows that also show the radial crack growth direction) on the fracture surface of notched specimen under torsional fatigue. 203

Figure 6.7 Relationship between the compliance variation and the crack depth in the two types of notched specimens under torsional loading. 204

Figure 6.8 Total fatigue lives plotted against nominal net stress σ_{net} for notched specimens (N1 and N2) and for smooth specimen under axial fatigue. 205

Figure 6.9 Total fatigue lives plotted against crack stress intensity factor (K_I) for notched specimens N1 and N2 under axial fatigue 206

Figure 6.10 Fatigue "initiation" lives plotted against nominal shear stress τ_{net} for notched specimens (N1 and N2) and smooth specimen under torsional fatigue. 208

Figure 6.11 Fatigue "initiation" lives plotted against crack stress intensity factor (K_{III}) for notched specimens N1 and N2 under torsional fatigue..... 209

Figure 6.12 Axial fatigue fracture surfaces of specimen N1 observed under SEM. (a) Under low magnification. (b) Under high magnification; the crack direction is from bottom to top in this photo..... 211

Figure 6.13 Axial fatigue fracture surfaces of specimen N2 observed under SEM. (a) Under low magnification. (b) Under high magnification; the crack direction is from bottom to top in this photo..... 212

Figure 6.14 "Factory-roof" fracture surfaces in torsional fatigue..... 214

Figure 6.15 Fracture surface caused by torsional fatigue (right), then by and axial fatigue (left). The ridgeline in the middle of the photo is the boundary between torsional fatigue and axial fatigue. Arrows show the crack propagation directions by torsional fatigue and by axial fatigue, and the direction of macro fracture is the same as that of the axial fatigue crack growth (N1T3)..... 215

Figure 6.16 Crack coalescence observed on torsional fatigue fracture surface of specimen N2T4 (arrow showing a crack propagating on the plane perpendicular to the main crack front)..... 216

Figure 6.17 Intensive friction observed on the torsional fatigue fracture surface close to the notch tip in specimen N2T4. The solid arrow shows the notch tip, and the dotted arrows show the cracks propagating on the plane perpendicular to the main crack front. 216

Figure 6.18 Microscopic coalescence on 45^0 crack planes leaves steps and ridges on the torsional fracture surface of specimen N2T4..... 217

Figure 6.19 Microscopic features observed on the torsional fracture surface of specimen N2T4. 217

Figure 6.20 Illustration of V-notch under axial loading. 219

Figure 6.21 Normalized normal stress σ_{zz} as a function of the distance r from the notch tip in specimens N1 and N2 under axial loading. 220

Figure 6.22 Illustration of V-notch under torsional loading. 222

Figure 6.23 Normalized shear stress distributions at notch tip in specimens N1 and N2 under torsional loading (smooth 1 and smooth 2 represent the stress distributions of smooth specimens with the same diameters as the notch specimens N1 and N2, respectively: the straight line represent the regression lines)..... 222

Figure 6.24 Axial total fatigue life plotted against mode I notch stress intensity factor K_I^N. 225

Figure 6.25 Torsional "initiation" fatigue life plotted against mode III notch stress intensity factor K_{III}^N. 226

NOMENCLATURE

a = crack depth or notch depth

2c = surface crack length

E = Young's modulus

G = shear modulus

GWP = Glinka-Wang-Plumtree

k = material constant to account for normal stress effect

K_I = mode I stress intensity factor

K_{II} = mode II stress intensity factor

K_{III} = mode III stress intensity factor

K_I^N = mode I notch stress intensity factor

K_I^{N1} = mode I notch stress intensity factor for the notched specimen N1

K_I^{N2} = mode I notch stress intensity factor for the notched specimen N2

K_{III}^N = mode III notch stress intensity factor

K_{III}^{N1} = mode III notch stress intensity factor for the notched specimen N1

K_{III}^{N2} = mode III notch stress intensity factor for the notched specimen N2

KBM = Kandil-Brown-Miller

N = fatigue life in number of cycles

N_i = initiation fatigue life

N_f = total fatigue life

N/N_f =fatigue life ratio

SEM = scanning electron microscopy

SIF = stress intensity factor

t = time

$t_{A,B}$ = reversed shear fatigue strength for case A and case B

γ = shear strain

γ_0 = applied shear strain amplitude

γ_{eq} = equivalent shear strain

γ_f' = shear fatigue ductility coefficient

γ_{max} = maximum shear strain amplitude

$\Delta\gamma_{max}$ = maximum shear strain range

γ_{max}^* = maximum shear strain amplitude on a plane driving the crack through the specimen thickness

ε = normal strain

ε_0 = applied normal strain amplitude

ε_f' = axial (bending) fatigue ductility coefficient

ε_i = principal strains (i=1,2,3)

ε_{max} = maximum normal strain amplitude

ε_n = normal strain amplitude on the maximum shear plane

$\Delta\varepsilon_n$ = normal strain range on the maximum shear plane

ε_n^* = normal strain excursion during one reversal of shear strain

θ = plane orientation, defined by the angle between its normal and tubular specimen axis

$\eta = \gamma_0/\varepsilon_0$ = ratio of applied torsional and axial strain amplitudes

$\lambda = \tau_0/\sigma_0$ = ratio of applied torsional and axial stress amplitudes

ν = Poisson ratio

σ = normal stress

σ_0 = applied normal (axial/bending) stress amplitude

σ_{-1} = fatigue limit for fully reversed axial (bending) fatigue

σ_a, $\sigma_{\theta,a}$= normal stress amplitude on a given plane

σ_{eq} = equivalent stress

σ_f' = axial (bending) fatigue strength coefficient

σ_H^m = mean hydrostatic stress

σ_H^{max} = maximum hydrostatic stress

σ_i = principal stresses (i=1,2,3, $\sigma_1 \geq \sigma_2 \geq \sigma_3$)

σ_m = mean normal stress

σ_n = normal stress on the maximum shear plane

$\Delta\sigma_n$ = normal stress range on the maximum shear plane

σ_n^{max} = maximum normal stress on the maximum shear plane (mean plus amplitude)

σ_{net} = nominal stress amplitude at net section for the notched specimen

σ_{UTS} = static ultimate tensile strength

σ_y = static yield strength

τ = shear stress

τ_0 = applied shear (torsional) stress amplitude

τ_{-1} = fatigue limits for fully reversed torsional fatigue

τ_a, $\tau_{\theta,a}$ = shear stress amplitude on a given plane

τ_f' = torsional fatigue strength coefficient

τ_m = shear/torsional mean stress

τ_{max} = maximum shear stress amplitude

$\Delta\tau_{max}$ = maximum shear stress range

τ^{max} = maximum shear stress on the maximum shear plane (mean plus amplitude)

τ_{net} = nominal stress amplitude at net section in the notched specimen

$\tau_{oct,a}$ = octahedral shear stress amplitude

ϕ = phase angle between axial and torsional waveforms

"max" as a subscript means the maximum value reached over all plane orientations
"max" as superscript means the maximum value reached over time on the critical plane

INTRODUCTION

Fatigue of materials refers to the changes in properties resulting from the application of cyclic loads. Mechanical failures of engineering materials and structures are often caused by fatigue. Many engineering applications involve multiaxial fatigue instead of uniaxial fatigue due to complex loadings and/or complex geometry. For example, pressure vessels and piping in power plants and refineries are often submitted to biaxial or triaxial stresses. Complex stress systems are also common at notches or geometric discontinuities such as the joints of gas turbine blades, aircraft wings, bolts and nuts. Fatigue under such complex stress systems is known as multiaxial fatigue. The assessment of multiaxial fatigue is an important design consideration for reliable operation and safe in-service inspection of many practical systems.

Historical background

Since the second half of the nineteenth century, scientists and engineers have made many contributions to the understanding of fatigue in a wide range of topics on a large spectrum of materials.

Some early research was devoted to the fatigue strength in application areas such as railway rolling stock axles, crankshafts, chains and wire ropes. For example, Wöhler conducted systematic investigations of fatigue failure during 1852-1869. He measured the strength of steel railway axles subjected to cyclic bending, torsion and axial loading. His work (e.g., Wöhler, 1860) led to the characterization of fatigue behavior in terms of stress amplitude – life (S-N) curves and to the concept of fatigue "endurance limit".

Later, researchers began to interpret fatigue mechanisms based on the crystallization theory. Ewing & Rosenhain (1900) and Ewing & Humfrey (1903) investigated the fatigue of Swedish iron and published optical micrographs of cyclic damage on the

specimen surface. They showed that slip bands developed in many grains of the polycrystalline material. With an increasing number of loading cycles, additional bands appeared, and some bands were broadened. Fatigue cracks were eventually formed in the slip bands.

During first half of the 20th century, fatigue research has encompassed many topics, such as fatigue limit, cyclic hardening and softening (Bairstow, 1910), corrosion fatigue (Haigh, 1917; Gough, 1933), damage accumulation (Palmgern, 1924; Miner, 1945), stress concentration effects (Neuber, 1946), variable amplitude loading effect (Langer, 1937) and statistical theories of the strength of materials (Weibull, 1939). For example, Bairstow (1910) made significant contributions to the early understanding of cyclic hardening and softening in metals. He presented the relation of the hysteresis of deformation and fatigue failure by using multiple-step tests and hysteresis loop measurements.

Coffin (1954) and Manson (1954) recognized that plastic strains are responsible for cyclic damage and proposed independently an empirical relation between the number of cyclic reversals until the fatigue failure and the plastic strain amplitude. This so-called Coffin-Manson relationship has remained the most widely used approach for the strain-based characterization of fatigue.

Irwin (1957) provided a quantitative treatment to fatigue failure of metals. He showed that the magnitude of the stress singularity ahead of a crack could be expressed in terms of a stress intensity factor, K. With the application of Linear Elastic Fracture Mechanics, attempts were made to characterize fatigue crack growth in terms of the stress intensity factor. Paris and his co-workers (1961, 1963) suggested that the increment of crack advance per cycle, da/dN, could be related to the range of the stress intensity factor, ΔK, during constant amplitude cyclic loading. This approach has been widely used to

characterize the growth of a fatigue crack under the conditions of small-scale plastic deformation at the crack tip.

With the application of electron microscope, some key microscopic features of fatigue have been identified. Thompson et al (1956) demonstrated the slip bands along which deformation was concentrated in fatigued metals persistently reappeared at the same locations during the continuous cycling; these surface markings were afterwards called "persistent slip bands". Zappfe and Worden (1951) observed "fatigue striations" on fatigue fracture surface. Forsyth and Ryder (1960) first presented the correlation of the spacing between adjacent striations with the rate of fatigue crack growth, which was the basis for developing various theories for crack growth and analysis of fatigue failure in engineering structures.

With the application of Fracture Mechanics concepts to fatigue failure, more attention was paid to crack growth. Conceptual and quantitative models were proposed to rationalize the experimentally observed fatigue crack growth resistance of engineering materials (e.g. Laird and Smith, 1962; McClintock, 1963; Rice, 1967; Neumann, 1969). Elber (1970, 1971) showed that fatigue cracks could remain closed even when submitted to cyclic tensile load. This implied that fatigue crack growth rate might no longer be determined by the nominal stress intensity factor range, ΔK, but rather by an effective value, ΔK_{eff} that accounts for the details of fracture surface contact in the wake of the advancing fatigue crack tip. Elber first put into evidence the so-called plasticity-induced crack closure. Later, Ritchie et al (1980) and Suresh et al (1981) categorized several types of crack closure.

Experimental observations have shown that at a given ΔK, small fatigue cracks (typically smaller than several millimeters in length) often exhibit growth rates that are significantly faster than those of long cracks (typically tens of millimeters in length). This "short crack problem", first identified by Pearson (1975), severely affects the design methodology of

engineering structures. In conjunction with the research efforts on the crack closure phenomenon, attempts were recently made to develop characterization methodology for the crack propagation of fatigue cracks in the presence of large-scale plastic deformation and at the vicinity of stress concentrations.

Fatigue failure often involves complex service conditions; such as variable amplitude loading, corrosive environment, high or low temperature and multiaxial loading. The development of reliable fatigue life prediction models, which are able to handle such complex service conditions, is a tough challenge in fatigue research. Although advances have been made in these areas, the application of fatigue concepts to practical conditions often involves semi-empirical approaches. Fatigue mechanisms under different service conditions are not fully understood. Many efforts are still going on to find more reliable life prediction models for different situations on the basis of a better understanding of fatigue mechanisms.

Overview on multiaxial fatigue

The effect of multiaxial stress states on fatigue behavior has emerged as one of the most rapidly developing area in fatigue research. The intensive focus on this subject may be attributed to the general recognition of its importance in the fatigue design of components, as well as to the relatively widespread availability of high quality multiaxial test equipments.

It is widely believed that fatigue crack nucleation and propagation are caused by cyclic plasticity. Persistent slip bands are formed, leading eventually to the initiation of fatigue cracks. Forsyth (1961) first identified the two stages of crack propagation: stage I along the plane of maximum shear stress amplitude (mode II) and stage II along the plane of maximum principal stress (mode I). This description of fatigue crack initiation and propagation applies to multiaxial fatigue (Kanazawa et al, 1977; Ohkawa et al, 1997), but

the relative fractions of life spent in initiation, stage I propagation and stage II propagation strongly depend on material as well as stress states and stress levels (Bannatine and Socie, 1985; Fash, 1985; Hua and Socie, 1984; Waill, 1983). Many materials such as 1045 steel and Inconel 718 fail predominately by the growth of a mode II shear crack (shear mode), while some materials such as 304 stainless steel and gray cast iron fail predominantly by the growth of a mode I tensile crack (tensile mode). For a given material, the fatigue cracking behavior is also a complex function of stress state and stress level.

In low cycle fatigue, many microcracks form; they usually increase in number and become coarser with increasing number of cycles, before a rapid linking process causes the final failure. In high cycle fatigue, fewer microcracks form; some of them extend with increasing number of cycles, and failure usually results from the growth of one dominating crack.

The orientations of the maximum shear planes with respect to the free surface result in two very different cases of fatigue cracks, termed case A and case B (Brown and Miller, 1973). Case A arises when the two extreme principal stress/strain amplitudes, which give rise to the greatest shear strain range during a loading cycle, lie in the plane parallel to the free surface. Case B arises when the minimum principal strain amplitude is the strain normal to free surface. A case B crack propagates into the specimen depth, is therefore more dangerous that a case A crack, which propagates along specimen surface.

A large number of multiaxial fatigue life prediction parameters have been proposed. Stress-, strain- and energy-based parameters have been used to correlate fatigue data. Early investigators (Gough, 1933; Stulen, 1954; Sines and Waisman, 1959) studied the long-life problem and proposed a shear stress-based model for ductile materials and a principal stress-based model for brittle materials. Findley (1959) and McDiarmid (1972) proposed stress models based on a critical plane concept; the critical planes are the planes

where cracks initiate and propagate. In the low cycle fatigue regime, equivalent strain (Taira et al, 1967; Pascoe and DeVilliers, 1967), plastic work (Garud, 1981), plastic strain energy (Ellyin and Valarie, 1982) and critical plane parameters (Brown and Miller, 1973; Fatemi and Socie, 1988; Lohr and Ellison, 1980) have been used to correlate fatigue life data. Since the plastic shear strain plays an important role in crack nucleation and early growth, it is not surprising that most of these approaches are based on shear stress or on shear strain. Either shear stress- or shear strain-based parameters can be considered as extensions of Tresca or von-Mises yielding criteria. Socie (1987) suggested that shear-based parameters are used for fatigue failure primarily due to the growth of mode II shear cracks, while mode I failure needs parameters based on principal stress or strain.

The complexity of multiaxial fatigue also arises from non-proportional loadings, where the ratio of applied shear and normal stresses/strains as well as the principal stress/strain directions can vary with time. In low cycle fatigue, it was found that strong out-of-phase loading can lead to a lower life than an in-phase loading (Kanazawa et al, 1977). For a fixed value of maximum shear strain amplitude, 90^0 out-of-phase loading gives the lowest fatigue life (Kanazawa et al, 1977). Fatemi and Socie (1988) stated that additional hardening is responsible for the worse fatigue performance in out-of-phase loadings as compared to in in-phase loadings. However, different results were reported in high cycle fatigue. When expressed in terms of maximum shear stress amplitude on the critical plane, the fatigue strength can either increase or decrease under 90^0 out-of-phase loading, depending on the axial-torsional stress ratio (Little, 1969; McDiarmid, 1987).

Despite the considerable amount of research carried out in multiaxial fatigue, no single parameter has been able to correlate the fatigue lives from a wide variety of materials and loading conditions. At the present time, the critical plane parameters are claimed to be more promising, since they are based on the fatigue cracking mechanisms. However, limits still exist for the critical plane life prediction parameters when applied to

mechanical parts submitted to complex service conditions and made of a large spectrum of engineering materials. Actual fatigue cracking mechanisms are often a complex function of material properties and loading conditions. Therefore, close observation of fatigue mechanisms is often necessary before applying any fatigue life parameter.

Scope of this thesis

In this thesis, we have used an axial-torsional servo-hydraulic machine to perform stress-controlled tests at room temperature and laboratory air. Apart from the literature review, the research work is devoted to the high cycle fatigue regime where the macroscopic cyclic deformation becomes predominately elastic as the stress level decreases to the fatigue limit.

Several loading conditions are applied to study the effects of out-of-phase loading and mean tensile stress on both fatigue mechanisms and fatigue life. Tubular specimens made of two materials, 1045 steel and 7075 aluminum alloy, are used for testing. The former material is generally considered as isotropic, while anisotropy effects are investigated with the 7075 aluminum alloy. Stress concentration effects are studied using circumferentially V-notched specimens made of 1045 steel. Through this research, an attempt is made 1) to understand the biaxial fatigue behavior of 1045 steel in terms of critical plane concept and to compare different existing stress/strain parameters in correlating fatigue lives under proportional and non-proportional loadings; 2) to understand the axial-torsional fatigue mechanisms and to find how to predict fatigue lives of an anisotropic material; 3) to understand the fatigue behavior of singular V-notches under mode I and mode III loadings and to propose a simple LEFM approach to predict notch fatigue life under axial and torsional loadings.

In Chapter I, the progress of multiaxial fatigue research over the last several decades is reviewed. The review includes fatigue cracking mechanisms and fatigue life prediction

approaches. With respect to the literature review, the objectives of this thesis will be set in Chapter II. The observation of biaxial fatigue cracking mechanisms in smooth specimens made of 1045 steel will be presented in Chapter III. In Chapter IV, the abilities of eight selected multiaxial fatigue parameters to predict high cycle fatigue life are evaluated. The limitations of these parameters are discussed in terms of fatigue mechanisms and stress analysis, and a modified critical-plane-based fatigue life prediction approach is suggested. Chapter V reports the results from the study of material anisotropy effects on axial-torsional fatigue mechanisms as well as on fatigue life in underaged and overaged 7075 aluminum alloy. In Chapter VI, stress concentration effects on axial and torsional fatigue are investigated. Mode I and mode III notch stress intensity factors are proposed to correlate crack initiation lives for two notches of different size. General conclusions are finally drawn.

CHAPTER I - LITERATURE SURVEY

1.1 Basic notions

Biaxial fatigue tests are generally carried out (1) on thin-walled tubular specimens (Figure 1.1(a)) using an axial-torsional testing machine, or (2) on cruciform specimens (Figure 1.1(b)) using a bi-axial testing machine. With an axial-torsional fatigue machine, axial loading and torsional loadings can be applied separately or simultaneously. Axial and torsional load cells are used to accurately control the applied axial load and torque. The distribution of stress/strain in the thin-walled tubular specimen is relatively uniform. However, only limited principal stress/strain ratios can be reached (Figure 1.2 (a) and (b)). To overcome this shortcoming, some modifications can be done to this type of machine. In addition to axial-torsional loading, internal-external pressure can be applied to the tubular specimen. With various combinations of these loadings, all principal stress/strain ratios can be reached (Figure 1.2 (c) and (d)). A bi-axial testing machine consists of two sets of orthogonal actuating mechanisms that apply biaxial loads in one single plane directly to the flat cruciform specimen. The advantage of this machine is that all biaxial stress ratios can be reached. However, it needs a more expensive and complex hydraulic system. In addition, there is only a limited area of specimen with uniform stress/strain state. The stress/strain distribution is often determined using empirical or numerical methods. It is largely dependent upon the specimen design, configuration of loading frame, specimen attachment and actuation method.

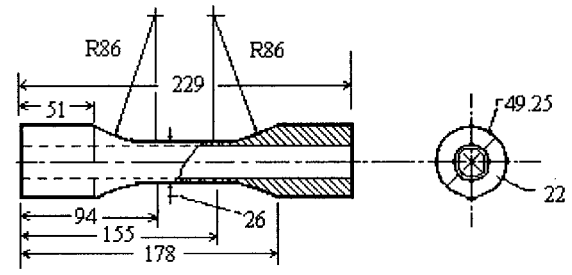

(a)

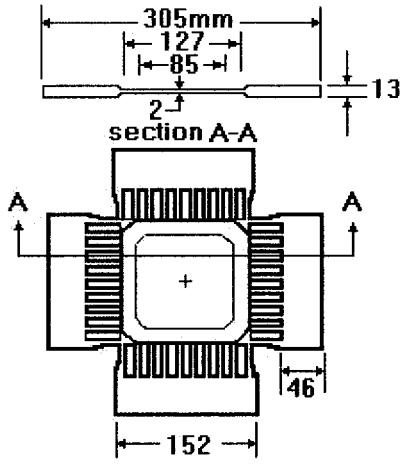

(b)

Figure 1.1 Typical specimens for biaxial fatigue tests. (a) Thin-walled tubular specimen (Lissenden et al, 1997); (b) Cruciform specimen (Batolotta et al, 1997). (All dimensions are in millimeters)

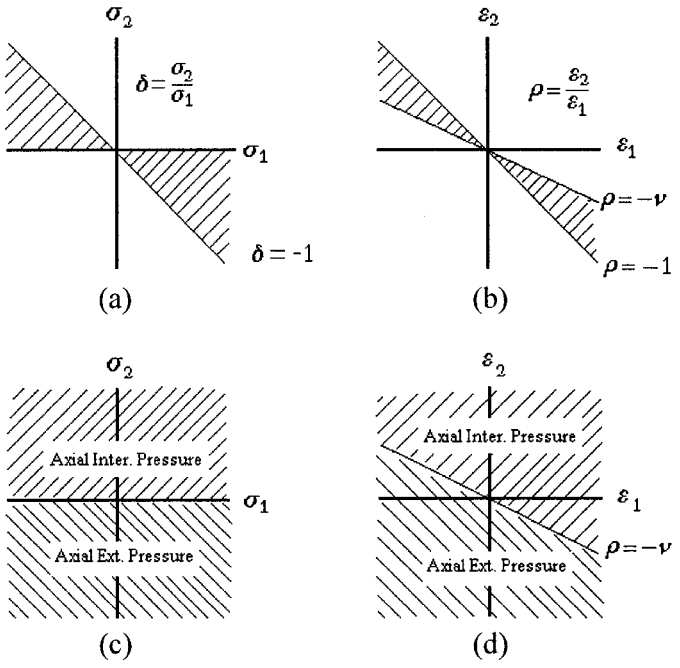

Figure 1.2 Principal stress/strain ratios reached (cross-hatched areas) under different loadings on a thin-walled tubular specimen.
(a) Stress ratios under axial-torsional loading;
(b) Strain ratios under axial-torsional loading;
(b) Stress ratios under axial-torsional loading with internal-external pressure;
(c) Strain ratios under axial-torsional loading with internal-external pressure.

The present study was carried out using simple axial-torsional machine. Thin-walled tubular specimens with smooth surface were employed to study the high cycle fatigue behavior. They have been submitted to stress-controlled axial-torsional loading defined by:

$$\begin{cases} \sigma=\sigma_0\sin(\omega t)+\sigma_m & (1.1) \\ \tau=\tau_0\sin(\omega t-\phi)+\tau_m & (1.2) \end{cases}$$

Here, σ and τ are the applied axial and shear (torsional) stresses, σ_0 and τ_0 are the axial and shear stress amplitudes, ω is the angle frequency and t is the time. ϕ is the phase angle between the applied axial and shear stresses. σ_m and τ_m are the superimposed axial and torsional static stresses, respectively. The stress ratio λ ($=\tau_0/\sigma_0$) is defined by the

ratio between the applied shear and axial stress amplitudes, with $\lambda=0$ corresponding to axial fatigue, and $\lambda=\infty$ corresponding to torsional fatigue. For in-phase loading, $\phi=0$ and when $\phi\neq0$, the loading is out-of-phase.

The out-of-phase loading effects on low cycle fatigue behavior are not considered in the thesis, but they are reported in the literature survey. Strain-controlled axial-torsional loading is defined by,

$$\begin{cases}\varepsilon=\varepsilon_0\sin(\omega t) & (1.3)\\ \gamma=\gamma_0\sin(\omega t-\phi) & (1.4)\end{cases}$$

Here, ε and γ are the normal and shear strain. ε_0 and γ_0 are the normal and shear strain amplitudes. ϕ is the phase angle between the applied shear and normal strains. The strain ratio is defined by $\eta=\gamma_0/\varepsilon_0$.

Different combinations of stress/strain ratios result in very different periodic histories and in very different fatigue behavior. However, for many materials, the cracks generally nucleate and propagate on the maximum shear plane (plane with the maximum shear stress or strain amplitude, τ_{max} or γ_{max}), and the normal stress σ_n (or strain ε_n) on this plane can accelerate ($\sigma_n>0$) or retard ($\sigma_n<0$) the cracking process. This introduces the so-called critical-plane concept (e.g. McDiarmid, Brown & Miller). It is proposed to use the shear and normal stress/strain components acting on the critical plane to correlate biaxial fatigue lives.

A detailed stress analysis will be presented later but the readers are invited to have a first glance at the results shown in Figures 3.6 (page 101) and 4.1 (page 139). Under in-phase loading, there are two orthogonal maximum shear planes (planes of maximum shear stress amplitude), and the normal stress amplitudes on these planes are equal to each other. The shear and normal stresses on the maximum shear plane are in-phase. Under 90^0 out-of-phase loading ($\phi=90^0$), the number of maximum shear planes and the stresses on the maximum shear plane depend on the stress ratio λ. When $\lambda<0.5$, there are two

maximum shear planes, on which the normal stress amplitudes are equal to each other. A normal and shear stresses on the maximum shear plane are out-of-phase (phase angle<45^0). When λ>0.5, there are two maximum shear planes. Only one plane has normal stress. The shear and normal stresses on this plane are also 90^0 out-of-phase. λ=0.5 represents a special loading case. The shear stress amplitudes on all planes are identical, but the normal stress amplitude is maximum on one plane. On this plane, the phase angle between the normal and shear stresses is 90^0.

The maximum shear stress/strain amplitude (τ_{max} or γ_{max}; Tresca parameter) alone cannot correlate fatigue lives under axial and torsional loadings. At the same τ_{max} or γ_{max}, torsional fatigue generally gives a higher life than axial fatigue (Figure 1.3 (a)). Comparing the stresses in these two loading cases, there is a normal stress (or strain) acting on the maximum shear plane under axial fatigue, but not under torsional fatigue. The tensile normal stress/strain can open the crack and accelerate the cracking process. Although the maximum shear stress/strain amplitude is the control parameter for fatigue damage, the normal stress/strain acting on the maximum shear plane also plays a second important role. Only the maximum shear stress/strain amplitude is not sufficient to correlate biaxial fatigue lives. Normal stress effects should be taken into account. For example, the McDiarmid parameter = $\tau_{max}+k\sigma_n^{max}$ (k is a constant obtained by fitting axial and torsional fatigue lives) takes into account the maximum normal stress σ_n^{max} (amplitude +mean) acting on the critical plane. It gives a good fatigue life correlation for axial, torsional and in-phase loadings (Figure 1.3(b)). Fatigue behavior under out-of-phase loading will be reviewed in section 1.3.1.

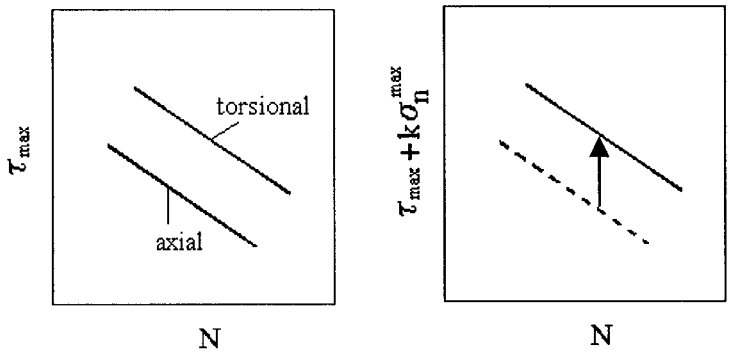

Figure 1.3 Correlation of axial and torsional fatigue lives

1.2 Biaxial fatigue mechanisms

Fatigue damage is characterized by the initiation, and the growth of cracks to final failure. This section reviews the mechanisms of crack initiation and crack propagation.

1.2.1 Crack initiation mechanisms

The definition of crack initiation is strongly linked to the scale of observation. Materials scientists generally consider the nucleation of flaws along persistent slip bands as the crack initiation stage of fatigue failure, whilst a mechanical engineer may associate the crack initiation with the detectable crack size. Crack initiation sites are generally located at the external surface. Cracks may nucleate at PSBs formed within surface grains, at microstructure discontinuities (e.g. grain boundary) and at geometry discontinuities (e.g. notch). Different mechanisms are involved in each case.

1.2.1.1 Crack initiation along persistent slip bands (PSBs)

In homogeneous ductile metals without stress concentrations, cracks often initiate from PSBs on the surface. Ewing and Humfrey (1903) described the fatigue process as follows: slip-lines were observed after a few reversals of stress; additional slip lines

appeared after more reversals. After many reversals, these lines changed into wide bands. As this broadening process continued, crystals eventually cracked. These slip lines, commonly called persistent slip bands, are caused by the movement of dislocations. The dislocations move only on the crystallographic slip planes along the slip directions. The combination of a slip plane and a slip direction is called a slip system. When the resolved shear stress on a slip system exceeds a critical shear stress, the dislocations move and result in slip steps on the surface of metals. Under cyclic stress, intrusions and extrusions can be formed on the surface of metals; cracks eventually nucleate from some intrusions. Intrusions and extrusions during fatigue process were observed by Forsyth in Al-Cu alloy (1953) and in single crystals and polycrystals of silver chloride (1957), and by Ma and Laird (1989) in copper single crystals. Figure 1.4 shows an example of extrusions and intrusions observed by Ma and Laird (1989) in copper crystals.

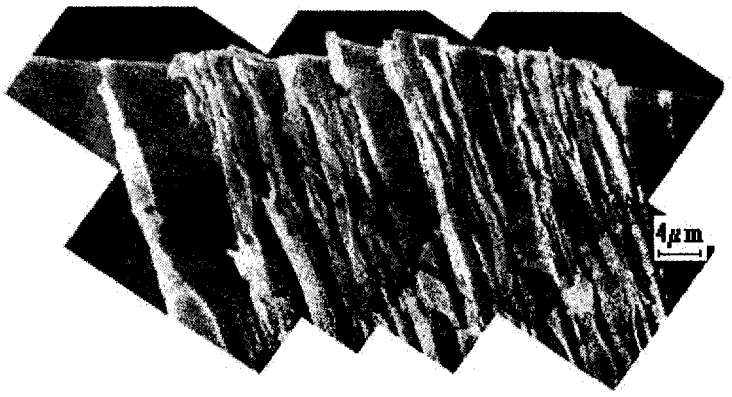

Figure 1.4 Scanning electron micrograph showing extrusions and intrusions on the surface of a Cu crystal fatigued at room temperature for 120000 cycles at γ_p= 0.002 (Ma and Laird, 1989)

Several models have been proposed to rationalize the fatigue crack initiation process. In 1958, Wood postulated that repeated cyclic straining causes different amounts of net slip on different slip planes in the material. The irreversibility of shear displacements along the slip bands results in the "roughening" of the material surface. The roughening consists of microscopic "hills" and "valleys" at sites where slip bands emerge at the free surface; these "hills" and "valleys" are called extrusions and intrusions. The valleys then act as micro-notches. The effects of stress concentration at the root of the valleys promote additional slip and fatigue crack nucleation. Fine and Ritchie (1979) proposed a dislocation model for crack initiation. Paired dislocation pile-ups against an obstacle on a metal surface are imagined to grow with cyclic straining until they reach a critical size. An avalanche then occurs, giving an intrusion or an extrusion depending on the sign of the dislocation.

The above models deal with uniaxial fatigue, but they can be extended to multiaxial fatigue. Parsons and Pascoe (1976) observed the crack initiation behavior in QT35 steel and AISI 304 stainless steel under biaxial straining; the ratio between principal strains, $\varepsilon_1/\varepsilon_3$, varying from -1 to $+1$. They showed that the first sign of damage, visible upon initial straining, is the appearance of slip markings accompanied at higher strains by surface rumpling. With continued cycling, a gradual accumulation of slip occurs and the surface distortion becomes more severe. The intensification of plastic strain at microscopic heterogeneities leads to cracking, sometimes at grain boundaries (especially for high strains) or at twin boundaries, but more commonly in slip bands.

Kanazawa et al (1977) conducted low cycle fatigue tests on thin-walled tubular specimens made of 1% Cr-Mo-V steel under in-phase and out-of-phase loadings. They observed that cracks form along slip planes oriented closely to the planes of maximum shear strain amplitude. The slip systems that experience the greatest amount of deformation are those align precisely with the maximum shear plane. Therefore most fatigue cracks initiate in these grains. But slip systems with a lower amount of shear also

initiate cracks at a slower rate. They concluded that most cracks initiate on the planes of maximum shear strain amplitude under all loading conditions.

1.2.1.2 Crack initiation at defects in materials

In engineering components made of commercial materials, the principal sites of crack initiation are defects such as inclusions, voids, slag, scratches, as well as any region of microstructural and chemical non-uniformity. The initiation of fatigue cracks can occur at near-surface and interior locations in commercial alloys.

The mechanisms of fatigue crack initiation at defects depend upon a number of mechanical, microstructural and environmental factors. These factors include the slip characteristics of the matrix, the relative strengths of matrix and the defect, and the strength of the matrix-inclusion interface (Bowels and Schijve, 1973; Cummings et al, 1958). The effect of inclusions on fatigue crack initiation is often specific to an alloy system. In high strength steel containing non-metallic inclusions, the initial stage of fatigue damage is the debonding of inclusions from the matrix (Figure 1.5, Lankford and Kusenberger, 1973). In 2024-T4 aluminum alloy, the debonding of the particle-matrix interface occurs over a large number of fatigue cycles. Another type of crack initiation in 2024-T4 alloys involves cracking along the slip bands emanating or terminating at the inclusions. Tanaka and Mura (1982) considered three different processes of crack initiation: a slip band crack emanating from a debonded inclusion, a slip band crack initiating from an uncracked inclusion and an inclusion cracking due to the impingement of slip bands. They assumed that the initiation of a crack is determined by an energy criterion. The fatigue flaw initiates when the strain energy of dislocation dipoles accumulated at the inclusion reaches a critical value.

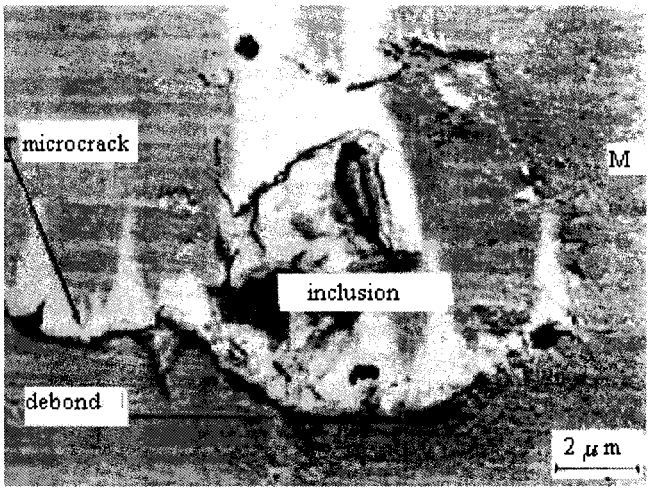

Figure 1.5 Scanning electron micrograph showing the nucleation of a fatigue crack normal to the tensile axis (vertical direction) at the site of an $MnO\text{-}SiO_2\text{-}Al_2O_3$ inclusion that is partially debonded from the 4340 steel matrix denoted M. (Lankford and Kusenberger, 1973)

1.2.1.3 Intergranular crack initiation

The nucleation of fatigue cracks at grain boundaries occurs under the influence of embrittling environments (which preferentially attack grain boundaries) and intergranular particles. It also occurs at elevated temperatures, at which grain boundary cavitation and sliding are promoted.

The occurrence of grain boundary fatigue crack initiation in ductile solid, in the absence of grain boundary particles, creep deformation or environmental influences may also occur. However, several cases have been documented. At low to intermediate axial plastic strain amplitude, the impingement of PSBs at grain boundaries cause cracks (Figueroa and Laird, 1983; Mughrabi et al, 1983). Doquet (1997) observed crack initiation at grain and annealing twin boundaries from intensive slip bands impinging on them at a high angle (ranging from70-90°). At high plastic strain amplitudes, grain

boundary cracking occurs as a consequence of surface steps formed at the boundary (Kim and Laird, 1978).

1.2.1.4 Crack initiation at stress concentrations

The initiation of fatigue cracks at stress concentrations is a topic of considerable interest in a wide variety of engineering applications. Fatigue cracks often initiate at stress concentrations that cannot be avoided in mechanical design. The notch effect on fatigue crack initiation depends very much on the notch severity. Different approaches are applied to deal with the notch fatigue cracking problem. Local stress or strain approaches can give good results for blunt notches while fracture mechanics approaches are used for sharp notches. This topic is treated in detail in section 1.7 (notch effects).

1.2.2 Crack propagation mechanisms

1.2.2.1 The three modes of crack growth

Three modes of cracking exist (Figure 1.6). Mode I is the opening mode in which the crack faces separate in the direction normal to the crack plane. The corresponding displacements of the crack faces are symmetric with respect to x-z and x-y planes. Mode II is the in-plane shear mode in which the crack faces are mutually sheared in a direction normal to the crack front. Here the displacements of crack faces are symmetric with respect to x-y plane and anti-symmetric with respect to x-z plane. Mode III is the anti-plane shear mode in which crack faces are sheared parallel to the crack front. The displacements of the crack faces then are anti-symmetric with respect to x-y and x-z planes.

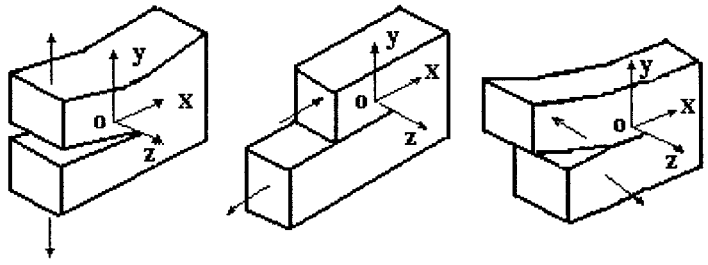

(a) (b) (c)

Figure 1.6 The three basic modes of crack growth. (a) Tensile opening (Mode I). (b) In-plane shear (Mode II). (c) Anti-plane shear (Mode III) (Suresh, 1998).

1.2.2.2 The three stages of fatigue crack propagation

There are three stages in fatigue crack propagation, which were first reported by Forsyth (1961) for uniaxial fatigue. As illustrated in Figure 1.7, cracks first grow in a shear mode (mode II). This is Stage I crack propagation. Here, the damage produced is generally crystallographic, associated to some specific slip systems where PSBs forms. Cracks are observed growing along the PSBs in surface grains (Basinksi and Basinski, 1985). These cracks are driven by the reversed shear deformation in PSBs. In this stage, cracks are closely oriented along the planes of maximum shear. Stage I propagation is a shear-controlled process. After growing through one or two grains, the crack orientation becomes normal to the maximum principal stress. This is Stage II crack propagation that is a tensile process (mode I). The transition from Stage I to Stage II involves in a fundamental change in cracking mechanisms. A third stage of crack propagation occurs at the very end of fatigue life that more often involves one or more static fracture mechanisms. Since crack propagates rapidly in this period, it has little effect on the total life. This stage will not be further discussed.

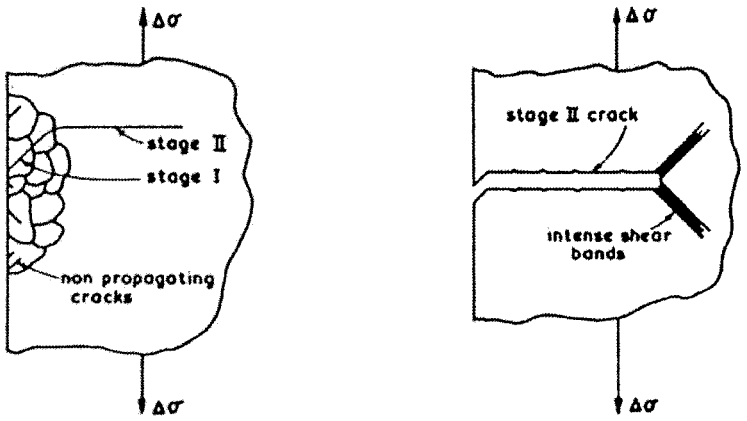

Figure 1.7 Illustration of Stage I and Stage II fatigue crack propagation (Brown, 1988).

Stage I and Stage II cracks are also observed under multiaxial loadings. Brown and Miller (1979) measured the crack paths in two steels under tension-torsion low cycle fatigue. They found that cracks fall into three distinct groups. The first group corresponds to Stage II where the crack planes are normal to the maximum principal strain axis. The second and third groups comprise cracks on two orthogonal planes, corresponding to the two orthogonal planes of maximum shear in the specimen. Ohkawa et al (1997) did a detailed observation of the orientation distribution of surface cracks in a S45C steel submitted to axial-torsional fatigue with different stress ratios λ. They found that the majority of cracks initiated near the maximum shear planes and then grew changing their orientations to a direction perpendicular to the maximum normal stress (Figure 1.8). The crack orientation θ in the figure is the angle between the normal of the surface crack plane and the axis of the tubular specimens.

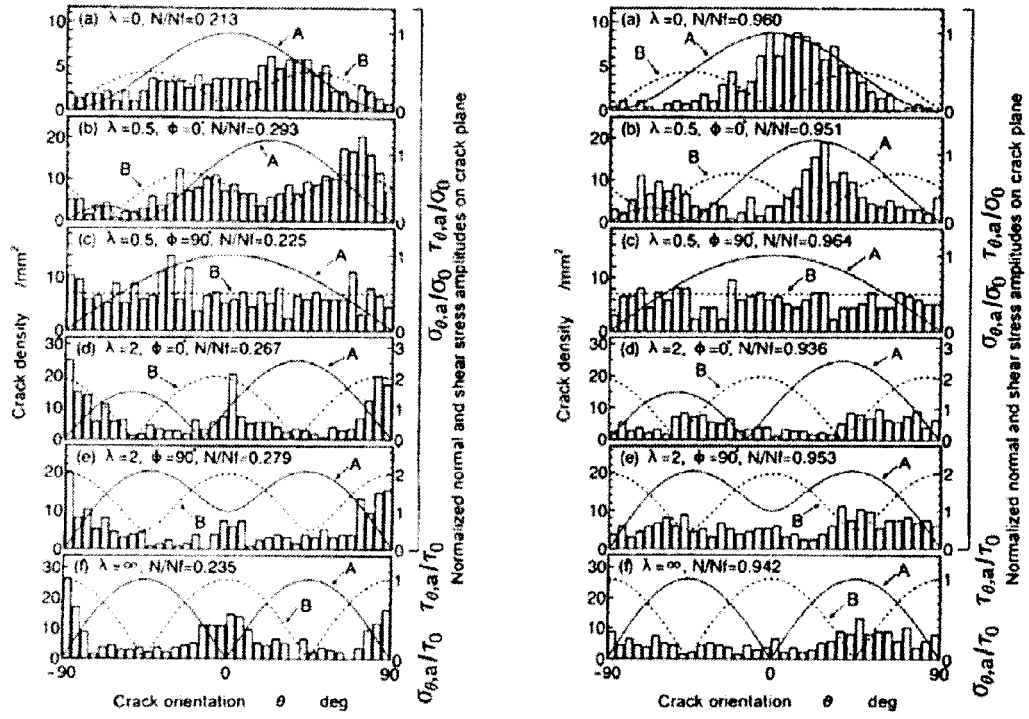

(a) (b)

Figure 1.8 Crack density versus orientation at (a) 25% and (b) 95% of the lifetime. Curves A and B (solid and dashed lines) show the variation of the normal and shear stress amplitudes acting on the crack plane, respectively. These stress amplitudes are normalized with respect to the applied axial or torsional stress amplitude (λ, stress ratio; Φ, phase angle; N/N_f, life ratio). (Ohkawa et al, 1997)

The transition from Stage I crack propagation to Stage II crack propagation is governed by the material microstructure and the applied loading. Compression and shear loadings favor Stage I shear growth. Low ductility materials have predominantly Stage II tensile growth. The transition can also be influenced by the environment, particularly in aluminum alloys (Socie and Marquis, 2000).

1.2.3 The three regions of fatigue behavior

Socie (1993) analyzed the biaxial fatigue cracking behavior under axial-torsional loading of AISI 304 stainless steel, Inconel 718, and 1045 steel (Hua and Socie, 1985; Socie et al, 1989; Bannantine and Socie, 1985). He concluded that there are three different cracking behaviors depending on the total fatigue life. From low cycle fatigue to high cycle fatigue, there can be Region A, Region B and Region C. In region A, the fatigue life is dominated by the shear crack growth (stage I/mode II). In Region B, shear crack nucleation is immediately followed by crack growth on the planes normal to the maximum principal strain (stage II/mode I). In Region C, the fatigue life is dominated by crack nucleation. Which region corresponds to the fatigue cracking behavior depends on material type, loading mode and stress level.

Figure 1.9 shows the fatigue cracking behavior in AISI 304 stainless steel. Under torsional fatigue (Figure 1.9(a)), Region A behavior was observed at short lives and Region B behavior was observed at long lives. Region C behavior was not observed even at the longest fatigue lives. On the other hand, no evidence of stage I crack growth was found in 304 stainless steel under tension fatigue. No Region A is shown in Figure 1.9 (b). The fracture surfaces appeared to be almost entirely dominated by stage II crack growth. Region B behavior was found in the low cycle fatigue regime, while the region C behavior dominates the high cycle fatigue regime.

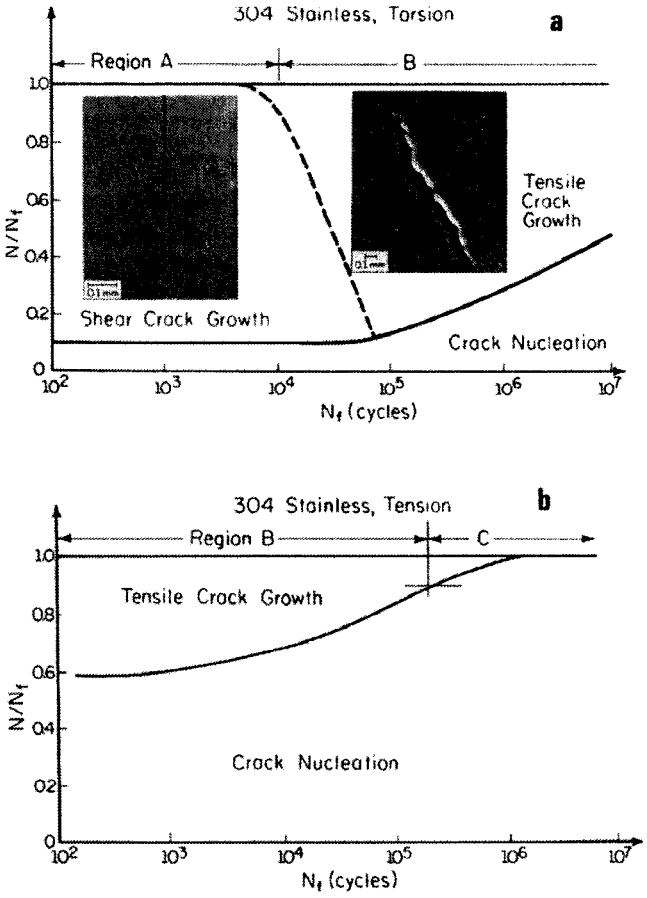

Figure 1.9 Cracking behaviors observed in 304 stainless steel.
(a) Torsion. (b) Tension. (Socie, 1993).

In contrast, in Inconel 718 subjected to torsional fatigue (Figure 1.10 (a)), the cracks initiated and remained on the maximum shear planes (Region A behavior) whatever the shear strain level. Even at the lowest strain amplitude, where stress-strain response is elastic, the cracks initiated and remained on the shear planes throughout the life. Under tension fatigue (Figure 1.10 (b), the cracks also remained on the shear planes for the majority of the fatigue life. A large Region A was observed. Final failure in all tension tests was in the macroscopic tensile direction, but it consisted of large portions of microscopic shear growth for short and intermediate fatigue life regimes. Stage II growth occurs only in the late life. Damage accumulation in Inconel 718 appears to be shear

predominated. This is attributed to the localized shear deformation bands that develop during cyclic loading. Reversed movement of dislocations progressively shears the precipitates in these bands. Crack propagation then occurs along the bands with extensive shear crack growth exhibited throughout the fatigue life. The cracking behavior of 1045 steel is very similar to that of Inconel 718. Region A behavior dominates in torsion fatigue. In tension fatigue, Region A behavior predominates at low lives, while Region B behavior dominates at intermediate lives. Region C behavior emerges at long lives (>10^6 cycles) where crack initiation predominates.

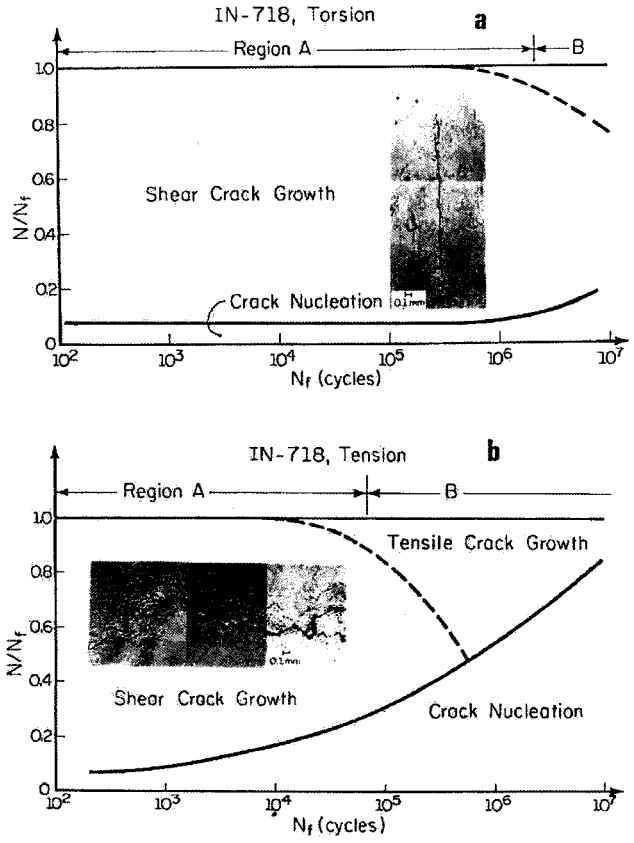

Figure 1.10 Cracking behaviors observed in Inconel 718.
(a) Torsion. (b) Tension. (Socie, 1993).

Parsons and Pascoe (1976) found that the applied strain system determines the crack growth behavior. The cracks grow in mode I for any strain system, except for pure shear, where they grow initially in mode II, but may transfer to tensile mode under certain conditions. Such conditions appear to be provided at low strain by the intersection of a microscopic slip bands (shear) crack at grain boundaries, or at high strains by the systematic linking of microscopic shear cracks.

Sakane et al (1987) investigated the crack growth directions in tubular specimens made of 304 stainless steel submitted to combined axial-torsional loadings at 923^0C in air. Their results indicate that macrocracks (>1mm) propagate in mode I when $-0.64 \leq \rho \leq -0.5$ ($\rho=\varepsilon_3/\varepsilon_1$, being the principal strain ratio), but in mode II when $-0.86 \leq \rho \leq -1$. Mixed mode fracture occurs when $\rho=-0.74$.

From the above discussion, it can be concluded that the fatigue cracking behavior is a function of material type, stress state and stress level. The damage mechanism is a major consideration for a fatigue life prediction model. Different mechanisms need different types of life correlating parameter. A shear type parameter is appropriate for fatigue life in Region A. For Region B, Socie (1987) suggested to use the Smith-Watson-Topper parameter (tensile type) to correlate fatigue lives. In region C, shear type stress parameters are recommended (Socie, 1993). However, only a few metals exhibit Region B behavior. Most fatigue life parameters are based on the shear stresses/strains. The multiaxial fatigue life parameters will be presented in detail in Section 1.4.

1.2.4 Case A and Case B cracks

The free surface orientation of a component can influence the crack speed and shape. Two particular cases for surface orientation have been identified by Brown and Miller (1973), known as Case A and Case B, which are defined by the principal stress/strain directions with respect to the specimen surface. As shown in Figure 1.11, Case A arises

when the two extreme principal stress/strain amplitudes ε_1 and ε_3, that give rise to the greatest shear strain range during a cycle of loading, both lie in the plane parallel to the free surface. The intermediate strain ε_2 is the principal strain normal to the specimen surface. For Case B, the minimum principal strain amplitude, ε_3 is normal to the free surface. The stage I crack will propagate on different sets of shear planes and shear directions in the two cases. In Case A, the cracks are driven fastest parallel to the surface, while they will propagate away from the surface into the specimen depth in case B. Therefore, a Case B crack is more dangerous than a Case A crack, because failure is always caused by fracture through the specimen thickness.

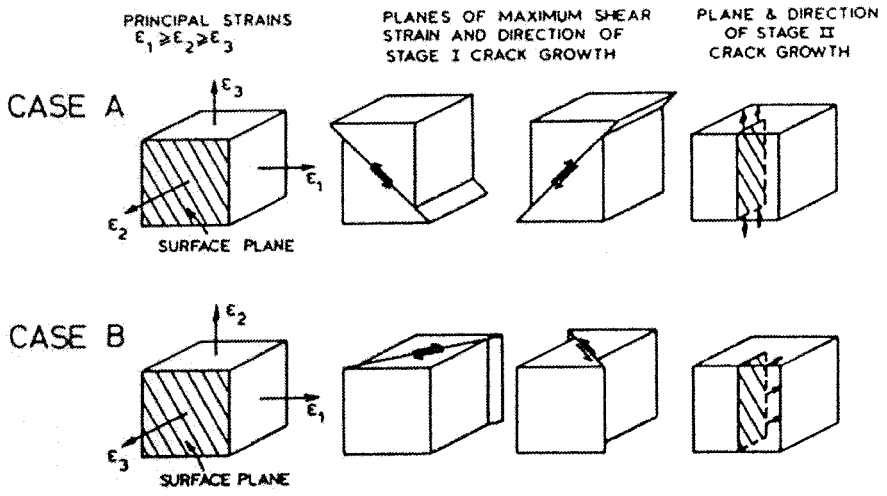

Figure 1.11 Case A and Case B crack formation, showing the importance of the free surface (cross hatched) orientation in multiaxial fatigue cracking (Brown and Miller, 1973).

Reversed torsion and tension/torsion are both classed into Case A, whereas plane strain and equal-biaxial loadings correspond to case B. The uniaxial loading is a special case. Both Case A and Case B cracks can occur. There is an infinity of maximum shear planes whose normal makes an angle of 45° with respect to the loading axis. It was found that a

torsional fatigue crack has a very low aspect ratio (crack depth/crack length) as compared to pure tension and combined tension-torsion fatigue cracks (Hua and Socie, 1984). At the failure, the surface crack length under torsional fatigue is much longer than under tension fatigue and combined tension-torsion fatigue.

1.3 Non-proportional loadings

An important consideration for multiaxial fatigue is whether the principal stress or strain axes are fixed or not with respect to specimen axes. If they are fixed, the loading is considered as proportional. The components of stress or strain tensors increase or decrease in constant proportion. Consequently, the maximum shear planes remain fixed in orientation as well. Under non-proportional loading, the principal stress/strain axes and the ratio of stress/strain components vary during a loading cycle. Axial-torsional in-phase loading is proportional loading. Axial-torsional out-of-phase loading and loadings with axial or torsional mean stress are two typical non-proportional loadings.

1.3.1 Out-of-phase loading

Out-of-phase loading and in-phase loading are periodic histories such as sine or triangular waveforms with or without a phase angle, respectively. Consider the cylindrical specimen subjected to axial-torsional loading in Figure 1.12 (a). The variations of axial and shear strains with time are illustrated in Figure 1.12 (b) for in-phase loading. Here, the axial and shear strains vary in constant proportion to each other and the phase angle between them is zero. Figure 1.12 (c) shows an axial-torsional 90^0 out-of-phase loading. The loading path for in-phase loading corresponds to a straight line in normalized strain space, while the 90^0 out-of-phase loading path is a circle (Figure 1.12 (d)).

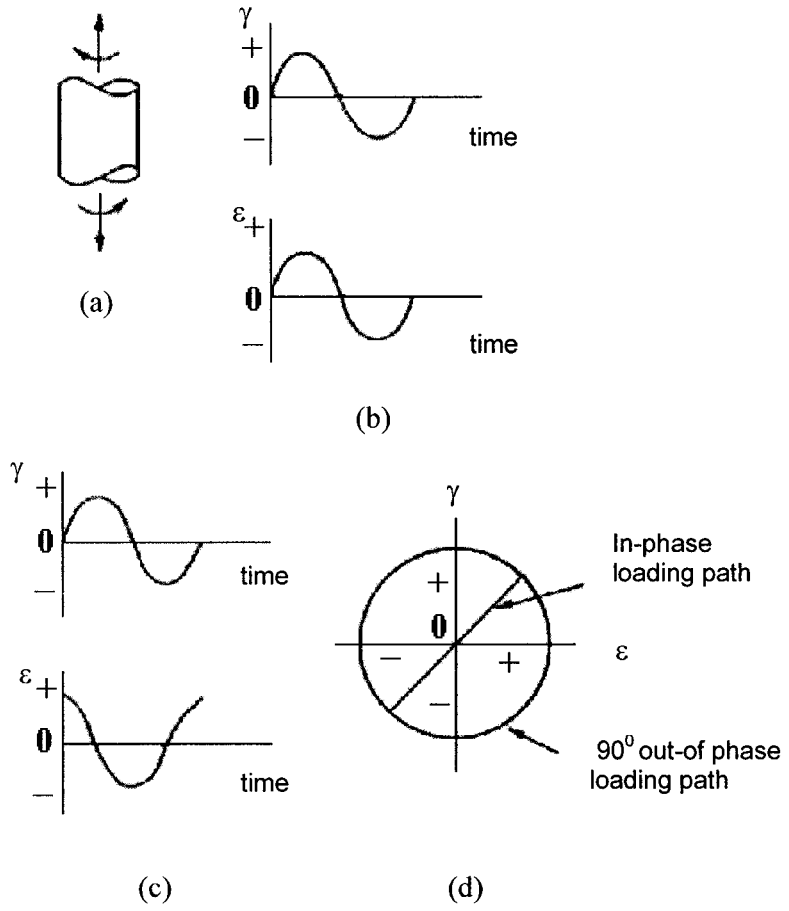

Figure 1.12 (a) A cylindrical specimen subjected to combined axial and torsional loadings. (b) Strain-time history for proportional loading where the axial and torsional strains are in-phase. (c) Strain-time history for non-proportional loading where the axial and torsional strains are 90^0 out-of-phase. (d) Loading paths for in-phase (straight line) and 90^0 out-of-phase loading (circle) in normalized strain space.

1.3.1.1 Out-of-phase loading and fatigue mechanisms

There is not much difference in fatigue cracking mechanisms between in-phase and out-of-phase loadings. In in-phase fatigue, crack initiation and early propagation occur on a maximum shear plane, and then crack growth plane becomes normal to the maximum principal stress or strain (Kanazawa et al, 1977; Ohkawa et al, 1997). In out-of-phase

loading, there are two sets of maximum shear planes, but one is submitted to a larger normal stress/strain than the other (Kanazawa et al, 1977; Ohkawa et al, 1997). As a consequence, the cracking may occur on only one set of maximum shear planes, on which the normal stress/strain is maximum. Socie (1993) also mentioned that the fatigue cracking behavior (Regions A, B and C) remains unchanged under out-of-phase loading as compared with in-phase loading. Mode I fracture prevails in 304 stainless steel, whereas Mode II fracture prevails in 1045 steel and Inconel 718 under both in-phase and out-of-phase loading conditions. The rate of damage accumulation might increase and fatigue life might decrease in certain conditions.

1.3.1.2 Effects of out-of-phase loading on fatigue life

Nishihara and Kawamoto (1945) showed that the fatigue limits of ductile materials are apparently higher for out-of-phase bending and torsion loading than for in-phase loading, in terms of the applied stress amplitudes. Little (1969) showed that this increase in high cycle fatigue strength can be misleading. For a given applied stress, the maximum shear stress amplitude under out-of-phase loading is lower than that under in-phase loading (as shown later in Table 4.3). Depending on the stress ratio λ, the out-of-phase loading can result in either an increase or a decrease of fatigue strength when it is expressed in terms of maximum shear stress amplitude. A maximum decrease of about 25% is obtained when λ=0.5. Garud (1981) and McDiarmid (1987) also reported that this special loading case (shear stress amplitudes equal on all plane orientations) gives the worst fatigue performance.

Kanazawa et al (1977) conducted a number of axial-torsional low cycle fatigue tests with various phase angles in a 1% Cr-Mo-V steel. They found that out-of-phase loading results in a shorter life as compared with in-phase loading in terms of maximum shear strain amplitude. The 90° out-of-phase loading gives the shortest life (Figure 1.13(a)). So the maximum shear strain is not able to correlate the fatigue lives for all loading conditions.

Instead, a parameter combining the amplitudes of normal and shear strains on the maximum shear plane was able to correlate the fatigue lives for in-phase and out-of-phase loadings (Figure 1.13(b)). Both Kanazawa et al (1977) and Jordan et al (1985) found that the relative phase angle between normal and shear strain on the maximum shear plane did not affect the fatigue life. Jordan et al (1985) suggested a life correlating parameter using an integral root mean square of positive normal strain on the maximum shear plane to replace the normal strain amplitude. However, Wang and Brown (1993) found that the above-mentioned phase angle did have influence on fatigue life and suggested to take it into account in a life correlating parameter.

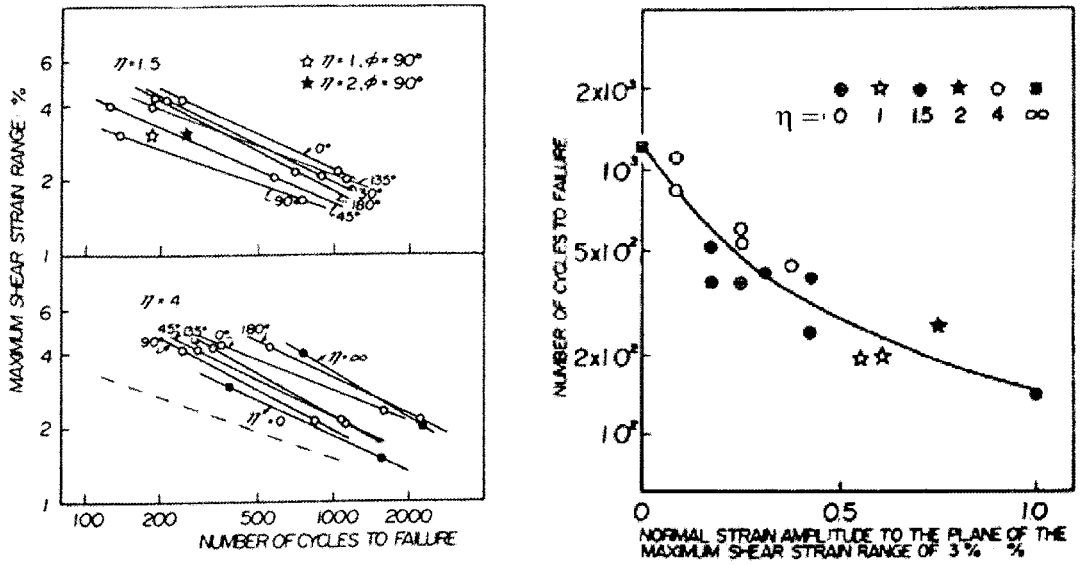

(a) (b)

Figure 1.13 (a) Maximum shear strain range versus fatigue lives in 1%-Cr-Mo-V steel. (b) Fatigue life as a function of normal strain range on maximum shear planes at the same maximum shear strain range (3%) in 1%-Cr-Mo-V steel (Kanazawa, 1977).

Fatemi and Stephen (1987) and Itoh et el (1995) also found that out-of-phase loading are detrimental for low cycle fatigue life in terms of maximum shear strain amplitude.

However, in contrast with the above approaches, it was claimed that the shorter fatigue life observed under non-proportional loading could be ascribed to the additional hardening associated with complex loading paths (Socie, 1987). Instead of normal strain amplitude, a normal stress has been incorporated in the Fatemi-Socie fatigue life parameter (Fatemi and Socie, 1988). Multiaxial fatigue life parameter will be reviewed in section 1.4.

It is found that the cyclic strain hardening along the non-proportional path is much more significant than that along the proportional one. This introduces the concept of additional hardening (Lamba and Sidebottom, 1978; McDowell and Socie, 1985). This additional hardening is attributed to different dislocation structures between in-phase loading and out-of-phase loading. Doong et al (1990) found that in planar slip materials, single slip occurs under proportional loading, and multi-slip under nonproportional loading. As a result, dislocation tangles are found for in-phase loading, whereas structures such as cells and labyrinths are observed for out-of-phase loading. Different materials show different amounts of additional hardening. Materials such as the 300 series stainless steels show a large amount of nonproportional cyclic hardening. The flow stress can increase by a factor of two. Carbon steel such as 1045 steel has an additional hardening of about 20%. Aluminum alloys do not exhibit any additional cyclic hardening. Nonproportional softening has not been observed in any material. The different additional hardening behaviors in different materials may also be related to the different dislocation structures, which are the results of different slip characters in different materials.

1.3.2 Mean stress effects

Mean stress effects are important in fatigue design since many engineering components are submitted to non-symmetrical loadings (mean stress not equal to zero). Common examples are superimposed static loads, residual stresses and non-symmetrical combined loads.

1.3.2.1 Normal mean stress effects

The experimental studies have considered axial mean stresses (e.g. Sines, 1955; Sines, 1961; Sines and Ohgi, 1981) and hoop mean stresses (e.g. Ei-Maged and Mielke, 1977; Marquis and Socie, 2000). Their effects on axial fatigue and torsional high cycle fatigue have been extensively investigated (e.g. Socie and Shield, 1984; Zhang and Akid, 1997).

Under axial fatigue, it is generally accepted that a tensile mean stress is detrimental to fatigue performance while a compressive mean stress is beneficial. The mean stress effects on the axial fatigue strength have been addressed in most design codes via the Goodman diagram (1899). Sines (1955, 1961) and Sines & Ohgi (1981) examined the effects of static tension and compression on alternating axial fatigue, and found that fatigue strength decreases with increasing static stress. After examining the fatigue data from several authors (Hohenemser and Prager, 1933; Sines, 1953; Sines, 1961), Sines and Ohgi (1981) argued that static axial tension and compression also have effects on the torsional fatigue strength. This strength also decreases with increasing static axial stress. They postulated that the mean stress effects on multiaxial fatigue can be taken into account with the mean hydrostatic stress.

Wang and Miller (1993) found that in a 1.99% NiCrMo steel under axial fatigue, a tensile mean stress accelerates both microstructurally and mechanically short crack growth rates, while a compressive mean stress does not.

Zhang and Akid (1997) studied the effect of static axial loads on torsional fatigue cracking behavior and the fatigue life of a high strength spring steel and a 316L stainless steel. They conducted fatigue tests on hourglass smooth specimens under fully reversed cyclic torsion, with or without superimposed tension or compression static axial loads. Tensile mean stresses were found to be detrimental to the fatigue life of the high strength steel but had no effects on the total life of 316L stainless steel. A compressive stress was

found to be beneficial to the life of both materials. Based on the observation of surface replicas, it has been found that the fatigue cracking behavior is material/stress state dependent (Figure 1.14). An axial tensile static stress made the Stage I (mode II) crack in the high strength steel change from the longitudinal direction to the direction normal to the specimen axis. But this was not observed in 316L stainless steel. However the transition crack lengths from stage I to stage II were reduced in both materials under axial static tensile stress; and they increased under axial compressive stress. For the high strength steel, in stage II, the crack growth rates always increased with increasing axial stress (from compression to tension). However, in stage I, growth rates increased under axial stress only. There was no obvious difference in crack growth rates under compressive axial stress. The influence of tensile axial stress on stage II crack growth rates in stainless steel was similar to that in high strength steel. However, contradictory effects on stage I crack growth were observed. The stage I crack growth rates decreased under the application of a tensile axial stress. The observation of crack orientations suggests that the effects of tensile stress on crack growth depend on the crack orientation. A tensile mean stress normal to a stage I crack accelerates the crack growth. However, a tensile mean stress parallel to the stage I crack reduces the growth rate.

Ei-Magd and Mielke (1977) investigated the effects of hoop mean stress on axial fatigue limit. They did a series of tests on tubular specimens made of low carbon steel and submitted to cyclic axial load and static internal pressure (hoop mean stress). Their results show that there is a decrease in the fatigue limit with increasing tensile hoop mean stress.

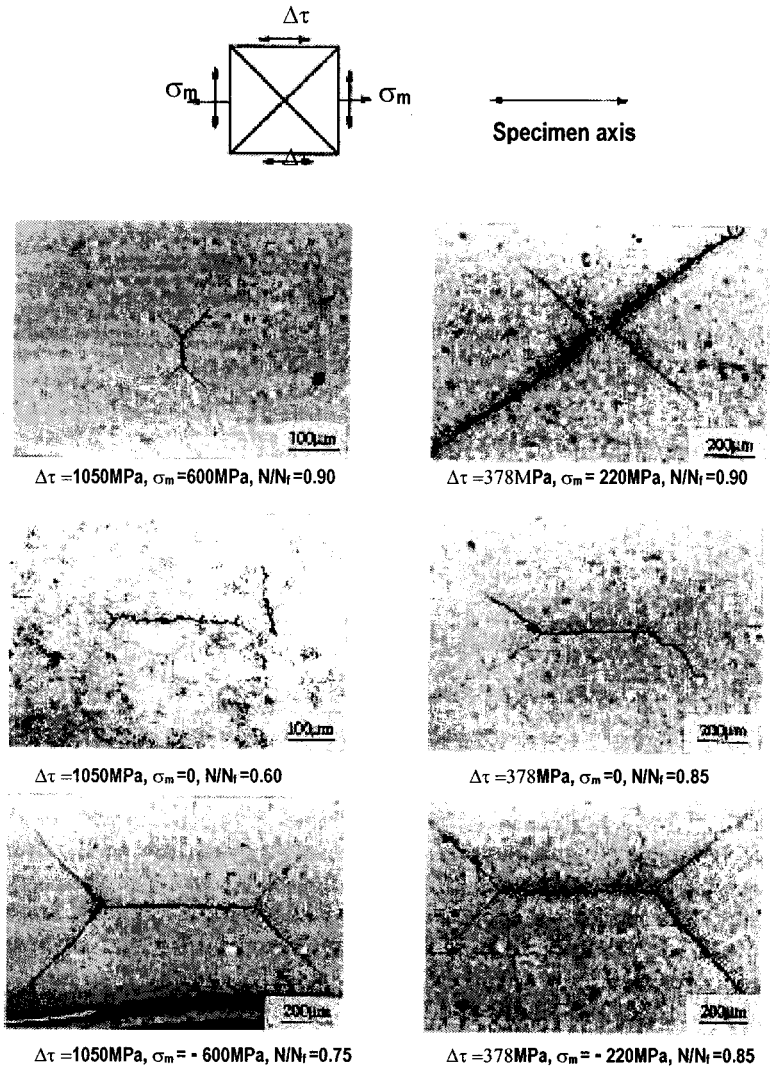

Figure 1.14 Characteristics of fatigue crack growth in torsion.
(a) High strength steel. (b) 316L stainless steel. (Zhang and Akid, 1997)

Marquis and Socie (2000) observed the effects of normal mean stresses on the torsional fatigue behavior of a carbon steel. They performed two kinds of tests on tubular specimens: pure torsional fatigue and torsional fatigue with superimposed axial compression and internal pressure. Under both loadings there is no hydrostatic stress. They found small cracks on both maximum shear planes under pure torsional fatigue. However, only longitudinal cracks (on the maximum shear plane with a tensile normal stress) were observed when there were superimposed normal static stresses. Fatigue lives in the two loading cases were also different. This implies that a fatigue life correlating parameter considering the hydrostatic stress is not appropriate. The lower life observed in the second loading case is attributed to the detrimental effects of the tensile normal stress on the longitudinal maximum shear plane. They argued that these detrimental effects cannot be compensated by the compressive normal stress on the transversal maximum shear plane. They concluded that the normal stress on the critical plane is a more appropriate term than the hydrostatic stress in fatigue life correlation.

1.3.2.2 Shear mean stress effects

As compared to the study of tensile mean stress effects on fatigue behavior, the studies on the effects of mean shear stress are relatively few.

The experiments by Gough et al (1949) showed that a superimposed mean shear stress of 170MPa only reduced the bending fatigue limit of a S65A steel from 370MPa to 340MPa (a reduction of 8.3%). The mean shear stress does not have large effects on the bending fatigue strength. Sines and Ohgi (1981) found that a static torsion does not influence the alternating torsional fatigue strengths of a medium and a low carbon steels, but it does influence their bending strengths if the applied static torque is high enough.

The effects of mean shear stress on axial fatigue performance were also investigated by Zhang and Akid in 1997 in a high strength spring steel. They found that a superimposed

torque reduced the axial fatigue strength. Stage I crack growth was accelerated by the application of the static torque. Stage II crack growth however, was independent of the applied mean shear stress.

Wang and Miller (1991, 1992) investigated the effects of mean shear stress on the torsional fatigue behavior of a NiCrMo steel. Mean shear stress had significant effects on the torsional fatigue life that decreased with increasing mean shear stress. They found that mean shear stress accelerates the growth of both microstructurally and physically short cracks. Cracks were found to initiate and propagate initially on maximum shear planes (stage I). Crystallographic growth was the major characteristic in stage I propagation and no rubbing trace was observed between the flanks of model II cracks, which is different from other observations made in different materials (Smith and Smith, 1988; Otsuka et al, 1980). The applied mean shear stress played a fundamental role in short crack growth. Two kinds of crack paths were found in stage II. Some cracks bifurcated and grew in mode I (stage II). Their growth depended on the level and the polarity of the mean shear stress. If no mean shear stress was applied, there were two branching cracks approximately of the same length. However, at high mean stress level, only one branching crack was favored; its orientation being determined by the mean shear stress polarity. Most of the other cracks grew in a zigzag path, and the microscopic segments were approximately perpendicular to the maximum principal stress.

1.3.2.3 Biaxial mean stress effects

Socie and Shield (1984) performed biaxial low cycle fatigue tests on thin-walled tubular specimens of Inconel 718 to investigate the mean stress effects. The loading histories of their tests are shown in Figure 1.15 in terms of applied shear and axial strains. These histories are designed to have the same maximum shear strain amplitude, but the normal stresses and strains across the planes of maximum shear strain amplitude are different.

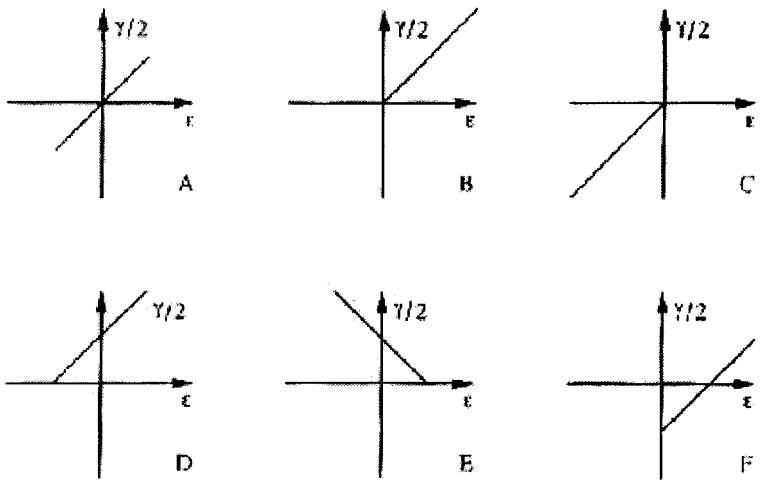

Figure 1.15 Loading histories employed by Socie and Shield (1984).

At the same maximum shear strain amplitude, fatigue life decreased with increasing normal mean stress on the maximum shear plane. The normal mean stress across the crack plane has a strong influence on the fatigue crack growth rate. The crack surfaces are irregularly shaped as the crack grows through the adjacent grains. This mechanical interlocking allows the crack surface to transmit shear loads. A tensile mean stress reduces this effect and results in a higher crack growth rate. The normal mean stress affects not only the crack growth rate, but also the distribution of cracks. Observations of specimen surfaces showed that all specimens have cracks on only one of the two maximum shear planes (the plane that experiences the maximum normal stress), except for loading history C in Figure 1.16. Under zero-to-compression loading (history C), the normal mean stress on both maximum shear planes is compressive. Multiple cracking is observed on both shear planes. Many cracks nucleate but grow with difficulty. Fatigue lives are greater so that more cracks have an opportunity to nucleate in grains that have crystallographic slip planes near the maximum shear planes.

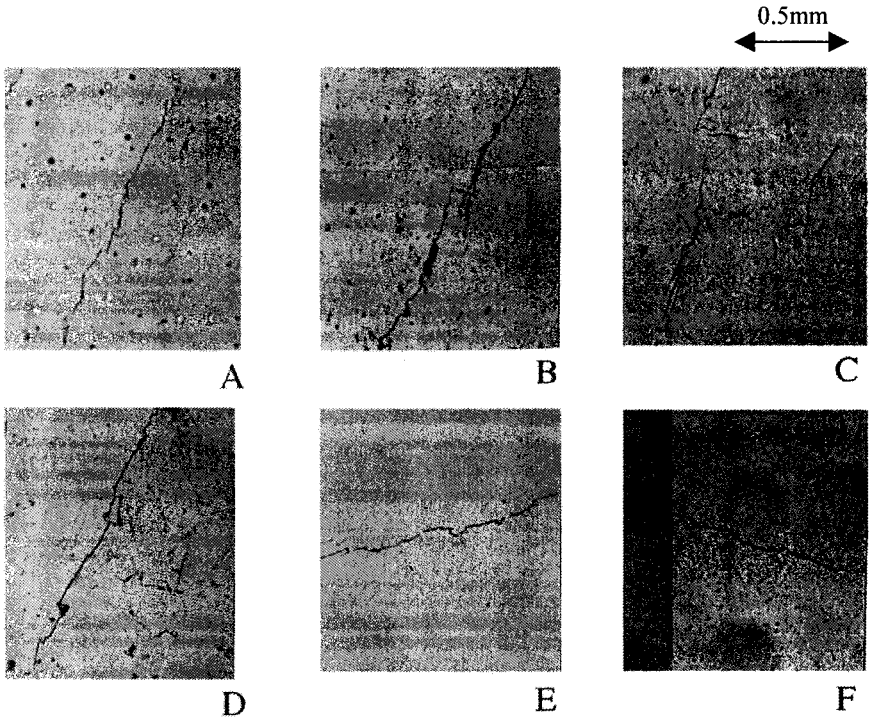

Figure 1.16 Crack observed under the loading histories in Figure 1.15 (the specimen axis is vertical in each photo; the scale is shown at the upright of this figure).

The effects of mean tensile stress on the crack plane can be understood in terms of an enhanced contribution to mode I opening, as well as an intensification of Mode II due to the reduction of crack face interference effects induced by the local plasticity, crack surface roughness or their combination (Socie, 1993).

Socie et al (1985) also reported low cycle fatigue test results on Inconel 718 under axial, torsional and combined axial-torsional in-phase cyclic loadings (strain-controlled, R_ε=-1 and R_ε=0). They observed at the surfaces of the specimens that cracks always formed on the plane of maximum shear strain amplitude. Crack growth along the plane of maximum principal strain was never observed under torsion and combined tension-torsion loadings. It was only observed very late in axial fatigue life. The mean principal strain did not change the crack direction. These observations suggest that fatigue life correlations based

on the maximum shear strain amplitude are appropriate. The mean strains did not have much influence on fatigue life at high strain amplitude, but they reduced the fatigue life when strain amplitude is low. This is related to mean stress relaxation that was observed in zero-to-tension tests (R=0); in particular, the mean stress relaxes to 0 for high strain amplitude tests. The authors argued that the mean stress rather than mean strain should be taken into account in a fatigue life parameter. They suggested a modification to Kandil-Brown-Miller parameter (1982) to account for the effects of the mean stress acting on the maximum shear plane.

1.4 Multiaxial fatigue life parameters

A multiaxial fatigue life parameter is a combination of some characteristic stress/strain components, used to correlate or to predict fatigue life under multiaxial loading. Many fatigue life parameters have been proposed. Several extensive reviews on multiaxial fatigue life parameters can be found in the literature (Brown and Miller, 1973; Garud, 1981; Macha and Sonsino, 1999; Papadopoulos et al, 1997; You and Lee, 1996). Fatigue life parameters include equivalent stress/strain parameters, which are extensions of the static yielding criteria. Some early researchers such as Gough et al (1951) employed different combinations of the applied normal and shear stresses as fatigue failure criteria. At the present time, the more prominent fatigue life parameters are based on the critical plane concept. For many materials crack initiation and shear crack growth (stage II) can represent an important part of fatigue life. The critical planes are generally the planes of maximum shear stress/strain amplitude. Different combinations of the maximum shear stress/strain amplitude and the normal stress/strain acting on the critical plane have been proposed (Findley, 1959; Brown and Miller, 1973). All fatigue life parameters fall into one of three categories: stress-based parameters, strain-based parameters and energy-based parameters.

1.4.1 Stress-based parameters

Stress-based parameters have been proposed to predict fatigue limit and high cycle fatigue life.

1.4.1.1 Early parameters

Among the earliest researchers, Gough and his co-workers (1935, 1951) systematically studied fatigue resistance under in-phase bending and torsion loadings. They proposed two models, the so-called ellipse quadrant (Eq. (1.5)) and ellipse arc (Eq. (1.6)), to describe the biaxial fatigue limits of ductile metals and brittle metals respectively.

$$\left(\frac{\sigma_0}{\sigma_{-1}}\right)^2+\left(\frac{\tau_0}{\tau_{-1}}\right)^2 \le 1 \tag{1.5}$$

$$\left(\frac{\sigma_{-1}}{\tau_{-1}}-1\right)\left(\frac{\sigma_0}{\sigma_{-1}}\right)^2+\left(\frac{\tau_0}{\tau_{-1}}\right)^2+\left(2-\frac{\sigma_{-1}}{\tau_{-1}}\right)\frac{\sigma_0}{\sigma_{-1}} \le 1 \tag{1.6}$$

where σ_0 and τ_0 are the applied bending and shear stress amplitudes, and σ_{-1} and τ_{-1} are the fatigue limits under fully reversed bending and torsion, respectively. It is noticed that these two formulae are proposed for in-phase loading. Further, they do not account for mean stresses, although the authors have studied their effects. They mentioned that a superimposed static shear does not alter the fatigue limits, but a tensile mean stress can reduce the fatigue limits significantly and a compressive mean stress is beneficial to fatigue life. No physical interpretations were given by the authors for the above two formulae.

Lee (1985) proposed a modification to the Gough's ellipse quadrant to deal with the problem of out-of-phase loading as follows:

$$\left[\left(\frac{\sigma_0}{\sigma_{-1}}\right)^g+\left(\frac{\tau_0}{\tau_{-1}}\right)^g\right]^{1/g} \le 1 \tag{1.7}$$

where g is a function of the phase angle ϕ, g (ϕ)=2(1+qsinϕ), and out-of-phase loading effect is included through g. However, this formula was only proposed for fully reversed loading. To include the mean stress effect on the fatigue strength, Lee (1989) made another modification,

$$\left[\left(\frac{\sigma_0}{\sigma_{-1}}\right)^g+\left(\frac{\tau_0}{\tau_{-1}}\right)^g\right]^{1/g}\left[1-\left(\frac{\sigma_m}{\sigma_{UTS}}\right)^n\right]^{-1}\le 1 \qquad (1.8)$$

where σ_m is the normal mean stress, and σ_{UTS} is the ultimate tensile strength. g has the same definition as in Eq.(1.7); q and n are material constants that can be identified experimentally. Since the above two equations include a high number of adjustable constants, it is not surprising that they can work well for some cases. However, as criticized by Papadopoulos (1994), if n is an even integer, Eq.1.8 cannot predict the beneficial effect of compressive mean stress that is experimentally observed on the fatigue strength.

Froustey and Lasserre (1989) also proposed a modification to the Gough's ellipse quadrant. Their model includes a mean stress term but it does not include the phase difference. Their observations on a 30NCD16 steel showed that the phase angle does not influence the fatigue limits under bending-torsion loadings.

1.4.1.2 Extensions of the static yield criteria

Because cyclic plasticity is the fatigue driving force, it is reasonable to extend the three static yielding criteria - maximum principal stress (Rankine criterion), maximum shear stress (Tresca criterion) and octahedral shear stress (von Mises criterion) - as fatigue failure criteria. Therefore, multiaxial stresses can be reduced to an equivalent uniaxial stress. These extensions can be formulated as follows:

i. Maximum principal stress (Rankine)

$$\sigma_{eq} = \sigma_1 \tag{1.9}$$

ii. Maximum shear stress or Tresca equivalent stress

$$\tau_{max} = \frac{\sigma_1 - \sigma_3}{2} \; ; \; \sigma_{eq} = \sigma_1 - \sigma_3 \tag{1.10}$$

iii. Octahedral shear stress or von Mises equivalent stress

$$\tau_{oct,a} = \frac{1}{3}\sqrt{(\sigma_1 - \sigma_2)^2 + (\sigma_2 - \sigma_3)^2 + (\sigma_3 - \sigma_1)^2} \; ;$$

$$\sigma_{eq} = \frac{1}{\sqrt{2}}\sqrt{(\sigma_1 - \sigma_2)^2 + (\sigma_2 - \sigma_3)^2 + (\sigma_3 - \sigma_1)^2} \tag{1.11}$$

where σ_1, σ_2 and σ_3 are the principal stress amplitudes. Although, it was sometimes claimed that the von Mises criterion gives good correlations of in-phase fatigue lives, it was generally found that these criteria cannot even correlate the life data of axial fatigue and torsional fatigue. With either Tresca or von Mises criterion (section 1.1), torsional fatigue life is generally higher than that of axial fatigue. However, because of the importance of shear stress on the fatigue damage, Tresca and von Mises criteria are often used as the basis for developing new parameters that also to account for other effects such as mean stress effects and out-of-phase loading effects under multiaxial fatigue.

Two equivalent stresses SALT and SEQA, based on Tresca and von Mises parameters respectively, are presented in ASME Boiler and Pressure Vessel Codes to account for the out-of-phase loadings. For out-of-phase torsion and bending, the SALT and SEQA parameters are expressed as follows,

$$SALT = \frac{\sigma_0}{2}\left[1 + 4\lambda^2 + \sqrt{1 + 8\lambda^2 \cos 2\phi + 16\lambda^4}\right]^{1/2} * \tag{1.12}$$

---

* ASME Boiler and Pressure Vessel Code, Section III, Division I, Subsection NA, Appendix XIV, American Society of Mechanical Engineers, New York, 1974.

$$SEQA = \frac{\sigma_0}{\sqrt{2}}\left[1 + 3\lambda^2 + \sqrt{1 + 6\lambda^2 \cos 2\phi + 9\lambda^4}\right]^{1/2} \text{ **} \qquad (1.13)$$

where σ_0 and τ_0 are the applied axial (or bending) and shear stress amplitudes, $\lambda=\tau_0/\sigma_0$ is the stress ratio, and ϕ is the phase angle between applied axial (bending) and shear stresses.

Lee (1985) found that both the Tresca type (SALT) and von Mises type (SEQA) criteria overestimate the fatigue damage for out-of-phase loadings at high stress ratios (where the torsional component is predominant), while they underestimate it at low stress ratios.

1.4.1.3 Modifications to von Mises criterion

Sines (1955) proposed a life model including the static (mean) hydrostatic stress in addition to the octahedral shear stress amplitude to account for the normal mean stress effects.

$$\tau_{oct,a} + k\sigma_H{}^m = f(N) \qquad (1.14\text{-a})$$

where $\tau_{oct,a}$ is the octahedral shear stress amplitude, $\sigma_H{}^m$ is the mean hydrostatic stress, and k is a material constant. The first term in Eq. (1.14-a) is proportional to the root-mean-square of the shear stress amplitudes over all planes and the second term is proportional to the average of the mean normal stress over all planes. The physical interpretation of the above criterion is that for a given fatigue life, the permissible amplitude of the root-mean-square of shear stress amplitudes over all planes is a linear function of the static normal mean stress averaged over all planes (Sines and Ohgi, 1981).

Crossland (1956) proposed a similar life parameter, except that the maximum value of hydrostatic stress is used instead of the mean value.

$$\tau_{oct,a} + k\sigma_H{}^{max} = f(N) \qquad (1.14\text{-b})$$

** ASME Boiler and Pressure Vessel Code, Section III, Code Case N-47-12, American Society of Mechanical Engineers, New York, 1980.

Based on the consideration that the fatigue strength is determined by both the resolved shear stress amplitude and the normal stress acting on the cracks, Papadopoulos (1995) proposed a rather complex model and claimed that it is applicable for high cycle biaxial and triaxial out-of-phase stress conditions. The model to describe the fatigue limit is the following,

$$\sqrt{\langle \tau_a^2 \rangle} + a\langle \sigma \rangle^{\max} \le b \tag{1.15}$$

$$\sqrt{\langle \tau_a^2 \rangle} = \sqrt{5}\sqrt{\frac{1}{8\pi^2}\int_{\phi=0}^{2\pi}\int_{\theta=0}^{\pi}\int_{\chi=0}^{2\pi}(\tau_a(\phi,\theta,\chi))^2 d\chi \sin\theta d\theta d\phi} \tag{1.16}$$

$$\langle \sigma \rangle = \frac{1}{4\pi}\int_{\phi=0}^{2\pi}\int_{\theta=0}^{\pi}\sigma(\phi,\theta)\sin\theta d\theta d\phi \tag{1.17}$$

where τ_a is the resolved shear stress amplitude, and σ is the normal stress acting on a given plane. The first term in Eq. (1.15) is the average value of τ_a defined as the root-mean-square over all plane orientations (Eq. (1.16)). This is motivated by the fact that under static loading the root mean square of shear stress leads to von Mises equivalent stress. The second term in Eq. (1.15) is the maximum value that is reached during one cycle by the average value $<\sigma>$ of the normal stress (Eq. 1.17). The material constants can be obtained experimentally. This criterion has a physical meaning similar to that of Sines and Crossland. In the case of axial-torsional loading, the criterion reduces to,

$$\sqrt{\frac{\sigma_0^2}{3} + \tau_0^2} + a\frac{\sigma_0 + \sigma_m}{3} \le b \tag{1.18}$$

The same expression would be obtained from Eq. 1.14-b. Note that it does not include the phase angle, so the author claimed that the phase difference does not influence the fatigue limit under an axial (bending)-torsional loading. Later, Papadopoulos (2000) used this parameter to predict finite high cycle fatigue life. A possible form of this parameter for axial-torsional fatigue is the following,

$$\sqrt{\frac{\sigma_0^2}{3} + \tau_0^2} + k\frac{\sigma_0 + \sigma_m}{3} = f(N) \tag{1.19}$$

where k can be experimentally identified, or derived from shear and normal fatigue limits.

As reviewed by Zenner et al (2000), the von Mises equivalent stress can be physically interpreted as: 1) the distortion energy, 2) the octahedral shear stress, 3) the root mean square of the principal stress, and 4) root mean square of the shear stresses over all plane orientations. Motivated by the last interpretation, Zenner et al (2000) proposed an integral approach to obtain an equivalent stress under complex loading. They modified the von Mises equivalent stress by including the mean shear stress, the normal stress amplitude and the normal mean stress acting on a given plane. A rather complex formula is proposed,

$$\sigma_{eq} = \left\{ \frac{15}{8\pi} \int_{\gamma=0}^{\pi} \int_{\varphi=0}^{2\pi} \left[a\tau_{\gamma\varphi a}^{2}(1 + m\tau_{\gamma\varphi m}^{2}) + b\sigma_{\gamma\varphi a}^{2}(1 + n\sigma_{\gamma\varphi m}) \right] \sin\gamma d\gamma d\varphi \right\}^{1/2} \qquad (1.20)$$

Here, angles γ and φ are used to define a plane orientation. $\tau_{\gamma\varphi a}$ and $\tau_{\gamma\varphi m}$ are the shear stress amplitude and mean shear stress on a plane $\gamma\varphi$, and $\sigma_{\gamma\varphi a}$ and $\sigma_{\gamma\varphi m}$ are the normal stress amplitude and the normal mean stress on a plane $\gamma\varphi$. The constants a, b, m, and n can be obtained from the fatigue strength under fully reversed tension-compression, fully reversed torsion, pulsating tension and pulsating torsion.

1.4.1.4 Modifications to Tresca criterion (critical plane parameters)

As compared with other approaches, the critical plane approaches for fatigue life correlation and prediction have a clear physical meaning. Because the fatigue crack initiation and propagation are often associated with some specific planes, the so-called critical planes, the fatigue life parameter should use the stress components related to these planes. The critical planes are generally defined as the planes of maximum shear stress amplitude, τ_{max}. Note that under non-proportional loading, the maximum shear stress amplitude can be different from that computed from applied stress amplitudes (Eqn.1.10).

Findley et al (1956) was among the first researchers who put forward the concept of critical plane. According to Findley, the alternation of shear stress is the primary cause of fatigue, while the normal stress amplitude on the critical plane has some effect. Findley

parameter was first developed for fully reversed biaxial proportional loading. Based on the observation that the effect of mean shear stress is weak and the effect of mean normal stress is strong, Findley (1959) extended his theory to include mean stress effects by using the maximum normal stress σ_n^{max} on the critical plane, instead of the normal stress amplitude. In the Findley parameter, the critical plane is the plane on which the combination of shear stress and normal stress are maximum. It is not necessarily the maximum shear plane. The Findley parameter is formulated as follows,

$$(\tau_a + k\sigma_n^{max})_{max} = f(N) \tag{1.21}$$

where the material constant k can be experimentally determined.

McDiarmid (1973, 1981, 1991, 1994) did a large amount of analytical and experimental work, and presented a general criterion for high cycle multiaxial fatigue as,

$$\tau_{max} / t_{A,B} + \sigma_n^{max} / 2\sigma_{UTS} = 1 \tag{1.22}$$

Where t_A and t_B are the reversed shear fatigue strengths for case A and case B cracks respectively. This failure criterion is based on the concept that fatigue strength is a function of the shear stress amplitude and the maximum normal stress on the plane of maximum shear stress amplitude (definition of the critical plane). This criterion takes into account Case A and Case B cracks. The author has shown that his criterion is applicable to a wide range of multiaxial high cycle fatigue data on combined bending and torsion of thin and thick pressure vessels. The effects of mean stress, out-of-phase loading, stresses with different frequencies and also a variety of waveforms are taken into account. In order to predict the finite high cycle multiaxial fatigue life, the author proposed the following formula,

$$\tau_{max} + k\sigma_n^{max} = f(N) \tag{1.23}$$

where k is a material constant to be adjusted with experimental data. This parameter is similar to Findley parameter, but the definition of the critical plane is different.

Dang-Van (1993) proposed a macro-micro approach that is widely used in industry in France to predict the high cycle fatigue failure under multiaxial loading. In this approach,

the current stress state is considered and damage happens at a precise instant of the loading path. As the cracks usually occur at slip bands, the local shear acting on the crack plane is an important parameter, and the hydrostatic stress can accelerate the damage. Dang-van formulated his fatigue limit criterion as,

$$\tau_{max} + a\sigma_H^{max} \leq b \tag{1.24}$$

where σ_H^{max} is the maximum hydrostatic stress, and constants a and b can be obtained from two simple tests. In the case of high cycle fatigue life prediction, Dang-Van equation can be written as,

$$\tau_{max} + k\sigma_H^{max} = f(N) \tag{1.25}$$

1.4.2 Strain-based parameters

Strain-based fatigue life parameters have been proposed for low cycle fatigue where the plastic strain amplitude is more dominant than the elastic strain amplitude.

1.4.2.1 Extensions of the static yielding criteria

In parallel with the stress models, the three yielding criteria are also extended to fatigue in terms of strains as follows,

i. Maximum principal strain

$$\varepsilon_{eq} = \varepsilon_1 \tag{1.27}$$

ii. Maximum shear strain (Tresca)

$$\gamma_{max} = \varepsilon_1 - \varepsilon_3 \tag{1.28}$$

iii. Octahedral shear strain (von Mises)

$$\varepsilon_{eq} = c\sqrt{(\varepsilon_1 - \varepsilon_2)^2 + (\varepsilon_2 - \varepsilon_3)^2 + (\varepsilon_3 - \varepsilon_1)^2} \tag{1.29}$$

In these equations, ε_1, ε_2 and ε_3 are the principal strain amplitudes ($\varepsilon_1 \geq \varepsilon_2 \geq \varepsilon_3$).

Like stress-based parameters, the von Mises equivalent strain was popular among early fatigue studies, but it is not a good life parameter for out-of-phase loadings (Kanazawa, 1977). Some modifications to von-Mises have been proposed. For example, Zamrik et al (1993) proposed a modification incorporating a concept of triaxiality factors, which is used to account for different loading paths.

1.4.2.2 Critical-plane parameters (modifications to Tresca criterion)

Brown and Miller (1973) postulated that fatigue damage occurs on some specific planes, the so-called critical planes, on which the shear strain amplitude is maximum. They recognized that the shear strain amplitude, γ_{max}, on the critical plane governs fatigue damage, while the normal strain amplitude on this plane, ε_n, plays a second important role in assisting fatigue damage. They proposed that for a given fatigue life, the shear strain amplitude on the critical plane is a function of the normal strain amplitude on this plane. Kandil, Brown and Miller (1982) later proposed a simple parameter (KBM parameter) as,

$$\gamma_{max} + k\varepsilon_n = f(N) \tag{1.30}$$

where k is a material constant obtained by consolidating axial and torsional fatigue data.

Kanazawa et al (1977) showed that such a parameter can correlate both in-phase and out-of-phase fatigue lives (see section 1.3). The phase difference under out-of-phase loading between the normal and shear strain on the critical plane has no influence on the fatigue life of 1%Cr-Mo-V steel. This was also shown by the investigation by Jordan et al (1985). However, contradictory results were obtained by Andrew and Brown (1989). They found that out-of-phase data for 316 stainless steel at high temperature fell above in-phase data when plotted against KBM parameter. This implies that the effect of normal strain amplitude on fatigue damage is overestimated, and that the phase difference between normal and shear strains on the critical plane affects fatigue life. Based on this point, Wang and Brown (1993) proposed the following model (Wang-Brown parameter),

$$\gamma_{max} + k\varepsilon_n^* = f(N) \tag{1.31}$$

where γ_{max} is the maximum shear strain amplitude and ε_n^* is the normal strain excursion during one reversal of shear strain on the critical plane. This model was initially proposed for variable amplitude multiaxial fatigue; of course, it is applicable to constant amplitude multiaxial fatigue. For constant-amplitude loading, the difference of this parameter with respect to KBM parameter is that it considers the normal strain excursion during one reversal instead of one cycle. The normal strain excursion, ε_n^*, is lower for out-of-phase loading.

Shang and Wang (1998) also regarded that the maximum shear strain range and the normal strain excursion during one reversal on the maximum shear plane are two important factors that govern the fatigue damage. However, the two factors are combined as follows:

$$\varepsilon_{eq} = \left[\varepsilon_n^{*2} + \frac{1}{3}(\gamma_{max})^2 \right]^{1/2} \tag{1.32}$$

For fully reversed loading, the fatigue life is predicted by,

$$\varepsilon_{eq} = \frac{\sigma_f'}{E}(2N_f)^b + \varepsilon_f'(2N_f)^c \tag{1.33}$$

Where σ_f', ε_f, b, c are material constants for fully reversed axial fatigue. To include the mean stress effects, Eq. (1.33) is modified as,

$$\varepsilon_{eq} = \frac{\sigma_f' - \sigma_m}{E}(2N_f)^b + \varepsilon_f'(2N_f)^c \tag{1.34}$$

Here, σ_m is normal mean stress on the maximum shear plane.

Jordan et al (1985) conducted fatigue tests with different loading paths, but with the same amplitude of maximum shear strain and normal strain across the maximum shear planes. They found that the fatigue lives were different for different loading paths, and the compressive half cycles were non-damaging. They proposed a modification to KBM parameter, using the average of the positive normal strains over time instead of the normal strain amplitude.

Lohr and Ellison (1980) proposed a simple model based on the hypothesis that the maximum shear strain, γ^*, on the plane driving the crack through the thickness controls the fatigue crack propagation rate and hence the life, whereas the normal strain ε_n^* acting on the plane of γ^* plays a secondary role in fatigue damage. They formulated this model as,

$$\gamma^* + k\varepsilon_n^* = f(N) \tag{1.35}$$

This is very similar to Eq. (1.30), except the critical plane here is defined as the plane on which the shear strain driving the crack into the specimen thickness is maximum. It is not necessarily the maximum shear plane.

During out-of-phase or non-proportional loadings, the principal axes rotate causing additional cyclic hardening in several materials (Fatemi, 1985; Fatemi and Socie, 1988). This additional cyclic hardening was claimed to be responsible for the additional damage in out-of-phase loadings (shorter lives are observed in γ_{max}-N plots in the region of 10^3-10^5 cycles). A parameter that uses both strain and stress has the potential to account for this strain path dependence of fatigue behavior. Fatemi and Socie (1988) proposed the following parameter

$$\gamma_{max}\left(1 + k\frac{\sigma_n^{max}}{\sigma_y}\right) = f(N) \tag{1.36}$$

and obtained reasonable correlations of in-phase, out-of-phase and mean stress/mean strain data of 1045 steel and Inconel 718. A further advantage of this parameter is that it does not predict fatigue damage under static-only load (it yields zero when $\gamma_{max}=0$).

1.4.3 Energy-based parameters

Energy-based fatigue life parameters have been developed for multiaxial fatigue, but they are not widely accepted. The main criticism to the energy-based parameters is that energy is a scalar quantity, unable to account for the fatigue damage that is often involved in some specific planes. Energy-based parameters will be briefly reviewed.

1.4.3.1 Parameters involving a critical plane

Glinka et al (1995) criticized the KBM parameter on two points: 1) the algebraic sum of normal and shear strain components is a lack of formal correctness from the continuum mechanics viewpoint; 2) the two components are weighted by a constant k, which is found to vary with fatigue life by Fatemi and Kurath (1988). Further, in the case of multiaxial fatigue, stress terms also contribute to the fatigue damage, especially for non-proportional loading. These authors initially proposed an energy criterion as:

$$W = \gamma_{max}\tau_{max} + \varepsilon_n\sigma_n = f(N) \tag{1.37}$$

where W is a cyclic strain energy density. The critical plane here is the same as for KBM parameter. In order to take into account the mean stress effects, Eq. (1.37) was modified as (Glinka et al, 1995):

$$W = \gamma_{max}\tau_{max}\left(\frac{1}{1-\tau^{max}/\tau_f'} + \frac{1}{1-\sigma_n^{max}/\sigma_f'}\right) = f(N) \tag{1.38}$$

where τ^{max} and σ_n^{max} are the maximum values reached over time by the shear stress and normal stress acting on the critical plane.

Liu (1993) proposed a critical-plane approach for multiaxial fatigue life prediction based on virtual strain energy parameters, which takes into account mode I and mode II fractures as well as Case A and case B cracks.

Chu et al (1993) proposed the following parameter to account for mean stress effects,

$$W = 2\tau^{max}\gamma_{max} + \sigma_n^{max}\varepsilon_n = f(N) \tag{1.39}$$

Varvani-Farahani (2000) proposed a critical-plane energy-based model as follows,

$$\frac{1}{(\sigma_f'\varepsilon_f')}(\Delta\sigma_n\Delta\varepsilon_n) + \frac{1}{(\tau_f'\gamma_f')}\left(\Delta\tau_{max}\Delta\left(\frac{\gamma_{max}}{2}\right)\right) = f(N) \tag{1.40}$$

$\Delta\tau_{max}$, $\Delta\gamma_{max}$ are the maximum shear stress and shear strain ranges obtained from the largest stress and strain Mohr's circles during the loading part and the unloading part of a

cycle. $\Delta\sigma_n$ and $\Delta\varepsilon_n$ are the corresponding normal stress and strain ranges. To take into account mean shear stress effects, the above equation was modified as follows:

$$\frac{1}{(\sigma_f'\varepsilon_f')}(\Delta\sigma_n\Delta\varepsilon_n)+\frac{1+\sigma_m/\sigma_f}{(\tau_f'\gamma_f')}\left(\Delta\tau_{max}\Delta\left(\frac{\gamma_{max}}{2}\right)\right)=f(N) \tag{1.41}$$

Here σ_m is the normal mean stress on the critical plane.

It is noticed that most of aforementioned critical plane parameters are associated with shear crack growth (Region A behavior, section 1.2.3). A shear-based parameter is not appropriate for a tensile crack growth (Region B behavior). The Smith-Watson-Topper (SWT) parameter, which was originally proposed to account for mean stress effects during uniaxial loading (1970), was used by Socie (1987) to correlate the fatigue lives in Region B (determined by mode I or tensile crack growth).

$$\sigma_n^{max}\varepsilon_{max}=f(N) \tag{1.42}$$

here ε_{max} is the maximum normal strain amplitude, and σ_n^{max} is the maximum stress on the critical plane. It is defined here as the plane of maximum normal strain amplitude, which is the plane of mode I cracks. The maximum normal stress is claimed to be able to account for mean normal stress effects as in the Fatemi-Socie parameter.

1.4.3.2 Modification to von Mises criterion

Ellyin and Kujawski (1993) proposed that an appropriate fatigue damage function Ψ would have the following form,

$$\Psi=\Psi(\Delta W, \rho, \sigma_H^m) \tag{1.43}$$

Here, ΔW is strain energy input per reversal, σ_H^m is the mean hydrostatic stress to account for mean normal stresses, and ρ is a measure of the multiaxial constraint. For an elastic-plastic isotropic material, the von Mises yield condition is equivalent to the distortional component of the strain energy density $W_d = \int s_{ij}de_{ij}$ ($s_{ij}=\sigma_{ij}-\sigma_{kk}\delta_{ij}/3$, and $e_{ij}=\varepsilon_{ij}-\varepsilon_{kk}\delta_{ij}/3$). The Ellyin-Kujawski criterion can be written as,

$$\Psi = \frac{\Delta W_d (1 + \alpha \frac{\sigma_H^m}{\overline{\sigma}})}{(\rho)^n} = f(N) \tag{1.44}$$

Where $\overline{\sigma}$ is an equivalent stress amplitude, and α is a material constant.

1.4.4 Remarks on the multiaxial fatigue life parameters

From the above review, several remarks are summarized as follows,

- Most fatigue life parameters can be considered as extensions of the von Mises criterion (e.g. Sines and Crossland parameters) or of the Tresca criterion (e.g. Findley, McDiarmid and Kandil-Brown-Miller parameters) by adding some terms to account for normal stress/strain effects.
- There are basically two ways to take into account the effects of normal stress or strain: normal stress/strain on the critical plane (e.g. McDiarmid, Kandil-Brown-Miller and Fatemi-Socie parameters) and the hydrostatic stress (e.g. Dang-Van and Papadopoulos parameters).
- Only parameters considering the maximum normal stress on the critical plane (e.g. McDiarmid and Fatemi-Socie parameters) or the maximum hydrostatic stress (e.g. Dang-Van and Papadopoulos parameters) can mathematically account for both normal stress amplitude and normal mean stress effects.
- The shear stress/strain effects and the normal stress/strain effects on the fatigue damage are generally weighted by a constant k, but some parameters (e.g. Glinka-Wang-Plumtree parameter) are formulated without this constant.

1.5 Material anisotropy effects

Most engineering materials exhibit some degree of anisotropy induced by crystallographic texture and/or by fibrous structure. As a consequence, their mechanical behavior may also show some extent of anisotropy. It is important to include the material anisotropy effects in multiaxial fatigue life prediction models in order to improve their

reliability in design as well as in safety evaluation. In an anisotropic material, cracking behavior may depend on the specimen orientation and loading path. The life prediction model should be based on the actual fatigue cracking behavior

Material anisotropic effects on biaxial fatigue cracking behavior and fatigue life have been studied from two approaches, which are: (1) compare the fatigue behavior in different test orientations in an anisotropic material; (2) compare the fatigue behavior between anisotropic and isotropic material.

1.5.1 Orientation-dependent fatigue behavior of anisotropic material

Fatigue behavior in an anisotropic material is generally anisotropic. The effects of material anisotropy on the fatigue behavior can vary with material type and/or loading conditions.

Both the crystallographic texture and the fibrous structure have effects on the fatigue properties of metals (Plumbridge, 1972). The influence of textures on the fatigue life may depend on the textures. The formation of a fibrous structure generally decreases the fatigue resistance in the transverse direction. Leese et al (1985) used transverse and longitudinal specimens to perform axial fatigue tests in hot-rolled 1045 steel. The results showed that specimens machined in the transverse direction have lower fatigue lives by a factor of 2 to 3 compared to longitudinal specimens. This life difference is attributed to the anisotropy induced by sulfide inclusions along the longitudinal direction.

Socie (1985) conducted similar tests with Inconel 718. Specimens were also cut from longitudinal and transverse directions with respect to the forging direction. The anisotropy effect was similar to that of 1045 steel.

Eswara Prasad et al (1996) studied the low cycle axial fatigue behavior as a function of the test direction in rolled plates of an 8089 aluminum alloy. Anisotropy of this material is induced by the crystallographic texture and grain fibering. Three test directions were studied: longitudinal L (specimen axis parallel to the rolling direction), L+45^0 (specimen axis at 45^0 to the rolling direction), and long transverse LT (specimen axis perpendicular to the rolling direction). Anisotropy in cyclic stress-strain response was evident in two ways. Firstly, the average stress amplitude at half-life for any particular total strain amplitude was typically lower in the L+45^0 direction than in the other two test directions. Secondly, the critical strain amplitude above which cyclic softening occurred varied with test directions. Softening was found to start in the LT direction at marginally lower strain amplitude than in the L direction. This is due to the selective relaxation of residual stresses, i.e., of the tensile stress amplitude in the L direction, and compressive stress amplitude in the LT direction. A comparison of the fatigue life data for different test directions revealed significant anisotropy. The fatigue life was significantly higher in the LT direction as compared with that in the L direction. However, the fatigue resistance in L+45^0 direction, when compared with that in L direction varies with strain amplitude. It is higher at a high strain amplitude, but it is the same at a low strain amplitude. The observed transition in Coffin-Manson plots is attributed to a change in deformation mechanism and to a deformation assisted fracture mode. A homogeneous dislocation structure at low strain amplitude gave way to a highly heterogeneous substructure with intense shear bands at high strain amplitude. The corresponding change in the fracture mode was from high-energy transgranular shear to low energy intergranular fracture.

Ohji et al (1976) investigated fatigue behavior of anisotropic rolled steel plates under cyclic torsion. The material anisotropy is introduced by the mechanical fibering or laminated structures. Tubular smooth specimens were cut from plates at different angles between the specimen axis and rolling direction (0^0, 45^0 and 90^0). Notched specimens, in which notch is at 45^0 with respect to the specimen axis, were also cut at different angles. They found that in 0^0 and 90^0 smooth specimens, the leading cracks (shear crack) were

parallel to the laminated structures, and the fracture surfaces were smooth. But in 45^0 smooth specimens, the fracture surface was rough, since shear cracking encountered the resistance from the lamellar interface. In all notched specimens, the cracks propagated in a tensile mode and were independent on the orientation of the specimen. Fatigue life was orientation-dependent (anisotropic) of both notched and smooth specimens. The 45^0 specimen had the longest life, while the 0^0 and 90^0 smooth specimens have approximately the same life, since the material anisotropy helps the crack advancing in latter two cases. In the notched specimen, anisotropy assisted the cracking process where the lamellae coincided with the notch and the maximum principal directions.

Kiyotsugu et al (1976) performed torsional fatigue on specimens cut from a rolled steel plate such that specimen axis is 0^0,45^0 and 90^0 with respect to the pearlite-ferrite laminar direction. They found that at the same stress level, 0^0 and 90^0 specimens have approximately the same lives, while the 45^0 specimen has highest life. The anisotropy caused by the fibrous structure assisted the cracking process when the rolling direction was the same as the maximum shear direction in torsion.

Lin and Nayeb-Hashmi (1993) studied the effects of material anisotropy on cyclic deformation and biaxial fatigue behavior of 6061-T6 aluminum alloy, in which anisotropy was caused by elongated grains and by the alignment of the precipitates along the rolling direction. Test specimens were machined in two orientations from an Al-6061-T6 plate, along the rolling direction (RD) and the transverse direction (TD). They found that TD specimens showed higher cyclic stress-strain response under tension-compression, while RD specimens showed higher cyclic stress-strain response under torsion. Fatigue cracks initiated and propagated on the maximum shear planes in both TD and RD specimens. The damage mechanism of this material appeared to be shear predominated. The material anisotropy seemed to have no effect on fatigue cracking behavior, although it did have effects on the fatigue life. It was found that under the same shear strain amplitude, RD specimens had higher lives in uniaxial fatigue, while TD

specimens had higher lives under torsional fatigue. They argued that this result coincides with the stress-strain responses observed in these two loading conditions. The authors showed that the tensile cracking model (SWT parameter), a plastic work model and an effective strain model gave poor correlation for the fatigue life data from TD and RD specimens. A new shear parameter incorporating material anisotropy effects was proposed, A (γ_{max}+Bε_n), in which A and B are anisotropic coefficients whose values depend on the material orientation. A is introduced to reduce the two torsional baseline obtained from TD and RD orientations into one. B is needed to consolidate the data from tension/compression with those from pure torsion. They showed a good correlation was obtained using this parameter.

1.5.2 Anisotropic material versus isotropic material

Verpoest et al (1985) investigated the biaxial fatigue cracking behavior of high carbon (0.83%C) and low carbon (0.06%C) steel wires under annealed or patented (isotropic) and cold drawn (anisotropic) conditions. In the cold drawn steel wires, anisotropy is formed by elongated cells and grains in the low carbon steel and by an axially oriented lamellar structure in the nearly eutectoidic (pearlitic) steel. In both materials, the ferrite shows additionally a (110) crystallographic texture. Biaxial in-phase tests were performed on solid cylindrical specimens with stress ratios λ= 0 (pure tension), 0.25, 0.50, 1, 2, 5, and ∞ (pure torsion). The observation on fatigue crack patterns shows that the isotropic high and low carbon steels are damaged by tensile cracking mode for all stress ratios. In anisotropic materials, shear damage mode was observed when $\lambda \geq 0.5$. They calculated the plastic zone for Mode I and Mode II cracks in both materials following the approach used by Gao et al (1982). They found that once the ratio of plastic zones of the Mode II crack over Mode I crack reached a critical value of about 4, Mode II crack appeared. In anisotropic materials, this ratio can easily attain a high value (>4), and then Mode II crack was observed. In isotropic materials, the maximum value of this ratio is 3.72 in pure torsion, so no Mode II cracks were observed. Moreover, it seems that a

loading case with high stress ratio favors mode II cracking. This is in agreement with the observation that torsion fatigue favors mode II damage (Socie, 1993).

Shatil et al (1994) performed axial and torsional fatigue tests on isotropic and anisotropic (caused by MnS inclusion strings) structural steel EN15R. They found that under pure torsional fatigue the lives of the isotropic specimens were about twice longer than those of the anisotropic specimens tested under approximately the same strain ranges. However, the lives of both types of specimens were very similar in tests carried out under pure axial fatigue. In axial fatigue, cracks are usually aligned at 45^0 from the longitudinal direction, and lives are not affected since inclusions are not aligned with the direction of crack growth. Under torsional fatigue, cracks are usually aligned in the longitudinal direction, and the inclusions, which are also aligned in the same longitudinal direction, assist the formation and growth of cracks.

1.6 Characterization of crack growth under multiaxial fatigue

Basically, fatigue designs involve two approaches: stress/strain-life approach and fracture mechanics approach (defect-tolerance approach). In the first approach, nominal stress or local strain is used to correlate or predict fatigue life. In the latter approach, fatigue crack growth rate is characterized by a fracture mechanics law. It is used to predict fatigue propagation life. This section reviews crack growth law under multiaxial fatigue.

1.6.1 Long crack growth under multiaxial fatigue

Long crack growth under uniaxial fatigue is characterized by the stress intensity factor. The characterization of long crack growth under mixed loading is complex, due to friction effects introduced by shear loading in both mixed Mode I and Mode II loading and mixed Mode I and Mode III loading.

1.6.1.1 Mixed mode I-mode II loading

One of the simplest approaches for theoretical crack growth prediction was first used by Erdogan and Sih (1963). They stated that the crack should grow perpendicular to the maximum tensile stress (MTS) adjacent to the crack tip. This therefore assumes a mode I mechanism of growth. This tensile stress is given by σ_θ in Eq. 1.45:

$$\sigma_\theta = \frac{1}{\sqrt{2\pi r}} \cos\frac{\theta}{2}[K_I \cos^2\frac{\theta}{2} - \frac{3}{2} K_{II} \sin\theta] \tag{1.45}$$

This tensile stress approaches infinity as r approaches zero, and so it can be represented by a generalized tensile stress intensity factor K_σ, for a crack beginning to grow in the direction θ, where

$$K_\sigma = \sigma_\theta \sqrt{2\pi r} \tag{1.46}$$

Here r and θ are the polar coordinates with the origin at the crack tip, and K_I and K_{II} are the applied stress intensity factors. The direction of crack growth under mixed mode I and Mode II load is found by calculating the value θ that gives the highest value of K_σ. Crack growth should occur when the maximum value of K_σ is equal to the mode I fracture toughness for brittle fracture, or the mode I threshold for fatigue crack growth.

In brittle material, cracks only propagate by the mode I mechanism. However, this is not always the case for the steels and aluminum alloys. Ostuka et al (1981, 1984) performed a wide variety of mixed mode I and Mode II tests in aluminum alloys and generated extensive mode II growth. Ostuka et al (1975) assumed that a crack either grow as a mode I crack, perpendicular to the maximum tensile stress direction (MTS), or as a mode II crack on the plane of the maximum shear stress (MSS). This MSS plane can be identified in the same way as the MTS plane by using the equations for the shear stress around the crack tip.

$$\tau_{r\theta} = \frac{1}{\sqrt{2\pi r}} \frac{1}{2} \cos\frac{\theta}{2}[K_I \sin\theta + K_{II}(3\cos\theta - 1)] \tag{1.47}$$

This shear stress approaches infinity as r approaches zero, and so it can be represented by a generalized shear intensity factor K_τ, for a branch crack beginning to grow in the direction θ, where,

$$K_\tau = \tau_{r\theta}\sqrt{2\pi r} \tag{1.48}$$

MTS and MSS theories can only provide the starting point for the prediction of mixed load crack behavior. They need to be modified to include the effects of friction, residual stress and plasticity to make them become reliable guide. Experimental work will always be required to take into account the different material behaviors.

Gao et al (1982, 1985) studied the growth of fatigue cracks in several ferrous and nonferrous alloys under mixed Mode I-Mode II loading. They obtained the fatigue fracture envelope for combined Mode I –Mode II crack growth. An example is shown in Figure 1.17. In this figure, the nominal value of shear stress intensity factor range ΔK_{II} is plotted against the nominal value of Mode I stress intensity factor range ΔK_I; both ΔK_{II} and ΔK_I are normalized by the Mode I threshold stress intensity factor range ΔK_{I0}. The solid curve indicates the low bound of threshold condition, below which no crack grows. The dashed line is a fracture locus outside of which a predominant mode I crack growth occurred. Between these two curves, the characteristic of crack growth was strongly influenced by the friction rubbing at crack faces. The location of the upper bound was dependent on crack closure due to the interlocking of fracture surface asperities and on the formation of oxide debris. When the amount of crack closure was reduced by increasing the load ratio of stress in tension, the upper bound curve began to approach the low bound threshold curve. When slit cracks (where the closure at the wake of crack tip is not a consideration), instead of sharp fatigue cracks, were subjected to the mixed mode loading, the upper bound curve for the onset of mode I crack growth coincided with the threshold (low bound) curve. These results clearly pointed to the significant role of frictional sliding in influencing mixed-mode fatigue crack growth.

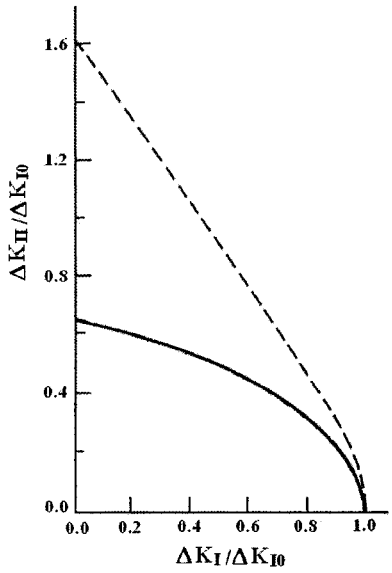

Figure 1.17 Combined mode I-mode II fatigue fracture envelope for AISI 316 stainless steel showing the locus of onset of fatigue crack growth (solid curve). The dashed curve indicates the mixed loading conditions at which fatigue fracture occurs on a plane normal to the maximum hoop stress, $\sigma_{\theta\theta}$ (Gao et al, 1985).

1.6.1.2 Mixed mode I-mode III loading

Failure under cyclic torsion may occur in anti-plane shear (mode III) along the transverse or longitudinal shear plane, or in mode I along the planes of ±45° with respect to the specimen axis.

Because of tortuous crack path and frictional contacts between crack faces at lower cyclic torsional loads, the characterization of fatigue crack growth in mode III or combined mode I and mode III become a difficult task. Nominal value of K_{III} does not provide a unique characterization of mode III fatigue crack growth. Instead, the cyclic crack tip displacement $(\Delta CTD)_{III}$ is commonly used, because of its simple definition. $(\Delta CTD)_{III}$ in fully reversed torsional loading is defined as $(\Delta CTD)_{III} \approx \frac{\Delta K_{III}}{\pi G \tau_y}$, where G is the shear

modulus and τ_y is the shear yield strength. A cyclic strain intensity parameter has also been used to characterize the mode III fatigue crack growth (Nayeb-Hashemi et al, 1983).

As a consequence of frictional effect in torsional fatigue, the apparent crack growth rates measured are substantially lower than the corresponding mode I crack growth rates at identical magnitude of nominal ΔK_I, as shown in Figure 1.18 (Tshegg, 1983). In this figure, fatigue crack growth rate da/dN in mode I and mode III is plotted against $(\Delta CTD)_I$ and $(\Delta CTD)_{III}$ for 4340 steel. The variation of da/dN in mode III as a function of crack length was experimentally determined by Tschegg (1983) at several different values of nominal ΔK_{III} or $\Delta(CTD)_{III}$. As shown in Figure 1.19, each of these curves representing a fixed level of far-field cyclic loading is extrapolated to zero crack length to obtain the crack growth rate in the absence of any fracture surface interference. The intrinsic mode III crack growth rate obtained by above procedure is somewhat higher than the corresponding mode I fatigue crack growth rates at an identical range of CTD. This result implies that the principal reason for the apparently superior resistance to crack growth under mode III loading is the existence of friction effects.

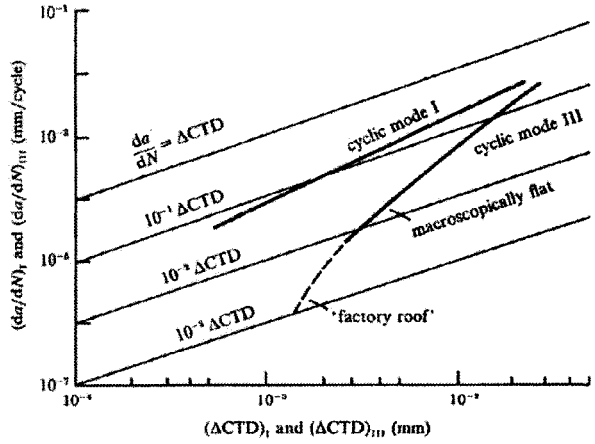

Figure 1.18 Variation of mode I and mode III fatigue crack growth rates with nominal values of $(\Delta CTD)_I$ and $(\Delta CTD)_{III}$, respectively, in 4340 steel (Tschegg, 1983).

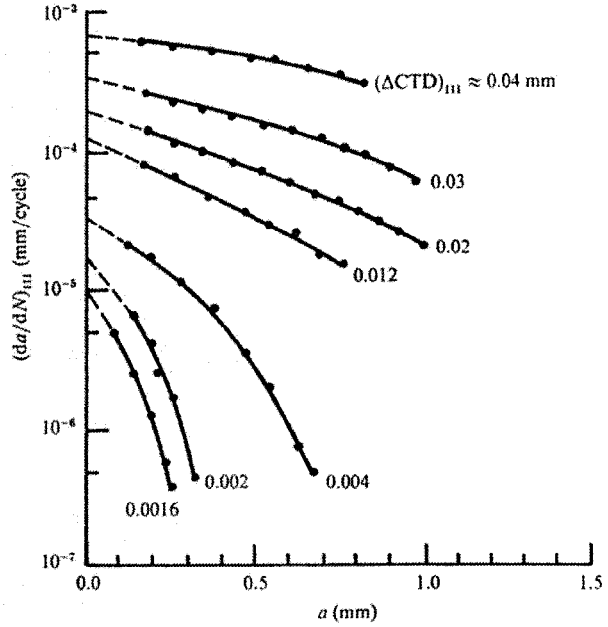

Figure 1.19 Variation of mode III fatigue crack growth rates as a function of crack depth a. (measured from the tip of the circumferential notch in the cylindrical specimen) in AISI 1018 steel. The numbers shown for each curve correspond approximately to the fixed values of $(\Delta CTD)_{III}$ in millimeters (Tschegg, 1983).

The application of even a small static tensile load, under certain condition, can markedly increase the rate of mode III fatigue crack growth by reducing the extent of crack closure (Nayeb-Hahemi et al, 1983; Tschegg, 1983a). The work of Hourlier et al (1978) and Akhust et al (1983) suggested that the superimposition of static K_{III} on the cyclic K_I causes the mode I crack to decelerate. This extent of reduction in crack growth rate increases with increasing static K_{III}.

1.6.2 Short crack propagation

On the basis of linear-elastic fracture mechanics (LEFM), studies on short cracks (10μm-1mm) in axial fatigue have shown that short cracks grow much faster than that would be predicted from large-crack data. This behavior is illustrated in Figure 1.20, in which the crack growth rate, da/dN or dc/dN, is plotted against the stress intensity factor range, ΔK. The solid curve shows the typical results for large cracks in a given material and environment under constant amplitude loading. Some typical results from short cracks are shown by the dashed lines. It is shown that short cracks can grow at ΔK level below the long-crack threshold and that they also grow faster than long cracks at the same ΔK level above the threshold. Over the past years, various studies on short-crack growth behavior in metallic materials have led to the realization that fatigue life of many materials is primarily consumed by the "crack growth" from microstructural features, such as inclusion particles, voids and slip bands formation. Currently, improved fracture mechanics analyses of some of the crack shielding mechanisms, such as plasticity-induced crack closure, and analyses of surface- or corner-crack configurations have led to more accurate crack growth and fatigue life prediction methods. Thus, "short crack theory" is the treatment of fatigue as a crack propagation process from a micro-defect (or crack) to failure.

The research on the short crack effects has concentrated on three possible explanations for the behavior of such cracks. They are plasticity effects, metallurgical effects and crack closure. All these features contribute to an inadequacy of LEFM and the use of the ΔK concept to correlate the fatigue crack growth rates. Nonlinear or elastic-plastic fracture mechanics concepts, such as J-integral, were developed to explain the observed small crack effects. However, the influence of plasticity of short crack growth and the appropriate crack-driving parameter is still being debated.

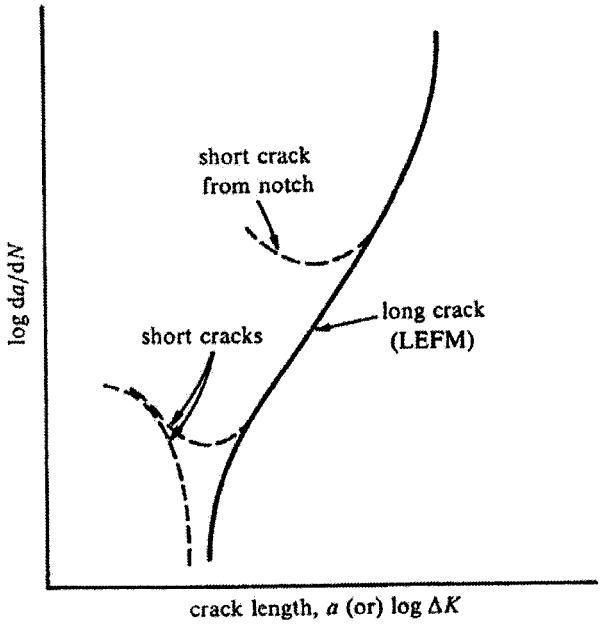

Figure 1.20 Typical fatigue crack-growth behaviors for short and long cracks.

Perez Carbonell and Brown (1986) studied the short crack growth behavior of a medium carbon steel under low cycle torsional fatigue. Crack growth was monitored by replicas taken at fixed intervals throughout the life of specimen. A shallow hourglass shape was chosen in order to have a restricted crack growth area for monitoring. Figure 1.21 shows the results of the measured crack length plotted against lifetime. The growth behavior of short cracks under torsional low cycle fatigue is similar to that under axial fatigue for the same material observed by Hobson (1985). Perez Carbonell and Brown (1986) proposed to use the same equation to describe both the axial and torsional short fatigue cracking behavior where the crack length is less than d, the prior austenite grain size:

$$da/dN = C(\Delta\bar{\sigma})^n(d-a) \tag{1.49}$$

where $\Delta\bar{\sigma}$ is the equivalent stress range ($\Delta\bar{\sigma} = \Delta\sigma$ in axial fatigue; $\Delta\bar{\sigma} = \frac{1}{\beta}\Delta\tau$ in torsional fatigue). C is stress related parameter. The same short crack growth equation

can be used for both axial and torsional fatigue, indicating that an equation based on the equivalent stress might be applicable to any stress condition.

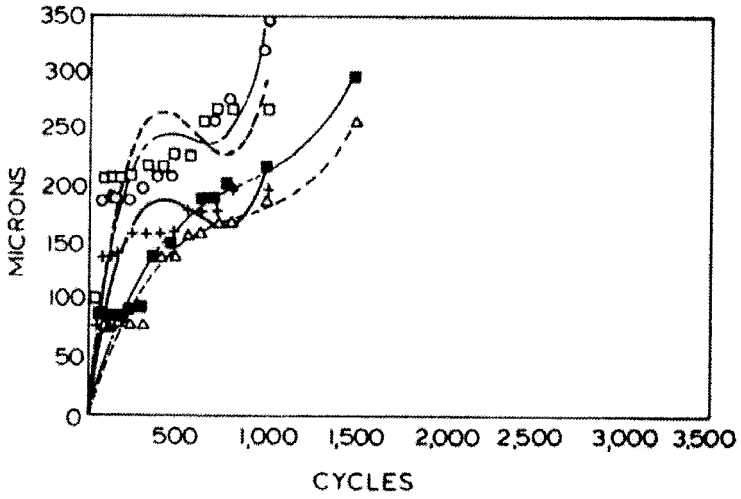

Figure 1.21 Measured crack length histories and fitted polynomials for individual crack under torsional fatigue at $\Delta\tau$=500 MPa (Perez Carbonell and Brown, 1986).

Ohkawa et al (1997) observed short fatigue crack growth in 1045 steel under different combinations of axial-torsional loadings (N_f=10^4-10^5cycles). The authors found that an equivalent strain intensity parameter $\Delta K\varepsilon$ (Eq.1.50) based on the strain components acting on the crack plane θc is useful for correlating fatigue crack growth rate under fully reversed combined loadings at various strain ratios and phase angles.

$$\Delta K\varepsilon = 1.12\sqrt{(F_1 E\Delta\varepsilon_{\theta_c})^2 + (F_2 G\Delta\gamma_{c})^2}\sqrt{\pi c} \tag{1.50}$$

$F_1 = \dfrac{k}{E(k)}$ and $F_2 = \dfrac{k(1-k^2)}{(1-k^2-\upsilon)E(k)+\upsilon k^2 K(k)}$, k=a/c is the crack aspect ratio and K(k), E(k) are complete elliptical integrals of the first and second kinds, respectively. E and G are axial and shear elastic modulus. $\Delta\varepsilon_{\theta_c}$ and $\Delta\gamma_{\theta_c}$ are the normal and shear strain ranges on

the crack plane respectively, and obtained from the following equations (Kanazawa, 1977),

$$\frac{\gamma_{\theta_c}}{\varepsilon_0} = \sqrt{\{\eta \cos 2\theta_c \cos\phi - (1+\upsilon)\sin 2\theta_c\}^2 + (\eta \cos 2\theta_c \sin\phi)^2} \tag{1.51}$$

$$\frac{\varepsilon_{\theta_c}}{\varepsilon_0} = \frac{\sqrt{\{1-\upsilon) + (1+\upsilon)\cos 2\theta_c + \eta \sin 2\theta_c \cos\phi\}^2 + (\eta \sin 2\theta_c \sin\phi)^2}}{2} \tag{1.52}$$

Here, ε_0 and γ_0 are the applied axial and torsional strain amplitudes, and η is the strain ratio of γ_0/ε_0. ΔK_ε then can be modified to consider phase difference $(\alpha_n-\alpha_s)$ between $\varepsilon_{\theta c}$ and $\gamma_{\theta c}$ to ΔK_ε^*, which gives better correlation than ΔK_ε.

$$\Delta K_\varepsilon^* = \frac{\Delta K_\varepsilon}{\sqrt{2}} \sqrt{1+\sqrt{1-2\left\{\frac{(F_1 E\Delta\varepsilon_{0c})(F_2 G\Delta\gamma_{0c})}{(F_1 E\Delta\varepsilon_{0c})^2 + (F_2 G\Delta\gamma_{0c})^2}\right\}^2 \{1-\cos^2(\alpha_n-\alpha_s)\}}} \tag{1.53}$$

Varvani-Farajani and Topper (1999) performed biaxial fatigue tests on thin-walled tubular 1045 steel specimens in a fixture that applied internal/external pressure and axial load. Four principal strain ratios (hoop strain to axial strain) of -υ, -0.625, -1 and +1 were employed in their tests. The magnitude and frequency of application of a periodic compressive overstrain was chosen so that there was closure-free crack growth. The observation revealed that crack growth rate increased dramatically with the magnitude of the compressive axial overstrains. The height of the surface irregularities decreased progressively as the compressive overstrain increased, and significantly flattened fracture surface irregularites were noted near the crack tip. This resulted in a reduced crack closure stress and a faster crack growth. Mode I and mode II strain intensity factors (K_I and ΔK_{II}) were calculated for a semi-elliptical surface crack under tensile mode straining and shear mode straining using,

$$\Delta K_I = F_I Q E \Delta\varepsilon_n \sqrt{\pi a} \tag{1.54}$$

$$\Delta K_{II} = F_{II} Q G \Delta\gamma_{\max} \sqrt{\pi a} \tag{1.55}$$

F_I and F_{II} are the shape factors for a semi-elliptical opening mode crack and shear crack, respectively, Q is a surface strain concentration factor, $\Delta\varepsilon_n$ and $\Delta\gamma_{max}$ are the normal and

shear strain ranges on the maximum shear plane. E and G are the Young's and shear moduli, respectively. *a* is the crack depth on the plane of maximum shear strain. The authors used effective strain intensity parameters to rationalize fatigue crack growth rate. The effective strain intensity factor ranges based on maximum shear strain parameter (Eq. (1.56)) and the Brown-Miller parameter (Eq. (1.57)) are given by,

$$\Delta K_{eff}^{S} = F_{II} QG \Delta\gamma_{\max} \sqrt{\pi a} \qquad (1.56$$

$$\Delta K_{eff}^{BM} = QG(F_{II} \Delta\gamma_{\max} + 0.78 F_{I} \Delta\varepsilon_{n}) \sqrt{\pi a} \qquad (1.57)$$

They found that these two strain intensity factors show roughly the same correlating ability. Cracks in pure shear straining propagate more rapidly than the other strain conditions. Fatigue life based on the crack growth rate by using the shear type parameter of critical plane showed a good agreement with the experimental fatigue life data.

1.7 Notch effects

Notches are not avoidable in mechanical design. The study of notch effects on cracking behavior and on fatigue life is essential. Fatigue cracks invariably start from some form of stress concentration. It may be a metallurgical defect, such as inclusions and precipitates, or a geometrical discontinuity in a mechanical part, such as a drilled hole, a keyway, etc. Notch effects on fatigue behavior include the effects on cracking mechanisms and on fatigue life. Different approaches have been proposed to deal with notch fatigue problems.

1.7.1 Local stress/strain approaches

A fundamental assumption of these approaches is that the initiation fatigue life is determined by the local stress/strain state at the notch tip. The maximum stress or strain gives the same initiation life as that of unnotched specimens at the same stress/strain level. In early research, elastic stress concentration factors K_t and some equivalent stress/strain criteria (e.g. Tresca or von-Mises) were used to predict fatigue life of notches

from smooth specimen data (Gough, 1949; Takahara et al, 1972, Williams et al (1985)). However, K_t was shown to be inadequate in predicting fatigue life of severely notched components (Frost and Phillips, 1956). Although detailed information on notch stresses/strains can be obtained by 1) analytical approaches (e.g. Neuber analysis), 2) experimental approaches, and 3) finite element analysis, and some successes have been shown in some cases, notch fatigue life prediction under multiaxial fatigue is a challenge (Grubisic and Simburger, 1976; Fash et al, 1985).

Fash et al (1985) performed axial-torsional fatigue tests on thin-walled tubular specimens and combined bending-torsion fatigue tests on simple notched shaft specimens made of hot-rolled 1045 steel. Three-dimensional stress-strain fields are determined for these specimens using elastic and elastic-plastic finite element models. The thin-walled tubular specimen has a simple uniform stress-strain state. The axial strain gradient along the gage length is less than 2%. The torsional strain gradient along the surface is nearly zero, and the torsional gradient between the inner and outer surfaces is 15%. More significant stress/strain gradients exist in notched specimens. Three commonly used approaches based on extensions of static yield criteria and two theories based on critical planes (Lohr-Ellison, Kandil-Brown-Miller) were selected for this investigation. Correlation for the thin-walled tube test series was within a factor of 3 in fatigue life. For the notched shaft specimen with the more complex stress-strain state, life estimates were in error by a factor of 10. If fatigue life is a function only of the local strain, similar correlation of test results should be obtained by applying the same strain-based theories to both types of specimens. However, this is not the case. This suggests that the local strain/stress is not enough to correlate the fatigue lives with different specimen geometries. The notch has intrinsic effects on the fatigue life. The authors thus suggested that emphasis should be placed on understanding the influence of notches in biaxial fatigue. A new method needs to be developed instead of local stress/strain method.

There are several limits for local stress-strain approach. A stress/strain gradient exists at the notch tip. This stress/strain gradient will lead to different fatigue behaviors as compared to the smooth specimen without stress/strain gradient. The local stress/strain approach that does not account for this stress/strain gradient tends to underestimate fatigue life of notched specimens. The local stress/strain approach can only be applied to fatigue initiation life, or to the cases in which most of the life is consumed by the fatigue crack initiation. However, for a severe notch, crack initiation life is very short, and propagation life is predominant among the total fatigue life. Thus, the local stress/strain approach is not applicable to severe notches. Other approaches are needed.

1.7.2 Critical distance approaches

In these approaches, notch fatigue life is characterized by the stress/strain in a critical zone ahead of the notch. Peterson (1959) used the stress at a critical point to correlate lives, while Neuber (1958) used the average stress over a critical length. However, the so-called critical distance was usually obtained in some empirical manner. The average stress in a critical volume or area has also been used to predict notch fatigue life (Kadi and Pluvinage, 2002).

Tanaka (1983) and Taylor (1999) attempted to relate the critical distance to material properties such as fatigue crack propagation threshold. Taylor and Wang (2000) showed that the critical distance approaches are useful for both blunt notch and sharp notches, even though two different mechanisms are involved in the two types of notches. A blunt notch behaves in the same way as a smooth specimen, crack "initiation" being the critical stage. In sharp notches, cracks initiate easily and fatigue failure is propagation-controlled. They may become non-propagating. A critical distance approach cannot explain the occurrence of non-propagating cracks.

It was first shown by Frost & Dugdale (1957) and Frost (1960) that fatigue cracks emanating from notches could arrest completely after growing some distance. A number of subsequent studies have documented the existence of non-propagating fatigue cracks ahead of stress concentrations in ductile solids (e.g., El Haddad et al. 1980; Smith & Miller, 1978; Tanaka & Nakai 1983; Verreman et al, 1987).

1.7.3 Fracture mechanics approaches

Fracture Mechanics approaches have been developed to study short crack propagation. The work of Smith and Miller (1977,1978) indicated two fatigue limit conditions for notches. The separation between failure and non-failure of a notched component should also consider if an initiated crack would propagate or not (Figure 1.22).

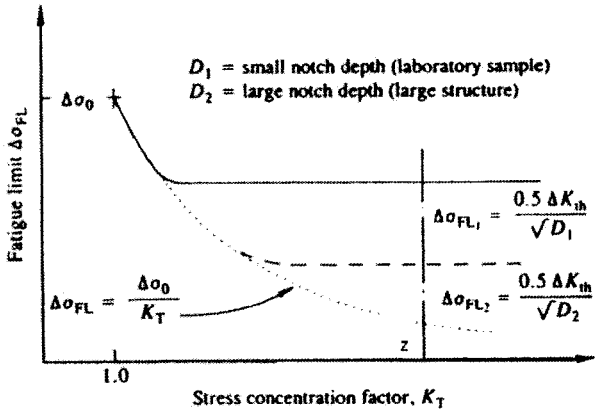

Figure 1.22 The fatigue limit depends on notch depth, threshold stress intensity factor and stress concentration factor. Note that the fatigue limit is independent of the stress concentration factor at $K_T = Z$. (Smith and Miller, 1977)

The fatigue limit propagation condition was given by the simple formula:

$$\Delta\sigma_{FL} = \frac{0.5\Delta K_{th}}{\sqrt{D}} \tag{1.58}$$

where D is the notch depth.

Under axial fatigue, the growth of a short crack propagating from a notch root can be strongly influenced by the plastic deformation caused by the notch. A "mechanical short crack" is initially surrounded by the notch plastic zone and the small scale yielding condition (LEFM) is violated.

In order to describe the propagation of a mechanically short crack from a notch tip, Smith and Miller (1978) have proposed that, when the crack is still within the notch plastic zone, its driving force is the sum of two contributions, one from the notch plasticity, and the other from the crack tip plasticity. LEFM underestimates the crack growth rate because only crack tip plasticity is taken into account. The relative importance of each contribution depends on the stress level and on the crack depth (Figure 1.23). The notch contribution decreases as the crack propagates while the crack contribution increases. If the notch contribution decrease is larger than the crack contribution increase, the propagation decelerates. The crack can become non-propagating if the crack tip plasticity is not sufficient when the notch plastic zone has been crossed ($\Delta K < \Delta K_{th}$).

Verreman and his co-workers (1986, 1987, 1997) investigated short crack behavior in severe V-notched geometries (V-notched members and fillet weld joints). They found that at a very beginning of fatigue life, a rapid crack growth is observed, and then crack growth rate decrease or remains constant before rejoining the long crack trend (Figure 1.24 (a)). LEFM cannot account for this short crack behavior since the stress intensity factor K increases with crack depth. At the endurance limit level, the crack becomes non-propagating. They measured the evolution of the crack opening level with crack depth, and found that opening level rapidly increases before reaching a stabilized level. The initial transient of the opening level explains what has been observed on crack growth rates. Although K increases with crack depth, the effective crack driving force decrease because of the rapid and important increase in the opening level. If crack growth rates are plotted against the effective stress intensity factor range ΔK_{eff}, short crack and long crack growth rates are consolidated in a single trend (Figure 1.24(b)).

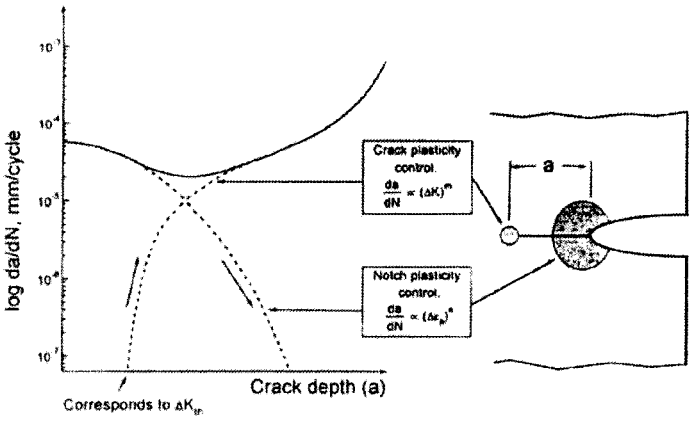

Figure 1.23 Crack growth rate from the root of a notch: the driving force is assumed to be the sum of two contributions: one from the notch plasticity, the other from the crack tip plasticity (Smith and Miller, 1978).

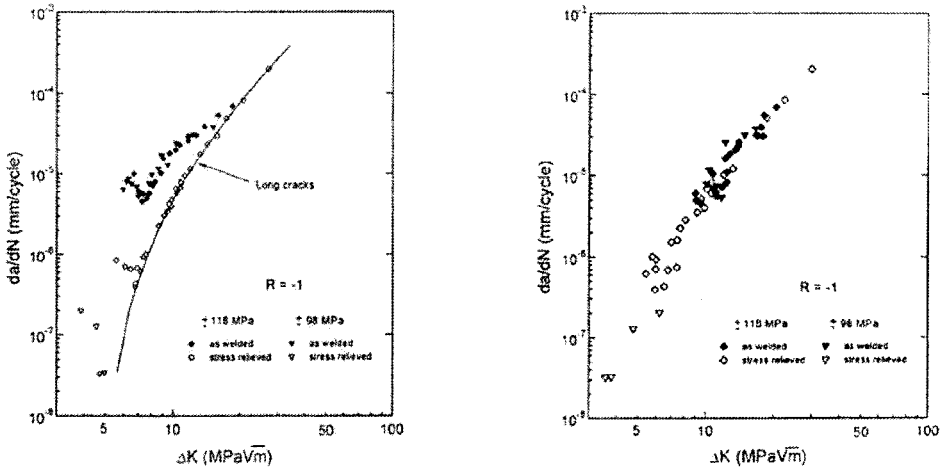

(a) (b)

Figure 1.24 Fatigue crack growth rates in welds. (a) Plotted against ΔK. (b) Plotted against ΔK_{eff}. The curve in (a) indicates the trend of long crack behavior obtained in stress-relieved specimens.

Espinosa (1995) and Verreman & Espinosa (1997) observed the short fatigue cracking behavior of cruciform L-notched specimen with notch radius of 0.1 mm and 3 mm. Elongated semi-elliptical cracks and fatigue crack growth deceleration were observed in small radius specimens. On the other hand, the specimens with 3mm radius showed a behavior approaching that of smooth specimens; isolated cracks with high aspect ratios propagated at a continuously increasing crack growth rate.

The fatigue notch factor (K_f) is a simple way to characterize the notch effects on the fatigue life. It is defined as the ratio of the fatigue limits of un-notched specimen and notched specimen. Nisitani and Kawano (1968, 1970) found that the fatigue notch factor is lower in torsional fatigue than in axial fatigue for circumferentially V-notched specimen. They attributed the low fatigue notch factor under torsional loading to the factory-roof fracture that results in higher cracking resistance. A similar observation was also made by Fatemi et al (2002).

Brown et al (1985) studied fatigue cracking behavior of notched specimens made of 1% Cr-Mo-V steel under reversed torsion with or without a static tensile load. They found that the stress intensity factor does not satisfactory correlate all fatigue growth data, but the strain intensity factor which is a function of material properties and notch plastic zone, shows a significant improvement and provides a single upper bound solution. This solution permits designer to make safe lifetime assessments. They observed crack initially propagating in mode II along the surface, and in mode III radially. At a low stress, crack propagation continued in mode I (see the "factory-roof" fracture surface; Figure 1.25(a)). At high stress, the transition to mode I is avoided (Figure 1.25 (b)). This cracking behavior could be understood from crack growth laws (Figure 1.25 (c)). The mechanism of faster crack growth rate prevails. The application of an axial load enhances the mode III crack propagation rate since this increases the effective crack tip strain intensity factor. Tschegg (1983) also observed similar trends in the cracking behavior in 4340 steel.

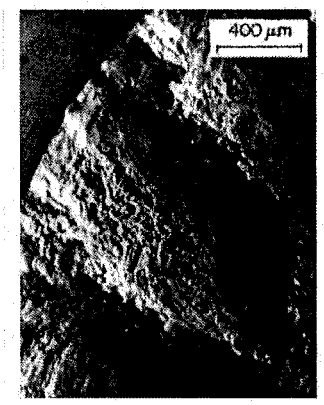

(a)

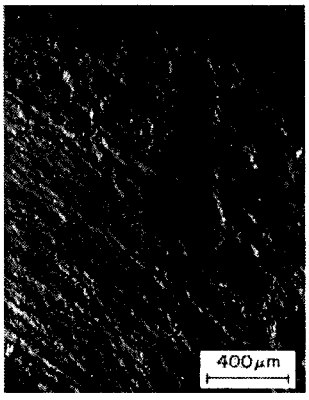

(b)

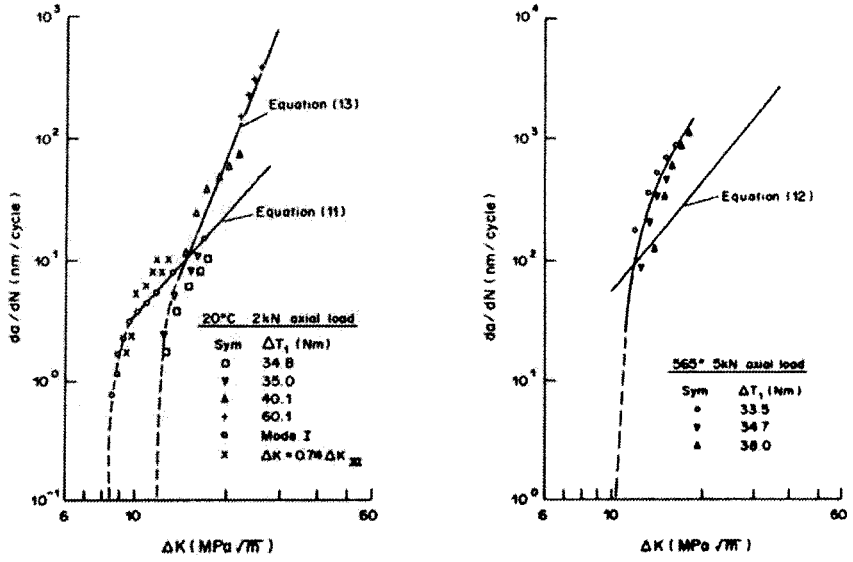

(c)

Figure 1.25 (a) "Factory-roof" fracture surface at a low torque without static axial load. (b) Flat mode III fracture surface at a high torque without static load. (c) Correlation of mode I crack growth data with "Factory-roof" cracking and "Flat" mode III cracking. (Brown et al, 1985).

1.7.4 Notch stress intensity factor

According to Williams (1952), the stress field at a V-notch tip (Figure 1.26) is singular. The normal stress σ_{xx} is expressed as

$$\frac{\sigma_{xx}}{S} = \lambda_0 \left(\frac{a}{B}\right)^{-\alpha} \tag{1.59}$$

where λ_0 is the function of the V-notch angle ψ, the loading system and the dimensionless geometry. S is the nominal stress, a is the distance from notch tip and B is a dimension parameter (e.g. notch depth). The exponent α is a function of ψ; it ranges from 0.5 in the case of a crack (ψ=0°) to 0 in the case of a uniform field at a smooth surface (ψ=180°). By analogy with a crack, one can write

$$\sigma_{xx} = \frac{K_I^N}{a^\alpha} \tag{1.60}$$

and define $K_I^N = \lambda_0 SB^\alpha$ as mode I notch stress intensity factor. K_I^N is a function of geometry and loading. For a given notch angle, different geometry/loading combinations giving the same K_I^N gives the same stress field and thus should give the same events ahead of the notch.

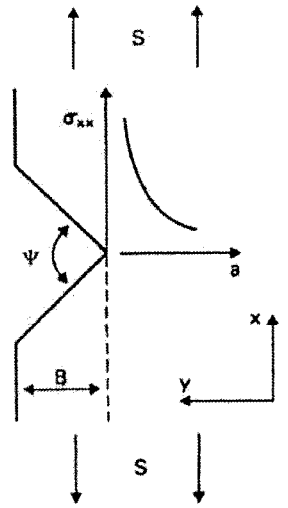

Figure 1.26 Illustration of V-notch

Notch stress intensity factor has been successfully used to predict crack initiation life for sharp notches (V-notched welded joints) under axial fatigue by Verreman and his co-workers (1987, 1996, 1999). Verreman and Nie (1996) have successfully used the notch stress intensity factor to rationalize the crack "initiation life", which is defined as the life for crack propagating to 0.5mm. Figure 1.27 shows the relations between applied nominal stress and "crack initiation life" for different joint thickness. B ranges from 16mm to 103mm. The scale effect is important. However, by using the notch stress intensity factor, T-joint data of different thickness are consolidated (Figure 1.28).

Boukharouba et al (1995) studied crack initiation behavior of welded joints and notched CT specimens made of mild steels. They consolidated fatigue lives using a notch stress intensity factor, which is a function of applied stress, notch angle and notch acuity. They found that this approach allows conservative design of structures.

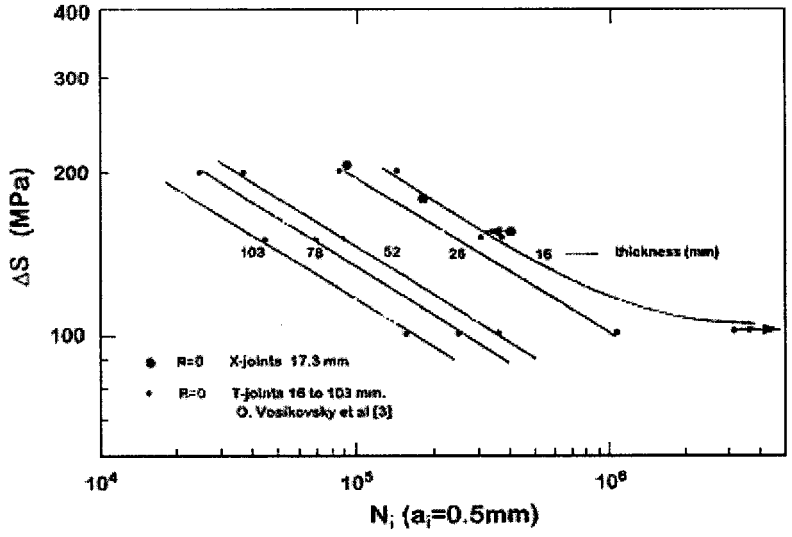

Figure 1.27 Nominal stress vs. "crack initiation life"

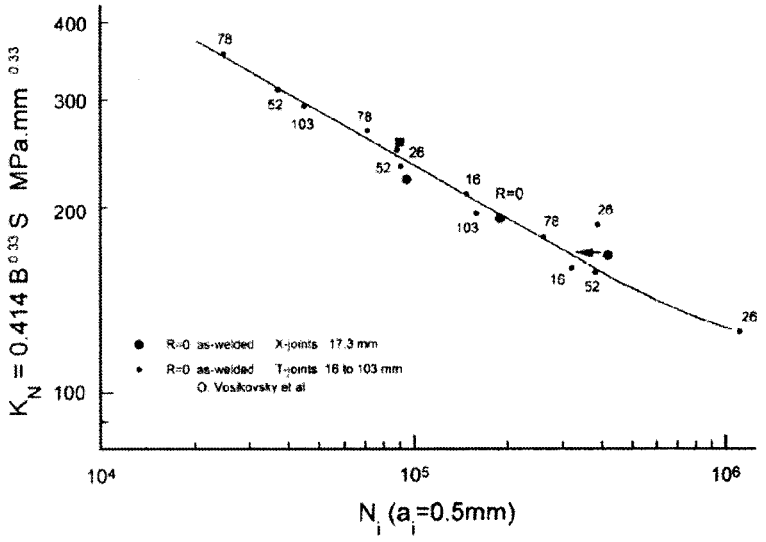

Figure 1.28 Notch stress intensity factor vs. "crack initiation life".

Tovo and Lazzarin (1998, 1999) analyzed the stress field close to the toe of welds in welded plates. The local stress field can be described in terms of notch stress intensity factor for different joints. They found that "hot-spot stress" approach is not able to predict accurately the fatigue behavior of welded joints, whereas notch stress intensity factor is more advantageous. Lazzarin and Livieri (2001) showed that notch stress intensity factor is useful to predict total fatigue life of steel and aluminum welded joints.

Dunn et al (1997) used the notch stress intensity factor to correlate fracture initiation at sharp notches under mode I, mode II, and mixed mode loadings. They determined mode I and mode II stress intensity factors for notched specimens using a combination of asymptotic method (Williams, 1952), dimensional considerations, and detailed finite element analysis. They showed that critical stress intensity factor gave an excellent correlation of fracture initiation for mode I loading. It also works well for mode II loading. In case of mixed mode loading, mode I behavior dominates, and critical mode I stress intensity factor works well to correlate fracture initiation.

1.8 Critical summary of literature review

Biaxial fatigue mechanisms and biaxial fatigue life parameters have been extensively reviewed. A critical summary is given as follows.

Fatigue damage is characterized by the mechanisms of crack initiation and propagation. For smooth specimen, cracks generally initiate from PSBs. However, the stress state and the material microstructure can influence the initiation mechanisms. For example, cracks can initiate at inclusions. Multiple crack initiation can occur at a high stress level, and failure can result from coalescence between microcracks. Under all stress states, there are two important stages of crack propagation: stage I and stage II. In stage I, cracks propagate on the maximum shear planes (mode II), while in stage II cracks propagate on the plane of maximum normal stress (mode I).

Basically, there are two types of fatigue failure in engineering materials: shear failure and tensile failure. The shear failure refers to a fatigue damage mainly caused by stage I crack growth (mode II), while a tensile failure is dominated by a stage II crack propagation (mode I). The failure mode is a complex function of material type, stress state and stress level. The specimen geometry (notch) may also influence the failure mode. It is important to know the failure mode, because it determines what kind of parameter can be used to correlate the fatigue life. Tensile failure needs a tensile-type parameter, whereas shear failure mode needs a shear-type parameter. Even though much research has been done in this area, we are still far from fully understanding how the fatigue mechanisms and stage I/stage II transition are controlled. Some materials (such as 304 stainless steel) show tensile failure, while other materials (such as Inconel 718) show shear failure mode. It seems that each material has its potential failure mode. It may be related to some material properties such as slip characteristics. However, for a given material, the stress state and the stress level also influence the failure mode. The competition between the two stages

determine the main failure mode for a given condition, hence the choice of the fatigue life correlating parameter.

In general, at the same maximum shear stress/strain amplitude, torsional fatigue has a longer life compared to axial fatigue. This is attributed to the friction effect induced by the crack face irregularities. The normal tensile stress on the maximum shear plane can open the crack, decrease or eliminate the friction effects, hence assist the crack propagation. This observation leads to the conclusion that only maximum shear stress or strain is not enough to characterize the biaxial fatigue damage. The normal stress on the maximum shear plane assists the cracking and should be taken into account. It is also noticed that the ratio of torsional fatigue life to axial fatigue life varies from one material to another, which means that the friction effects on the fatigue life can vary with materials. At the present time, the weight of normal stress effects is generally determined by a experimental material constant, k.

Non-proportional loading is an important consideration in biaxial fatigue. Under out-of-phase loading, crack mechanisms are similar to those under proportional loading. It is widely accepted that in low cycle fatigue, out-of-phase loading gives lower fatigue life as compared with proportional loading at the same maximum shear strain amplitude. This life difference has been claimed to be the effects of the normal strain amplitude and phase angle between shear and normal strains on the critical plane. Considering additional hardening due to the rotation of principal axes under non-proportional loading, Fatemi and Socie (1988) used a maximum normal stress term instead of the normal strain amplitude on the maximum shear plane in their life correlating parameter. In high cycle fatigue, macroscopic plasticity and additional hardening become less significant as the stress level decreases to the fatigue limit. However, a maximum normal stress term can account for mean stress effect. Tensile mean stress can accelerate fatigue crack growth, thus decrease fatigue life, while compressive mean stress is beneficial for fatigue life.

Shear mean stress has less effect on fatigue life, although it has been observed that shear mean stress can also decrease fatigue life for some materials.

There are essentially two ways to predict fatigue life: stress/strain–life approach and Fracture Mechanics (defect-tolerance) approach. In the first approach, a parameter is used that is a combination of some characteristic stress/strain components. The fracture mechanics approach is based on fatigue crack propagation. The fatigue life can be predicted through the integration of a crack growth rate law to a specified length.

Up to now, many stress-based and strain-based parameters have been proposed for correlating biaxial/multiaxial fatigue life. However, no widely accepted theory exists. This is due to the complexity of fatigue mechanisms under biaxial fatigue. Early life prediction models based on the static yielding criteria cannot successfully correlate the fatigue lives under different loadings, even between axial and torsional loadings. For many materials, crack initiation and stage I propagation represent an important part of fatigue life. The maximum shear stress/strain amplitude is the driving force of fatigue. The so-called critical plane parameters are modifications of Tresca criterion by introducing some terms to account for the effects of normal stress/strain. Parameters based on the critical plane concept seem to be more promising in rationalizing fatigue lives obtained under different loading conditions. For example, the Fatemi-Socie parameter seems to be able to correlate well high and low cycle fatigue lives in materials where shear failure prevails.

Short fatigue cracks under biaxial fatigue also present irregular and high growth rates at low stress intensity factor range. Several attempts have been made to rationalize the short crack growth rates with modified ΔK and ΔJ. However, as compared with the stress/strain-life method, the Fracture Mechanics method is less developed. It is noticed that fatigue crack propagation law is helpful in predicting crack propagation life, while the stress/strain-life method is more appropriate for crack initiation life.

Many engineering materials show some degree of anisotropy, which can be introduced either by fibrous structure or by crystallographic texture. As a consequence, their mechanical behavior can be also anisotropic. For example, under torsional fatigue, the alignment of inclusions can assist the formation and growth of shear cracks in the longitudinal direction. Since anisotropy influences fatigue mechanisms and fatigue life, a life prediction parameter should take into account the material anisotropy. Material anisotropic effects on biaxial fatigue cracking behavior and fatigue life have been studied from two aspects: (1) to compare the fatigue behavior in different test orientations in an anisotropic material; (2) to compare fatigue behavior between an anisotropic material and an isotropic material. Up to now, very few parameters consider material anisotropy effects.

Local stress/strain approaches, critical distance approaches and fracture mechanics approaches have been used to deal with the problem of fatigue at notches. In a local stress/strain approach, the local stresses/strains at the notch tip and data from smooth specimens are used to predict initiation fatigue life for notches. This approach does not take into account the stress/strain gradients ahead of notch tip. It can only be applied to the cases in which initiation life is predominant. In the case of a severe notch, the initiation life is negligible. In a critical distance approach, the determination of the critical distance is often empirical. Further, this approach cannot differentiate a blunt notch from a sharp notch in which different cracking mechanisms are involved. The fatigue limit at a sharp notch is controlled by a crack propagation condition.

The crack driving force for notched specimens has been shown to be the sum of two contributions (crack tip plasticity and notch plasticity). The notch plasticity contribution decreases as the crack advances. This can explain the deceleration of fatigue cracks. If the notch is severe enough, they become non-propagating at low stress range. The crack closure evolution may be also responsible for the short crack behavior at notches. A simple and conservative fracture mechanics approach for fatigue life prediction can be

developed with the limit case of severe V-notches. The stress field ahead of a V-notch is singular and is uniquely determined by a notch stress intensity factor. The notch stress intensity factor has been successfully used to predict the fatigue initiation life of V-notch members and welded joints under axial loading. The applicability of this approach to multiaxial fatigue should be examined in a future study.

CHAPTER II -OBJECTIVES

Multiaxial fatigue is a broad topic. For example, advanced research is undertaken to develop fatigue life prediction methods for practical applications in the automotive industry, including notches and variable-amplitude loadings. Since stress concentrations and/or periodic overloads can cause cyclic plastic deformation, complex effects of strain path on both cyclic plasticity and fatigue damage have to be investigated in the high and the low cycle fatigue regimes (Kurath et al, 1999).

This thesis is restricted to axial-torsional high cycle fatigue of metals where cyclic plasticity and fatigue cracking mechanisms are localized at the microscopic scale in a few well-oriented grains at the material surface. As the stress level decreases to the fatigue limit, the macroscopic cyclic deformation becomes predominantly elastic, and fatigue damage is usually evaluated either in terms of stress or in terms of elastic strain.

The general objectives of the thesis are the following:

- Microscopic analyses of the biaxial high-cycle fatigue mechanisms in 1045 steel, under proportional and non-proportional loadings;
- Critical evaluation of the ability of different existing stress-based and strain-based multiaxial fatigue parameters to predict high cycle fatigue life of a ferritic-pearlitic steel;
- Study of material anisotropy effects on axial and torsional fatigue of underaged and overaged 7075 aluminum alloy;
- Study of notch effects on axial and torsional fatigue of 1045 steel, using a linear elastic fracture mechanics approach developed in the limit case of severe V-notches.

Although much research has already been done, a full understanding of fatigue mechanisms is still far away. In the present study, the replica technique has been used to

monitor crack initiation and propagation on the surface of smooth tubular specimens. Direct observation under SEM of specimen surfaces and fracture surfaces has also been made. It is essential to capture the fatigue mechanisms on a microscopic scale since much of the fatigue life is often consumed in a small number of grains. Special attention has been paid to non-proportional loadings for which the details of cracking mechanisms are rarely reported.

Axial-torsional high cycle fatigue tests (10^5-10^7 cycles) have been carried out on thin-walled tubular specimens made of 1045 steel. Five loading cases are considered: axial and torsional loadings, combined axial-torsional in-phase (λ=0.5) and out-of-phase (λ=2 and 0.5; $\Phi=90^0$) loadings, and torsional loading with different levels of static axial tension. Both effects of cyclic and static normal stresses on the critical plane can be evaluated. Special attention has been paid to the worst loading case ($\Phi=90^0$; λ=0.5) for which all planes have the same shear stress amplitudes.

Many multiaxial fatigue life parameters have been proposed. Which stress/strain combination is the most appropriate in high cycle regime? It is better to use the normal stress on the critical plane or to use the hydrostatic stress? Our own fatigue life data and those from a different author serve to evaluate the abilities of eight selected parameters to predict the axial-torsional high cycle fatigue life of ferritic-pearlitic steels in various loading conditions. The prediction errors have been compared and discussed on the basis of stress analysis and observation of fatigue mechanisms. From an engineering point of view, it is important to study how to obtain at least a conservative life prediction (no overestimation).

7075 aluminum alloy was initially chosen in both underaged and overaged conditions to investigate the effects of slip characteristics on fatigue behavior. Preliminary testing under torsional fatigue revealed anisotropy effects due to the alignment of inclusions in the longitudinal direction; these effects being more important in the underaged condition.

Then it was decided to perform two series of fatigue tests under three loading cases: axial loading, torsional loading and torsional loading with different levels of static axial tension. Anisotropy effects can be clearly put into evidence under torsional loading with static tension. There is a competition between two fracture mechanisms: longitudinal shear cracking (weak plane of material) and transverse shear cracking (normal stress effect). After observing and understanding the fatigue cracking mechanisms, we try to find an approach to predict the fatigue life of an anisotropic material under axial-torsional loading.

Notches are inevitable in mechanical parts. Fatigue mechanisms at notches can be very different from those at smooth surfaces. It is important to find models to predict biaxial fatigue lives in notched components. A simple and conservative linear elastic fracture mechanics approach can be developed with the limit cases of severe V-notches with very small root radii. The stress field distribution ahead of V-notches is singular and is uniquely determined by notch stress intensity factors, provided that notch plasticity is confined within this singularity. Our objective is to investigate pure axial fatigue (mode I) and pure torsional fatigue (mode III) of two circumferentially V-notched specimens with different notch sizes. Can the mode I and mode III notch stress intensity factors correlate the axial and torsional fatigue lives, respectively?

CHAPTER III - BIAXIAL FATIGUE MECHANISMS IN SMOOTH TUBULAR SPECIMENS MADE OF AS-ROLLED 1045 STEEL

3.1 Introduction

In general, in smooth specimens, the fatigue cracks nucleate at PSBs on the surface. The cracks first propagate along the maximum shear planes (stage I, mode II), then their orientation changes to the maximum normal stress plane(s) (stage II, mode I) (Forsyth, 1961). However, complication of multiaxial fatigue cracking mechanisms arise from the fact that the relative fatigue lives consumed for crack initiation, stage I propagation and stage II propagation are very much dependent on material properties, loading conditions and stress level (Socie, 1989; 1993). Socie et al (1989) found that materials such as Inconel 718 and 1045 steel show mode II fracture, while 304 stainless steel shows mode I fracture. As a consequence, different fatigue life parameters should be applied for different fracture modes. Even though many fatigue cracking behaviors have been investigated, we are still far from a full understanding of fatigue cracking mechanisms under different conditions. A further investigation on fatigue mechanisms is still necessary in order to have a more solid basis to discuss fatigue life correlation or prediction.

As mentioned in chapter II, one main objective of the present study on biaxial fatigue of as-rolled 1045 steel is to have a better understanding of biaxial fatigue cracking mechanisms. Several detailed observations on the biaxial fatigue cracking behavior of 1045 steel have been carried out. Hua and Socie (1984) have observed that a single dominant crack (mainly stage I) usually developed in the HCF region (N_f>10^4 cycles). On the other hand, equally developed multi-cracks are observed over the entire gauge section in the LCF region (N_f<2000 cycles). It is noted that they only studied in-phase loading and they did not observe fatigue cracking behavior under high cycle fatigue, in which stage II propagation could appear. Ohkawa et al (1997) also observed fatigue cracking

behavior of S45C steel (similar to 1045 steel) under combined axial-torsional in-phase and out-of-phase loadings in the intermediate fatigue life region. They found that initiation and stage I propagation occur on the maximum shear planes whatever the stress ratio and the phase angle. The higher the stress ratio, the longer the crack at the transition from stage I to stage II. However, they did not give detailed information on the cracking process for different loading conditions. Therefore, it is still of interest to make further studies on the cracking behavior of 1045 steel. First, we can verify the findings by the other researchers by our study. Secondly, more attention will be paid to out-of-phase loadings, for which the details of cracking mechanisms are rarely reported.

3.2 Experiments

3.2.1 Material

The raw material is as-rolled 1045 steel in the form of a round bar with a diameter of 38.1mm. 1045 steel is a material often used for automotive shafts, where biaxial fatigue is often involved. The chemical composition (Metals Handbook) and the monotonic tensile properties (evaluated by us with the same thin-walled tubular specimen as for fatigue tests) of this material are shown in Table 3.1. A constant hardness of HRB=96 was measured on several samples. The microstructure of this material consists of pearlite and ferrite (Figure 3.1 (a)). The average grain size of ferrite is 15μm and the average pearlite colony size is approximately 22μm. The relative volume fraction of ferrite is approximately 40%. The ferrite grain and pearlite colony sizes were determined using intercept procedures according to ASTM standard E112-96. The volume fraction was measured according to ASTM standard E562-95. It is noted that the theoretical volume fraction of ferrite in 1045 steel is 45%. However, the carbon content in 1045 steel can vary from 0.42-0.5%, hence the volume fraction of ferrite can vary from 38% to 48%. In addition, there are inclusions elongated in the rolling direction up to 0.1mm in length (Figure 3.1 (b)).

Table 3.1 Chemical composition and tensile properties of as-rolled 1045 steel

Chemical composition (% in weight)	C	Mn	P_{max}	S_{max}	Fe
	0.43-0.50	0.60-0.90	0.040	0.050	Remain
Tensile properties	Yield strength (MPa)	Tensile strength (MPa)		Elongation (%)	E (GPa)
	387	703		31	205

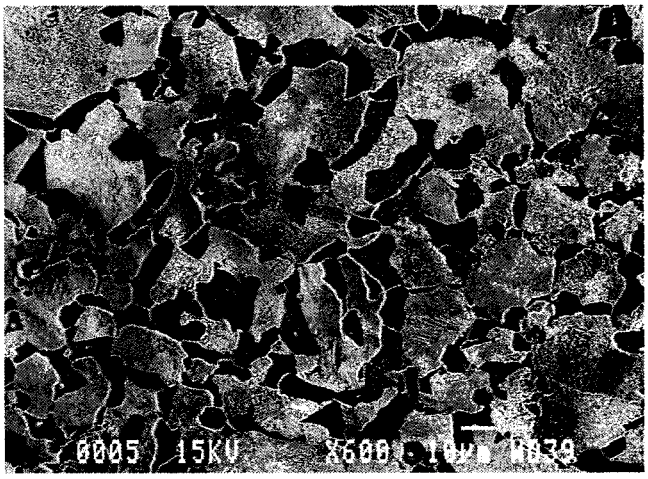

(a)

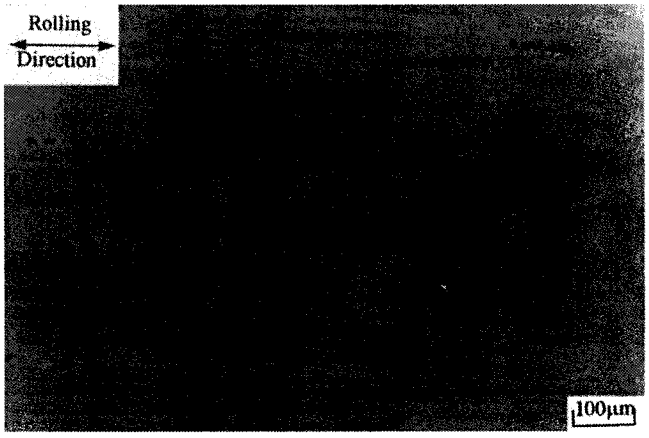

(b)

Figure 3.1 (a) Microstructure of as-rolled 1045 steel consisting of pearlite colonies (bright) and ferrite grains (dark) (transverse section etched by 2% Nital). (b) Inclusions along the rolling direction (longitudinal section without etching).

3.2.2 Specimen geometry and preparation

Two specimen geometries are selected for testing: a thin-walled tubular specimen (Figure 3.2 (a)) and an hourglass solid specimen (Figure 3.2 (b)). Thin-walled tubular specimens are used for axial-torsional fatigue loadings with a torsional component, while hourglass specimens are only used for axial fatigue. The thin-walled tubular specimen is the most versatile geometry available for characterizing biaxial properties in materials. The advantages of thin-walled tubular specimen include accurate control and measurement of the multiaxial stresses/strains, relatively uniform distribution of stress and strain and capability for monitoring crack initiation and propagation. However, only a limited range of principal stress/strain ratios can be obtained with a tubular specimen under axial-torsional loadings (section 1.1). The reason an hourglass solid specimen was chosen in axial fatigue is to avoid premature crack initiation from the inner surface of tubular specimen. The inner surface machining was not as good as that of the outer surface. Using a solid specimen force the cracks to initiate from a surface that has a finishing condition comparable to that at the outer surface of a tubular specimen. It is noted that in any other loading combination with torsional components, fatigue cracks always nucleate at the outer surface of the tubular specimen.

All the specimens were polished before being tested in order to have a better resolution in observing crack initiation and early propagation. The specimens were first ground using sand paper up to 600 grit to remove machining marks. Then they were chemically polished with a solution of 100ml H_2O, 100ml H_2O_2 (30%) and 14ml HF (Vander Voort, 1984). The specimens were immersed into the chemical solution for 30 s and shaken occasionally, then rinsed in 30% H_2O_2. This chemical polishing not only gives good surface finish, but it also reveals the material microstructure, which is helpful for observing the interaction between cracking and microstructure. The surface finish of hourglass specimens is comparable with the outer surface finish of tubular specimens. One question remains however: can axial fatigue data obtained with the hourglass solid

specimen be comparable with data obtained with tubular specimen in the other loading conditions?

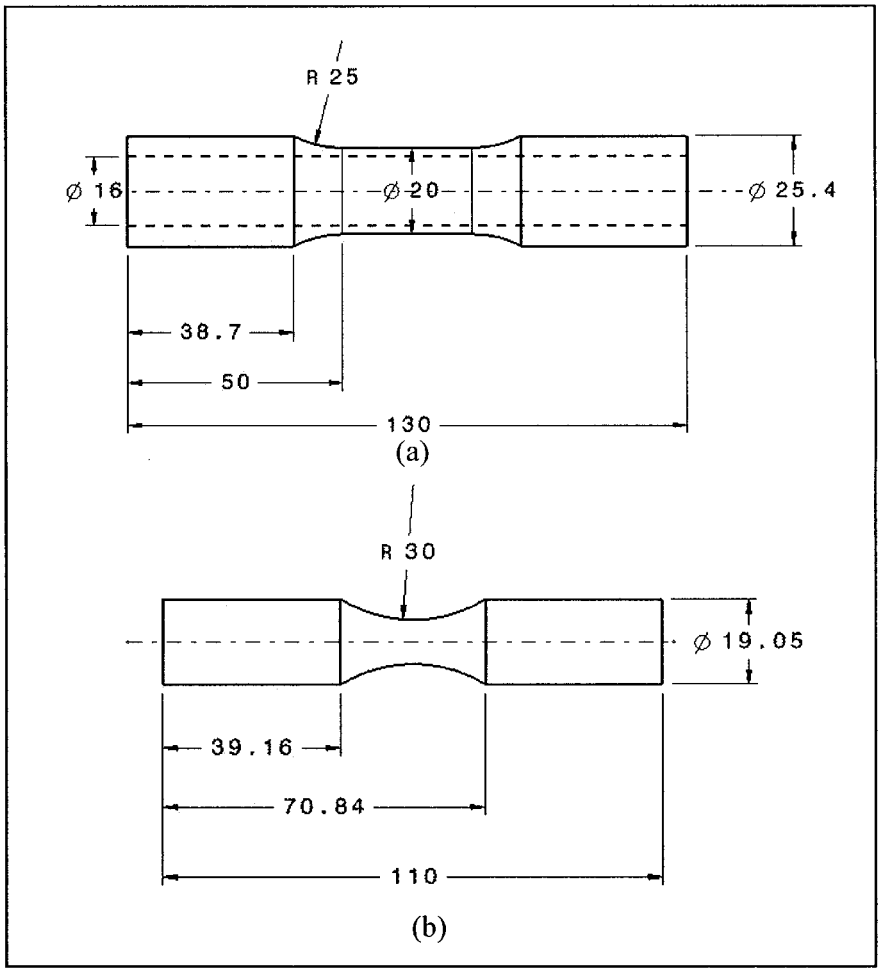

Figure 3.2 Specimens geometry. (a) Thin-walled tubular specimen for torsional and biaxial fatigue (wall thickness = 2 mm). (b) Hourglass solid specimen for axial fatigue (minimum diameter is 10 mm; $k_t \approx 1.07$). (Unit: mm)

Under torsional fatigue, fatigue lives of thin-walled tubular specimens and solid specimens are different. The effects of specimen geometry on torsional fatigue life can be understood from the shear stress distribution. The shear stress in the solid specimen is linearly increasing from zero at the center to a maximum value at the outer surface; whereas, the thin-walled tubular specimen has almost uniform stress distribution through the wall thickness. As a result of different stress distributions, the measured torsional fatigue life of solid specimens is higher than that of tubular specimens under the same nominal shear stress at the surface (Miller and Chandler, 1969-1970).

For axial fatigue, Socie et al (1985) found that there is no difference in total fatigue life between solid and tubular specimens. The effect of specimen geometry in axial fatigue is different from that in torsional fatigue. In axial fatigue, the normal stress/strain is uniformly distributed over the specimen cross section. Thus, at least for high cycle fatigue where the crack initiation predominates the total life, axial life data from solid specimens are comparable with those from tubular specimens, provided that there is the same stressed volume in both specimens. However, for low cycle fatigue, initiation life is a relatively small part in total fatigue life, and propagation plays an important role. The effects of specimen geometry and dimensions should be not neglected even for axial fatigue.

Table 3.2 presents axial stress-life data obtained with the hourglass specimen and those first obtained with tubular specimens that failed prematurely from internal surface. These last specimens give an underestimation of the actual fatigue performance that would have been obtained with a better machining of internal surface. On the other hand, the hourglass specimens, despite some stress concentration ($K_t \approx 1.07$), could slightly overestimate the fatigue performance because the stressed volume is significantly lower than that in a tubular specimen. However, at lives of the order of 10^5 cycles, fatigue strength of the hourglass specimens is 290-300MPa while that of the tubular specimens

failed from internal surface is 260-300MPa. The possible overestimation of axial fatigue strength using hourglass specimen is less than 10%.

3.2.3 Fatigue tests

High cycle fatigue tests (10^5-10^7 cycles) were performed using an Instron 8521 servo-hydraulic axial-torsional machine (Figure 3.3). Five loading paths were employed, (a) axial fatigue; (b) torsional fatigue; (c) axial-torsional in-phase loading (λ=0.5); (d) axial-torsional out-of-phase loading (Φ=90^0, λ=0.5 and 2) and (e) torsional fatigue with static tensile load (λ=0.75,1 and 1.67, here $\lambda=\sigma_m/\tau_o$). These loading paths are illustrated in Figure 3.4. The effects of two types of non-proportional loadings (out-of-phase loading and mean tensile stress) are investigated. All cyclic loadings are fully reversed (sinusoidal waveform, frequency of 5-10Hz, R=-1). All tests are stress-controlled and conducted in laboratory air at room temperature. Table 3.2 shows the details of the fatigue test program and life results.

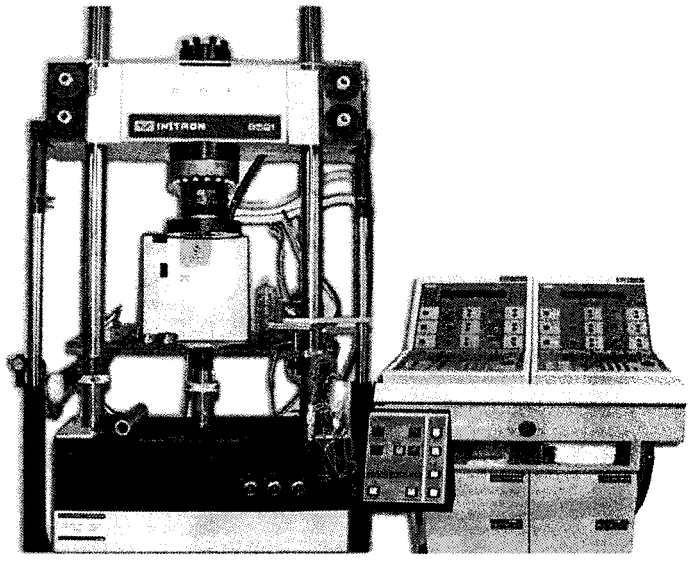

Figure 3.3 Instron biaxial test machine (can perform static and cyclic axial-torsional tests including out-of-phase loadings; axial load = ±100kN; torque = ±1130 N.m)

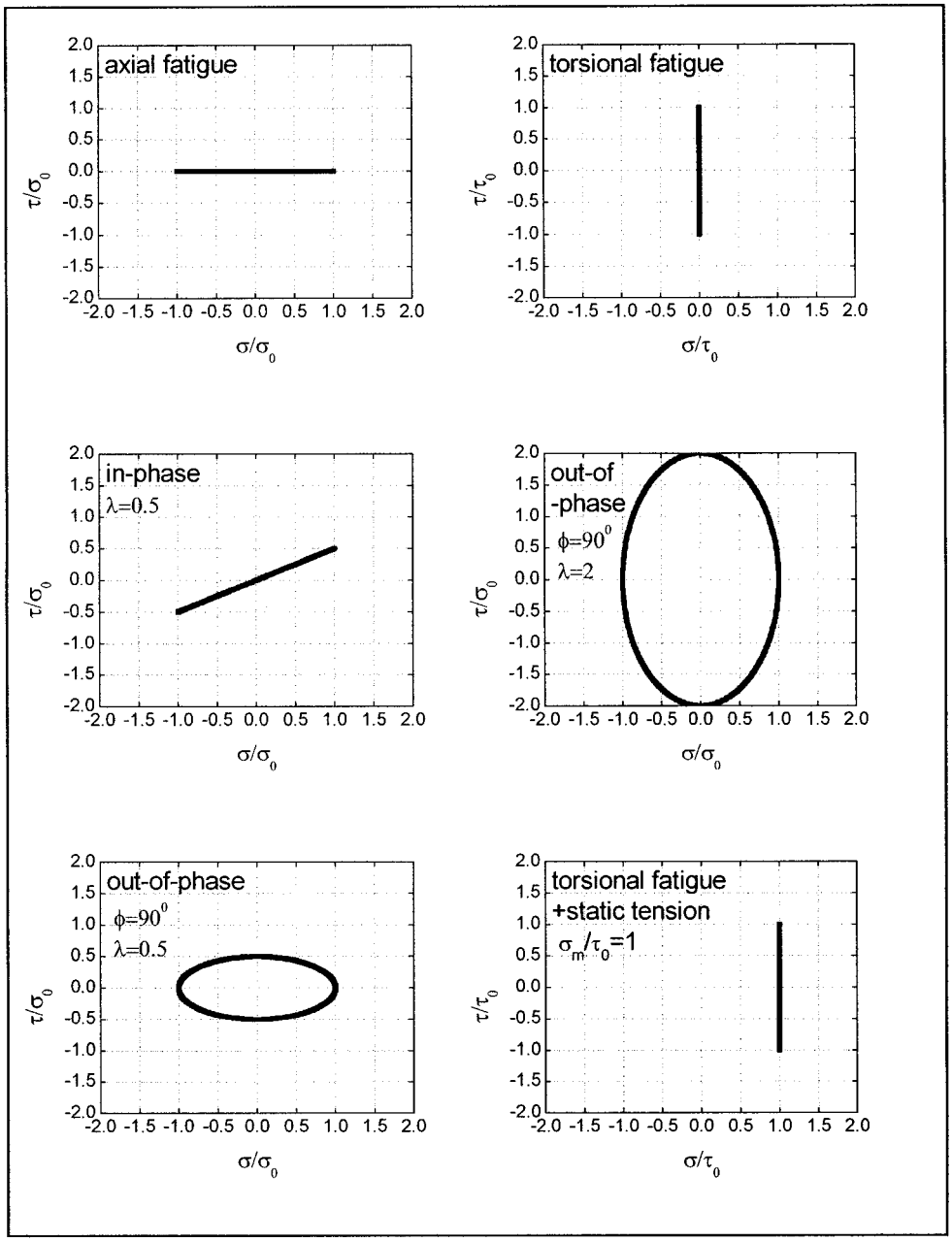

Figure 3.4 Loading paths employed in our tests: axial fatigue, torsional fatigue, axial-torsional in-phase fatigue (λ=0.5), 90^0 out-of-phase axial-torsional with λ=0.5, 90^0 out-of-phase axial-torsional with λ=2, and torsional fatigue with static axial tension.

Table 3.2 Biaxial tests and fatigue lives

Loading case	Specimen	σ_0 (MPa)	τ_0 (MPa)	σ_m (MPa)	$\lambda = \frac{\tau_0}{\sigma_0}$	ϕ (deg)	N_f (cycles)
Torsional	T4	0	166.5	0	∞		4,917,324
	T8	0	180	0	∞		498,000
	T7	0	180	0	∞		440,920
	T5	0	175	0	∞		317,943
	T3	0	180	0	∞		257,679
Axial+ (tubular specimen: internal failure)	*Atub9*	*260*	*0*	*0*	*0*		*404,617*
	Atub8	*280*	*0*	*0*	*0*		*114,613*
	Atub10	*300*	*0*	*0*	*0*		*102,316*
	Atub7	*300*	*0*	*0*	*0*		*76,109*
	Atub6	*333*	*0*	*0*	*0*		*22,606*
	Atub3	*300*	*0*	*0*	*0*		*21,231*
Axial (hourglass solid specimen)	Asol1	275	0	0	0		5,417,503
	Asol4	285	0	0	0		5,148,389
	Asol2	300	0	0	0		379,178
	Asol3	290	0	0	0		366,512
	Asol5	300	0	0	0		238,236
	Asol6	300	0	0	0		214,908
Axial-torsional in-phase	AT1	220	110	0	0.5	0°	573,978
	AT2	220	110	0	0.5	0°	177,263
Axial-torsional out-of-phase	AT4	220	110	0	0.5	90°	2,420,570
	AT7	250	125	0	0.5	90^0	397,940
	AT12	230	115	0	0.5	90^0	377,718
	AT10	240	120	0	0.5	90^0	151,109
Axial-torsional out-of-phase	AT5	80	160	0	2	90^0	>5,485,960
	AT11	82.5	165	0	2	90^0	1,490,671
	AT8	85	170	0	2	90^0	727,149
	AT6	87.5	175	0	2	90^0	345,774
Torsional with static tension	TS2	0	150	90	1.67*		2,855,000
	TS1	0	150	150	1*		616,542
	TS3	0	150	200	0.75*		462,000

T: torsional fatigue
Atub: axial fatigue with tubular specimen
Asol: axial fatigue with hourglass solid specimen.
AT: axial-torsional fatigue
TS: torsional fatigue with static tension
*: $\lambda=\tau_0/\sigma_m$
+: axial data from tubular specimens are not comparable to other data due to premature failure from internal surface

3.2.4 Fatigue cracking monitoring

The replica technique is used to monitor the process of surface fatigue crack initiation and propagation. It is probably the most popular technique for surface crack monitoring. Several researchers (e.g. Hua and Socie, 1984; Ohkawa et al, 1997; Sakane et al 1987) have used the replica technique to monitor the cracking behavior under multiaxial fatigue.

Cellulose acetate is a popular replicating material in fatigue studies; it is available from the electron microscope supplier. This material can reproduce fine details very accurately and has good wetting properties. In this experiment, an acetate sheet produced by Oken Shoji Co. Ltd in Japan was employed. An acetate thickness of 0.385mm was found to give the best results. A piece of replica material, of size suitable to cover the area to be replicated, is cut from the sheet. For the cylindrical or hourglass specimens, it is more convenient to cover the full circumference with two replicas, each covering slightly more than half of the circumference in order to allow some overlapping. The piece of acetate film is softened with acetone for a few seconds, and is positioned on the surface of the specimen, allowing the surface tension force to pull it down. After the film dries completely, we carefully strip it from the specimen surface and fix it on a microscope glass slide. In the entire procedure, the replica film is handled with tweezers. For the successive replicas taken during the test, the gauge section has to be carefully cleaned each time with compressed air to remove dust, or with acetone to remove debris adhering to the surface.

Replicas are taken intermittently at the desired time interval during fatigue tests. Note that the specimen was removed from the grips for taking each replica, that is, replicas were taken at zero-load. The replicas are observed in the reverse order, commencing with the last replica where the main crack can be easily located, and working backwards to the very early stage of cracking. Figure 3.5 shows an example of the replication technique.

The replicas can be observed under an optical microscope if they are flat enough. However, even after careful mounting the plastic replica on a microscope glass slide, it may not be sufficiently flat, particularly for the replicas taken from cylindrical and hourglass specimens. In this case, it is necessary to observe the replicas under a scanning electron microscope. While observed under SEM, replicas need to be trimmed to a suitable size to be mounted on a plate and be coated with a thin conductive layer such as a layer of gold-platinum. To obtain better results and to avoid the damage by the heat produced by the high accelerating voltage, the replica is usually observed under accelerating voltages lower than 10KeV. From the observation, one can obtain information on crack initiation site(s), number of cracks and eventual coalescence, as well as crack length and crack orientation as a function of loading cycles. This detailed information is useful to understand the cracking process, and hence to establish a basis to understand or to develop approaches for fatigue life prediction.

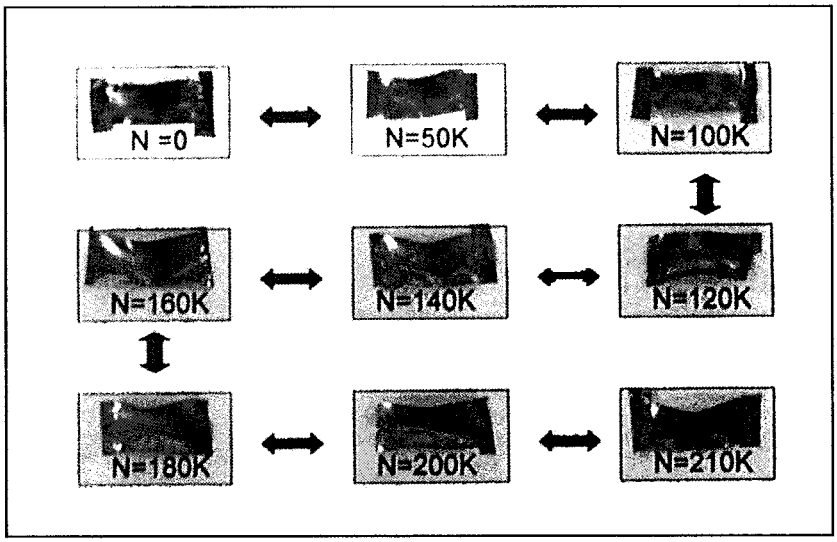

Figure 3.5 Illustration of the replica technique. These replicas are taken during an axial fatigue test on an hourglass specimen at different number of cycles (N). The replicas are observed backwards under SEM to trace the fatal crack initiation and propagation process.

3.3 Observation on biaxial fatigue cracking mechanisms

3.3.1 Crack initiation

Fatigue crack initiation was observed in three different manners. 1) The surfaces of several selected specimens were directly observed under SEM to have a general view on early crack nucleation. 2) The replicas taken during fatigue tests were observed under SEM to trace back fatigue crack initiation sites to determine the life at initiation. 3) The observation of the external surface of a failed specimen on an area away from main cracks was employed to obtain statistical information on the orientation distribution of slip-bands and grain-size cracks.

For the convenience of discussion, the shear and normal stress amplitudes on different plane orientations under different loading conditions will first be examined. The detailed stress analysis for axial-torsional fatigue of thin-walled tubular specimens is presented in Appendix I. To simplify writing, the planes of maximum shear stress amplitude and of maximum normal stress amplitude are called hereafter the maximum shear planes and the maximum normal stress planes, respectively. For axial-torsional fatigue, the maximum shear planes are always perpendicular to the specimen surface, except for axial fatigue where two additional sets of maximum shear planes make an angle of ±45° with respect to both specimen axis and specimen surface. The variations of shear and normal stress amplitudes acting on crack planes that are perpendicular to surface are shown in Figure 3.6. For axial fatigue, there are two maximum shear planes (±45°) in addition to the two planes mentioned above, and the normal stress amplitudes on these two planes are equal. For torsional fatigue, the two maximum shear planes are at 0° and 90°, and the normal stresses on these two planes are zero. There are two maximum normal stress planes in torsional fatigue (±45°) and only one in axial fatigue (0°). For in-phase fatigue, there are two orthogonal maximum shear planes but only one maximum normal stress plane. The normal stresses on the two maximum shear planes are equal. For high λ (λ>0.5) 90° out-

of-phase loading, there are also two maximum shear planes (always at 0° and 90°), but there is no normal stress acting on the plane at 90°. The 90° out-of-phase loading with λ=0.5 is a special loading case. All planes have the same shear stress amplitude, and the normal stress amplitude is maximum on the 0° plane. For low λ (λ<0.5) 90^0 out-of-phase loading, there are two maximum shear planes (±45°) and only one maximum normal stress plane (0^0) as for axial fatigue. The normal and shear stress amplitude variations with plane orientation in torsional fatigue with static tension are the same as those for pure torsional fatigue, but there is a static tensile normal stress acting on the 0° maximum shear plane.

Observations on the specimen surfaces during tests shows that persistent slip bands (PSBs) are the first stage of fatigue damage under all stress states (Figure 3.7). After several thousands of cycles, slip bands can be observed in the ferrite grains in which slip systems are oriented to or close to the maximum shear planes (see the corresponding plots in Figure 3.6). With increasing number of cycles, the density of the slip bands increases, and the existing slip bands become wider and deeper. Crack initiation always occurred at PSBs for all loading cases.

A statistical evaluation of the orientation distributions of slip bands and grain-size cracks has been made using replicas taken at the end of lifetime. It is difficult to distinguish the small cracks from the wide slip bands. Then we measure the orientations for both. Since cracks always initiate from slip bands, this statistical evaluation can represent crack initiation event. An area of about $0.2mm^2$ away from the main crack is observed under SEM. Figure 3.8 shows the plots of the frequency of cracks at different orientations under different loading conditions. The orientation of a grain-size crack (or a group of slip bands) is also defined by the angle between the normal of the crack plane and the specimen axis.

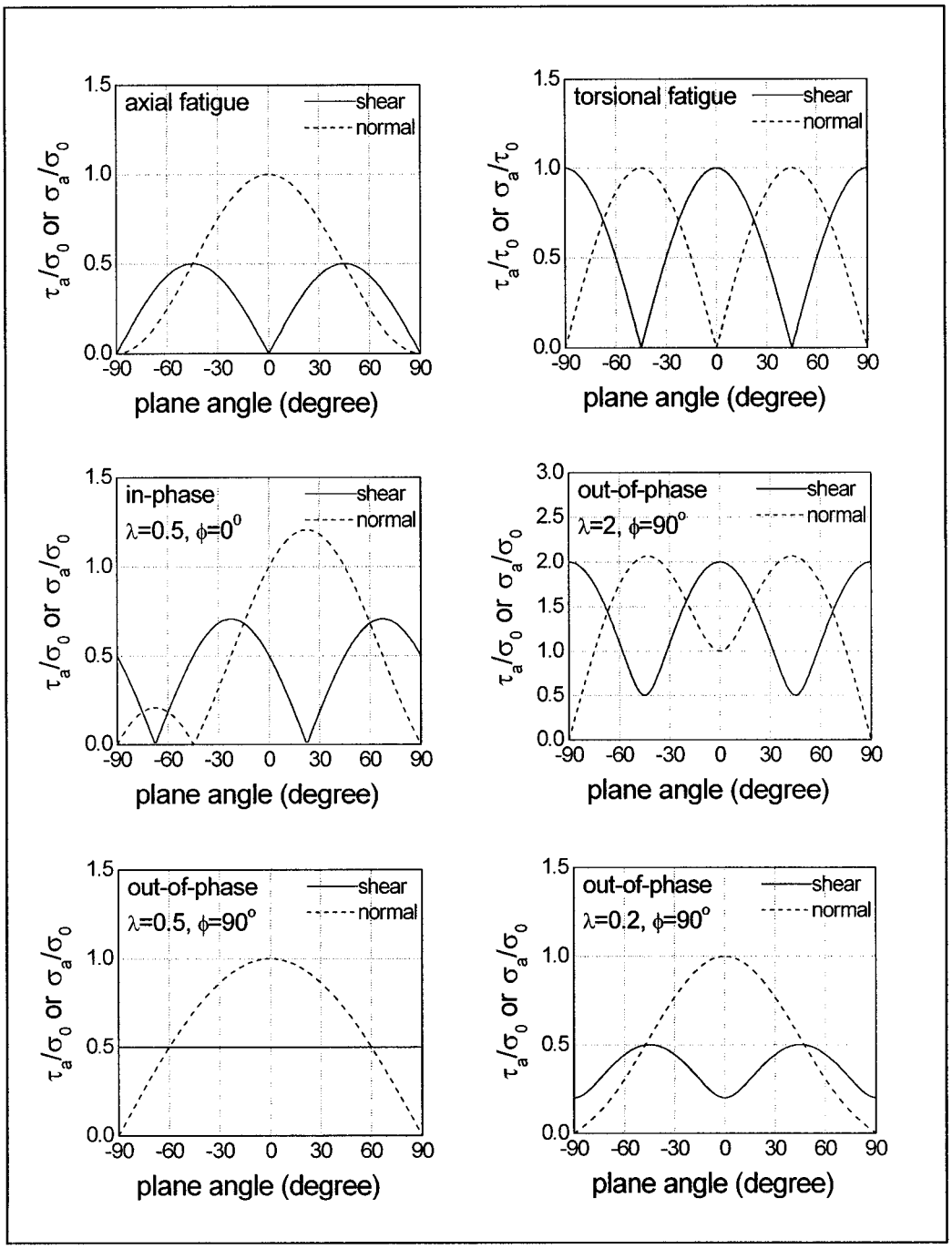

Figure 3.6 Variations of shear stress amplitude τ_a and normal stress amplitude σ_a (normalized by the applied axial stress amplitude σ_0 or the shear stress amplitude τ_0) with plane orientation for different loading conditions. The plane orientation is defined by the angle between the normal of the plane and the specimen axis.

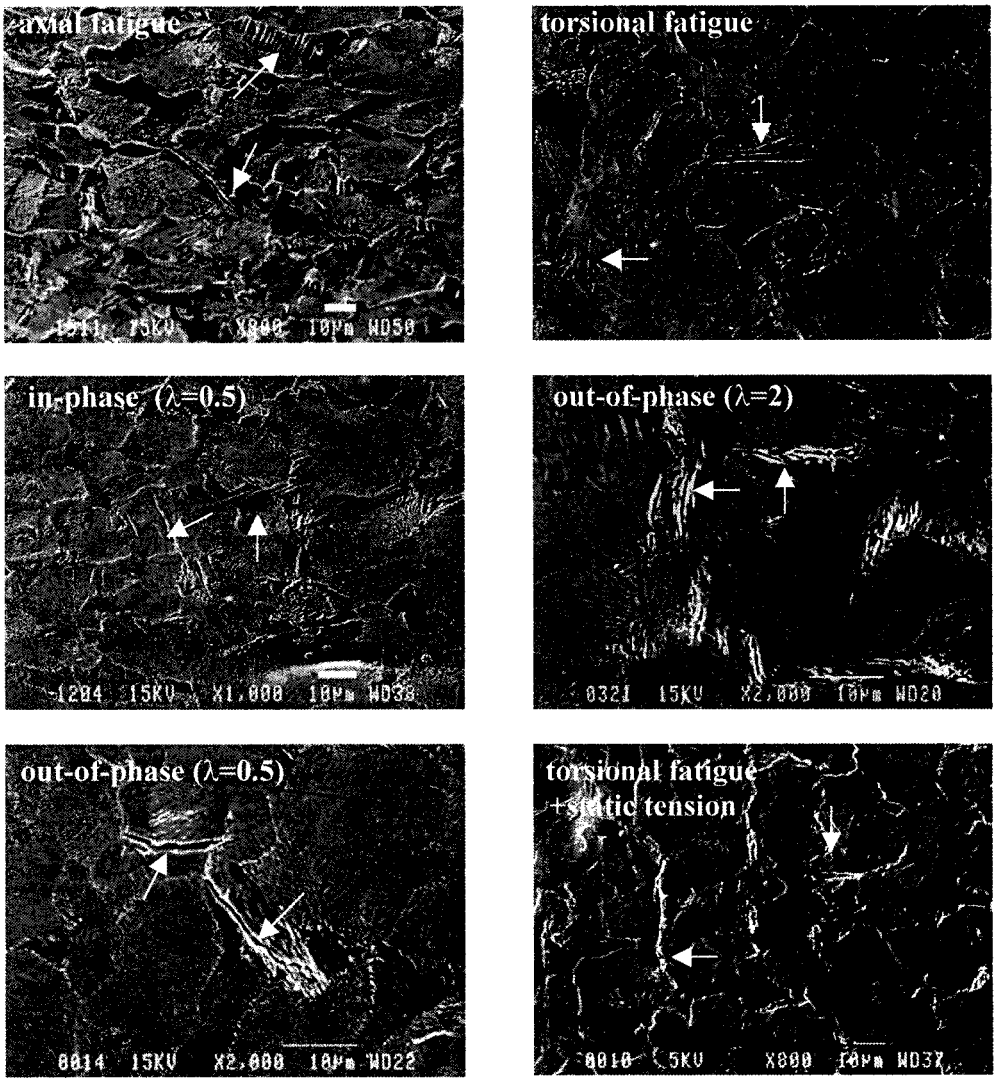

Figure 3.7 Typical slip-bands and grain-sized cracks (see arrows) observed in 1045 steel under SEM for different loading conditions. Specimen axis is horizontal in each photo.

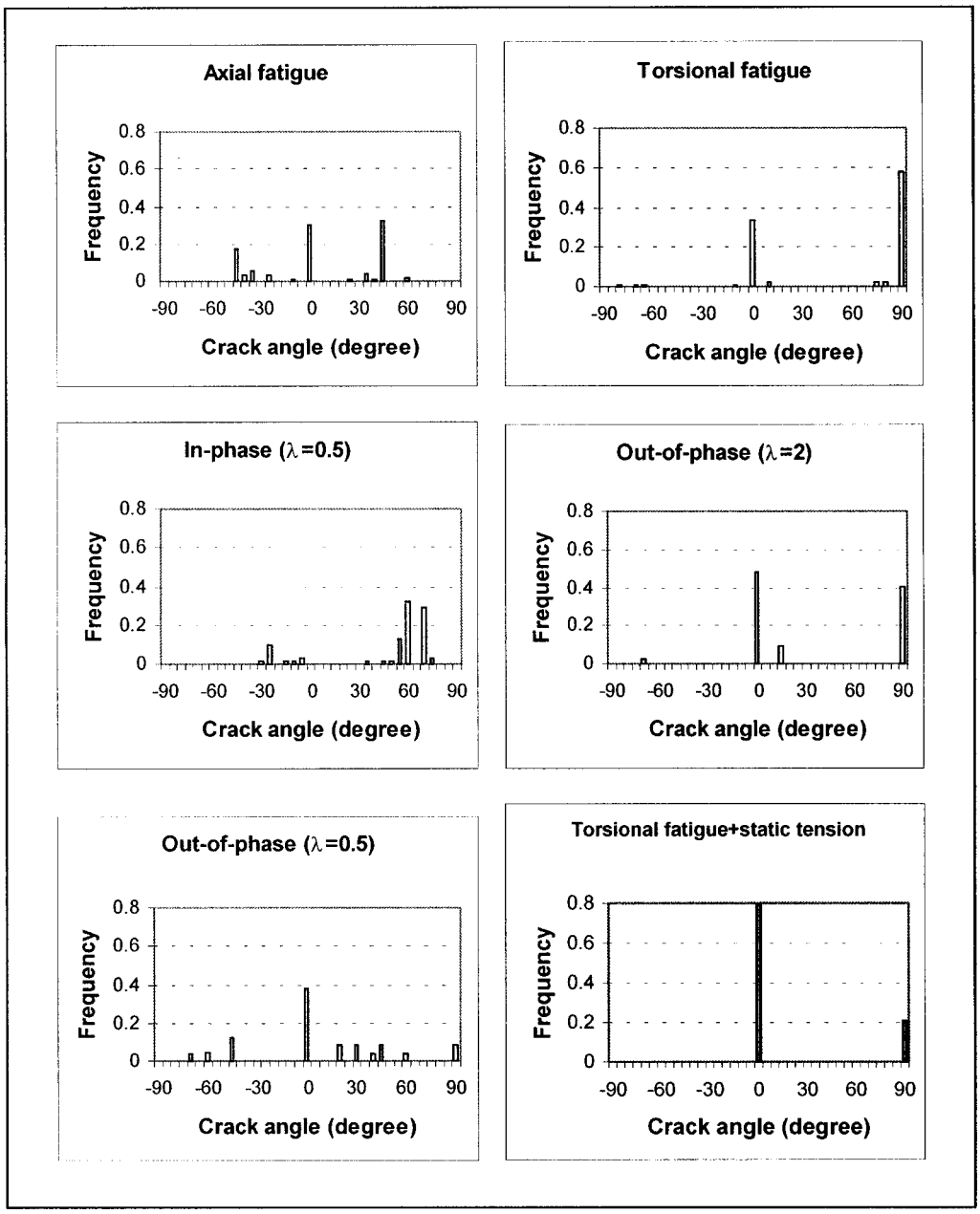

Figure 3.8 Frequency of grain-size cracks and slip bands in 1045 steel at different orientations under different loading conditions.

The critical plane concept is consistent with the observed fatigue mechanisms. For all loading cases (except for the special case: $\Phi=90^0$, $\lambda=0.5$), there are two peaks (Figure 3.8) at angles corresponding well to the two maximum shear planes (Figure 3.6) (the third peak at 0° under axial fatigue corresponds to case B cracks, not perpendicular to the surface). One peak is often higher than the other. In torsional fatigue and in-phase fatigue, this can be related to the effect of longitudinal inclusions in the material. However, the higher peak at 0° in 90° out-of-phase fatigue with $\lambda=2$ and in torsional fatigue with static tension can be attributed to normal stress effects. More cracks initiate on the maximum shear plane with higher normal stress amplitude (90° out-of-phase; $\lambda=2$) or with higher mean normal stress (torsion plus static tension). For the special loading case (90° out-of-phase; $\lambda=0.5$), the cracks are scattered in a large range of directions, because all planes have the same shear stress amplitude (Figure 3.6). However, a higher peak is still found at 0° where the normal stress amplitude is maximum

The common feature of these observations is that slip bands and grain-size cracks develop on all maximum shear planes, but in higher number on those where the normal stress (amplitude or mean value) is the largest. Similar results have also been found in other investigations on out-of-phase fatigue (Kanazawa et al, 1977; Ohkawa et al, 1997). But our results also put into evidence the effect of a tensile mean stress on the crack initiation process. It is clear that crack initiation is governed by a shear process. The maximum shear stress or strain amplitude is the control parameter for crack initiation. But the normal stress amplitude and the static tensile stress on the maximum shear plane can assist crack initiation. The normal stress (both amplitude and mean) on the maximum shear plane plays a second important role in crack initiation. The special loading case, where cracks can initiate in many directions, deserves a particular attention. Fatigue damage is expected to be faster, and further explanation will be given later.

3.3.2 Crack propagation

As the cycle life increases, a small number of the cracks, which initiated at PSBs in a ferrite grain, grow across the grain boundaries into the adjacent network of ferrite grains. The crack growth occurs along the maximum shear planes (stage I or shear crack growth). After growing across several ferrite grains, the cracks branch into the plane(s) of maximum normal stress amplitude (stage II or tensile crack growth). Note that stage I here does not refer to a single slip mechanism. Micro-fractographic observations reveal that in both stage I and stage II propagations; the grains offer two or more slip systems to accommodate the macroscopic cracking path (section 3.3.4).

An example of surface crack propagation process under axial fatigue is shown in Figure 3.9. The photographs (a), (b) and (c) were taken at the same site from replicas taken at three different cycle lives. The crack has initiated at slip bands in a ferrite grain (arrow A). Then the crack has changed its direction normal to the specimen axis (arrow B). This direction can be also the result of a shear process (case B shear). In the following crack propagation, the crack direction returns to 45° with respect to the specimen axis (case A shear) (arrow C). Such propagation by a shear process is defined as stage I propagation. As it becomes longer, the crack changes its local direction again, but it is now globally perpendicular to the specimen axis (Figure 3.9 (c)). Then it joins with another crack also perpendicular to the specimen axis. This is stage II crack propagation on the planes of maximum normal stress.

It is difficult to identify the transition from stage I to stage II propagation because the local crack path is very tortuous for axial fatigue. There are several possible reasons: (1) the crack prefers to propagate in ferrite; (2) the crack may follow the direction of pearlite lamellae; (3) the crack can grow by local shear on an infinity of maximum shear planes.

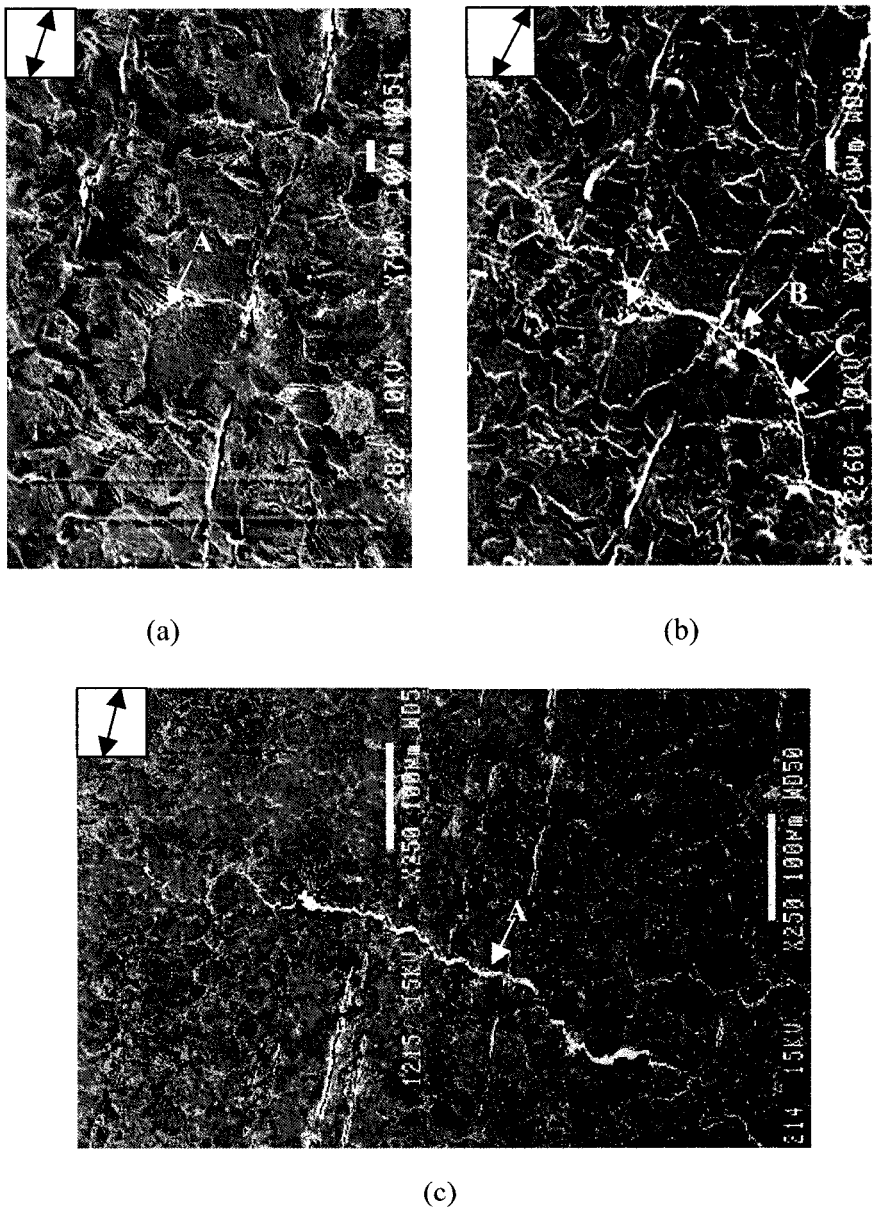

(a) (b)

(c)

Figure 3.9 Crack propagation in 1045 steel under axial fatigue. (a) N/N_f=23.2%; (b) N/N_f=55.8%; (c) N/N_f=74.5%. (The arrow on the top-left of each photo showing the specimen axis).

As shown in Figure 3.10, the two stages of fatigue crack propagation are clearly put into evidence under torsional loading. These three photographs were taken at the same location from replicas taken at different cycle lives. A stage I crack first developed along the maximum shear plane parallel to the specimen axis (arrow A). Then, after about 200 μm, there is the stage II crack propagation along the two maximum normal planes (±45° with respect to the specimen axis) (arrows B). There are also two sets of maximum shear planes (parallel or perpendicular to the specimen axis), but more final cracks occur on the maximum shear planes parallel to the specimen axis (90^0 plane). This could be attributed to an assisting effect of elongated inclusions on the cracking process. The observations on other specimens have shown that cracks can also initiate and propagate (stage I) on the transverse maximum shear planes (0^0 plane).

In-phase axial-torsional fatigue cracks also present two stages of crack propagation (Figure 3.11). Stage I can occur on the two orthogonal maximum shear planes, but stage II cracks can only branch into the planes of maximum normal stress amplitude. This observation is more or less documented in the literature. Looking at the normal stress amplitude variations shown in the corresponding plot in Figure 3.6, there is only one maximum normal stress plane for in-phase loading. This is why in this loading case the crack can only branch into one plane instead of two orthogonal planes in torsional fatigue.

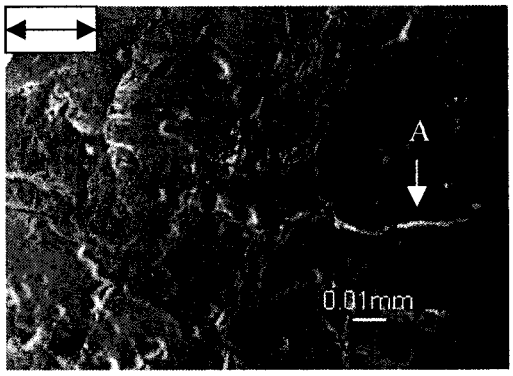

(a)

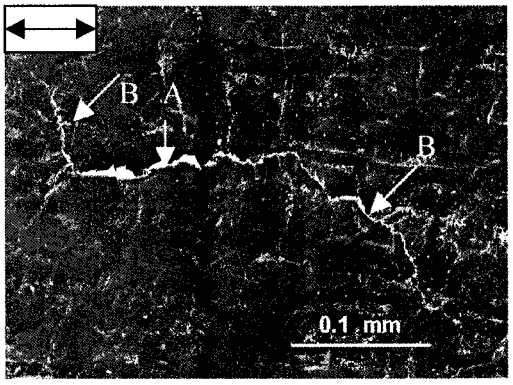

(b)

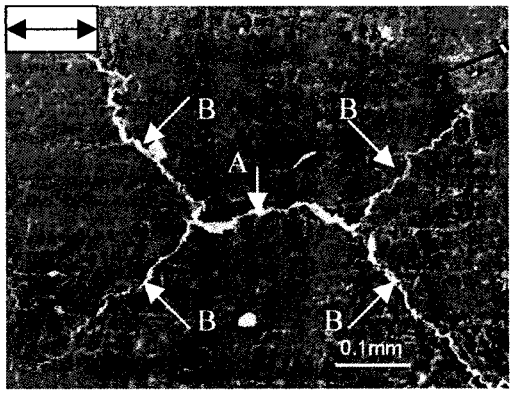

(c)

Figure 3.10 Crack propagation in 1045 steel under torsional fatigue. (a) N/N_f=24%. (b) N/N_f=58.2%. (c) N/N_f=92.5%. (Specimen axis is shown by the arrow in each photo)

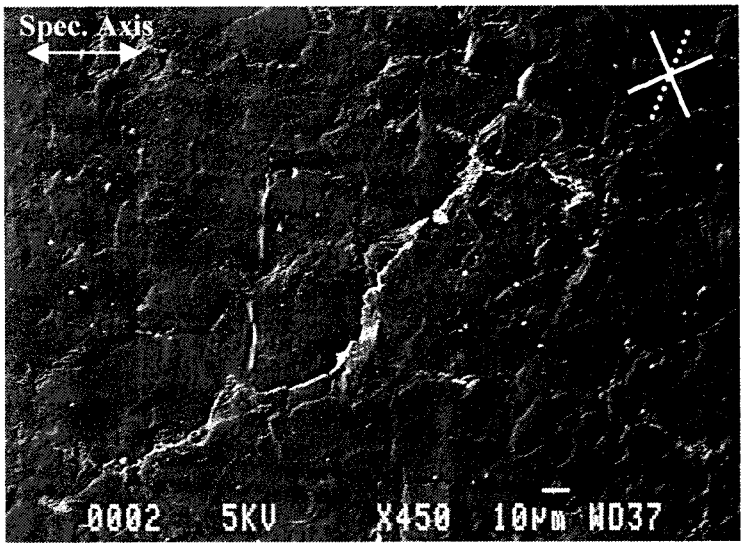

Figure 3.11 Typical fatigue crack in 1045 steel under in-phase axial-torsional fatigue. The specimen axis is shown by the arrow at the top-left of the photo. The solid white lines at the top-right show the maximum shear planes, and the dotted white line shows the maximum normal plane.

In torsional and in-phase fatigue, the transition from stage I to stage II is clearly observed. The two stages of crack propagation, first identified by Forsyth (1961) in axial fatigue, have been already observed in biaxial in-phase fatigue by several researchers (Kanazawa et al, 1977; Ohkawa et al, 1997). Note that Hua and Socie (1984) did not observe the stage II crack propagation in torsional and in-phase fatigue. The possible reasons for this difference can be 1) their observations were made under low to intermediate cycle fatigue; 2) the carbon content or the inclusion fibering may vary in the two materials employed by them and by us even though both are 1045 steel.

Further attention is paid here to non-proportional loadings. Figure 3.12 shows the crack evolution under 90° out-of-phase loading with λ=2. The crack initiates on the critical plane (θ=0°). It propagates on the same plane until about 0.15 mm in length, then it

branches into a plane of maximum normal stress amplitude. This process resembles that of torsional fatigue. However, in torsional fatigue stage I cracks can propagate on both maximum shear planes, while in the present case they only propagate on the maximum shear plane with the larger normal stress (Figure 3.6).

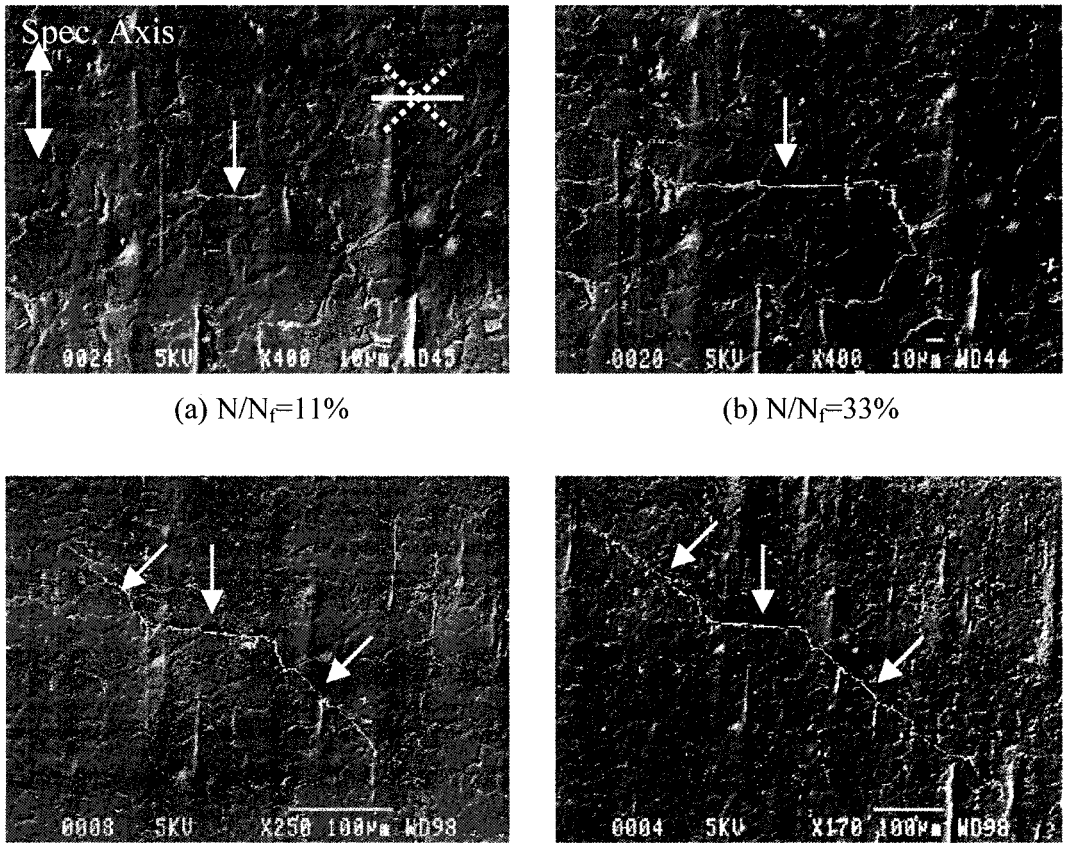

(a) N/N_f=11%

(b) N/N_f=33%

(c) N/N_f=66%

(d) N/N_f=80%

Figure 3.12 Crack evolution under 90^0 out-of-phase loading (λ=2) observed on replicas taken under SEM at different lifetime. (In each photo, specimen axis is vertical; N/N_f is life ratio; cracks are pointed by arrows; white solid lines represent the critical plane while dashed lines represent the planes of maximum normal stress amplitude, see (a).)

A possible reason for the single stage II branching could be that the phase angle between the normal and shear stresses on one maximum normal plane is higher than that on the other, even though the shear and normal stress amplitudes are the same on both planes (Figure 3.13). The plane with lower phase angle is more damaging. As a result, the crack only branches into plane of maximum normal stress with less de-phasing.

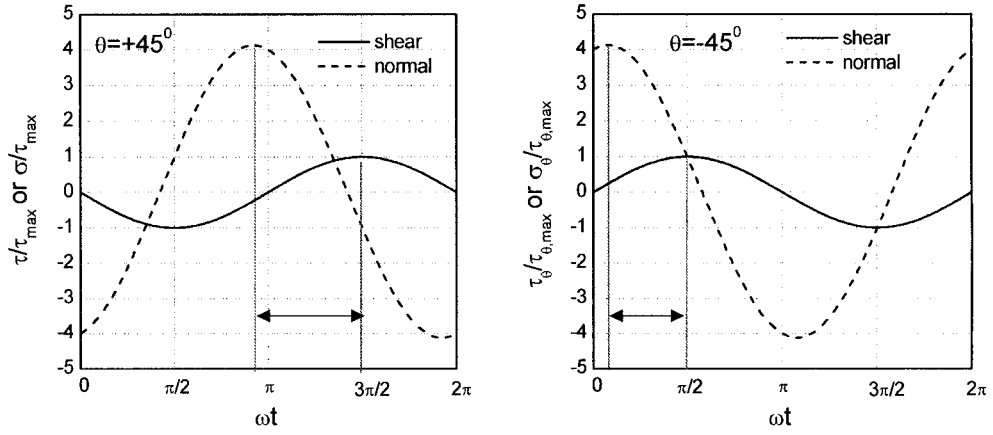

Figure 3.13 Normalized shear and normal stress variations with time on the two maximum normal stress planes ($\pm 45^0$). The phase angles between shear and normal stresses on these two planes are different (arrows); the phase angle on the $+45^0$ plane is larger than that on the -45^0 plane.

Figure 3.14 shows the crack evolution under 90° out-of-phase loading with λ=0.5. This is what we call the "special loading case" for which the shear stress amplitudes on all planes are equal. The crack is horizontal until the end of the fatigue life. Despite some local fluctuations in orientation, no crack branching is observed for this loading case. According to stress analysis (Figure 3.6), the critical plane (initiation and stage I) is the same plane as that of maximum normal stress amplitude (stage II). This explains why no crack branching occurs. Ideally the surface crack should remain horizontal throughout the fatigue life. However, because all planes are maximum shear planes, the crack can

propagate on such other planes for a certain distance, but it comes back to the critical plane after a certain distance. The fact that all planes are maximum shear planes, and that stage I and stage II propagations occur on the same plane could result in faster crack propagation.

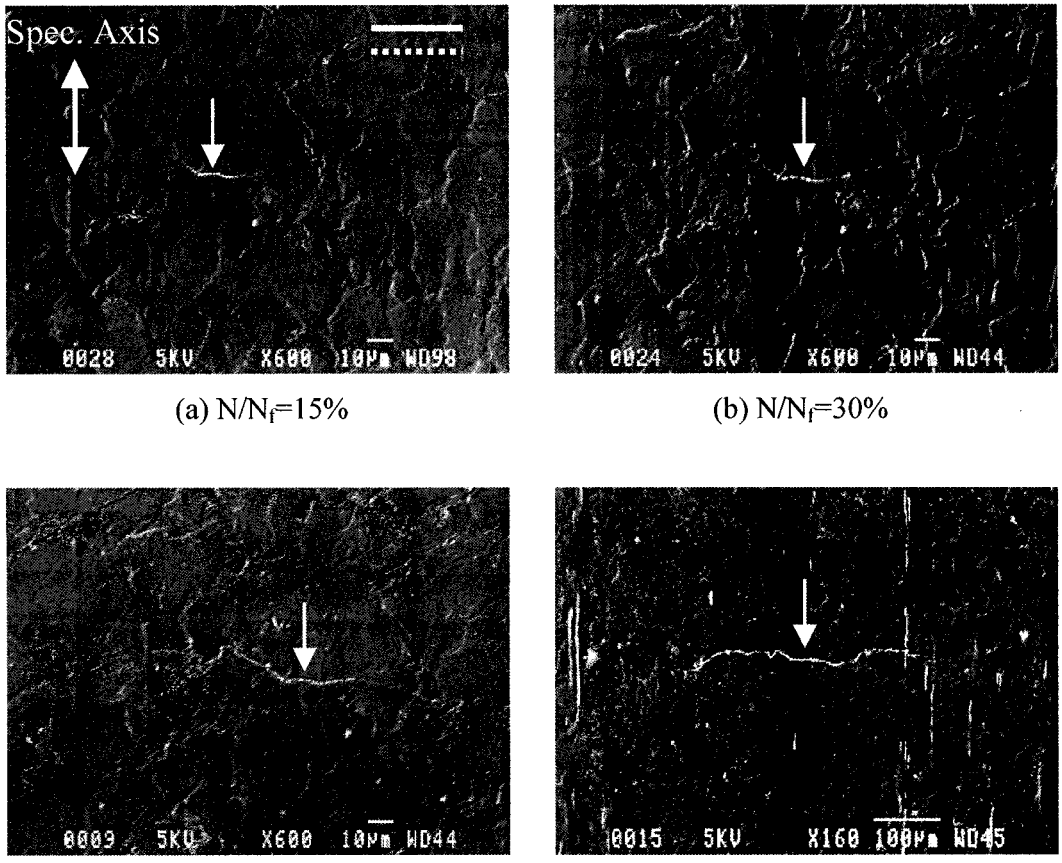

(a) N/N_f=15% (b) N/N_f=30%

(c) N/N_f=63% (d) N/N_f=88%

Figure 3.14 Crack evolution in 1045 steel under 90^0 out-of-phase loading (λ=0.5) observed on replicas taken at different lifetimes. In each photo, specimen axis is vertical; cracks are pointed by arrows; white solid line in photo (a) represents the critical plane while dashed line represents the plane of maximum normal stress amplitude.

Note that no detailed information is obtained on fatigue cracking process under torsional fatigue with static tension, since the specimens were damaged due to a problem of the machine.

3.3.3 Crack length and depth versus cycle life

In Figure 3.15, the surface crack lengths are plotted against the fatigue life ratio N/N_f for several loading cases. The surface crack lengths were measured from replicas taken at different lifetimes. In medium cycle fatigue ($10^5<N<10^6$ cycles), crack initiation occurs early in lifetime for all loading cases. But crack initiation and small crack propagation (<0.5mm) represent a large part (>80%) of the total life under all loading conditions observed. In high cycle fatigue life ($N>10^6$ cycles), crack initiation represents more than 80% of the total life for axial fatigue.

It is difficult to quantify the crack initiation life. It is not easy to distinguish grain-size cracks from wide PSBs. Initiation can be detected with full confidence only when the crack is observed propagating in a second grain. However, we have more interest to observe the transition from stage I to stage II crack propagation, in order to estimate what fraction of total life is controlled by a shear process. The stage I to stage II transition is easily identifiable for torsional fatigue and high λ 90^0 out-of-phase fatigue. For axial fatigue, it is not easy to identify the stage I/stage II transition due to the infinity of maximum shear planes. However, the transition can be defined as the number of cycles after which no inclined (45^0) shear crack can be observed. The arrows point out the approximate transition from stage I to stage II for these three loading cases. The transition from stage I to stage II occurs between 30% and 50% of total life. It is impossible to identify the stage I/stage II transition for 90^0 out-of-phase loading when $\lambda=0.5$.

Note that for a given total life, the surface cracks propagate initially faster under torsional fatigue and high λ out-of-phase loading than that under axial fatigue and the special loading case. However, crack depth is always more crucial for fatigue damage. Different pictures are observed when fatigue crack depths are plotted against the fatigue life ratio.

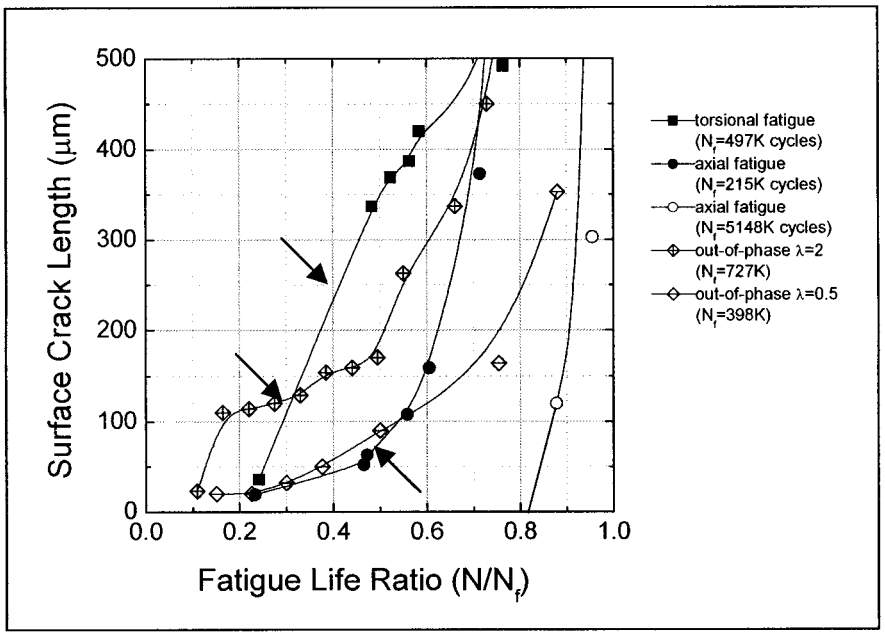

Figure 3.15 Surface crack length versus fatigue life ratio for several loading cases in 1045 steel, with the arrows pointing out the approximate transition from stage I to stage II. No cracks or PSBs are observed until 80% of total life under high cycle fatigue axial loading.

Figure 3.16 shows the relations between crack depth and life ratio for the same loading conditions. An interesting result is that, whatever the loading in medium cycle fatigue ($10^5<N_f<10^6$), these curves are consolidated until 50% of total life. This confirms that the crack depth is more appropriate than the surface crack length to describe fatigue damage. All transitions from stage I to stage II occur approximately at the same depth of 20-40μm. This depth is larger than one ferrite grain size. The transition from stage I to stage II propagation could correspond to a microstructural barrier in depth. After propagating in a network of some ferrite grains (near prior austenitic grain boundary), the crack must grow through pearlite colonies.

Crack depth was derived from the surface crack length by using crack aspect ratios, which were measured from small cracks on the fracture surface. The fracture surfaces of different loading cases were carefully examined under SEM. Several small cracks, away from the main crack, were observed for each loading case, and their average aspect ratio was measured. Figure 3.17 shows examples of small cracks observed on the fracture surface for several loading cases. The average aspect ratios are also listed in Table 3.3. These investigations show that cracks are almost semi-circular for axial fatigue and axial-torsional in-phase fatigue, and for the special loading case. On the other hand, shallow cracks are observed for torsional and high λ out-of-phase fatigue. The crack aspect ratios measured in the present study under axial, torsional and in-phase loadings are comparable to those measured by Hua and Socie (1984).

Table 3.3 Crack aspect ratios for several loading cases.

Loading cases	**Axial**	**Torsional**	**In-phase λ=0.5**	**Out-of-phase λ=2**	**Out-of-phase λ=0.5**
Aspect ratio (a/2c)	0.45	0.10	0.45	0. 15	0. 44

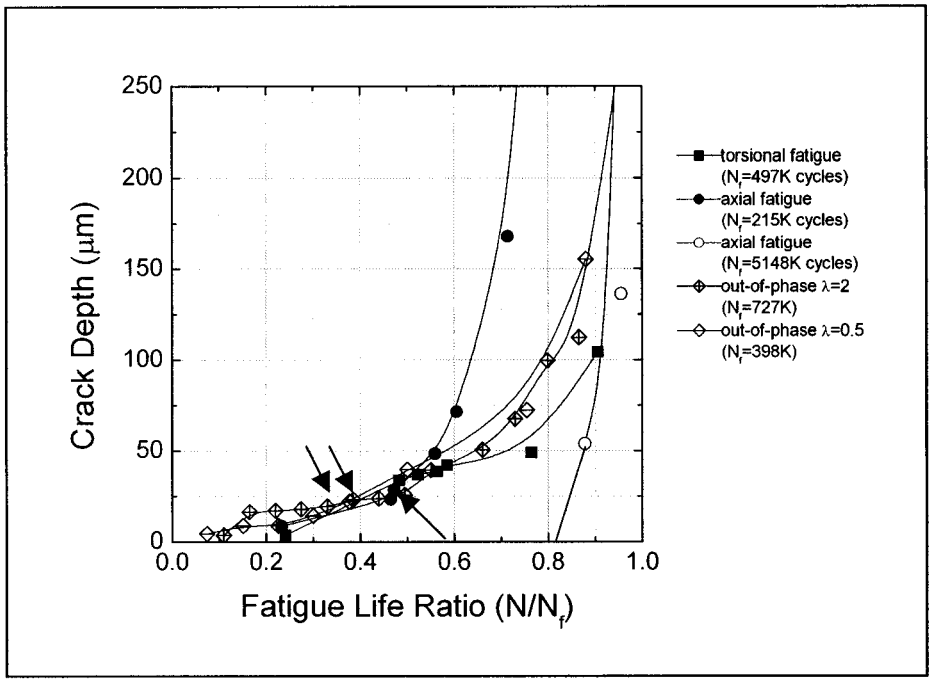

Figure 3.16 Crack depth versus fatigue life ratio for several loading cases in 1045 steel (arrows pointing out the approximate transition from stage I to stage II).

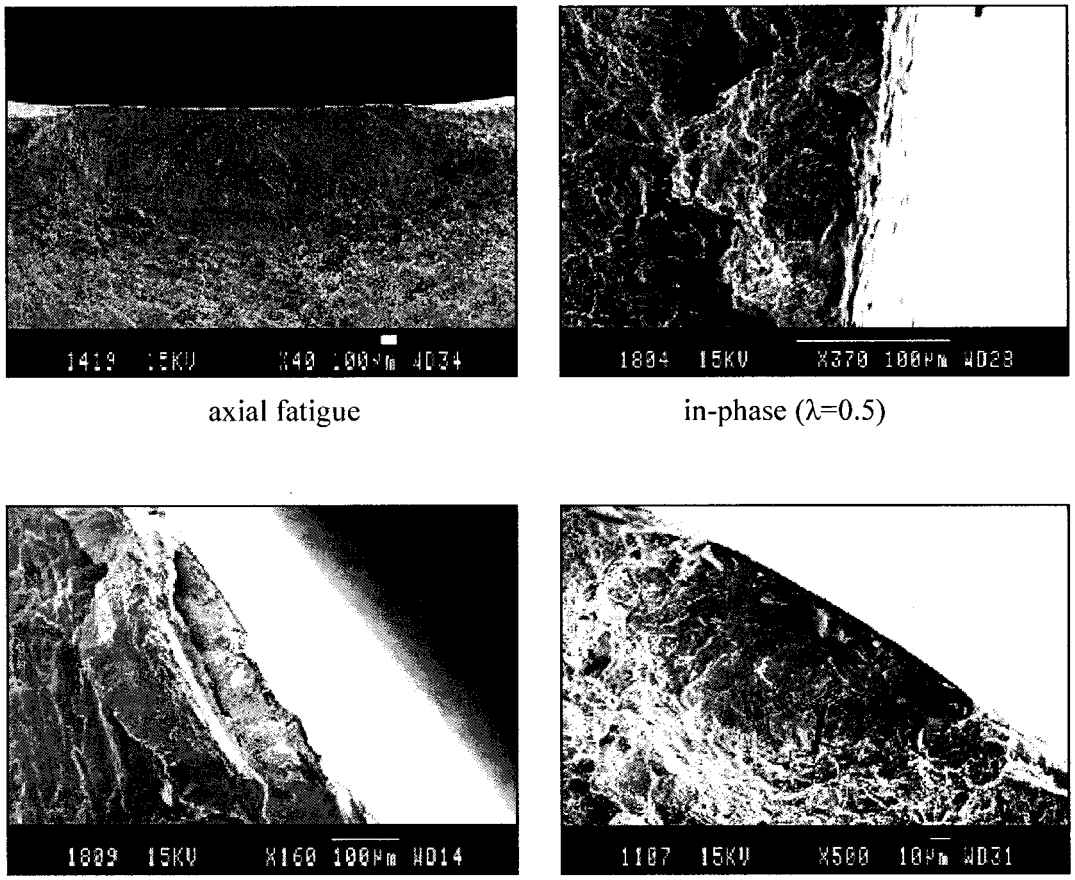

axial fatigue

in-phase (λ=0.5)

90^0 out-of-phase (λ=2)

90^0 out-of-phase (λ=0.5)

Figure 3.17 Small cracks observed on the fracture surface in 1045 steel. The crack aspect ratio depends on the loading case.

3.3.4 Fractography

In addition to the above-mentioned observation of the fracture surface for measuring crack aspect ratios, other fractographic features were also observed under SEM.

Multiple crack initiations were observed under the axial loading case (Figure 3.18). Cracks always initiated at the specimen surface. Figure 3.18 shows multiple crack initiations observed on the macro-scale as well as on microscopic scale. Lines representing crack coalescence are pointed out by arrows in Figure 3.18(a). These observations were similar to those made on the replicas. Multiple initiations were also observed under other loading cases.

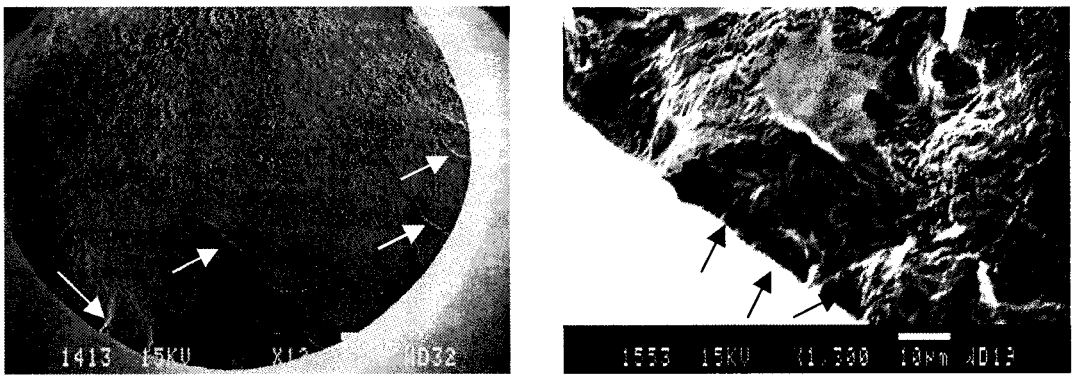

(a) (b)

Figure 3.18 Multiple crack initiation in 1045 steel under axial fatigue observed under SEM. (a) On large scale. (b) On microscopic-scale.

Figure 3.19 shows the fracture surface of torsional fatigue at low magnification. There is a ridge in the middle of this photograph (see arrow), which shows the graduate transition from stage I to stage II propagation.

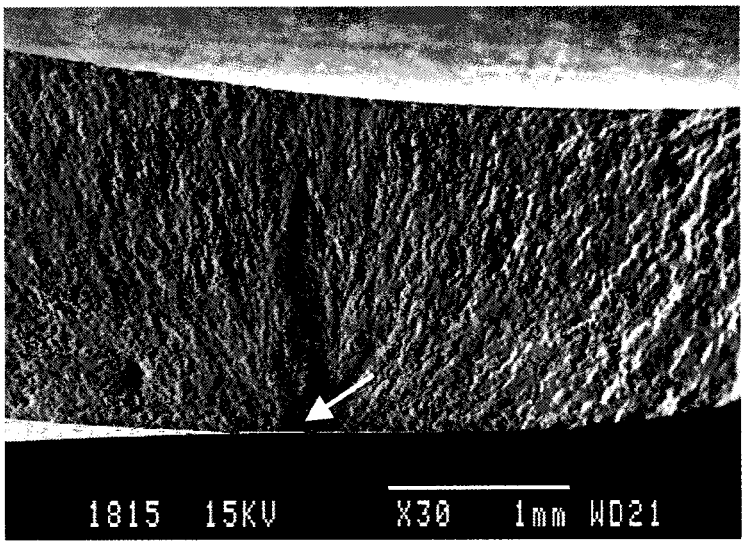

Figure 3.19 Fracture surface of torsional fatigue in 1045 steel under SEM at low magnification. The globe fracture surface is oriented at 45^0 with respect to the specimen axis. The arrow shows the stage I crack.

In the area close to crack initiation, roughness was observed on the fracture surface for the different loading cases. Figures 3.20 (a) and (b) show the fracture features of axial fatigue and out-of-phase fatigue (λ=2). Not much difference was observed for these two loading cases.

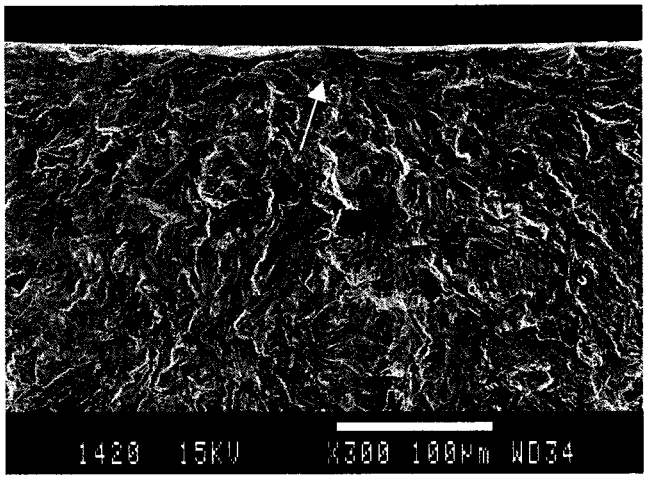

Axial fatigue

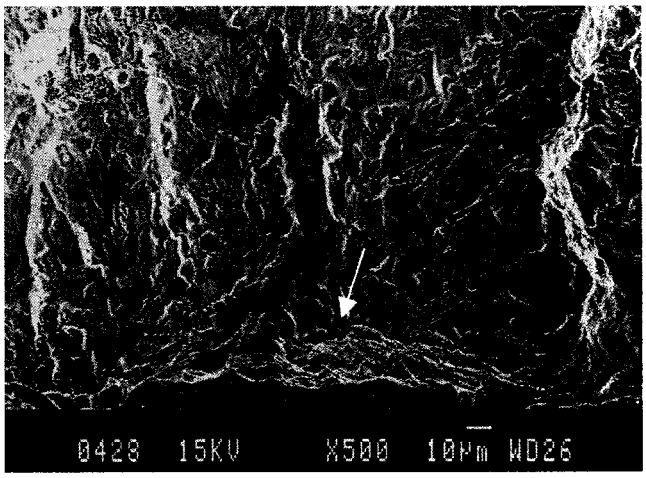

Out-of-phase loading (λ=2)

Figure 3.20 Fracture features at area close to initiation observed in 1045 steel (arrows showing the initiation sites).

In areas away from initiation regions, striations, a characteristic fracture feature of fatigue, were observed in different loading cases (Figure 3.21). These striations are generally observed at ferrite grains. They show the local propagation direction. In the special loading case, local crack coalescences were observe. This coincides to the high surface crack density measured on replicas (section 4.5.3).

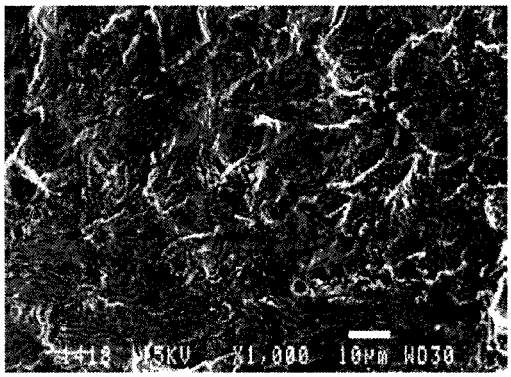

Axial fatigue

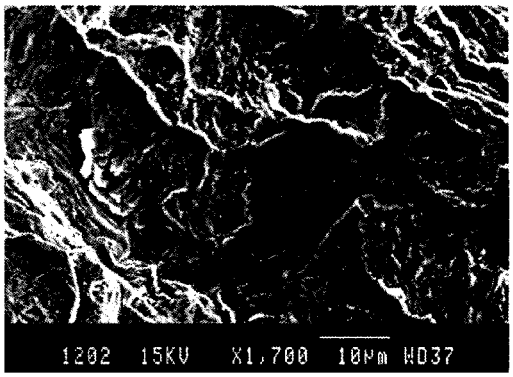

In-phase fatigue (λ=0.5)

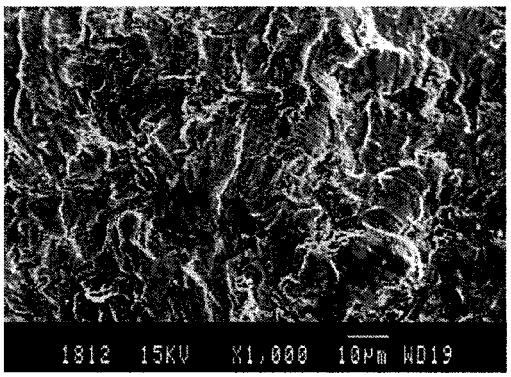

90^0 out-of-phase (λ=2)

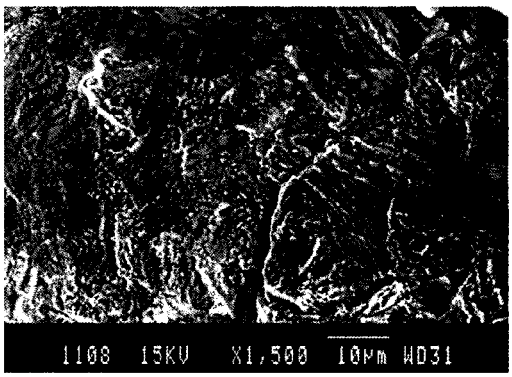

90^0 out-of-phase(λ=0.5)

Figure 3.21 Fatigue fracture features at area away from the crack initiation sites observed in 1045 steel under several loading cases.

Fracture surface observations at different depths revealed similar propagation micro-mechanisms. There are two or more slip systems to accommodate the cracking path. Figure 3.22(a) shows the small steps formed by the different slip systems under axial fatigue. Similar observations were made for torsional fatigue (Figure 3.22 (b)). In both stage I and stage II, the grains seem to offer two (or more) slip systems to accommodate the macroscopic cracking path.

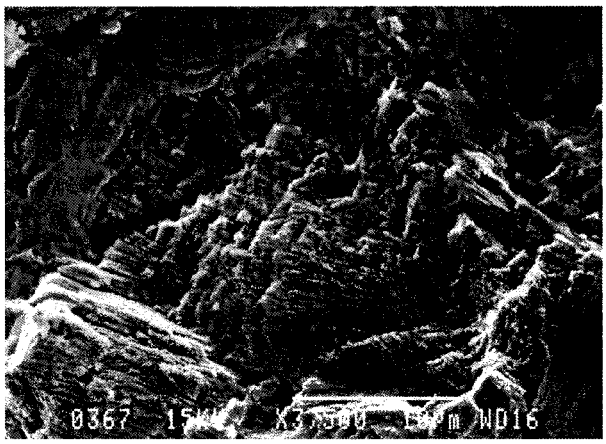

(a) Axial fatigue

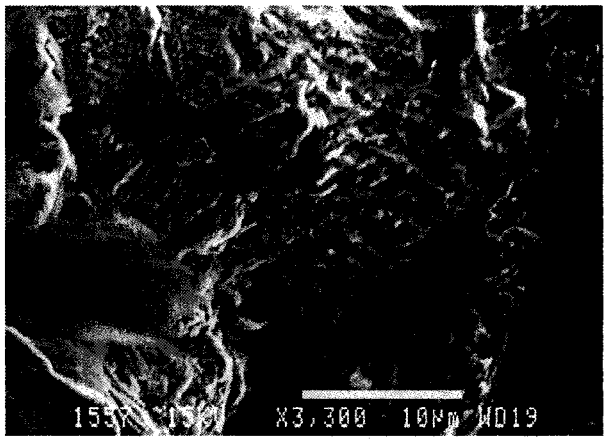

(b) Torsional fatigue

Figure 3.22 Multiple slips accommodate cracking paths under different loading cases observed in 1045 steel.

Under both torsional fatigue and combined axial-torsional loadings, extensive rubbing of fracture surfaces was observed (Figure 3.23). This shows the importance to consider the effect of the normal stress on the critical plane.

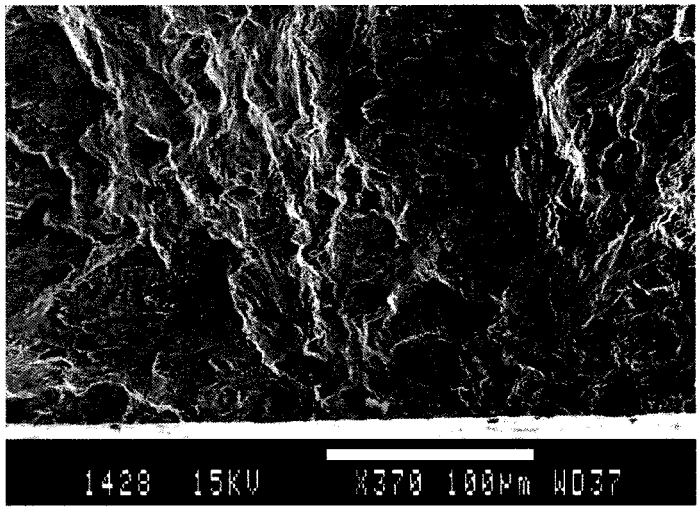

In-phase fatigue (λ=0.5)

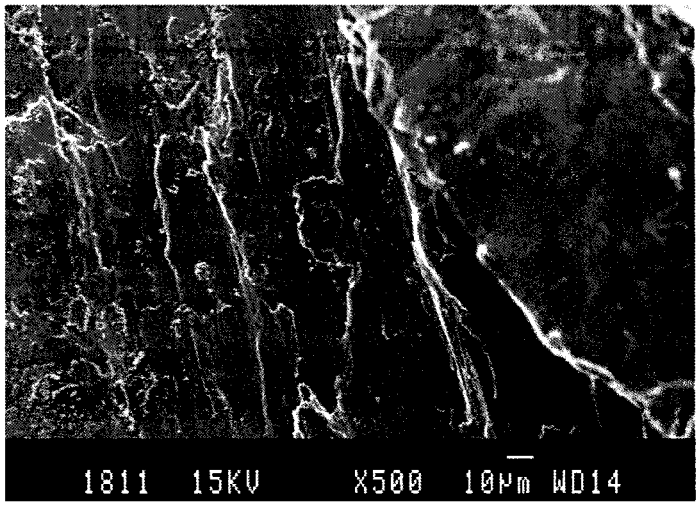

90^0 out-of-phase fatigue (λ=2)

Figure 3.23 Rubbing traces on the fracture surface observed in 1045 steel under axial-torsional in-phase and out-of-phase loadings.

Finally, Figure 3.24 shows fractographic features in the area of static fracture. Dimples were the main feature for this ductile material.

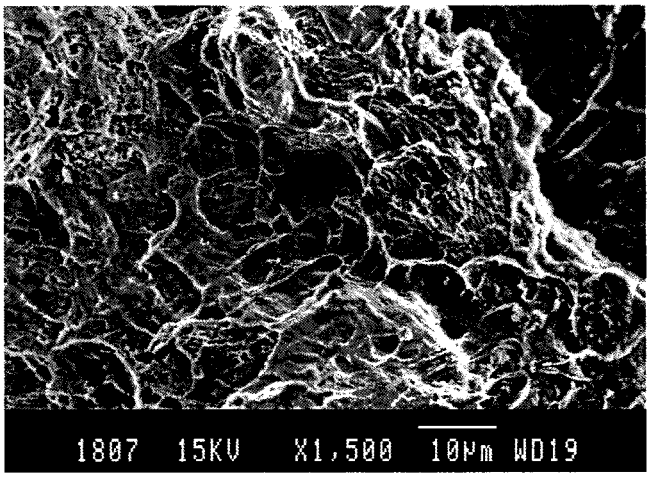

Figure 3.24 Dimples in the static fracture area observed in 1045 steel in axial loading.

3.4 Discussion

3.4.1 Factors influencing crack initiation

For all loading cases, the fatigue cracks initiate at PSBs on the specimen surface. This is a well-documented observation for smooth specimens under cyclic loading. Fatigue crack initiation is a shear predominant process. The maximum shear stress amplitude has primary role in fatigue crack initiation. The peak crack densities always appear on the maximum shear planes in all loading cases (Figures 3.6 and 3.8). The effects of normal stress acting on maximum shear planes are also put into evidence in Figure 3.8. Both normal stress amplitude and normal mean stress have a significant effect on the crack initiation process. The higher peak of crack density always observed is present on the maximum shear plane with either higher normal stress amplitude or higher normal mean stress. In the special loading case, although cracks can initiate on many planes (all planes are maximum shear planes), the highest peak still corresponds to the plane with highest normal stress amplitude. Therefore, the critical plane for crack initiation should be the maximum shear plane with the largest normal stress (both amplitude and mean).

Some researchers (Hua and Socie, 1984) have reported that under torsional fatigue, crack can initiate at inclusions on the longitudinal shear plane. In our fatigue tests, we did not directly observe this kind of crack initiation. However, in Figure 3.8, we found that under torsional and axial-torsional in-phase fatigue, more cracks appear at the maximum shear plane that corresponds to the longitudinal alignment of inclusions (torsional fatigue) or that is close to this direction (in-phase fatigue). This implies that the inclusions help the crack initiation process in the loading cases where there is a maximum shear plane parallel or close to the inclusion strings.

3.4.2 Stage I and stage II crack propagation

Although many cracks initiate, only a few cracks can propagate to specimen failure. Which crack will propagate depends on the neighboring microstructure and grain orientations. The cracks always initiate in ferrite grains, since ferrite has a lower fatigue resistance than pearlite. For the same reason, the cracks prefer to propagate in ferrite. Therefore, if more ferrite grains surround a grain-size crack, there is more chance of propagation for this crack. This is why the initial crack propagation is often observed to occur in a large network of ferrite grains.

The two stages of crack propagation, first reported by Forsyth in 1961, are put into evidence in several loading cases in the present tests. In torsional fatigue and 90^0 out-of-phase loading with λ=2, stage I cracks are clearly observed propagating on the maximum shear plane for a surface length ranging from 125μm to 750μm before they branch at 45^0 plane on a maximum normal stress plane. The transition from stage I to stage II is not obvious in axial fatigue from the observation of surface cracking. This is understandable because in axial fatigue, both case B type stage I cracks and stage II cracks intersect the external surface on a line perpendicular to the specimen axis (see Figure 1.11). Note that Hua and Socie (1984) did not observe the stage II propagation in 1045 steel under torsional fatigue. Two possible reasons for this difference could be: (1) their observations were made in low cycle fatigue, in which shear crack propagation is preferred; (2) their material has a strong mechanical fibering.

It was reported that the transition from stage I to stage II depends on material, stress state and stress level (Socie, 1987, 1993). In some materials (e.g. 1045 steel, Inconel 718), stage I propagation prevails, and in other materials (e.g. 304 stainless steel) stage II propagation prevails. High stress level and torsional loading favor stage I propagation. How these factors influence the transition however is not well explained.

Plumbridge (1972) stated that in axial fatigue as the stage I crack extends along the active slip plane further into the body of the specimen, shear crack growth becomes more difficult due to an increase of the tensile stress component. Eventually the constraint is sufficient to cause a gradual macroscopic rotation of cracks to a non-crystallographic plane approximately normal to the direction of the applied stress; this marks the onset of stage II crack propagation. He also reported that the proportion of the total fatigue life spent in each stage is largely controlled by the stress amplitude. At low stress level, the majority of the life (up to 90%) is taken by the initiation and stage I growth; whereas, at high stress level, stage II propagation may occupy a similar portion of the life. This seems in contradiction with Socie's observation that high stress level favors stage I propagation.

Suresh (1998) used the concepts of near-crack tip plasticity to explain the microscopic mode of fatigue crack growth under axial fatigue. In ductile solids, cyclic crack growth is envisioned as a process of intense localized deformation in macroscopic slip bands near the crack tip. When the crack and the zone of plastic deformation surrounding the crack tip are confined to within a few grain diameters, crack growth occurs predominantly by single shear, in the direction of the primary slip system. This single slip mechanism leads to a zig-zag crack path (stage I). Stage I crack growth has also been observed for a crack length substantially larger than the grain size provided that the zone of near-tip plasticity is smaller than the grain dimensions (long cracks at very low ΔK levels). At higher stress intensity ranges, the plastic zone at the crack tip encompasses many grains. The crack growth involves simultaneous or alternating flow along two slip systems. This duplex slip mechanism results in a planar crack path normal to the far-field tensile axis (stage II crack growth). Factors such as material slip characteristics, characteristic microstructural dimensions, applied stress level can strongly affect the crack growth mode.

On the contrary to Suresh's explanation, several other authors found that shear crack growth is preferred when the plastic zone size at the crack tip is large. This is easily

achieved in torsional fatigue (Verpoest et al, 1985). This could explain the dependence of crack growth mode on the stress ratio λ. On the other hand, tensile mean stress on the critical plane can also assist stage I crack propagation and results in a longer stage I cracks (Zhang and Akid, 1997). Brown et al (1985) showed that the competition between mode I growth and mode III growth leads to shear crack growth at high stress level, and tensile crack growth at low stress level (Figure 1.22).

In this investigation, it is found that the transition from stage I to stage II occurs approximately at the same crack depth (20-40μm) for three different stress states. This depth could correspond to a characteristic microstructural dimension, such as the prior austenite grain size. The transition from stage I to stage II crack propagation could occur at a depth where crack propagation meets a microstructural barrier, such as pearlite colonies. Our argument is that the transition from stage I to stage II depends on the steel microstructure.

In our opinion, no confusion should be made between stage I crack propagation and single slip mechanism. Stage I crack is a macroscopic crack that propagates on the maximum shear plane. This is clearly observed in torsional fatigue. Single slip mechanism describes the crack propagation on a microscopic scale and only one slip system is operating in one grain. Our observations have shown that multiple slips can occur in stage I crack propagation (Figure 3.22). On the other hand, in 7075 aluminum alloy (Chapter V), the stage I cracks can be as long as 10mm, and as deep as 1mm. They encompass many grains and single slip concept is not necessarily involved.

3.4.3 Relative life consumed under shear control

Both crack initiation and stage I crack propagation are controlled by a shear process, while stage II crack propagation, on macro-scale, is a tensile controlled process. Different damage modes require different fatigue life parameters (Socie, 1993).

In the present material, the life consumed under shear control is an important part of the total life. In present observations, it was found that Fatigue life for crack initiation and stage I crack propagation is about 30-45% of the total life for $N_f \approx 5x10^5$ cycles. For high cycle fatigue life ($>10^6$ cycles), initiation represents more than 70% of the total life. Shear-based parameters seem to be appropriate in high cycle fatigue life prediction. However, it should not be forgotten that an important part of life can be consumed by stage II propagation at high stress level (medium cycle fatigue).

3.4.4 Special loading case (90^0 out-of-phase; λ=0.5)

From the observation of the cracking behavior, it is found that whatever the stress state, crack initiation occurs on the maximum shear plane, and is then followed by stage I and stage II crack propagation. However, attention must be paid to the fatigue mechanisms in the special loading case. In this case, crack can initiate on many planes since all planes are maximum shear planes. Crack initiation is easier as compared with the other loading cases. High crack density and crack coalescences are observed in the special loading case (Section 4.5.3). Further, there is no stage II branching, which can also lead to faster crack propagation. Therefore, the special loading case results in more damaging mechanisms. It deserves a special consideration in fatigue life prediction.

3.5 Summary

Detailed fatigue cracking processes have been observed in as-rolled 1045 steel under different loading conditions.

The observation of the replicas under SEM and the direct observation of the specimen surfaces show that cracks initiate at PSBs on the specimen surface whatever the loading condition. The orientation distribution of small cracks (or PSBs) shows that most of cracks initiate on the maximum shear planes under all loading conditions. But with the

assistance of normal stress amplitude or normal mean stress on the maximum shear plane, more cracks initiate on the plane of maximum shear stress with highest normal stress, i.e., the critical plane.

The two stages of crack propagation are evident in three loading cases: torsional loading, in-phase and 90^0 out-of-phase (λ=2) axial-torsional loadings. In axial fatigue, the transition from stage I and stage II is not obvious, since both case B type stage I crack and stage II crack intersect external surface at a line perpendicular to the specimen axis. In the special loading case, there is no crack branching for stage II propagation, since the maximum shear plane is the same as the maximum normal stress plane.

Differences in surface crack growth lives and in crack aspect ratios are observed between axial, torsional, in-phase and out-of-phase loadings. However, curves of crack growth against fatigue life ratio are approximately consolidated when crack growth is defined in terms of crack depth. In other words, the relative fraction of total life spent to initiate a crack of given depth would not depend on the loading condition. In particular, the transition from stage I to stage II occurs at about 30-45% of total life in the region of 10^5-10^6 cycles. While the stage I crack length ranges from 50 μm to 750 μm depending on the loading conditions, their depth is approximately the same of about 20-40 μm. The stage I/stage II transition could correspond to a microstructural barrier in depth.

Special attention should be paid to the special loading case (90^0 out-of-phase; λ=0.5) for which fatigue crack initiation and propagation are easier as compared to the other loading cases. More damaging mechanisms result from this loading case. This should be taken into account in fatigue life prediction.

CHAPTER IV - EVALUATION OF CRITICAL-PLANE FATIGUE LIFE PREDICTION PARAMETERS

4.1 Introduction

Fatigue life prediction is one of the main objectives of fatigue research. As reviewed in Chapter I, many fatigue life prediction parameters have been proposed over the last decades. Early fatigue life parameters were often based on some equivalent stress/strain. More recent parameters were developed according to the critical plane concept. The stress/strain components resolved on the critical planes are used to characterize fatigue performance.

Fatigue crack initiation and growth are caused by cyclic plasticity. Even in high cycle fatigue, local plastic deformation occurs in some well-oriented grains and generates slip bands at the specimen surface. Cracks eventually nucleate from these slip bands where intrusions and extrusions have developed. Stage I crack propagation occurs on the maximum shear plane. Stage II crack propagation occurs on the plane of maximum normal stress, but local growth at the crack tip is still a shear strain-controlled process (Laird, 1967). Therefore it is not surprising that equivalent stress/strain developed for static yielding criteria were also used for multiaxial fatigue life prediction. But many researchers (e.g. Kanazawa et al, 1977) reported that these parameters failed to correlate fatigue lives obtained under axial and torsional loadings, as well as under proportional and non-proportional loadings. However, both Tresca and von-Mises equivalent stress/strain are the basis for developing multiaxial fatigue life parameters.

Fatigue strength of metals is also fundamentally related to ductility and this ductility depends on the applied hydrostatic stress (Bridgman, 1952) or on the normal stress/strain acting at the crack tip (Kanazawa et al, 1977). The normal stress acting on the maximum shear plane is believed to contribute to fatigue damage process; it can open the crack and

assist cracking process (Findley, 1959). Many multiaxial fatigue life parameters include either the hydrostatic stress (Sines, Dang Van and Papadopoulos) or the normal stress or strain on the maximum shear plane (e.g. Fatemi-Socie, McDiarmid and Kandil-Brown-Miller), in addition to the maximum shear stress/strain (Tresca) or the octahedral von-Mises stress/strain.

At the present time, the critical plane parameters are most prominent. They are based on the cracking mechanisms (Chapter III). These parameters are extensions of the Tresca criterion. They focus on the "critical plane", i.e. the plane of maximum shear stress or strain amplitude, that experiences the maximum normal stress or normal strain. The critical plane parameters have obtained some success in correlating fatigue lives under various loading conditions (e.g. Kanazawa, 1977). However, there are many different parameters that use different combinations of stresses and/or strains on the critical plane. Which combination is the most appropriate? What are the limits of each parameter?

In this study, the life prediction abilities of eight selected parameters have been evaluated under various biaxial high cycle axial-torsional and bending-torsional loadings. Fatigue life data on ferritic-pearlitic steels from two different authors are employed for this evaluation. The capabilities and the limits of the different parameters in predicting biaxial high cycle fatigue life are compared and analyzed. The discussions are based on the stress analysis and the fatigue cracking mechanisms. Particular attention is paid to two loading cases: 90^0 out-of-phase axial-torsional loading (with various stress ratio λ) and torsional loading with axial tensile mean stress.

4.2 The eight parameters

The fatigue life prediction parameters selected for evaluation are the following. The mathematical formulas are listed in Table 4.1.

- **Tresca parameter** (Maximum shear stress amplitude) – the basis of the critical plane parameters for fatigue failure dominated by the crack initiation and shear crack growth.
- **McDiarmid parameter** – a stress-based parameter, an extension of Tresca parameter that considers the maximum normal stress on the critical plane; it accounts for the effects of both the static and cyclic normal stresses.
- **Dang-Van parameter** – a stress-based parameter, using again the maximum shear stress amplitude, but using the maximum hydrostatic stress to account for normal stress effects.
- **Papadopoulos parameter** – an extension of von Mises criterion by adding the maximum "average normal stress" to account for normal stress effects; it reduces to Crossland parameter under axial-torsional loading.
- **Kandil-Brown-Miller (KBM) parameter** – a strain-based parameter (LCF); the second term takes into account the normal strain amplitude on the critical plane.
- **Wang-Brown parameter** – a strain-based parameter proposed for variable amplitude fatigue; it is a modification of KBM parameter, that uses the normal strain excursion during one reversal of shear strain on the critical plane, which makes the difference between in-phase and out-of-phase loadings.
- **Fatemi-Socie parameter** – a strain-based parameter, using the maximum normal stress on the critical plane to account for the additional hardening under out-of-phase loading and for the mean stress effects.
- **Glinka-Wang-Plumtree (GWP) parameter** – an energy-based parameter, considering shear stress and strain amplitudes on the critical plane as well as maximum shear and normal stresses to account for mean stress effects.

The stress-based parameters are proposed for high cycle fatigue. The strain-based parameters have been proposed for low cycle fatigue, but they are applicable for high cycle fatigue where the macroscopic deformation becomes predominantly elastic. The GWP parameter is claimed to be applicable to both high cycle fatigue and low cycle

fatigue. All parameters are based on the critical plane concept, except the Papadopoulos parameter, that uses the average of the resolved shear stress amplitude over all plane orientations and the maximum average normal stress. It can be considered as an extension of the von Mises criterion. It was recently used for predicting high cycle fatigue life under out-of-phase loading. In the mathematical formulas listed in Table 4.1, parameters have an adjustable constant k (except for the GWP parameter). This constant can be experimentally determined from two simple tests (e.g. torsional fatigue and axial fatigue).

Table 4.1 The eight parameters to be evaluated.

4 Stress-based parameters	3 Strain-based parameters
Tresca $=\tau_{max}$	KBM $=\gamma_{max}+k\varepsilon_n$
McDiarmid $=\tau_{max}+k\sigma_n^{max}$	Wang-Brown $=\gamma_{max}+k\varepsilon_n$ *
Dang-Van $=\tau_{max}+k\sigma_H^{max}$	Fatemi-Socie $=\gamma_{max}(1+k\frac{\sigma_n^{max}}{\sigma_y})$
Papadopoulos * $=\tau_{oct,a}+k\sigma_H^{max}$	

1 Energy-based parameter

$$GWP=\gamma_{max}\tau_{max}\left(\frac{1}{1-\tau^{max}/\tau_f'}+\frac{1}{1-\sigma_n^{max}/\sigma_f'}\right)$$

* For axial (bending)-torsional fatigue, the Papadopoulos parameter reduces to the Crossland parameter.

4.3 Fatigue data

Two sets of fatigue data (data 1 and data 2) from different authors are employed to evaluate the above-mentioned eight fatigue life parameters:

Data 1: this set of data is obtained from the present axial-torsional fatigue tests on as-rolled 1045 steel reported in this thesis. The fatigue life results for these tests (data 1) have been shown in Table 3.2 (page 96). A thin-walled tubular specimen

was used for axial-torsional fatigue, and an hourglass solid specimen for axial fatigue. Five loading cases were employed: axial fatigue, torsional fatigue, combined axial-torsional in-phase fatigue ($\lambda=\tau_0/\sigma_0=0.5$), combined axial-torsional 90^0 out-of-phase fatigue ($\lambda=\tau_0/\sigma_0=2$ and 0.5), and torsional fatigue with static tensile load ($\lambda= \tau_0/\sigma_m =1.67$, 1, 0.75). Both the effects of normal stress amplitude and mean normal stress can be evaluated on the same material.

Data 2: This set of data was obtained by Nishihara and Kawamoto (1942) on normalized mild steel with a carbon content of approximately 0.1%. In their fatigue tests, solid specimens were submitted to various reversed bending and torsional loadings. Eight loading cases have been selected: bending fatigue, torsional fatigue, in phase bending-torsional fatigue (λ =1.2, 0.5 and 0.2) and out-of-phase bending-torsional fatigue (λ =1.2, 0.5 and 0.2). Data 2 are listed in Table 4.2.

The influence of the stress ratio λ in out-of-phase fatigue is emphasized, and a special attention is paid to the special loading case ($\Phi=90^0$ and $\lambda=0.5$). In torsional fatigue with static tensile load (data 1), there is a mean normal stress on the maximum shear plane. The mean normal stress effect can be discriminated from the normal stress amplitude effect in the other symmetrical loading cases. Note that data 1 and data 2 are not comparable, since different materials, loadings and specimen geometries were involved.

Table 4.2 Data 2 from Nishihara and Kawamoto (1942).

Loading case	τ_0 (MPa)	σ_0 (MPa)	λ (τ_0/σ_0)	ϕ (Degree)	N_f (Cycles)
Torsional	170	0	∞		123,000
	150	0	∞		1,496,000
	145	0	∞		5,196,000
	140	0	∞		11,041,000
Bending	0	300	0		108,000
	0	270	0		944,000
	0	260	0		1,470,000
	0	250	0		1,419,000
	0	240	0		10,036,000
	0	230	0		10,084,000
	0	220	0		11,028,000
Bending-torsional in-phase	124.7	103.3	1.2	0	5,323,000
	120.1	99.5	1.2	0	10,184,000
	95.4	190.9	0.5	0	2,253,000
	91.9	183.8	0.5	0	10,637,000
	49.8	240.2	0.2	0	1,312,000
	47.1	227.3	0.2	0	10,111,000
	45.9	221.7	0.2	0	10,374,000
Bending-torsional out-of-phase	143.2	118.6	1.2	90	790,000
	138.6	114.8	1.2	90	1,645,000
	134	111	1.2	90	10,182,000
	120.2	240.4	0.5	90	182,000
	113.1	226.2	0.5	90	2,608,000
	106.1	212.1	0.5	90	1,635,000
	102.5	205	0.5	90	11,094,000
	51.7	249.5	0.2	90	592,000
	49.8	242.2	0.2	90	4,726,000
	47.8	231	0.2	90	10,172,000

4.4 Parameter computation and stress analysis

Each parameter has been computed for the different loading cases. The results are presented in Table 4.3. This computation is based on the stress analysis described in Appendix I. The computation permits us to make mathematical comparisons between parameters. The evaluation of fatigue life parameter is made in the high cycle fatigue regime where the macroscopic cyclic deformation becomes predominantly elastic. Plastic strain is neglected and a purely elastic stress-strain response (Hooke's law) is used to compute strain-based and energy-based parameters from applied stress (e.g. $\gamma_{max}=\tau_{max}/G$).

Several recordings of applied torque versus rotation angle were made at different cycles through the life of a specimen under torsional cyclic loading (specimen TS1, τ_{max}=150MPa, N_f = 616,542 cycles; Table 3.2). After 1000 cycles, the specimen behavior was almost elastic, with a cyclic plastic strain (loop hysteresis) of the order of 1% with respect to elastic strain computed from the specimen gauge length. However, plastic strain could be non-negligible at higher τ_{max} values. Possible consequences of a non-elastic stress-strain response are discussed at the end of this chapter.

Table 4.3 Fatigue life parameters computed for different loading cases

Parameters	Torsion	Axial	In-phase	Out-of-phase $\Phi=90^0$ $\lambda\geq0.5$	Out-of-phase $\Phi=90^0$ $\lambda<0.5$	Torsional fatigue +static tension
Tresca	τ_0	$\frac{1}{2}\sigma_0$	$\frac{\sqrt{4\lambda^2+1}}{2}\sigma_0$	$\lambda\sigma_0$	$\frac{1}{2}\sigma_0$	τ_0
McDiarmid	τ_0	$\frac{1}{2}\sigma_0+\frac{k}{2}\sigma_0$	$\frac{\sqrt{4\lambda^2+1}}{2}\sigma_0+k\frac{\sigma_0}{2}$	$\lambda\sigma_0+k\sigma_0$	$\frac{1}{2}\sigma_0+k\frac{\sqrt{4\lambda^2+1}}{2}\sigma_0$	$\tau_0+k\sigma_m$
Dang-Van	τ_0	$\frac{1}{2}\sigma_0+\frac{k}{3}\sigma_0$	$\frac{\sqrt{4\lambda^2+1}}{2}\sigma_0+k\frac{\sigma_0}{3}$	$\lambda\sigma_0+k\frac{\sigma_0}{3}$	$\frac{1}{2}\sigma_0+\frac{k}{3}\sigma_0$	$\tau_0+k\frac{\sigma_m}{3}$
Papadopoulos	τ_0	$\frac{\sqrt{3}}{3}\sigma_0+\frac{k}{3}\sigma_0$	$\sqrt{\frac{1+3\lambda^2}{3}}\sigma_0+k\frac{\sigma_0}{3}$	$\sqrt{\frac{1+3\lambda^2}{3}}\sigma_0+k\frac{\sigma_0}{3}$	$\sqrt{\frac{1+3\lambda^2}{3}}\sigma_0+k\frac{\sigma_0}{3}$	$\tau_0+k\frac{\sigma_m}{3}$
KBM	$\frac{\tau_0}{G}$	$\frac{\sigma_0}{2G}+\frac{k(1-\upsilon)}{2E}\sigma_0$	$\frac{\sqrt{4\lambda^2+1}}{2G}\sigma_0+k\frac{1-\nu}{2E}\sigma_0$	$\frac{\lambda\sigma_0}{G}+k\frac{\sigma_0}{E}$	$\frac{\sigma_0}{2G}+\frac{k}{2}\sqrt{(1-\upsilon)^2+4(1+\upsilon)^2\lambda^2}\frac{\sigma_0}{E}$	$\frac{\tau_0}{G}$
Wang-Brown	$\frac{\tau_0}{G}$	$\frac{\sigma_0}{2G}+\frac{k(1-\upsilon)}{2E}\sigma_0$	$\frac{\sqrt{4\lambda^2+1}}{2G}\sigma_0+k\frac{1-\nu}{2E}\sigma_0$	$\frac{\lambda\sigma_0}{G}+k\frac{\sigma_0}{2E}$	$\frac{\sigma_0}{2G}+\frac{k}{2}\sqrt{(1-\upsilon)^2+4(1+\upsilon)^2\lambda^2}\frac{\sigma_0}{E}$	$\frac{\tau_0}{G}$
Fatemi-Socie	$\frac{\tau_0}{G}$	$\frac{\sigma_0}{2G}\left(1+k\frac{\sigma_0}{2\sigma_y}\right)$	$\frac{\sqrt{4\lambda^2+1}}{2G}\sigma_0\left(1+k\frac{\sigma_0}{2\sigma_y}\right)$	$\frac{\lambda\sigma_0}{G}\left(1+k\frac{\sigma_0}{\sigma_y}\right)$	$\frac{\sigma_0}{2G}\left(1+k\frac{\sqrt{4\lambda^2+1}\sigma_0}{2\sigma_y}\right)$	$\frac{\tau_0}{G}\left(1+k\frac{\sigma_m}{\sigma_y}\right)$
GWP	(1)	(2)	(3)	(4)	(5)	(6)

$$(1)=\frac{\tau_0^2}{G}\left(\frac{1}{1-\tau_0/\tau_f'}+1\right) \qquad (2)=\frac{\sigma_0^2}{4G}\left(\frac{1}{1-\sigma_0/2\tau_f'}+\frac{1}{1-\sigma_0/2\sigma_f'}\right) \qquad (3)=\frac{4\lambda^2+1}{4G}\sigma_0^2\left(\frac{1}{1-\sqrt{4\lambda^2+1}\sigma_0/2\tau_f'}+\frac{1}{1-\sigma_0/2\sigma_f'}\right)$$

$$(4)=\frac{\lambda^2\sigma_0^2}{G}\left(\frac{1}{1-\lambda\sigma_0/\tau_f'}+\frac{1}{1-\sigma_0/\sigma_f'}\right) \qquad (5)=\frac{\sigma_0^2}{4G}\left(\frac{1}{1-\sigma_0/2\tau_f'}+\frac{1}{1-\sigma_0\sqrt{4\lambda^2+1}/2\sigma_f'}\right) \qquad (6)=\frac{\tau_0^2}{G}\left(\frac{1}{1-\tau_0/\tau_f'}+\frac{1}{1-\sigma_m/\sigma_f'}\right)$$

In above calculations, E = 205Gpa, and $\upsilon = 0.30$. σ_f' and τ_f' have been evaluated for two materials, respectively. For 1045 steel, σ_f' = 388.6 MPa and τ_f' = 246.9 MPa. For Nishihara et al's material, σ_f' = 595.4 MPa and τ_f' = 278.9 MPa.

For the convenience of later discussion, Figure 4.1 is introduced here, in which the variations of shear and normal stresses on the critical plane with time are given for different loading conditions. For a given maximum shear stress amplitude, the normal stress amplitude varies with loading cases:

- $\sigma_n = 0$ under torsional loading;
- $\sigma_n = \tau_{max}$ under axial loading;
- $\sigma_n = 0.707\ \tau_{max}$ under in-phase loading ($\lambda = 0.5$);
- $\sigma_n = 0.5\tau_{max}$ under out-of-phase loading ($\lambda = 2$);
- $\sigma_n = 2\tau_{max}$ under out-of-phase loading ($\lambda = 0.5$);
- $\sigma_n = 1.077\tau_{max}$ under out-of-phase loading ($\lambda = 0.2$).

The phase angle between shear and normal stress on the critical plane is 0^0 for axial and in-phase loadings. It is 90^0 for 90^0 out-of-phase loading when $\lambda \geq 0.5$. It is smaller than 45^0 for 90^0 out-of-phase loading with $\lambda < 0.5$.

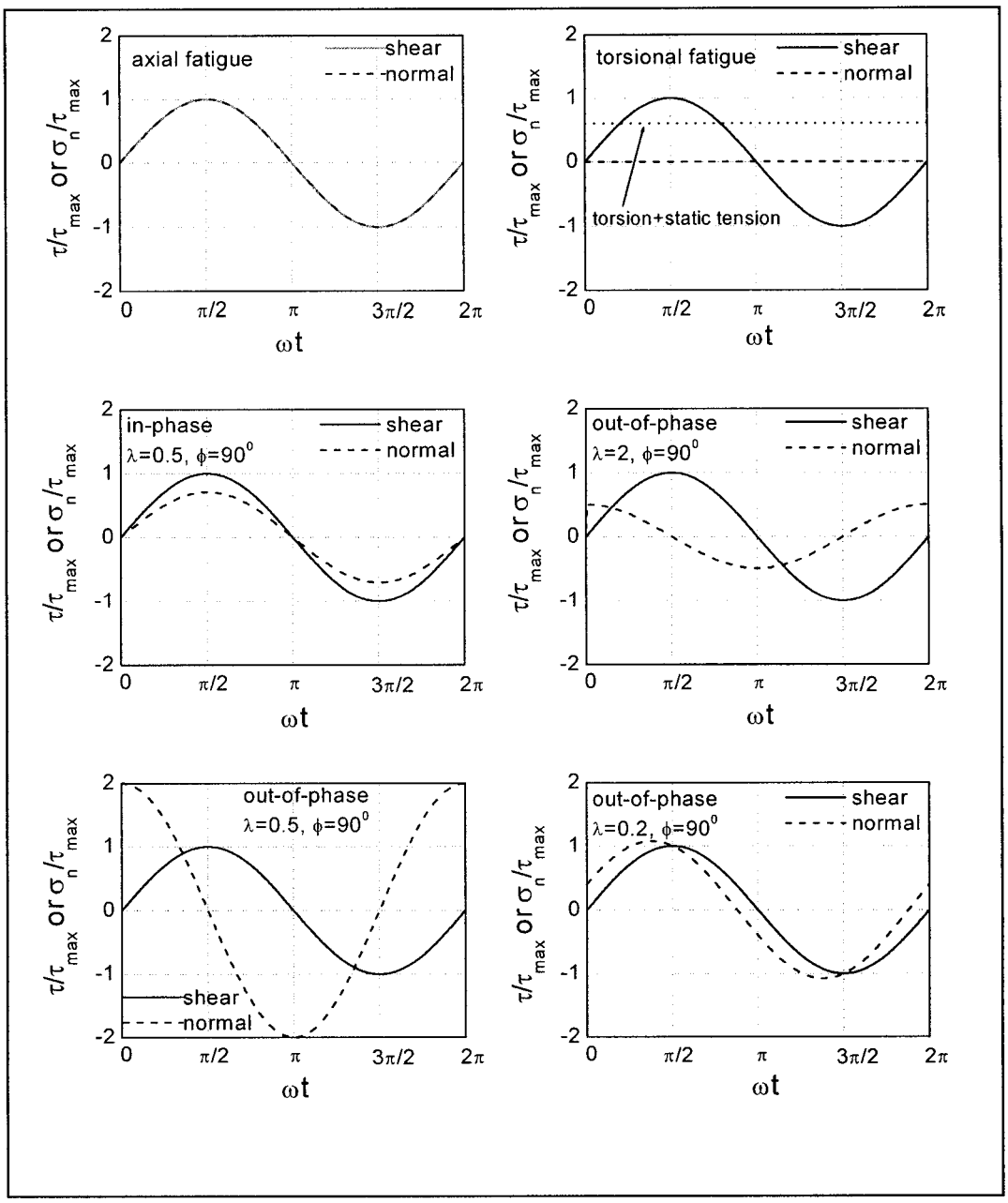

Figure 4.1 Normalized shear and normal stresses on the critical plane during one loading cycle under different loading conditions.

4.5 Evaluation results

The two sets of data (data 1 and data 2) are plotted against the eight selected parameters in Figure 4.2 and Figure 4.3, respectively. All plots using the same stress scale for the purpose of comparison. The symbols corresponding to the different loading conditions are given in the plot of McDiarmid parameter in both Figures 4.2 and 4.3. Except for the Tresca and GWP parameters, the solid baseline in each plot represents the linear regression made after consolidation of pure axial and pure torsional fatigue data (constant k is determined by this consolidation). Above the baseline, the fatigue life is underestimated, while below the baseline it is overestimated. The dotted lines correspond to deviations from the baseline by a factor of 3.

4.5.1 The Tresca and GWP parameters

In Figures 4.2(a) and 4.3 (a), large discrepancies are observed when fatigue data are plotted against the Tresca parameter. The maximum shear stress amplitude alone cannot correlate biaxial fatigue data. This is a well-documented result. Although the shear stress amplitude is the main driving force of fatigue damage, the normal stress on the critical plane can influence the fatigue life. The effects of normal stress (both amplitude and mean stress) on the critical plane are well illustrated on the plots against the Tresca parameter. The fatigue performance decreases with increasing normal stress amplitude or with a tensile normal mean stress (Figure 4.1).

GWP parameter gives a better correlation than Tresca parameter (Figures 4.2(h) and 4.3(h)). In both materials, σ_f' and τ_f' have been determined using axial and torsional fatigue data respectively. The prediction errors are not much larger than that of the other parameters. But GWP parameter cannot consolidate pure axial fatigue and torsional fatigue data. The second term in parentheses of this parameter (Table 4.1) accounts for

normal stress effect but in the present evaluation it is not sufficient to consolidate axial and torsional fatigue data in our case.

4.5.2 The six other parameters

For the six other parameters (Figure 4.2 (b)-(g) and Figure 4.3 (b)-(g)), a constant k is adjusted to a value such that pure axial and pure torsional data are consolidated. Note that the parameters have different k-values. But these values are related to each other. For example, $k_{McD} = k_{KBM} \cdot \frac{1-\nu}{2(1+\nu)}$ (ν is the Poisson ratio) (see computation results in Table 4.3). It is remarkable that all six parameters predict well fatigue life for in-phase loading cases. They can account for the in-phase normal stress amplitude effects. However, their prediction of fatigue life under out-of-phase loadings and mean stress effects gives varying results.

4.5.2.1 90° out-of-phase loading

Three different cases are distinguished: high λ (λ>0.5) out-of-phase loading, low λ (λ<0.5) out-of-phase loading and the special loading case (λ=0.5, in which all planes are maximum shear planes). All parameters work relatively well for low λ out-of-phase loading, but fatigue life for high λ and for the special loading case can be either underestimated or overestimated.

(1) The McDiarmid and Fatemi-Socie parameters give similar results. They both underestimate fatigue lives for high λ out-of-phase loading and overestimate fatigue lives for λ=0.5.

(2) The KBM parameter underestimates lives for both high λ and λ =0.5.

(3) Both the Dang-Van and Wang-Brown parameters work relatively well for high λ out-of-phase loadings, but both seriously overestimate fatigue lives for λ=0.5.

(4) The Papadopoulos parameter works relatively well for high λ out-of-phase loading, but underestimates fatigue life for out-of-phase loading with λ=0.5.

4.5.2.2 Torsional fatigue with mean tensile stress (Data 1 only)

The KBM and Wang-Brown parameters do not include any mean normal strain or stress term. As a result, these two parameters give coarse overestimation of lives obtained for this loading case.

Both the Dang-Van and Papadopoulos parameters that account for mean normal stress in terms of maximum hydrostatic stress overestimate fatigue lives for this loading case.

The McDiarmid and Fatemi-Socie parameters, which account for mean normal stress in terms of maximum normal stress, can predict relatively well fatigue lives for this loading case.

In a summary, the Tresca parameter cannot correlate biaxial fatigue lives. The GWP parameter accounts for normal stress effect but it cannot consolidate fatigue lives under in-phase loading. The six other parameters work well for in-phase and low λ out-of-phase loadings, but prediction errors exist for other non-proportional loadings. Fatigue lives under high λ out-of-phase loading are underestimated by McDiarmid, Fatemi-Socie and KBM parameters. Fatigue lives for the special loading case are often overestimated expect for the KBM and Papadopoulos parameters. Only the McDiarmid and Fatemi-Socie parameters that use the maximum normal stress on the critical plane work relatively well in the loading case of torsional fatigue with a mean tensile stress. In the subsequent sections, the limitations of these parameters will be discussed on the basis of stress analysis and observations of cracking mechanisms.

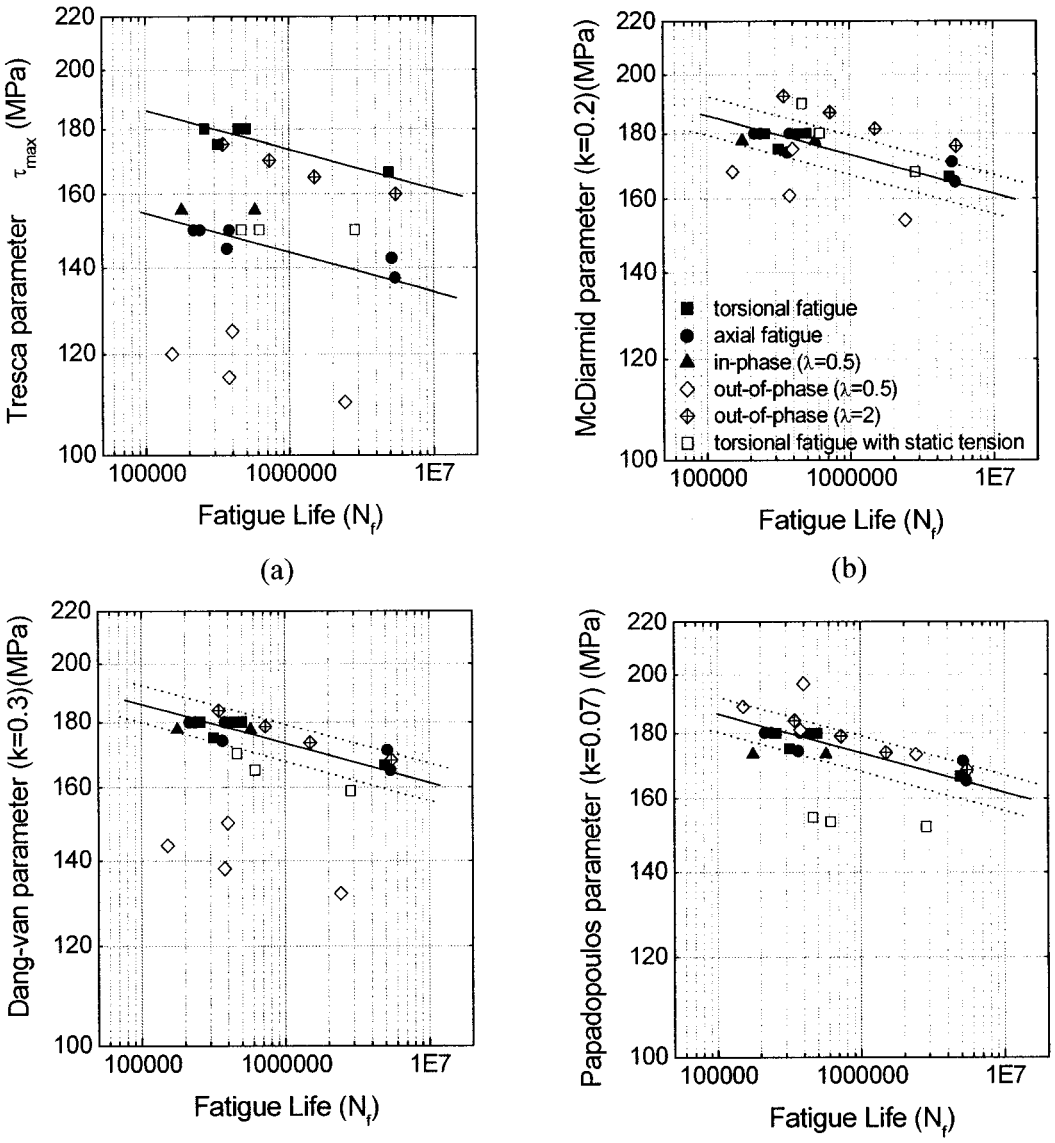

Figure 4.2 Fatigue lives plotted against the eight selected parameters (data 1). Loading conditions and symbols are given in the plot of McDiarmid parameter (b). (Continued on the next page).

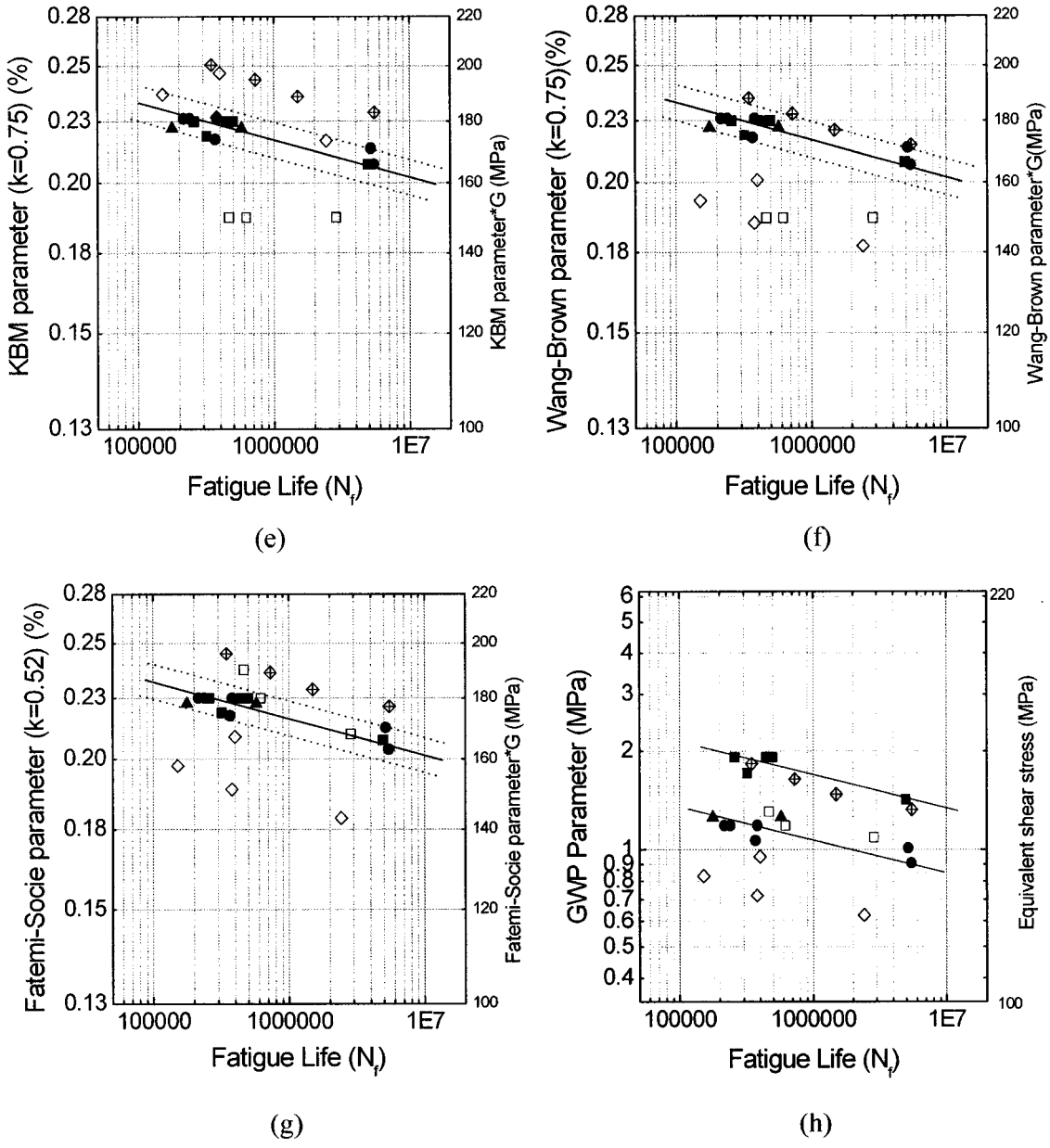

Figure 4.2 Fatigue lives (data 1) plotted against the eight selected parameters (continued from the previous page).

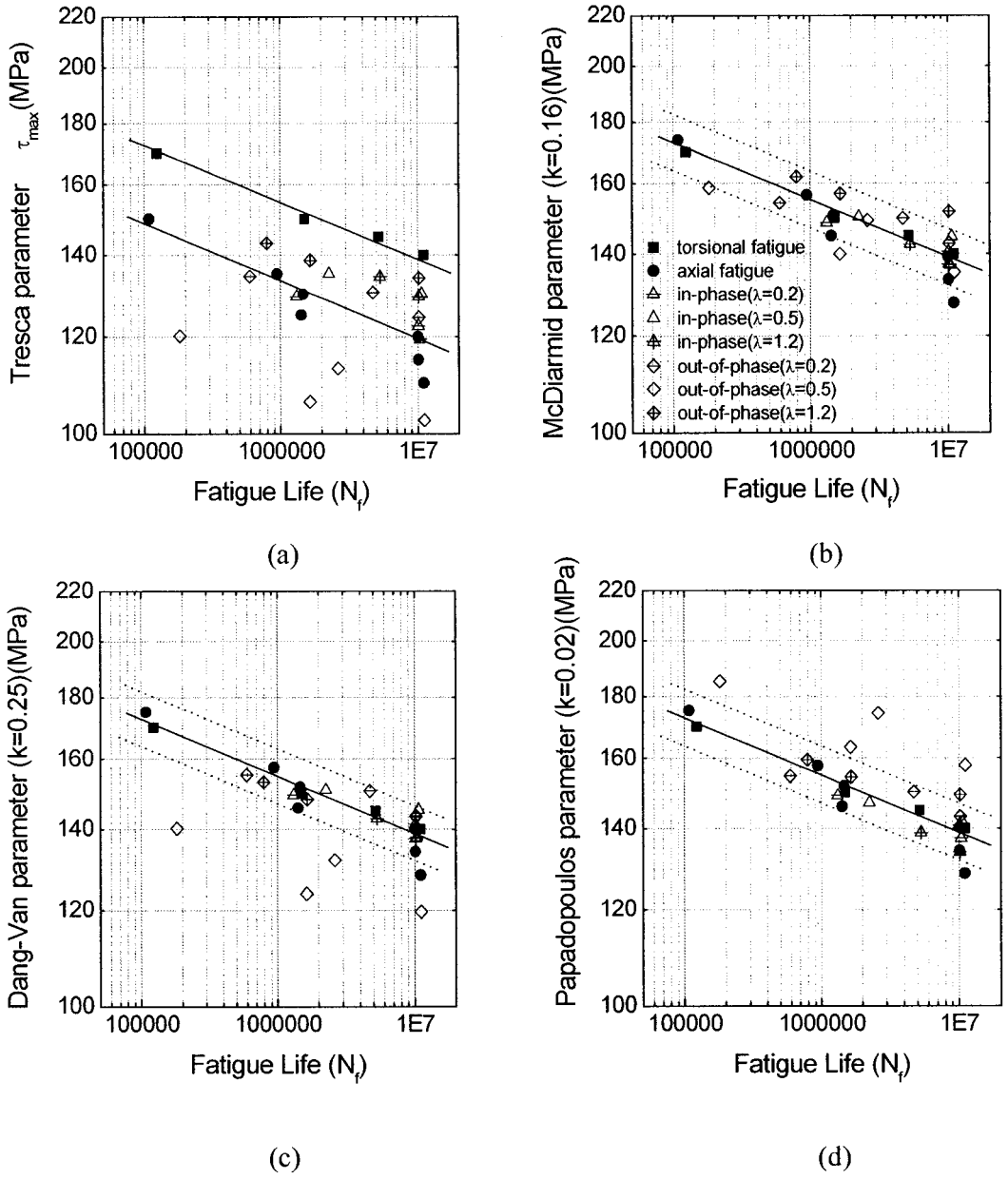

Figure 4.3 Fatigue lives plotted against the eight parameters (data 2). Loading conditions and symbols are given in the plot of McDiarmid parameter (plot (b)). (Continued on the next page).

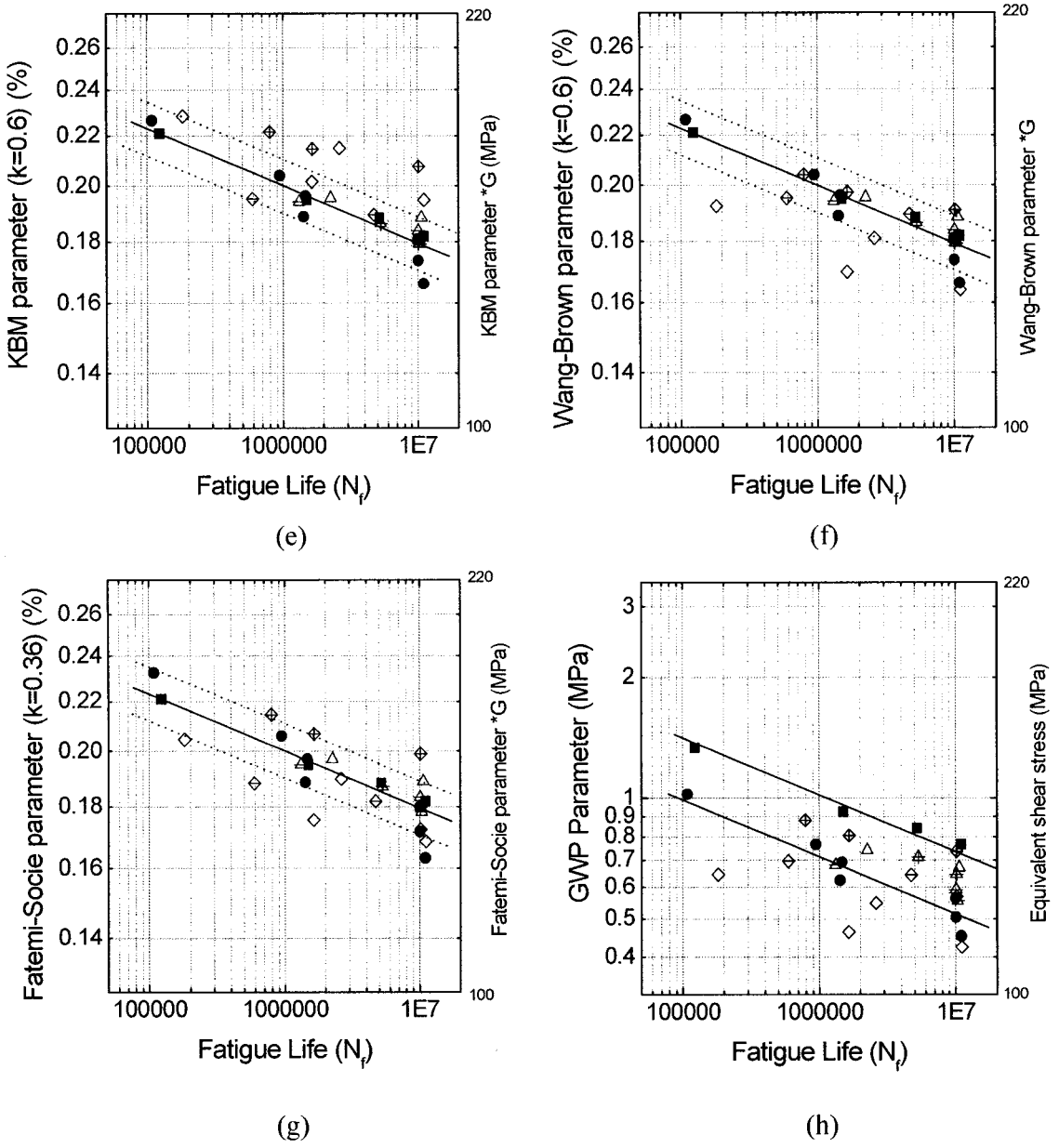

Figure 4.3 Fatigue lives (Data 2) plotted against the eight selected parameters (continued from the previous page).

4.6 Discussion

According to the observation of fatigue cracking mechanisms (Chapter III), both crack initiation and stage I propagation occur on the maximum shear plane. These two phases of crack damage process represent an important part of fatigue life. Therefore, fatigue life prediction approaches based on the concept of critical plane are qualitatively appropriate. The shear and normal stresses/strains on the maximum shear plane are appropriate terms in a life prediction parameter. Different combinations of these stresses/strains have been used in different parameters but result in different life prediction abilities in different loading cases, as summarized above. It is of interest to look at the characteristics of shear and normal stress variations on the critical plane. These characteristics can be described by shear stress/strain amplitude, normal stress/strain amplitude, normal mean stress/strain and phase angle between cyclic shear and normal stresses/strains.

4.6.1 High λ out-of-phase loading and phase angle effects

Fatigue lives for high λ out-of-phase loading are underestimated by the McDiarmid, Fatemi-Socie and KBM parameters. This can be explained by the large phase angle between the normal and shear stresses on the critical plane. As shown in Figure 4.1, a maximum phase angle of 90° is reached when $\lambda \geq 0.5$. The phase angle is small when $\lambda<0.5$, and it reduces to 0^0 under in-phase loading. The material should be more damaged when the shear and normal stresses reach their peak values simultaneously such as under in-phase loading. With increasing phase angle, the normal stress amplitude effect is attenuated. Parameters that do not consider this phase angle can overestimate the normal stress amplitude effect and consequently underestimate lives for high λ out-of-phase loading. In the case of low λ out-of-phase loading, the small phase angle does not have much influence on the normal stress amplitude effect, and then a relatively good prediction is obtained by different parameters.

Kanazawa et al (1977) claimed that the phase angle has no significant effect on fatigue life, but later Wang and Brown (1993) recognized its importance and proposed a modification to the KBM parameter by using the normal strain excursion during one shear reversal, which reduces the normal strain term for out-of-phase loading. A better correlation is then obtained for high λ out-of-phase data with the Wang-Brown parameter (Figures 4.2(f) and 4.3(f)). McDiarmid (1987) also recognized the phase angle effects and defined the critical shear plane as the plane at 45° or 135° with respect to the plane of maximum normal stress where the phase angle between shear and normal stresses is smaller. A better prediction was obtained for the fatigue strength under out-of-phase loadings.

Note that in addition to the Wang-Brown parameter, the Dang-Van and Papadopoulos parameters also work relatively well for high λ out-of-phase loading. These two parameters use the maximum hydrostatic stress to account for the normal stress effect. This can make a difference in the life correlation as compared to the parameters using the maximum normal stress on the critical plane. For example, under out-of-phase loading (λ=2), the McDiarmid parameter=$\tau_{max}+0.2\sigma_n^{max}$ and the Dang-Van parameter= $\tau_{max}+0.1\sigma_n^{max}$. The Dang-Van parameter is smaller than McDiarmid parameter. This explains why the Dang-Van parameter gives a better correlation than the McDiarmid parameter. Similar explanation applies to the Papadopoulos parameter.

On the other hand, the above explanation of phase angle does not apply to the special loading case. The phase angle is the largest (90^0) but this case has a negative influence on fatigue performance. A further explanation for the worst fatigue performance in the special loading case will be given in section 4.6.3.

4.6.2 Tensile mean stress effects (data 1 only)

It is obvious that the parameters considering only the normal strain amplitude (KBM and Wang-Brown) overestimate the fatigue lives for torsional fatigue with a static tensile load. These parameters were proposed for low cycle fatigue where stress relaxation occurs under 0-Max strain cycling. In the other parameters, normal mean stress effect can be taken into account by the maximum normal stress on the critical plane (the McDiarmid and Fatemi-Socie parameters) or by the maximum hydrostatic stress (e.g the Dang-Van and Papadopoulos parameters).

The effect of the normal stress amplitude and the effect of the normal mean stress on the critical plane can be different. The normal stress amplitude is an intrinsic mode I driving force, while the tensile mean stress can open the crack and assist crack propagation. It is reasonable to separate these two effects. Separate calibrations of constant k in the McDiarmid parameter for normal stress amplitude (fitting axial and torsional fatigue data) and for normal mean stress (fitting fatigue data for torsional loading with or without static tension) result in values of 0.2 and 0.16 respectively. Therefore, the cyclic and static normal stresses have approximately the same contribution to fatigue damage. Parameters such as those of McDiarmid and Fatemi-Socie that consider the maximum normal stress on the critical plane can fortunately account for both the in-phase normal stress amplitude effect and the normal mean stress effect on the critical plane.

The maximum normal stress is a more appropriate term than maximum hydrostatic stress to account for the normal mean stress effects, as observed by Marquis and Socie (2000). They did two kinds of critical tests in which the hydrostatic stress is zero but the maximum normal stress is different (see section 1.3.2). The material has different fatigue performances in the two loading cases. They concluded that the normal stress on the critical plane is more appropriate to describe fatigue damage than the hydrostatic stress. Under axial-torsional fatigue, the hydrostatic stress includes both the normal stress on the

critical plane and the normal stress on the plane perpendicular to the critical plane. However, physical reason to consider the latter normal stress is not clear. Our correlation results quantify how much the Dang-Van and Papadopoulos parameters overestimate fatigue life for torsional loading with static tension (Figure 4.2 (c)-(d)). The static part of hydrostatic stress has a more important contribution on fatigue damage than the cyclic part.

4.6.3 Extra damage in the special loading case (90° out-of-phase; λ= 0.5)

Among all out-of-phase loadings, the worst case is 90° out-of-phase loading with λ= 0.5. Even after correcting the Tresca parameter for the normal stress amplitude effect, most parameters still overestimate the poor fatigue performance in this special case.

Other authors also found that this loading case has a detrimental effect on fatigue performance. Garud (1981) stated that the effect of out-of-phase loading on fatigue strength is more evident when the phase angle is 90° and λ is 0.5. McDiarmid (1987) also realized the difficulty of predicting fatigue strength for this worst loading case and he redefined the critical plane as already mentioned. A slightly better prediction was obtained but was still nonconservative.

In this special loading case, all planes have the same shear stress amplitude (Figure 3.6). Cracks can initiate in a large range of orientations. This is confirmed by the crack orientation distribution for this loading case (Figure 3.8).

At the same time, a high crack density is observed, because a large number of grains are well oriented. Figure 4.4 shows the crack densities for the different loading conditions plotted against McDiarmid parameter. Exceptional high crack densities for the special loading case demonstrate much easier crack initiation.

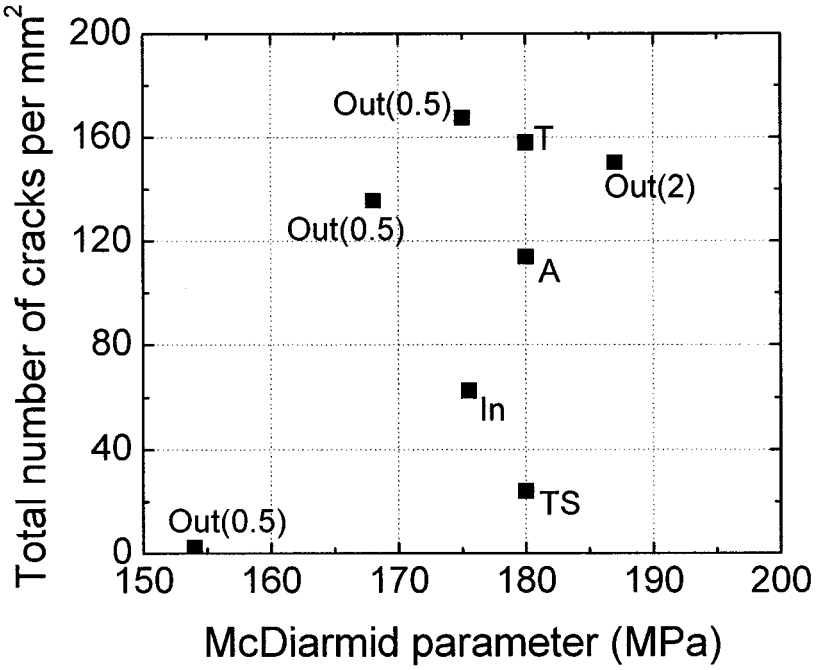

Figure 4.4 Crack densities for the different loading conditions, plotted against McDiarmid parameter (A: axial fatigue; T: torsional fatigue; In: in-phase loading; Out: out-of-phase loading; TS: torsional fatigue with static tension; the number in the parentheses is the stress ratio λ).

Once there are more cracks initiated, easier crack propagation can be expected as a result of crack coalescence. Figure 4.5 shows typical short cracks and a possibility of crack coalescence in this loading case. There can be also less resistance as stage I crack propagates from one ferrite grain to the other, since these ferrite grains are always well oriented. Further, no stage II crack branching has been observed in this loading case (Chapter III; Figure 3.14).

More damaging mechanisms are involved in crack initiation and crack propagation. This extra damage could explain why the fatigue life in this special loading case is often

overestimated, in spite of the large phase angle between shear and normal stresses on the critical plane.

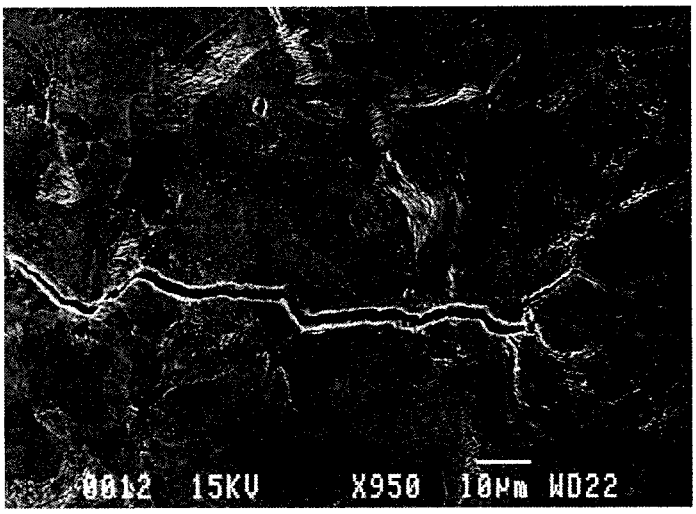

(a)

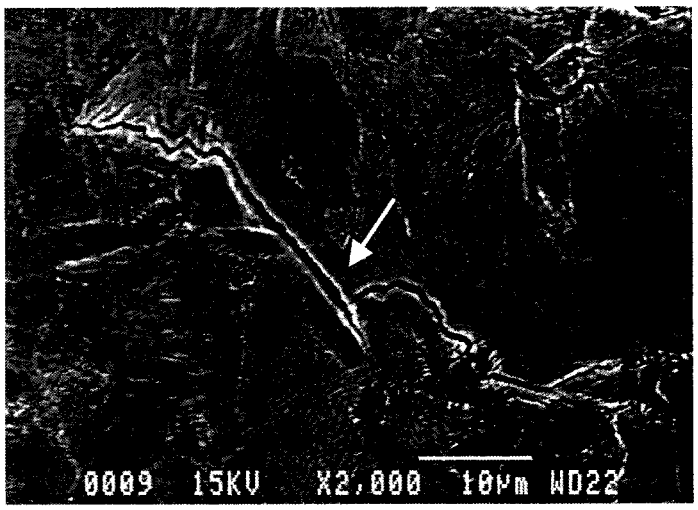

(b)

Figure 4.5 (a) A typical crack in the special loading case. (b) Possibility of coalescence between two cracks with different orientations (see arrow).

On the other hand, the KBM and Papadopoulos parameters underestimate the fatigue lives. In the KBM parameter, the normal strain term includes the effect of normal stress on the plane perpendicular to the critical plane. This normal stress is zero for this special loading case, while for axial loading, which is used to calibrate the constant k, it has the same value as the normal stress on the critical plane. Normal strain has more of a contribution in the special loading case than in axial loading. As a result, the fatigue lives appear to be underestimated for the special loading case. However, the physical justification for this normal stress is not clear. Attention should be paid to the Papadopoulos parameter that uses the average shear stress over all plane orientations. From a mathematical point of view, the Papadopoulos parameter is larger than the McDiarmid parameter in the special loading case. Then an underestimation rather than an overestimation could be obtained when the Papadopoulos parameter is used to predict fatigue life.

One should not forget that more damaging mechanisms are involved in the special loading case. The fatigue life in this loading case is not comparable with that in other loading cases. It is difficult to account for this difference in mechanisms in a single parameter-life correlation.

In engineering design, any overestimation of the fatigue life is not acceptable. Therefore, in order to obtain at least a conservative life prediction, it is recommended to perform tests in the worst case (the special loading case). A simple modification to McDiarmid parameter is suggested by introducing an Extra Damage Factor (EDF) to account for the extra damage in the special loading case:

$$EDF(\tau_{max}+k\sigma_n^{max})=f(N) \qquad (4.1)$$

EDF can be calibrated as the ratio between the fatigue strengths in torsion and in the special case. An important conclusion here is that the most damaging case must be tested for a reliable engineering design. EDF≈1.13 for our 1045 steel (Figure 4.2(b)).

4.7 Summary

Eight multiaxial fatigue life parameters have been selected for evaluation of their life prediction abilities for biaxial high cycle fatigue of ferritic-pearlitic steels. These parameters include stress-based, strain-based and energy-based parameters. Seven of them are critical-plane parameters, and one of them is an extension of von-Mises parameter. Two sets of high cycle fatigue data obtained from different authors are used for this evaluation.

The Tresca parameter cannot predict well biaxial high cycle fatigue life, due to the effects of normal stress (both amplitude and mean) on fatigue performance. With increasing normal stress amplitude or with a mean tensile stress on the critical plane, the fatigue performance decreases.

The GWP parameter accounts for the normal stress effect but it cannot consolidate fatigue lives under in-phase loading. However, the overall prediction errors are not larger than those obtained with the other parameters.

The other six parameters can predict fatigue life well under in-phase and low λ out-of-phase loadings. Fatigue lives under the other non-proportional loadings (high λ out-of-phase loading, special loading case and torsional fatigue with static tension) are often either underestimated or overestimated.

For the high λ out-of-phase loading, the McDiarmid, Fatemi-Socie and KBM parameters underestimate the fatigue lives. An attenuation of the normal stress/strain amplitude effect due to the large phase angle with shear stress on the critical plane can explain this underestimation. The Wang-Brown parameter, which considers this phase angle effect, gives a better life prediction. Both the Dang-Van and Papadopoulos parameters, which use the maximum hydrostatic stress, also work well for this loading case. In axial-

torsional fatigue, the hydrostatic stress includes the normal stress on the plane perpendicular to the critical plane, in addition to the normal stress on the critical plane. This can make a difference in the life correlation in comparison to the parameters using the maximum normal stress on the critical plane.

The maximum normal stress on the critical plane can fortunately account for both effects of normal mean stress and in-phase normal stress amplitude on the critical plane. Fatigue life for torsional fatigue with static tension can be relatively well predicted by the McDiarmid and Fatemi-Socie parameters. Parameters such as the KBM and Wang-Brown cannot account for tensile mean stress effects, since no mean stress/strain terms are used in these parameters. The parameters using the maximum hydrostatic stress (Dang-Van and Papadopoulos) overestimate the fatigue life for torsional fatigue with static tension. This implies that the static part of hydrostatic stress has a more important contribution to fatigue damage than the cyclic part.

The worst fatigue performance in the special loading case ($\phi=90^0$; $\lambda=0.5$) is attributed to more damaging mechanisms for crack initiation and propagation. This can explain the overestimations of fatigue lives in the special loading case. To obtain a conservative life prediction, McDiarmid parameter can be modified with an extra damage factor (EDF). Fatigue testing in the special loading case is needed to calibrate the EDF.

The above conclusions have been drawn assuming a purely elastic stress-strain response of the material. As discussed in section 4.4, plastic strain can be non-negligible for τ_{max} higher than 150MPa. In such conditions, a parameter using both stress and strain terms (e.g. Fatemi-Socie parameter) can be required to account for different stress-strain responses between in-phase and out-of-phase loadings. Additional cyclic hardening caused by the rotation of principal axes has been reported in the low cycle regime. For our stress-controlled tests in high cycle regime, a slight difference in γ_{max}-values could bring together fatigue lives obtained under in-phase and high λ out-of-phase loadings

(Figures 4.2 (g) and 4.3 (g)). In other words, the phase angle effect could be reflected in the stress-strain response of the material. This point should be clarified in a further study by recording strain paths resulting from different applied stress paths. However, higher hardening (or less softening) cannot account for the opposite effect observed in the special loading case ($\phi=90^0$; $\lambda=0.5$). More damaging mechanisms are involved when all grains are well-oriented (same shear amplitude in all plane orientations) and they result in a detrimental effect on fatigue performance.

CHAPTER V - BIAXIAL FATIGUE BEHAVIOR OF UNDERAGED AND OVERAGED 7075 ALUMINUM ALLOY: MATERIAL ANISOTROPY EFFECTS

5.1 Introduction

Many engineering materials exhibit some degrees of anisotropy. Basically, there are two kinds of material anisotropy: fibrous structure and crystallographic texture. Fibrous structures are caused by the alignment of second phase particles or inclusions or by elongated grains. A metal that has undergone a significant amount of plastic deformation will also develop preferred orientation or texture. Certain crystallographic planes and directions tend to align themselves with the directions of deformation.

The important consequence of fibrous structure is that mechanical properties may be different for different orientations of test specimen with respect to the fiber (working) direction. Both the crystallographic texture and the fibrous structure have effects on the fatigue properties of metals (Plumbridge, 1972). The influence of textures on the fatigue life may depend on the formed textures. The formation of fibrous structure generally decreases the fatigue resistance in the transverse direction. Leese and Marrow (1985) used transverse and longitudinal specimens to perform axial fatigue tests on hot-rolled 1045 steel. The results showed that the specimens cut parallel to the transverse direction have lower fatigue lives by a factor of 2 to 3 compared to the longitudinal specimens. This life difference is attributed to the anisotropy induced by sulfide inclusions along the longitudinal direction, which is then perpendicular to the stress axis. Socie (1985) conducted similar tests with Inconel 718. Specimens were also cut from longitudinal and transverse directions with respect to the forging direction. Unlike 1045 steel, the anisotropy effect on fatigue life was small.

There are relatively few studies on anisotropy effects on multiaxial fatigue (Lin and Nayeb-Hashmi, 1993; Verpoest et al, 1985; Nouailhas et al, 1993; Shantil et al, 1994, etc). These authors studied the material anisotropy effects from two aspects: 1) by comparing the fatigue performance in different test orientations in anisotropic material (e.g. Kiyotsugu et al, 1976; Lin and Nayeb-Hashmi, 1993); and 2) by comparing the fatigue behavior of isotropic and anisotropic materials (Verpoest et al, 1985). Kiyotsugu et al (1976) found that different orientations of steel specimens with respect to the rolling direction resulted in different fatigue cracking mechanisms in torsional fatigue, since cracks preferred to follow the rolling direction. Therefore, fatigue lives were different in different specimens. Lin and Nayeb-Hashmi (1993) found that the orientation of the specimen axis with respect to fibers did not influence the cracking behavior of Al-6061-T6, but did influence the fatigue life. Then they proposed a shear-type parameter incorporating material anisotropy effects. Verpoest et al (1985) found that the biaxial fatigue behavior was different in isotropic and anisotropic carbon steels. In anisotropic material, mode II cracks appeared as soon as $\lambda \geq 0.5$, while mode I cracks appeared in isotropic material whatever the stress ratio. Material anisotropy effects on the multiaxial fatigue behavior are complex, and they are strongly dependent on material microstructure and applied loading conditions. Life prediction for anisotropic material is a challenge.

In this study, focus is placed on the effects of material anisotropy on fatigue mechanisms and fatigue life under different loading conditions. Underaged and overaged 7075 aluminum alloys, in which anisotropy can be at least caused by fibrous structures, are tested under three loading conditions: axial fatigue, torsional fatigue and torsional fatigue with different levels of static tensile loads. The fatigue cracking behavior in underaged and overaged material in different loading cases will be investigated. Based on the understanding of fatigue cracking mechanisms, we try to find a parameter to correlate the fatigue lives for different loading conditions in these anisotropic materials.

5.2 Experiments

5.2.1 Material

A high strength 7075 aluminum alloy, an often employed aircraft structural material, was used in this study. It was produced by Alcoa as a rod of 1.5 inch (38.1mm) in diameter in the T7351 temper condition. The chemical composition and the tensile properties are shown in Tables 1 and 2, respectively. Carter et al (1984) and Suresh (1993) found that, for 7000 series aluminum alloys, underaged and overaged materials have different fatigue behavior. In underaged material, the precipitates are coherent with the matrix, and are shearable by the dislocations. Planar slip behavior results in underaged condition. Hence, in near-threshold axial fatigue cracking, the crack path is tortuous and serrated; it follows the crystallographic planes (slip planes). In overaged condition, the precipitates are incoherent with the matrix. They are non-shearable by the dislocations that loop or by-pass them. Multiple slip is promoted in this heat treatment condition. As a result, the near-threshold cracking path is straight. These effects of slip characteristics on fatigue failure mode reminded us the so-called tensile failure and shear failure defined by Socie (1987). It seems that under axial fatigue, underaged material shows Mode II (shear) failure and overaged material shows Mode I (tensile) failure. Motivated by these findings, Initially this material was chosen to investigate if underaged and overaged conditions can also result in Mode I and Mode II failures under torsional fatigue.

Table 5.1 Chemical composition of 7075 aluminum alloy (in weight %).

	Si	Fe	Cu	Mn	Mg	Cr	Zn	Ti	Others	Others	Al
Max	0.40	0.50	2.0	0.30	2.9	0.28	6.1	0.20	0.05	0.15	Remain
Min			1.2		2.1	0.18	5.1		Each	Total	

Table 5.2 Tensile properties of 7075 aluminum alloy (T7351).

	U.T.S. (MPa)	T.Y.S. (MPa)	% Elongation	%Area Reduction
Max	510	438	15.0	39.1
Min	508	436	14.0	39.1

Two heat treatment conditions, underaged and overaged, are used in this study. The overaged condition corresponds to the raw material. The T7351 temper is developed to obtain a microstructure with a good stress-corrosion resistance. The underaged condition has been obtained by reheat-treating the T7351 tempered material. To find out an appropriate aging condition, after solution heat treatment, aging tests at 120^0C were first carried out to obtain the aging curve shown in Figure 5.1. Then, the underaged conditions were determined to obtain a hardness similar to that under T7351 temper (HRB≈ 85). This could eliminate the material strength influence on the fatigue behavior. The heat treatment is chosen as following: (1) Solution heat treating the T7351 tempered material at 490°C for 2 hours; (2) Quenching in cold water with minimum delay; (3) Aging at 120°C for 4 hours.

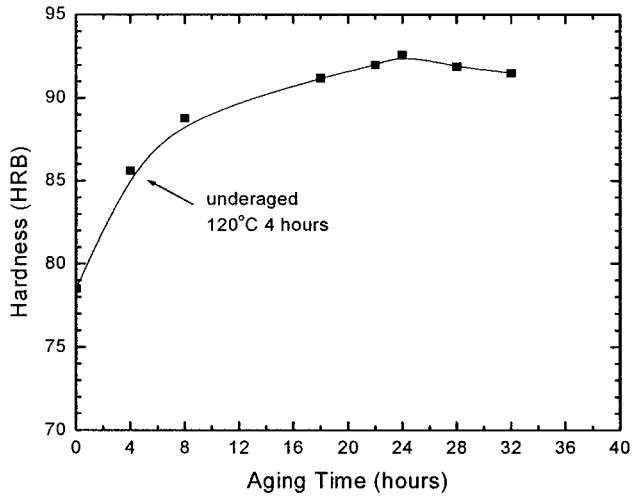

Figure 5.1 Aging curve of 7075 aluminum alloy at 120^0C,

Metallographic samples were cut along two directions in both the underaged and overaged materials: longitudinal direction (the rolling direction) and transverse direction (normal to the rolling direction). As shown in Figures 5.2 and 5.3, in both ageing conditions, the grains are elongated along the rolling direction (see arrows), and are approximately equiaxed in the transverse direction. Many inclusion strings can also be found along the rolling direction. Anisotropy in both underaged and overaged material is caused by elongated grains and aligned inclusions. In both materials, the grain size is 60-70μm and the grain aspect ratio is 8:1. These data were determined using the method for anisotropic material designated in ASTM standard E112.

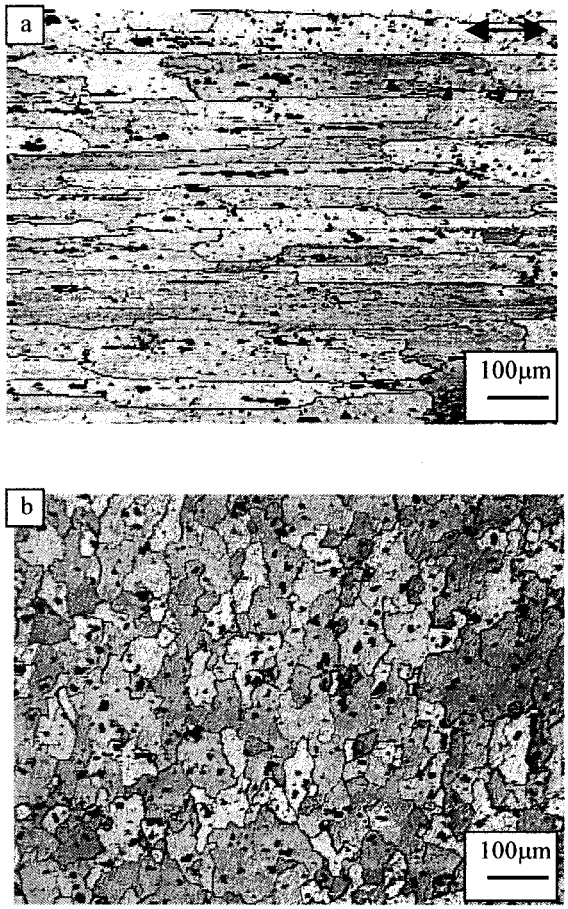

Figure 5.2 Microstructures of underaged 7075 aluminum alloy in (a) longitudinal section and in (b) transverse section (Etchant: Keller's regent).

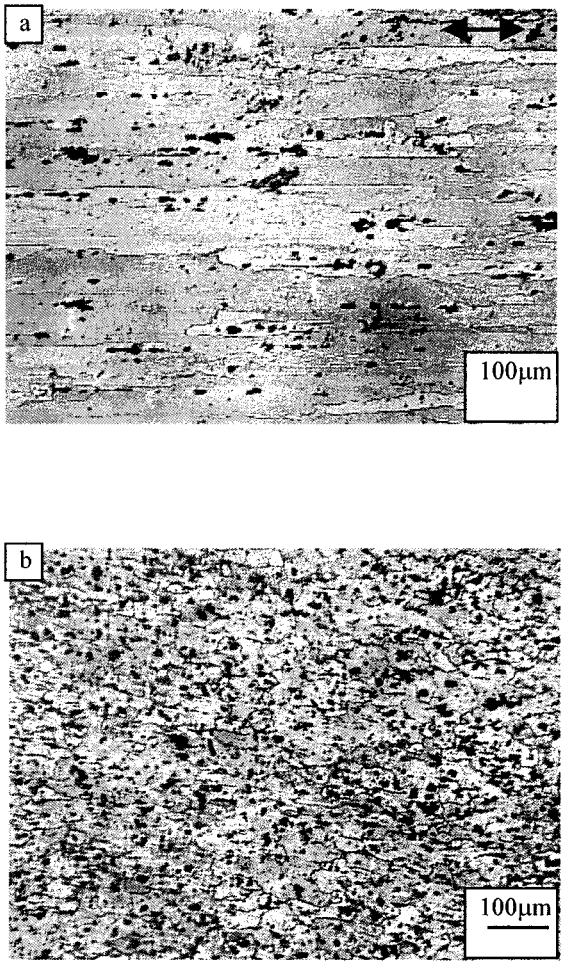

Figure 5.3 Microstructures of overaged 7075 aluminum alloys in (a) longitudinal section and (b) transverse section (Etchant: Keller's regent).

5.2.2 Specimen geometry

A thin-walled tubular specimen was used. The advantage of thin-walled tubular specimen is the uniform stress and strain distribution within the cross section. The specimen geometry is shown in Figure 5.4. To obtain a good finish on the interior surface of the specimen, the hole was honed after being drilled and reamed. The external surface was polished up to 600 grit to eliminate the machining scratches. The specimen was finally chemical polished at 85°C in a solution of 75%H_3PO_4 + 20%H_2SO_4 + 5%HF. A satisfactory surface finish was obtained by this procedure. Further, the grain boundaries can be clearly seen under microscope after chemical polishing. This is beneficial for understanding the interaction of the crack path with the grain boundaries.

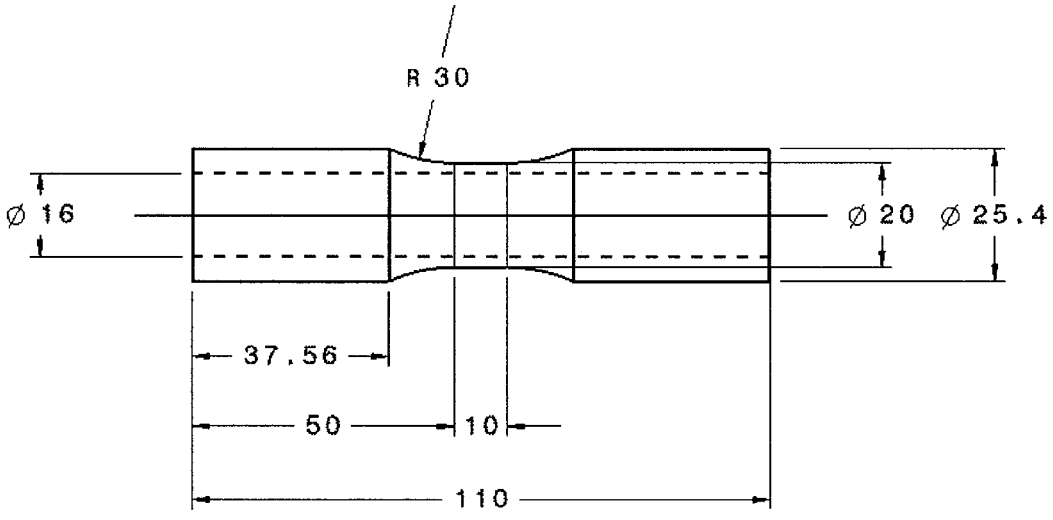

Figure 5.4 The geometry of thin-walled tubular specimen (units: mm).

5.2.3 Fatigue tests

The fatigue tests were performed using the same Instron 8521 axial-torsional servohydraulic machine as that described in section 3.2.3. Three loading cases are employed: axial fatigue, torsional fatigue, and torsional fatigue with different levels of static tension. Through these basic tests, we can get some understandings of multiaxial fatigue behavior. It is of interest to see how the static tension load influences the fatigue mechanism in the anisotropic 7075 aluminum alloy. All tests are stress controlled. The cyclic loading is a fully reversed sinusoidal waveform. The tests are performed in laboratory air at room temperature. The detailed test program and the fatigue life results are listed in Table 5.3.

Table 5.3 Fatigue tests and life data of underaged and overaged 7075 aluminum alloys

Heat Treatment	Loading Cases	Specimen	τ_{max} (MPa)	σ_m (MPa)	Fatigue Life Number of Cycles (N)
Overaged	Axial fatigue	AL7A7	100	0	14,314
		AL7A3	70	0	57,449
		AL7A2	75	0	66,926
		AL7A4	70	0	93,412
		AL7A5	50	0	268,701
		AL7A6	40	0	>8,000,000
	Torsional fatigue	AL7T2	100	0	89,240
		AL7T1	100	0	105,525
		AL7T4	60	0	331,497
		AL7T5	60	0	385,413
		AL7T3	70	0	624,613
	Torsional fatigue with static tension	AL7TS2	100	100	36,636
		AL7TS3	100	60	49,055
		AL7TS1	60	60	259,509
Underaged	Axial fatigue	ALUA5	100	0	74,214
		ALUA2	70	0	144,684
		ALUA1	70	0	316,663
		ALUA3	60	0	569,061
		ALUA4	50	0	>4,000,000
	Torsional fatigue	ALUT2	100	0	35,000
		ALUT1	100	0	66,438
		ALUT3	70	0	126,829
		ALUT4	60	0	386,950
	Torsional fatigue with static tension	ALUTS5	100	165	24,923
		ALUTS3	100	60	30,000
		ALUTS4	100	135	31,220
		ALUTS2	100	100	33,108
		ALUTS1	50	50	703,883

5.3 Observations of fatigue cracking mechanisms

Before discussing the fatigue life correlations between the different loading cases, it is important to understand the fatigue cracking mechanisms. The fatigue cracking process was investigated at different levels by surface crack monitoring by the replica technique and by macroscopic and microscopic observations of fracture surfaces. Replicas were taken intermittently during fatigue test at regular time intervals. The replicas were observed under the SEM after coating with a thin gold-palladium film. From this observation, information such as crack initiation, cracking path, crack length with respect to life ratio as well as crack densities can be obtained. These replicas were also observed backwards under the SEM to trace the cracking process of the failure crack. The macroscopic observation of fracture surfaces can provide information on crack initiation sites, the macroscopic crack path with respect to specimen axis, and macroscopic features on the fracture surfaces. The micro-fractographic features under different stress states in different materials can be compared in order to understand the micro-mechanisms of fracture.

5.3.1 Surface crack evolution

5.3.1.1 In overaged material

The crack initiation and propagation processes in overaged 7075 aluminum alloy under axial fatigue are shown in Figure 5.5(AL7A4, σ_0 =140MPa, N_f=57449 cycles). In Figure 5.5 (a), no crack is observed on the replica taken at 35% of total life. Figure 5.5(b) shows two very small cracks initiated at inclusions at 52% of total life. Several cracks are clearly observed in Figure 5.5 (c) at 70% of total life. Within one grain, the cracks are almost straight. The small tortuousness within the grain could be attributed to the effects of sub-grain boundaries. The cracks appear more or less perpendicular to the specimen axis. These early cracks can be tensile cracks or case B shear cracks, since there is an

infinity of maximum shear planes under axial fatigue. Some case A shear cracks, inclined at 45^0 from specimen axis, were also observed. It is difficult to identify the so-called stage I - II transition, similar to axial fatigue in 1045 steel.

This observation shows that crack initiation occurs at about 50% of total life. Many crack initiation sites are observed in this specimen; then crack coalescence is also observed. The observations show that crack initiation is not always at inclusions, and that crack propagation can change direction from one grain to the other.

Figure 5.6 shows the surface crack evolution in overaged aluminum alloy under torsional fatigue (AL7T2, τ_0=100MPa, N_f=89,240 cycles). In Figure 5.6 (a), a small crack was found to nucleate at an inclusion, then the crack propagated longitudinally (Figure 5.6 (b)). It is noticed that the crack does not propagate along the grain boundary, which means the fracture here is transgranular. As long as 2mm, the crack is still longitudinal (Figure 5.6(c)). At the very final stage of life, some stage II branching can be found. In this specimen, no crack occurs along the transverse plane (the other maximum shear plane).

This is different from what observed in 1045 steel, in which crack initiation and stage I propagation can occur on both maximum shear planes. The strong anisotropy of the 7075 aluminum alloy should be responsible for this kind of cracking behavior. The material anisotropy makes the longitudinal shear plane weaker and less resistant to cracking as compared with the transverse shear plane. However, when the shear stress level is low, cracks can initiate and propagate on the transverse maximum shear plane.

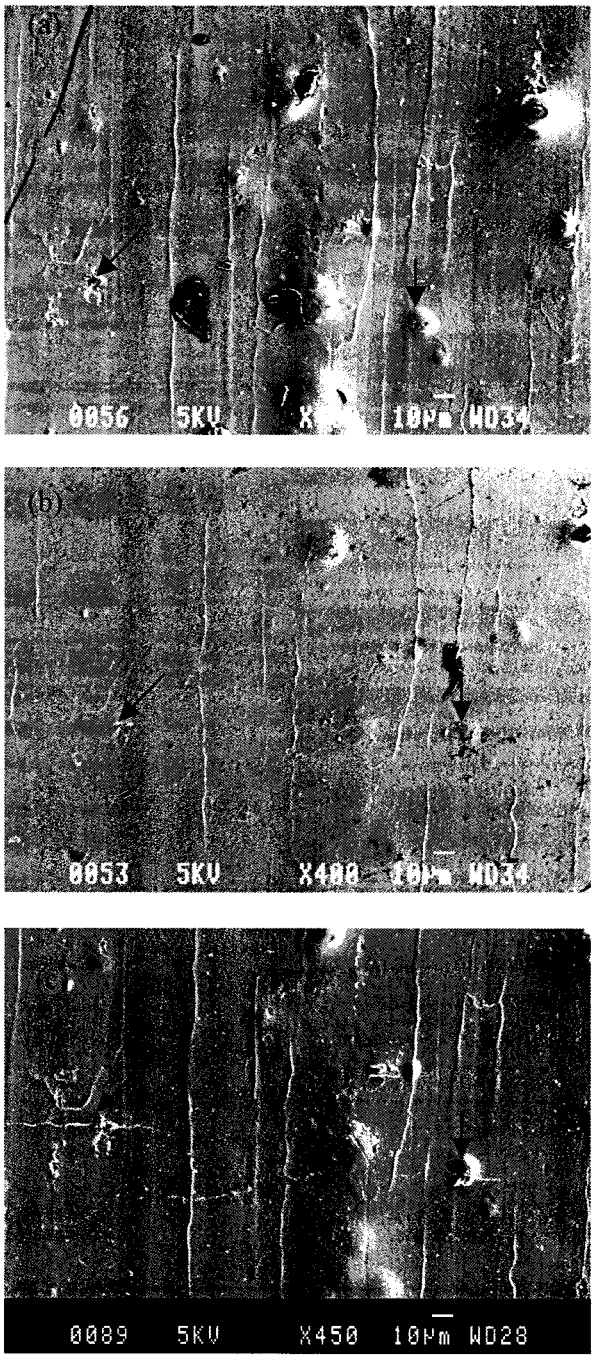

Figure 5.5 Axial fatigue crack evolution in overaged 7075 aluminum alloy observed from replicas under SEM (AL7A4, σ_0=140MPa, N_f=57,449 cycles.). Arrows show two crack initiation sites. Specimen axis is vertical in each photo. (a) N=20,000 cycles. (b) N=30,000 cycles. (c) N=40,000 cycles.

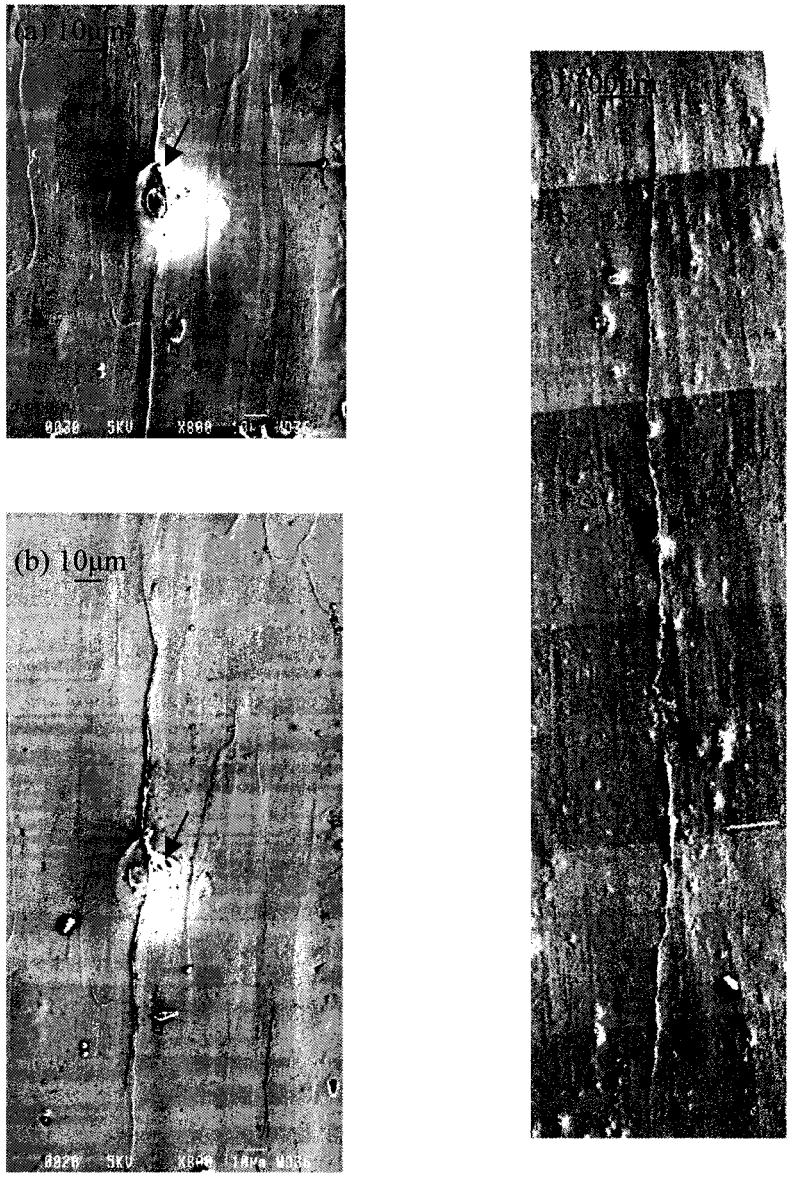

Figure 5.6 Surface crack evolution in overaged 7075 aluminum alloy under torsional fatigue (AL7T2, τ_0=100MPa, N_f=89,240 cycles) observed on replicas under SEM. (a) N=20,000 cycles. (b) N=30,000 cycles. (c) N=60,000 cycles. Specimen axis is vertical in each photo. Crack initiation site is pointed by arrow.

In Figure 5.7 (AL7T5, τ_0=60MPa; N_f=385,431 cycles), both horizontal and vertical shear cracks are observed (specimen axis is vertical). In this specimen, horizontal shear cracks predominate, and their coalescence and 45^0-branching are evident. It is noted that horizontal shear cracks are not necessarily nucleated at inclusions, unlike longitudinal shear cracks for which initiations are always associated with inclusions.

Under torsional fatigue with static tension, even if the cyclic shear stress level is high, when there is a superimposed static tensile load, the main cracks initiate and propagate on the transverse maximum shear plane. Few secondary cracks are observed in the longitudinal direction.

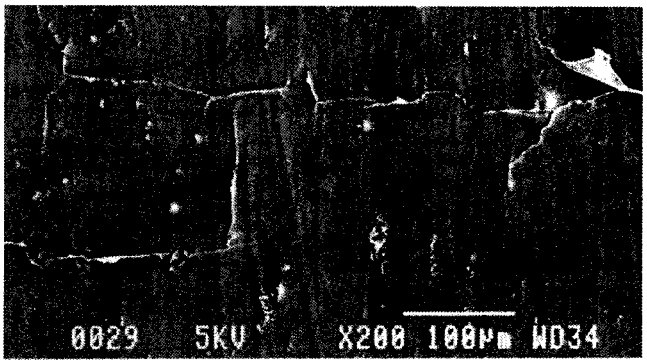

Figure 5.7 Cracks in overaged 7075 aluminum alloy under torsional fatigue at low shear stress level (AL7T5, τ_0=60MPa, N_f=385,431 cycles), observed on a replica taken at 78% of total life. Specimen axis is vertical.

5.3.1.2 In underaged material

The surface cracking process under axial fatigue of underaged material is not very different from that of overaged material, except that crack initiation sites are relatively few in underaged materials. This can be understood from the different slip characteristics of the two materials. In overaged material, non-shearable precipitates promote uniform deformation and then multiple initiations. In underaged material, shearable precipitates promote localized deformation. Hence initiation sites are less numerous in this material as compared with the overaged material.

The cracking process in underaged material under torsional fatigue is shown in Figure 5.8 (ALUT2, τ_0=100MPa, N_f=35,000). No crack is observed at 10,000 cycles. At 15,000 cycles (43% of total life), a crack about 0.5 mm in length was observed, and it is believed to nucleate at the inclusion. The crack is more or less longitudinal. Under high magnification, it was found that the crack did not follow the grain-boundary as the propagation path, which means the fracture is transgranular in this material under torsional loading. The crack continued propagating longitudinally as shown in Figure 5.8(c) (85% of total life), until the final failure.

In this specimen, other longitudinal cracks are also observed, and their initiations are also related to inclusions. No crack branching and no transverse cracks are observed in this specimen. However, as in overaged material, transverse cracks are observed under torsional fatigue with low stress level, such as τ_0=60MPa.

Under torsional fatigue with static tension, cracking can occur on transverse maximum shear planes, only when the superimposed static tensile load is high enough. As shown in Figure 5.9, at the same maximum shear stress amplitude of 100MPa, when the tensile load is 100MPa, failure crack is still longitudinal (Figure 5.9(a)). However, when tensile load is as high as 165MPa, the final crack is transverse (Figure 5.9(b)), despite

longitudinal shear cracks also being observed. This is different from that observed in overaged material, where transverse shear cracks predominate at lower static tensile loads. This observation implies that the anisotropy effect on torsional fatigue is stronger in underaged material than in overaged material. Again, the transverse cracks are not always observed to be related to inclusions.

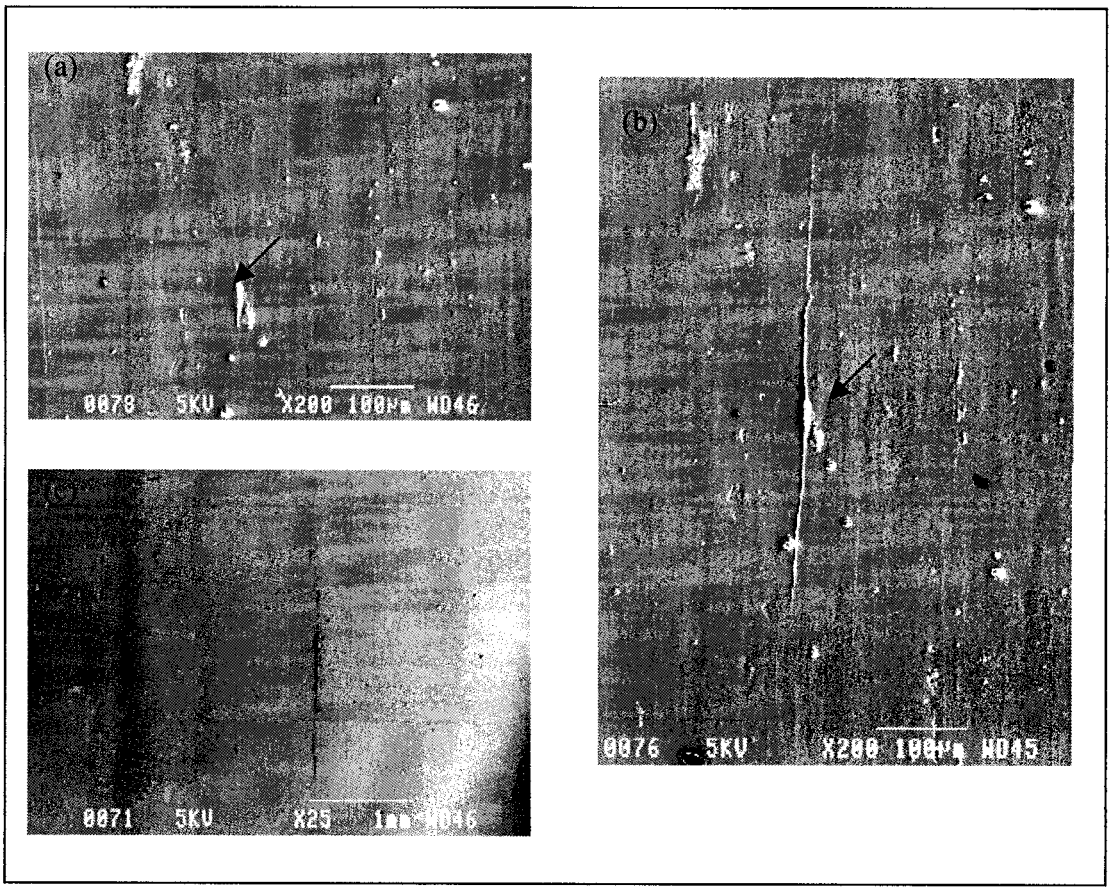

Figure 5.8 Crack evolution in underaged 7075 aluminum alloy under torsional fatigue (ALUT2, τ_0=100MPa, N_f=35,000 cycles), observed on replicas under SEM. (a) N=10,000 cycles. (b) N=15,000 cycles. (c) N=30,000 cycles. Specimen axis is vertical in each photo. Crack initiation site is indicated by arrows.

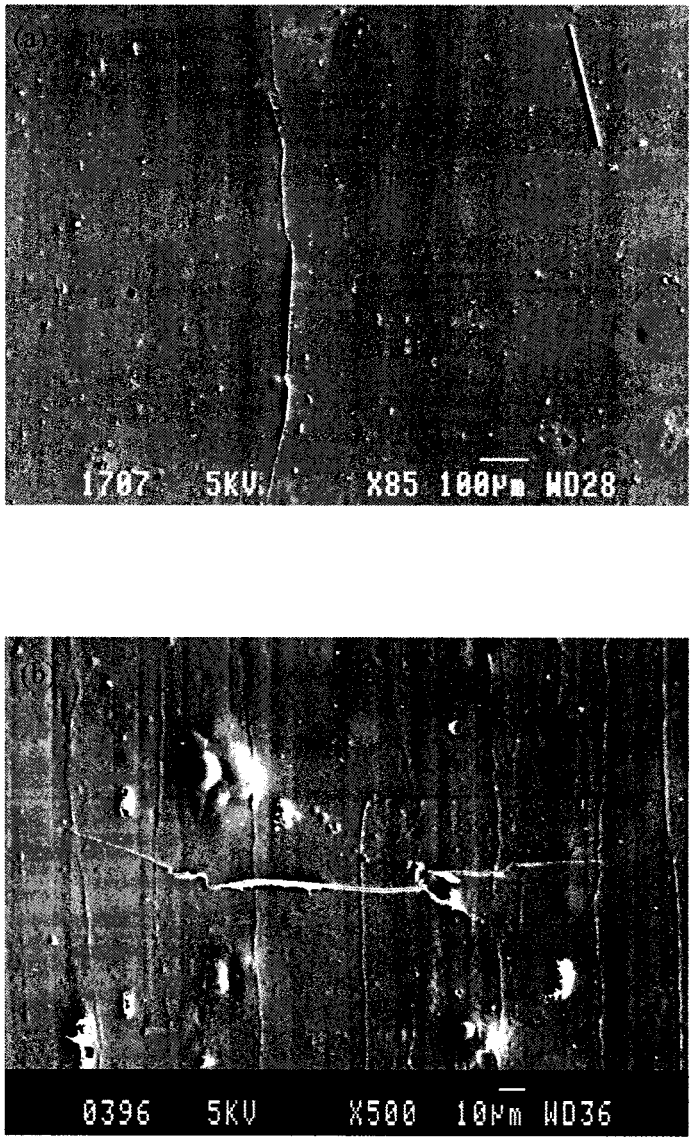

Figure 5.9 Cracking behavior of underaged 7075 aluminum alloy under torsional fatigue with static tensile load, observed on replicas under SEM. (a) τ_0 =100MPa, σ_m=100MPa. (b) τ_0=100MPa, σ_m=165MPa. Specimen axis is vertical in each photo.

The observation of the surface cracking process can be summarized as follows.

- For axial fatigue, both underaged and overaged materials behave similarly. Final cracks are more or less horizontal, as those observed in 1045 steel. Crack initiations are often at inclusions. Overaged materials have multiple initiation sites, while initiation sites for underaged materials are relatively few.
- For torsional fatigue, at high stress level, both underaged and overaged materials have longitudinal shear cracks. No transverse shear crack is observed. Stage II crack branching occurs at the very end of life in overaged material; it never occurs in underaged material. When the shear stress level is low, transverse shear cracks appear in both materials.
- For torsional fatigue with static tension, transverse shear cracking predominates when a low static tensile load is applied to the overaged material. In underaged material, this happens only when the static tensile load reaches a high level.
- Longitudinal shear cracks always nucleated at inclusions, while transverse shear cracks did not necessarily nucleate at inclusions.

5.3.2 Surface crack length versus life ratio

Surface crack lengths measured from replicas on the underaged and overaged materials are plotted against life ratio for different loading conditions and materials (Figure 5.10). Crack nucleate soon (about 20% of life) for pure torsional fatigue and for torsional fatigue with static tension, when the longitudinal shear cracking occurs. For torsional fatigue with high static tension (transverse shear cracking), crack initiation occurs at a higher life ratio. For axial fatigue, crack initiation is the slowest among the three loading conditions. Surface cracking behaviors can well reflect different mechanisms in different conditions. The cracking behavior under axial fatigue in 7075 aluminum alloy resembles that in 1045 steel.

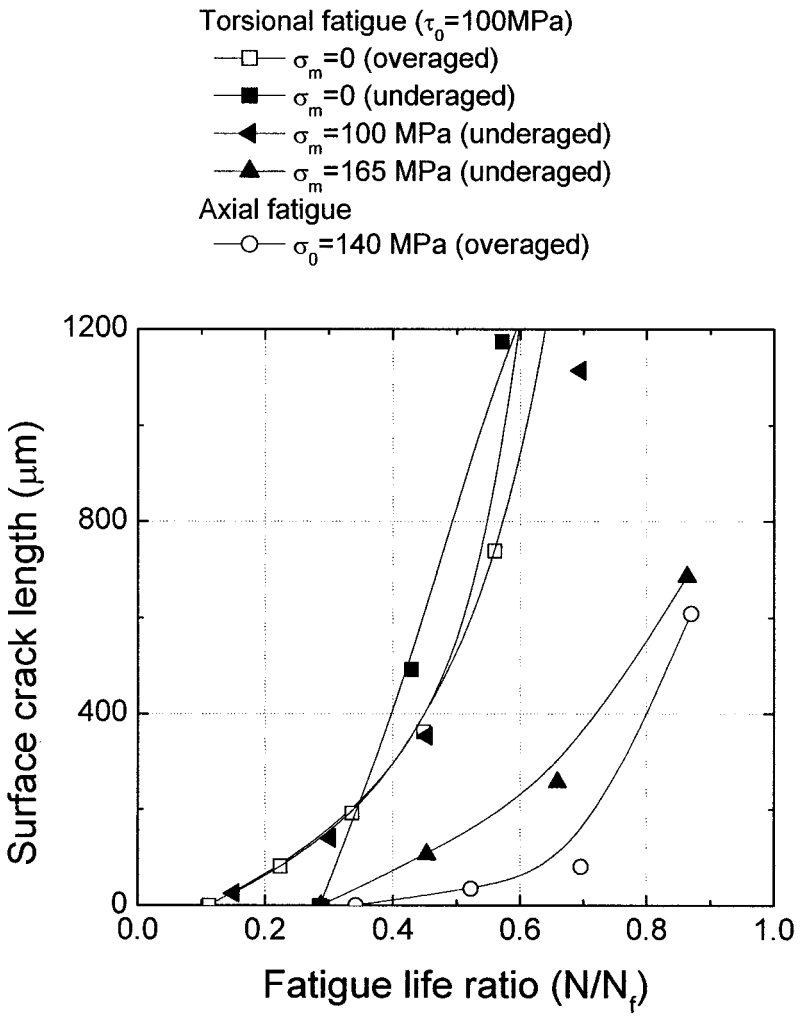

Figure 5.10 Surface crack length plotted against fatigue life ratio for different loading conditions in underaged and overaged materials (solid symbols for underaged material, and open symbols for overaged material).

5.3.3 Fracture surface observations

5.3.3.1 Macroscopic observations

Microscopic fracture plane orientations as well as the features on these planes were observed and compared in the different material-loading conditions. In axial fatigue, the fracture in 7075 aluminum alloys resembles that in 1045 steel. The macro-cracks for axial fatigue are basically normal to the specimen axis in both underaged and overaged materials. The fracture surface of the underaged material is flatter than that of the overaged material. A number of multiple crack initiation sites are macroscopically observed in the overaged material; whereas, there is only one macroscopic initiation site in the underaged material. This observation coincides with those made on the replicas. The rougher fracture surface for overaged material can be associated with crack coalescence from multiple initiation sites.

Under torsional fatigue, when the stress level is high, all cracks are longitudinal in both materials. Stage I cracks can be as long as tens of millimeters, and as deep as the wall thickness of the tubular specimen. There is a little stage II branching at the very end of cracking in the overaged material (Figure 5.11(a)); whereas, the cracks remain always longitudinal in the underaged condition (Figure 5.11 (b)). When the stress level is low, the cracks tend to propagate on the transverse maximum shear planes in both materials, before stage II branching (Figure 5.11(c)). Stage I cracks are shorter compared to those at the high shear stress level. Many longitudinal lines are observed on the longitudinal fracture surfaces in both the underaged and overaged materials. This feature was not observed in the isotropic 1045 steel. The elongated grain structures in 7075 aluminum alloys could be responsible for these longitudinal lines on the fracture surfaces under torsional fatigue.

Under torsional fatigue, a static tensile load can change the cracking mechanisms in both materials. In the underaged material, when there is a superimposed tensile load, cracking occurs on transverse maximum shear planes. In the overaged material, transverse cracking occurs only when the tensile load is high enough (Figure 5.11(d)). The stage I crack can be as long as tens of millimeter and go through the entire wall thickness of the specimen.

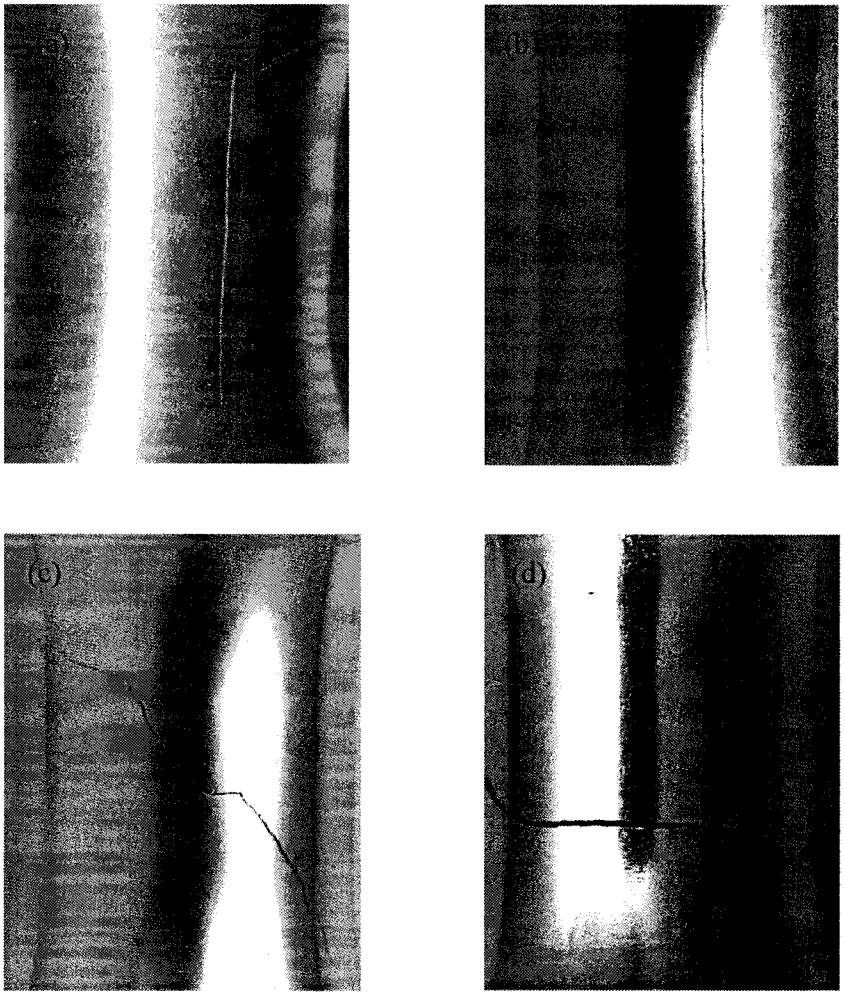

Figure 5.11 Macro-fractures of underaged and overaged 7075 aluminum alloys under different loadings. (a) Overaged, torsional fatigue, τ_0=100MPa. (b) Underaged, torsional fatigue, τ_0=100MPa. (c) Underaged, torsional fatigue, τ_0=60MPa. (d) Underaged, torsional fatigue with static tensile load, τ_0=100MPa, σ_0=165MPa.

5.3.3.2 Microscopic observations

The fracture surfaces near the initiation sites in both the underaged and overaged alloy under axial fatigue present crystallographic features (Figure 5.12). The cracks in both materials initiate at inclusions (highlighted by arrows). Fracture surface within the first grain is flatter in the underaged material than that in the overaged material. The different slip characteristics in these two materials can cause this difference between the fracture surfaces. In the underaged material, the precipitates are coherent with the matrix and can be sheared by dislocations. Thus, dislocations can slip on a single set of planes, which result in a flatter fracture surface. In the overaged material, the precipitates are incoherent with the matrix and the dislocations can only by-pass the precipitates. As a result, the striations appear closer to the initiation site in overaged material as compared with the underaged material. Fracture surfaces do not reveal much difference between fracture mechanisms in the underaged and the overaged materials, although more crystallographic features are observed in the underaged material. In both materials, the fractographic features from initiation towards propagation direction are crystallographic facets, crystallographic facets mixed with striations, striations and striated dimples.

Under torsional fatigue, fractographic features are quite different in the underaged and overaged materials, although some common features such as striations were observed in both materials. In underaged material, the striations are always mixed with crystallographic facets. In overaged material, regions with pure striations are observed. Further, a very crystallographic fracture (Figure 5.13(a)) is predominant on the entire fracture surface in underaged material. That could be caused by the microstructure feature in the underaged material (the shearable precipitates) and by the loading condition (torsion fatigue), and both promote shear damage. Figure 5.13 (b) shows the early fracture in the overaged material, which is not so crystallographic as in Figure 5.13 (a). The crystallographic features in underaged material leads to a lower torsional fatigue life at the same shear stress amplitude as compared with overaged material.

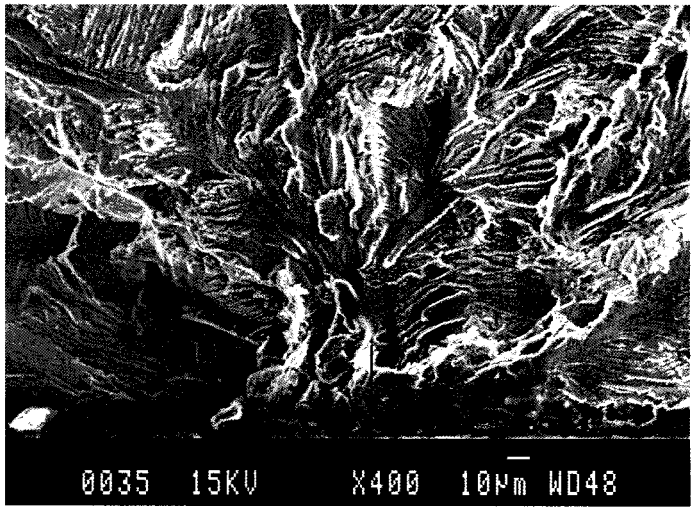

(a)

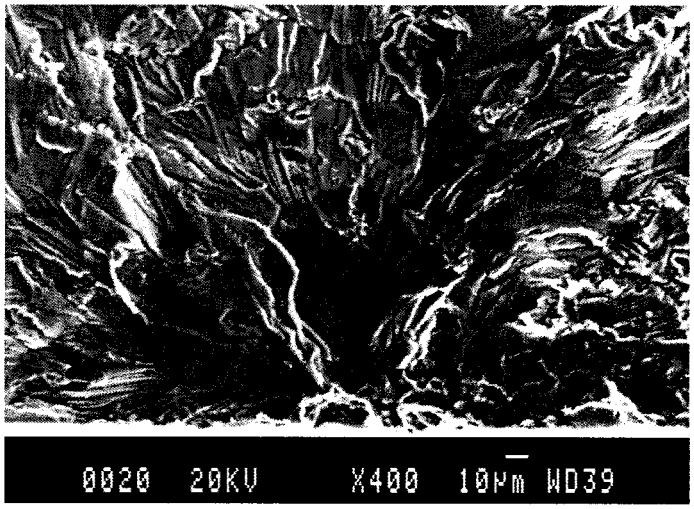

(b)

Figure 5.12 Fractographic features in 7075 aluminum alloy under axial fatigue. (a) Underaged material. (b) Overaged material.

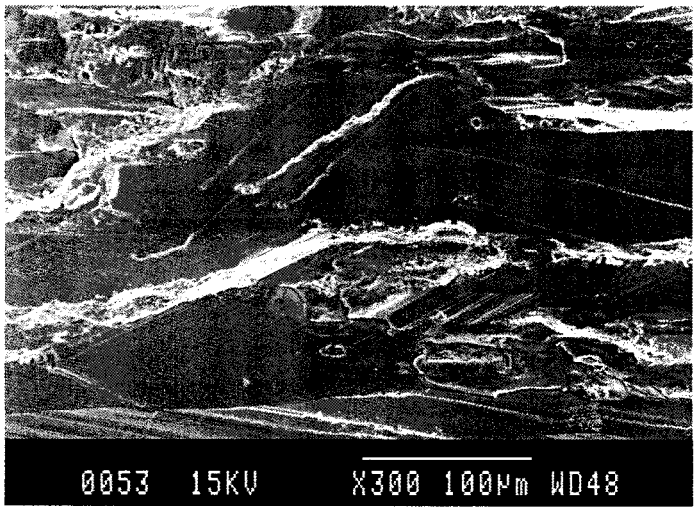

(a)

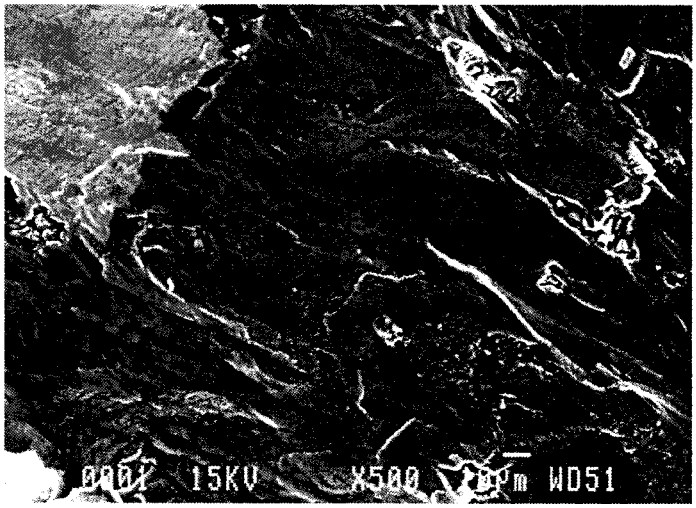

(b)

Figure 5.13 Fractographic features in 7075 aluminum alloy under torsional fatigue. (a) Underaged material. (b) Overaged material.

5.4 Fatigue life

5.4.1 Overaged material

In Figure 5.14, fatigue life data for overaged 7075 aluminum alloy are plotted against the maximum shear stress amplitude (Tresca criterion). At the same maximum shear stress amplitude, torsional fatigue life is longer than axial fatigue life. Further, a static tensile load decreases torsional fatigue life. This result is similar to that obtained in 1045 steel. It is generally accepted that both normal stress amplitude and normal (tensile) mean stress on the maximum shear plane can assist the cracking process and reduce the fatigue life. The McDiarmid parameter would be appropriate in predicting the fatigue life of this material.

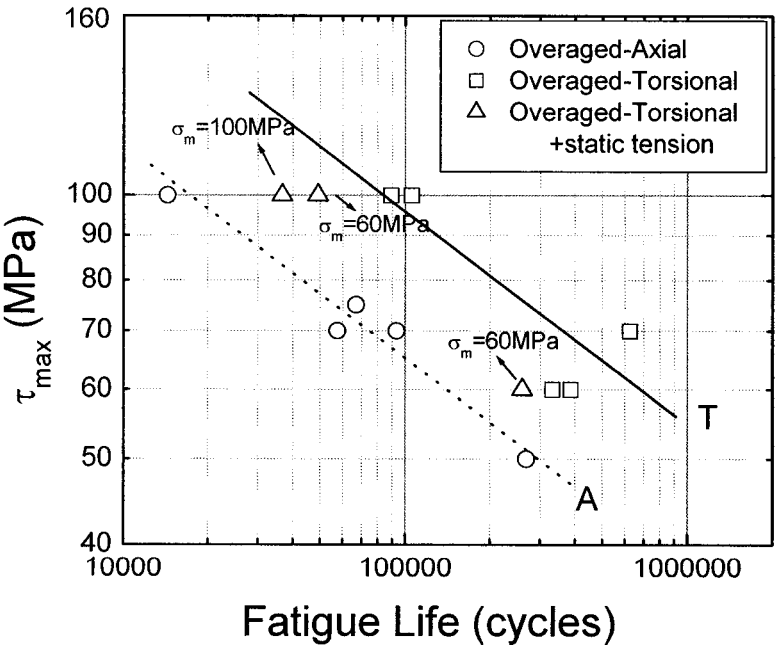

Figure 5.14 Fatigue life data of overaged 7075 aluminum alloy plotted against maximum shear stress amplitude.

5.4.2 Underaged material

Figure 5.15 shows the fatigue life data plotted against the maximum shear stress amplitude for underaged material. The opposite trend is observed in this material. Axial fatigue has a slightly higher life than torsional fatigue at the same τ_{max}. This result is not reported in the literature. Besides the stress state effect, the material properties play a fundamental role on the fatigue damage process. This worse fatigue performance in underaged material under torsional fatigue is attributed to the material anisotropy. Further, a static tensile stress superimposed on torsional fatigue does not have an important effect on the fatigue life. A slight decrease in fatigue life can be observed only when static tensile stress is high enough (σ_m=165MPa).

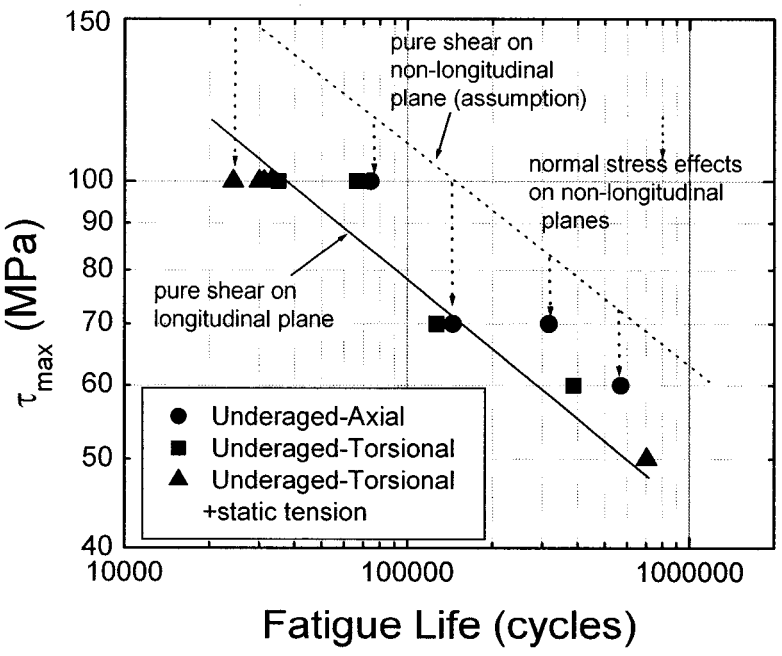

Figure 5.15 Fatigue life data of underaged 7075 aluminum alloy plotted against maximum shear stress amplitude (the values of the static tensile load σ_m refer to Table 5.3).

5.4.3 Static tensile stress effects

To illustrate the effects of the superimposed static tensile stress on the torsional fatigue life of the underaged and overaged materials, the torsional fatigue lives obtained at the same cyclic shear stress (τ_0=100MPa) are plotted against the static tensile stress (Figure 5.16). In general, a superimposed static tensile load decreases the torsional fatigue life. Tensile mean stress makes the fatigue performance worse on the transverse shear planes. This is true for the overaged material. However, torsional fatigue life of underaged material remains approximately constant until the static tensile stress reaches 165MPa. This means that the anisotropy effects are more significant in underaged material than in overaged material.

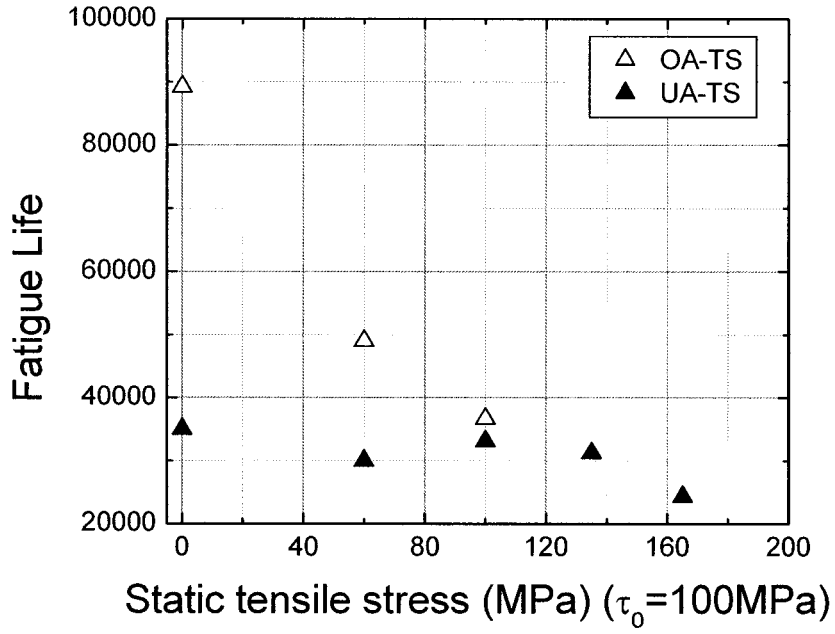

Figure 5.16 Effects of the static tensile stress on the torsional fatigue life of underaged and overaged 7075 aluminum alloys. The applied torsional stress amplitude is τ_0=100MPa for all data points.

5.5 Discussion and analysis

5.5.1 Anisotropy effects and materials

Anisotropy effects on the fatigue crack behavior are observed during torsional fatigue of both the underaged and overaged materials. No transverse shear crack is observed at high stress level. This is understandable since under torsional fatigue the weak plane (longitudinal plane) coincides with one of the two maximum shear planes. Therefore, the longitudinal shear plane is the weakest plane and damage occurs on this plane. Under axial fatigue, there is no shear stress acting on the plane weakened by material anisotropy. The material anisotropy effects are not observed in axial fatigue.

The material anisotropy effects are different in the underaged and overaged materials under fatigue loading. First, in the underaged material, shear cracks appear along the longitudinal direction in torsional fatigue (at high stress level), even when there is a superimposed static tensile load of 100 MPa (Figure 5.9), while cracking tends to occur on the transverse shear plane in the overaged material once there is a static tensile load of 60 MPa. As a result, a superimposed tensile load has little influence on torsional fatigue strength in the underaged material, while it decreases the torsional fatigue strength of the overaged material (Figure 5.16). Secondly, at the same shear stress amplitude, the torsional fatigue life is lower than that of axial fatigue in the underaged material, while the overaged material behaves like an isotropic material. All of these results indicate that material anisotropy effects (weakness of longitudinal plane) are more significant in the underaged material than in the overaged material.

The underaged and overaged materials have approximately the same strength, the same grain structure and the same inclusions. One difference elated to their microstructure is that they have different slip characteristics. In underaged material, the precipitates are coherent with the matrix and are shearable by dislocations, while in overaged material the

precipitates are incoherent with the matrix and are non-shearable. Then underaged material deforms preferably by single-slip and overaged material deforms preferably by multiple-slip (Carter et al, 1984; Suresh et al, 1984). As a result of the different slip characteristics, a crystallographic fracture is favored in the underaged material. The difference in the slip characteristics of the underaged and overaged materials can explain the low fatigue performance of the overaged material under axial fatigue. In overaged material, multiple crack initiations sites and crack coalescence due to the multiple slip accelerate the cracking process.

The other difference between the microstructures of the two materials is that there is a preferred orientation (crystallographic texture) in the underaged material but not in the overaged material. Figure 5.17 shows the X-ray diffraction patterns of the overaged material on the longitudinal and transverse planes. The two patterns are identical. There is no preferred orientation in this material. Different X-ray diffraction results are obtained in the underaged material. Figure 5.18 shows the X-ray diffraction patterns of the underaged material on the longitudinal and transverse planes. The X-ray strength resulting from the diffraction by {111} plane is much higher on the longitudinal plane than that on the transverse plane. The {111} planes are oriented parallel to the specimen axis. The {111} planes are the slip planes. Under torsional fatigue, these slip planes coincide with the longitudinal maximum shear plane and help longitudinal shear cracking. Therefore, one can understand why an easy crystallographic fracture occurs in the underaged material under torsional fatigue. The combination of (111) texture and planar slip enhances the material weakness along the longitudinal direction. This unique crystallographic fracture is responsible for the low torsional fatigue performance of the underaged material.

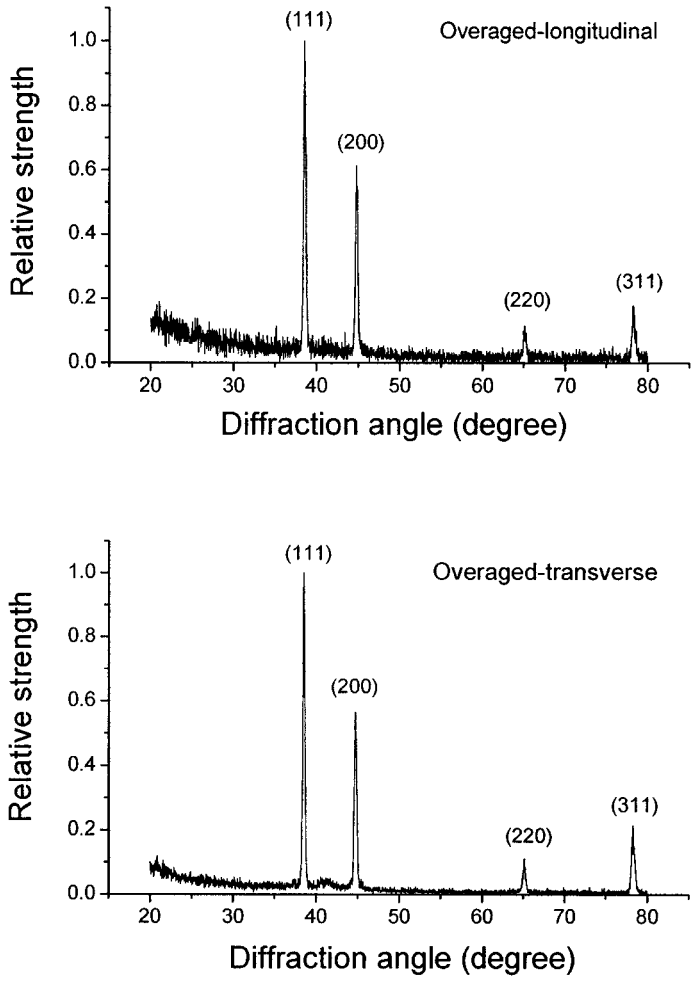

Figure 5.17 The X-ray diffraction patterns on the longitudinal and the transverse planes in the overaged material (relative strength being the X-ray count normalized by the highest peak count).

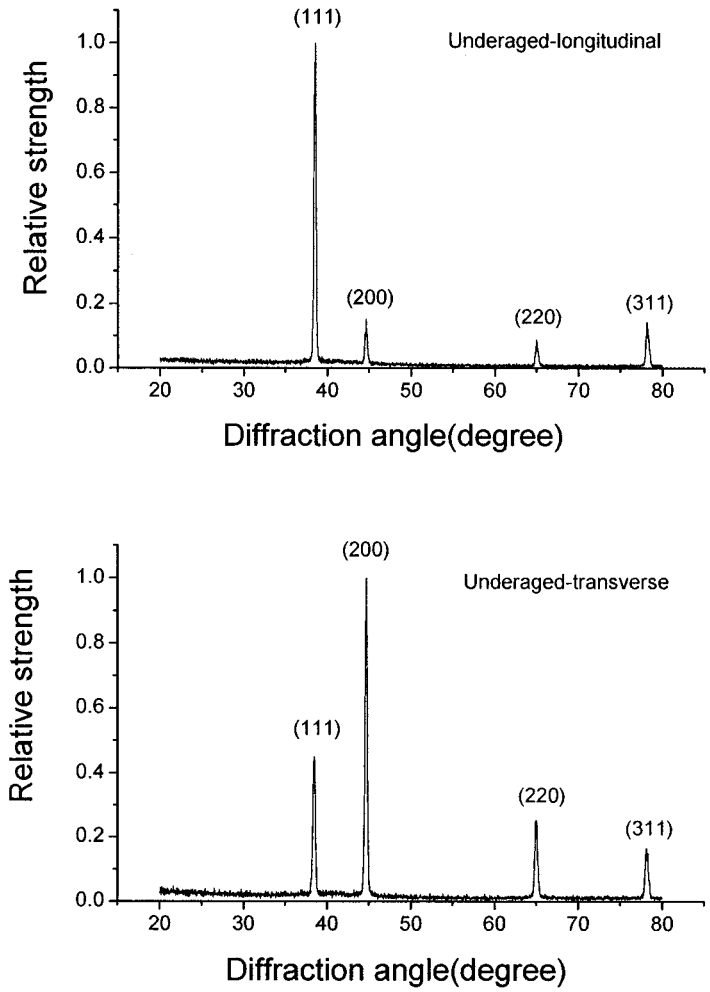

Figure 5.18 The X-ray diffraction patterns on the longitudinal and the transverse plane in the underaged material (relative strength being the X-ray count normalized by the highest peak count).

5.5.2 Anisotropy effect and stress level

In torsional fatigue, fatigue cracks in both materials are observed along the longitudinal direction at high stress level, but that cracking can occur on the transverse plane at low stress level. This observation indicates that material anisotropy effects are more significant at high stress level than at low stress level. The reason of the changeover of shear cracking plane with stress level could be that material anisotropy is detrimental only at the high shear stress level. At a high stress level, the plastic zone ahead of crack tip is larger than that at low stress level. It can encompass more inclusions. Because of the stress intensity at the crack tip, the interfaces between inclusions and the matrix could open, leading to a local strain concentration in the adjacent matrix (Kaynak et al, 1996). Therefore, inclusion-enhanced shear cracking should be easier at a high stress level. It seems that only when the stress level is high enough to overcome the bonding strength between inclusion and matrix, inclusions can help fatigue cracking. Further, at low stress level, the transverse shear cracks are not necessarily nucleated at inclusions. This indicates that inclusions do not help crack initiation and propagation in torsional fatigue at low stress level. More shear cracks were observed to nucleate and propagate on the transverse shear planes at low stress level. A possible explanation is that inclusions could act as a strengthening phase when the applied shear stress is not enough to break the interface between inclusion and matrix. The elongated grains are helpful for longitudinal shear cracking, since less grain boundaries and therefore less resistance to the crack crossing such boundaries are encountered in longitudinal direction.

5.5.3 Fatigue life prediction parameters

Very few multiaxial fatigue life prediction parameters have considered material anisotropy even though its importance has been reported (Fernando, 1990; Shatil et al, 1994). Lin and Nayeb-Hashemi (1993) found that an effective strain could correlate in-phase biaxial fatigue lives of RD specimens (specimen axis along rolling direction), but

not those of TD specimens (specimen axis normal to rolling direction). They proposed the following parameter to predict fatigue life:

$$A(\gamma_{max} + B\varepsilon_n) = f(N) \tag{5.1}$$

Here A and B are material anisotropy coefficients, the values of which depend on the material orientation. A is introduced to reduce the two torsional baseline data obtained from RD and TD specimens into one, and B is obtained by fitting torsional and axial fatigue life data.

Engineering applications involved in biaxial fatigue behavior in anisotropic material differ from case to case. The life prediction parameters should be proposed according to the actual fatigue cracking behavior.

In the present study, two types of mechanisms contribute to fatigue failure in axial and torsional fatigue of the underaged and overaged 7075 aluminum alloys: anisotropy enhanced fatigue mechanisms (along weak longitudinal planes) and critical plane failure mechanisms. Both mechanisms should be taken into account in fatigue life correlation.

Anisotropy effects are not important in overaged 7075 aluminum alloy. The fatigue behavior was almost similar to that observed in the isotropic 1045 steel. Fatigue failure occurred on the critical plane, even though longitudinal shear cracks predominated in pure torsional fatigue. In Chapter IV, the McDiarmid parameter has been shown to be a good life prediction parameter for in-phase fatigue of steel, and also relatively good one for torsional fatigue with static tension (slight underestimation). The same results are obtained for overaged 7075 aluminum alloy. As shown in Figure 5.19, the McDiarmid parameter gives a relatively good correlation of fatigue lives obtained from three loading conditions. However, it still slightly underestimates lives under torsional fatigue with static tension. Note that the normal stress effects (k=0.5) is twice that obtained for 1045 steel (k=0.2).

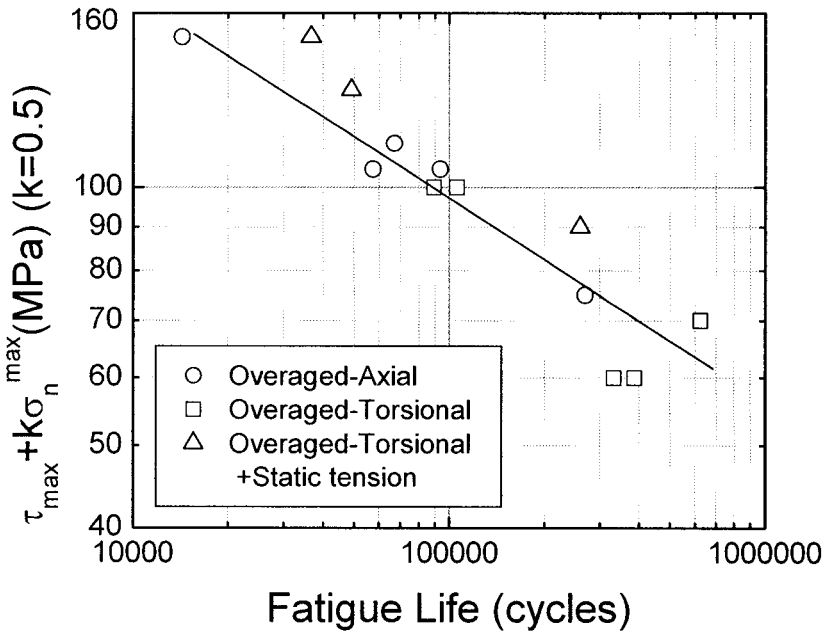

Figure 5.19 Fatigue life versus McDiarmid parameter in overaged material.

However, a different fatigue behavior was observed in the underaged material (Figure 5.15). For the same τ_{max}, even when additional normal stresses (cyclic or static) act on the critical plane (planes at $\pm 45^0$ in tension or the transverse plane in torsion), pure shear fatigue cracking is much easier along the weak longitudinal planes and it results in a lower life (solid line in Figure 5.15). In this material, there is a competition between transverse cracking (critical plane failure mechanism) and the easier longitudinal cracking (anisotropy enhanced failure mechanism). Only one stress-life relationship cannot account for two possible mechanisms (longitudinal cracking and non-longitudinal cracking). For the transverse cracking, fatigue life can be correlated with a usual critical plane parameter:

$$\tau_{max} + k\sigma_n^{max} = f(N) \tag{5.2}$$

in which k can be calibrated by axial, torsional (+ high σ_m) or in-phase axial-torsional fatigue. In the case of easier longitudinal cracking, lives can be correlated with the stress components acting on the longitudinal plane:

$$(\tau_a + k'\sigma_n^{\max})_{\text{longitudinal plane}} = g(N) \tag{5.3}$$

here, k' can be calibrated by torsional fatigue and torsional fatigue with internal pressure. To predict fatigue life for a given loading condition, one computes the lives given by the two parameters, and takes the smaller life as the predicted life.

In summary, the McDiarmid parameter correlates axial and torsional (with or without static tensile load) fatigue lives of the overaged material. It could be used to give reasonable life predictions for other loading conditions. The Tresca parameter (maximum shear stress amplitude) correlates the fatigue lives recorded for the underaged material. However, two stress-life relationships should be considered to predict fatigue lives for other loading conditions. Here, again we can see the importance of observing the fatigue cracking mechanisms for appropriately correlating or predicting fatigue life under biaxial fatigue.

5.6 Summary

Underaged and overaged 7075 aluminum alloys have been tested under three loading conditions: axial fatigue, torsional fatigue and torsional fatigue with static tension. The fatigue cracking behavior was observed through surface crack monitoring by the replica technique and by fractography. Based on the understanding of the fatigue cracking mechanisms, different fatigue life prediction parameters are proposed for the underaged and overaged materials.

Cracking occurs on the weakest planes. Two kinds of weakness are involved in the fatigue of 7075 aluminum alloy: intrinsic weakness caused by the material anisotropy and extrinsic weakness caused by the applied loading. The former makes the longitudinal

plane weaker, and the latter favors the so-called critical planes as the possible cracking planes.

- Under axial fatigue, anisotropy effects are not observed in both materials, since the weak plane caused by material anisotropy does not coincide with the critical plane.
- Under torsional fatigue, critical planes are the longitudinal maximum shear plane and the transverse maximum shear plane. Anisotropy does have important effects and results in longitudinal shear cracking in both materials, especially at high stress level, since the longitudinal shear plane coincides with the weak plane.
- Under torsional fatigue with static tensile load, only the transverse maximum shear plane is the critical plane. The competition of two mechanisms results in two kinds of fractures: 1) transverse shear cracking in the overaged material once a tensile load is applied; 2) longitudinal fracture in the underaged material as long as the applied static tensile load is not high enough.

Material anisotropy effects are more important in the underaged material. Inclusions play a role in both materials but the combination of (111) texture and planar slip enhances the weakness of the underaged material in the longitudinal direction.

The fatigue life results showed that under the same maximum shear stress amplitude, torsional fatigue life is higher than axial fatigue life in overaged material, and the application of static tension decreases torsional fatigue life. A different trend is observed in underaged material. Axial fatigue life is higher than torsional fatigue life, and the application of static tensile stress does not have much influence on the torsional fatigue life.

These life differences are associated with the difference in fatigue mechanisms. The observation of fatigue cracking shows that two mechanisms compete in fatigue cracking of 7075 aluminum alloy: a material anisotropy enhanced failure mechanism and a critical

plane failure mechanism. It is not appropriate to use one parameter to correlate fatigue lives corresponding to different fatigue mechanisms. It is suggested to use the McDiarmid parameter to correlate fatigue life for the overaged material, since anisotropy effects are not pronounced. However, for the underaged material, strong anisotropy effects have been observed. Two stress-life relationships are needed to account for the two failure mechanisms. To predict fatigue life for a given loading condition, the fatigue lives corresponding to two stress-life relations are computed and the lower life is taken as the predicted life. However, these conclusions are based on a limited number of tests. Further investigation is required for confirmation.

CHAPTER VI - AXIAL AND TORSIONAL FATIGUE BEHAVIOR OF CIRCUMFERENTIALLY V-NOTCHED CYLINDERS MADE OF AS-ROLLED 1045 STEEL

6.1 Background of this study

The study of notch effects on fatigue is important, since notches are unavoidable in mechanical components. Several approaches have been used to deal with notch fatigue problems, such as local stress/strain approaches, critical distance approaches and fracture mechanics approaches.

A fundamental assumption of local stress/strain approaches is that fatigue crack initiation life at notches corresponds to that measured on smooth laboratory specimens at the same stress/strain level. They are successfully used in practical applications where crack initiation dominate fatigue life (blunt notches). However, local stress/strain approaches are not applicable for sharp notches where fatigue failure is controlled by fatigue crack propagation. They do not account for the stress/strain gradient that exists at the notch tip. Further the applicability of biaxial fatigue criteria developed for smooth specimens to notches is questionable. Even though some success has been obtained in some cases by different approaches (Gough, 1949; Takahara et al, 1972, Williams et al (1985)), notch fatigue life prediction under multiaxial fatigue is a challenge (Grubisic and Simburger, 1976; Fash et al, 1985), since fatigue mechanisms could be different in smooth and notched specimens.

Critical distance approaches attempt to consider the stress gradient at the notch root by using a stress at a critical point (Peterson, 1959; Tanaka, 1983; Taylor, 1999) or the average stress over a critical length (Neuber, 1958), etc. More often, the critical distance is obtained in an empirical manner. Tanaka (1983) and Taylor (1999) attempted to relate the critical distance to material properties such as the fatigue crack threshold. Taylor and

Wang (2000) showed that critical distance approaches are useful for both blunt and sharp notches, even though two different mechanisms are involved. However, any critical distance approach cannot explain the occurrence of non-propagating cracks at severe notches.

Fracture mechanics approaches have been developed to predict short crack propagation life. As reviewed in Chapter I, short crack behavior at a notch is strongly influenced by the notch plasticity. The condition of small scale yielding at the crack tip is violated and LEFM cannot account for behaviors such as crack deceleration and non-propagating cracks in notched specimens. Smith and Miller (1977,1978) assumed that the effective driving force for short crack growth is the sum of contributions of notch plasticity and crack tip plasticity. Verreman et al (1986, 1987, 1997) measured the evolution of the crack opening level with crack depth, and found that the opening level rapidly increases before reaching a stabilized level. The initial transient of the opening level explains what has been observed on crack growth rates. Although K increases with crack depth, the effective crack driving force decreases because of the rapid and important increase in the opening level. They found that if crack growth rates are plotted against the effective stress intensity factor range ΔK_{eff}, short and long crack growth rates are consolidated in a single trend. Considering short crack behavior, both Smith & Miller (1977, 1978) and Verreman et al (1987) related fatigue limit to fatigue crack growth threshold and notch geometry.

A simple and conservative linear elastic fracture mechanics approach can be developed for the limiting case of severe V-notches with very small root radii. Williams (1952) found that the stress field distribution at sharp re-entrant corners is singular and is uniquely determined by a notch stress intensity factor. Provided that notch plasticity is confined within this singularity, different notches having the same notch stress intensity factor have the same stress-strain field, and hence should have the same fatigue performance. The notch stress intensity factor has been successfully used in initiation life

prediction of welded joints and V-notched members under mode I, mode II and combined mode I and mode II loadings (Boukharouba et al, 1995; Dunn et al, 1997; Lazzarin and Livieri, 2001; Tovo and Lazzarin, 1998 and 1999;Verreman and Nie, 1996; 1999). No application of this approach for mode III loading has been reported.

The advantage of the notch stress intensity factor approach lies in three aspects: 1) it is theoretically appropriate for predicting fatigue crack initiation and propagation within the notch field; 2) it avoids making complex computation of local cyclic plastic strains and/or finding complex relations between crack growth rate and crack stress intensity factor; 3) it gives a conservative life prediction for blunt notches. On the other hand, the difficulty of this approach is that the stress singularity depends on the notch angle and the loading modes. At the present time, the objective is limited to the behavior under pure axial fatigue (mode I) and pure torsional fatigue (mode III) of two V-notched specimens with same angle (90^0) but different notch size. It is expected that the mode I notch stress intensity factor (K_I^N) could correlate fatigue lives obtained from the two specimens under axial fatigue. The applicability of mode III stress intensity factor (K_{III}^N) in correlating fatigue lives of the two specimens under torsional fatigue is also examined. If these correlations could be made, a door can be opened for a future study on notch fatigue behavior under combined axial-torsional loadings.

6.2 Experiments

6.2.1 Material

As-rolled 1045 steel was used as test material. This is the same material as that used for axial-torsional fatigue tests of smooth specimens. The material microstructure and properties have been described in Chapter III.

6.2.2 Specimen geometry

As shown in Figures 6.1 and Figure 6.2, two types of notched specimens N1 and N2 are used. They both have a circumferentially 90^0 V-notch around the cylindrical surface. They were machined to have a notch radius as small as possible (<0.075mm). The two specimens are designed so that the ratio between their notch stress intensity factors under the same nominal stresses is maximized. Their global dimensions are also determined by the grip size and the specimen design standard for axial fatigue.

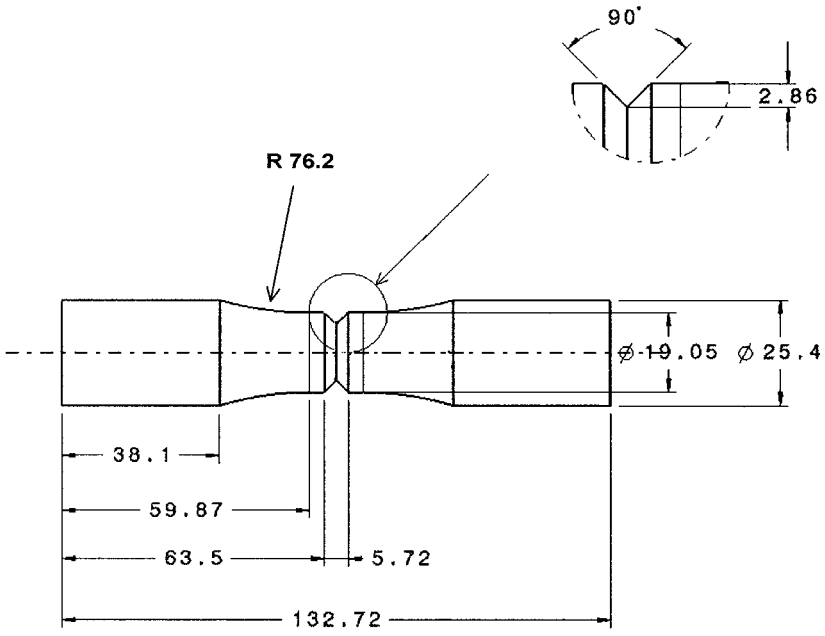

Figure 6.1 Geometry of N1 specimen (unit: mm); notch depth is 2.86mm

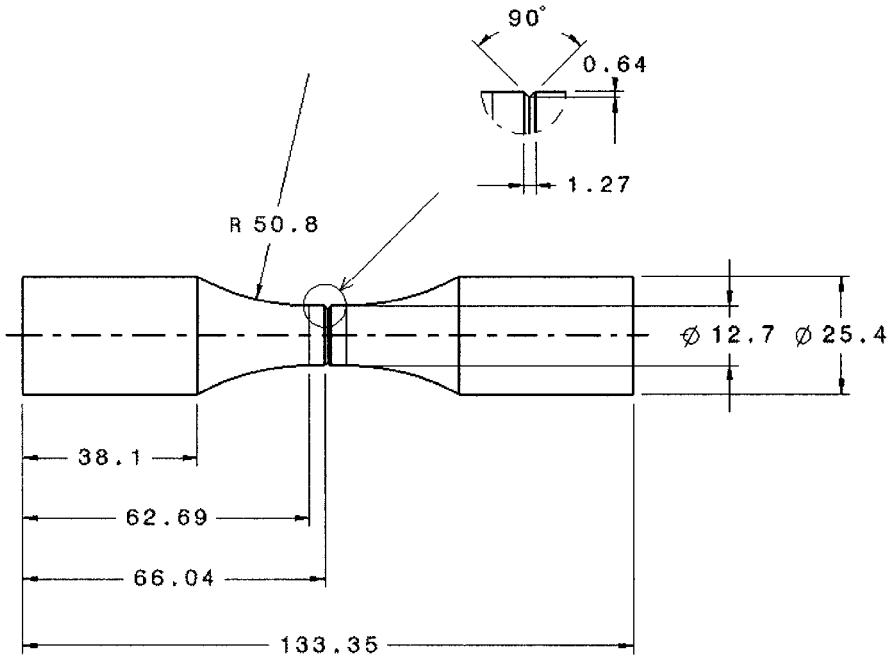

Figure 6.2 Geometry of N2 specimen (unit: mm).; notch depth is 0.635mm

Before computing numerical solutions of mode I and mode III notch stress intensity factors, the stress intensity expressions for cracks (Eq. 6.1 and 6.2) were used for the purpose of specimen design (Rooke and Cartwright, 1980).

$$\frac{K_I}{K_0} = \frac{1-N^2}{(1-(1-N)X)^2 - N^2}\left\{0.80 + \frac{(1-N)X}{1-(1-N)X}\left[4 + \frac{1.08N}{(1-N)(1-X)}\right]\right\}^{\frac{1}{2}} \tag{6.1}$$

$$\frac{K_{III}}{K_0} = \frac{(1-N^4)(1-(1-N)X)}{(1-(1-N)X)^4 - N^4}\left\{1 + \frac{(1-N)X}{1-(1-N)X}\left[7.111 + \frac{2.468N}{(1-N)(1-X)}\right]\right\}^{\frac{1}{2}} \tag{6.2}$$

Eqs. 6.1 and 6.2 are stress intensity factors for an external circumferential crack in a tube under axial and torsional loading respectively. Note that $K_0 = \sigma_{nom}\sqrt{\pi a}$ in Eq. 6.1 and $K_0 = \tau_{nom}\sqrt{\pi a}$ in Eq. 6.2, where σ_{nom} is the nominal axial stress and τ_{nom} is the nominal

shear stress at the specimen surface, and "a" is the crack depth. In both equations, N= R_1/R_2 and X=a/ (R_2-R_1), where R_1 and R_2 are the internal and external radii of the tube. The shear stress $\tau_{nom} = \frac{2R_2T}{\pi(R_2^4 - R_1^4)}$, where T is the applied torque.

In the present case, R_1=0, N=0, X=a/R_2=2a/D (D being the specimen diameter). The mode I and mode III stress intensity factors are plotted against 2a/D, as shown in Figure 6.3. Both K_I and K_{III} are normalized with respect to the nominal axial and shear stresses over the net (smallest) section, σ_{net} and τ_{net}. Since the net section decrease with increasing crack depth, the curves reach maximum value then decrease. The two notch geometries N1 and N2 chosen are specified in Table 6.1. The notch N1 (a/D=0.15, D=19.05mm) corresponds to the highest stress intensity factor (SIF). The notch N2 (a/D=0.05; D=12.7mm) is smaller but it is still large with respect to the microstructure (average ferrite grain size of 15μm).

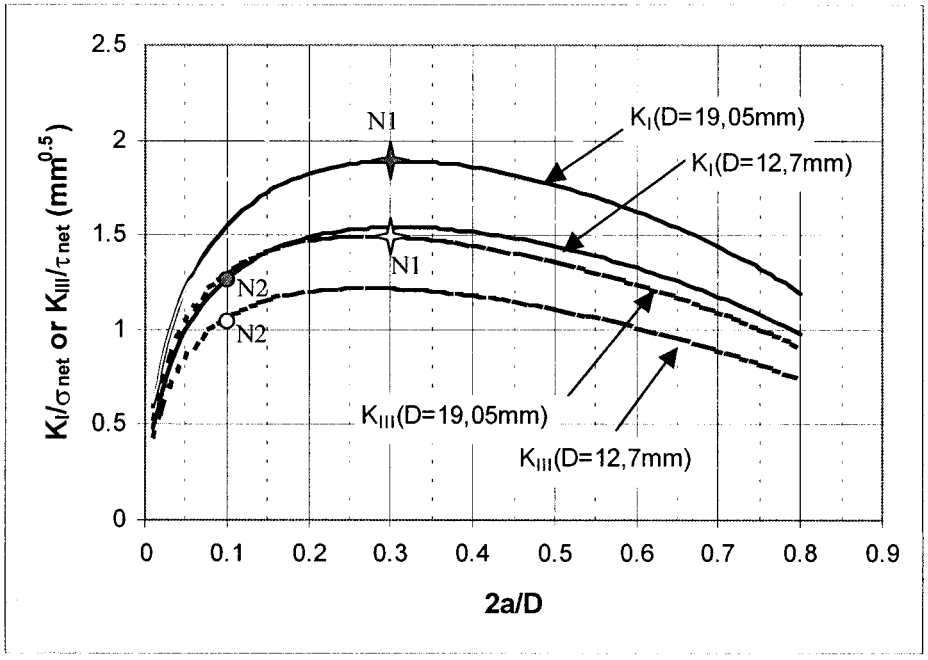

Figure 6.3 Normalized SIFs K_I and K_{III} plotted against a/2D for circumferentially cracked round bars. (Stars and circles show K_I and K_{III} for notches N1 and N2.)

Table 6.1 Geometry specifications of the two notched specimens (Figures 6.1 and 6.2).

Specimen	D (mm)	d* (mm)	a (mm)	a/D	K_I/σ_{net} ($mm^{0.5}$)	K_{III}/τ_{net} ($mm^{0.5}$)
N1	19.05	13.335	2.86	0.15	1.89	1.48
N2	12.7	11.43	0.635	0.05	1.27	1.06

* d=D-2a, being the diameter at the smallest (net) section of the specimen.

Note that the above SIF solutions for cracks (notch angle = 0^0) are only approximations of those for notches (notch angle = 90^0). FEA analysis of notch SIFs will be presented in section 6.5.1.

6.2.3 Fatigue tests

Fully reversed axial fatigue and torsional fatigue tests are performed on both types of specimens N1 and N2, respectively. All tests are load (torque)-controlled using the Instron 8521 servo-hydraulic biaxial machine. Tests are conducted at room temperature in laboratory air. Load waveforms are sinusoidal with a frequency of 10HZ. The detailed fatigue test programs are shown in Tables 6.2 and 6.3.

Table 6.2 Axial fatigue tests and life results for N1 and N2 specimens.

Specimen	σ_{net} (MPa)	Load (KN)	σ_{nom} (MPa)	K_I ($MPa.mm^{0.5}$)	N_f (cycles)
N1A1	150	20.95	73.5	283.5	40,929
N1A2	100	13.97	49.0	189.0	145,995
N1A4	85	11.87	41.7	160.7	314,635
N2A1	150	15.39	121.5	190.5	149,829
N2A2	100	10.26	81.0	127.0	1,442,225
N2A3	125	12.83	101.3	158.8	283,485

σ_{net}: nominal stress amplitude in net section
σ_{nom}: nominal stress amplitude in full section
K_I: stress intensity factor for a crack
N_f: life at final fracture

Table 6.3 Torsional fatigue tests and life results for N1 and N2 specimens.

Specimen	τ_{net} (MPa)	Torque (N.m)	τ_{nom} (MPa)	K_{III} (MPa.mm$^{0.5}$)	N_i (Cycles)
N1T2	129	60.06	44.25	190.9	>5,000,000
N1T3	160	74.50	54.88	236.8	616,343
N1T4	200	93.12	68.60	296.0	55,000
N1T5	180	83.81	61.74	266.4	100,000
N1T2B	220	102.43	75.46	325.6	16,920
N2T1	125	36.65	91.13	132.5	>5,000,000
N2T2	180	52.80	131.22	190.8	270,000
N2T3	210	61.57	153.09	222.6	135,000
N2T4	160	46.91	116.64	169.6	1,500,000
N2T5	140	41.04	102.06	148.4	>5,000,000
N2T6	235	68.90	171.32	249.1	15,000
N2T1B	230	67.40	167.67	243.8	40,000
N2T5B	235	68.90	171.32	249.1	30,000

τ_{net}: nominal shear stress amplitude in net section
τ_{nom}: nominal shear stress amplitude in full section
N_i: initiation life (rotation amplitude increase of 1%)
K_{III}: stress intensity factor for a crack

6.3 Fatigue life results

The main objective of our work is to validate that mode I and mode III notch stress intensity factors can correlate the "initiation lives" of the two notched specimens, under axial and torsional fatigue respectively. The earliest initiation life (that for the microstructural scale) is negligible at very sharp notches (Verreman and Espinosa, 1997). The "initiation life" considered here is in fact the short crack propagation life spent in the first tenths of millimeter. For a given loading mode, the same notch SIF gives the same stress field and thus should give the same events ahead of the notch, provided that they remain confined at this singularity.

The fatigue life results are listed in Tables 6.2 and 6.3. Note that in axial fatigue, most of the life is spent in initiating the crack (N/Nf>50% at 0.5mm crack depth; Verreman and Espinosa, 1997). Lazzarin and Livieri (2001) made successful correlations between notch stress intensity factor and total axial fatigue life. However, in torsional fatigue, the initiation life is only a small part of the total life, especially for solid specimens where the stress gradient resulting from specimen thickness is strong. Total lives of specimens with different diameters would not be comparable. Only initiation life can be comparable, since it is controlled by the notch stress field.

The variations of displacement amplitude and rotation angle amplitude are monitored during axial fatigue and torsional fatigue, respectively. Both displacement amplitude and rotation angle amplitude increase with fatigue cracking. These variations are uniquely related to the crack depth for a given specimen geometry. They represent the compliance variations in both cases. Figure 6.4 shows a typical curve of the relative variation of the displacement amplitude ($=\frac{v/P - v_0/P}{v_0/P}$, v_0 and v are the displacements at 0 and N cycles, and P is the applied load) versus cycle life under axial fatigue. It can be seen that once the displacement amplitude changes, it increases rapidly until final failure. This confirms that in axial fatigue, propagation life is not significant. Then the total lives from different specimen geometries are comparable. On the other hand, in torsional fatigue, once a change in rotation angle amplitude is detected, the subsequent evolution of rotation angle amplitude develops slowly. A typical curve of rotation amplitude variation ($=\frac{\alpha/T - \alpha_0/T}{\alpha_0/T}$, α_0 and α are the rotation angles at 0 and N cycles, and T is the applied torque) with lifetime is shown in Figure 6.5. Therefore, the propagation life is a significant part of the total life. If the propagation lives in two geometries are not comparable, then the total life is also not comparable. In torsional fatigue, it is appropriate to compare initiation life in two geometries. Initiation life is defined as the number of cycles at which an increase of 1% in rotation angle amplitude is detected.

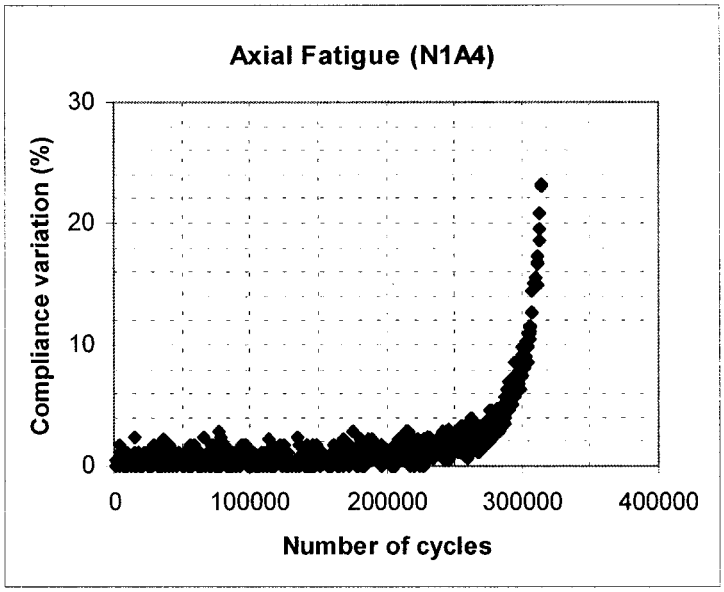

Figure 6.4 Typical curve of compliance variation, plotted against fatigue lifetime under axial fatigue.

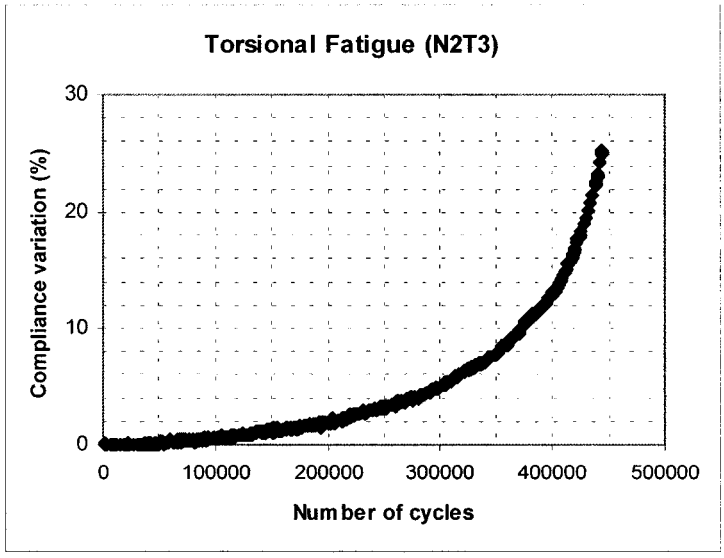

Figure 6.5 Typical curve of compliance variation plotted against fatigue lifetime under torsional fatigue.

The relations between the crack depth and the variation of rotation angle amplitude are experimentally characterized for both geometries by periodically marking the crack front using intermittently axial fatigue. Figure 6.6 shows an example of marks found on the fracture surface (see arrows). The cracks depths corresponding to the marks have been measured with an optical microscope. Figure 6.7 shows the relationship between compliance variation versus crack depth obtained by the marking procedure. It can be seen that under torsional fatigue, the crack depth corresponding to 1% increase in compliance is approximately the same in the two notched specimens, of the order of 0.4-0.5mm. Then, the fatigue initiation life defined by a 1% increase in compliance is comparable in the two notched specimens. The stress fields at the notch tip control the short crack behavior. It is appropriate to correlate the notch stress intensity factor and the crack initiation life for these two notched specimens under torsional fatigue.

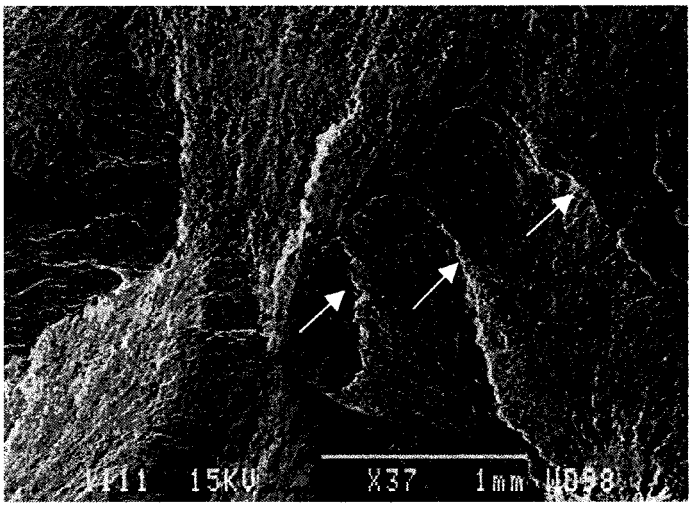

Figure 6.6 Illustration of marks, made by intermittent axial fatigue, (indicated by arrows that also show the radial crack growth direction) on the fracture surface of notched specimen under torsional fatigue.

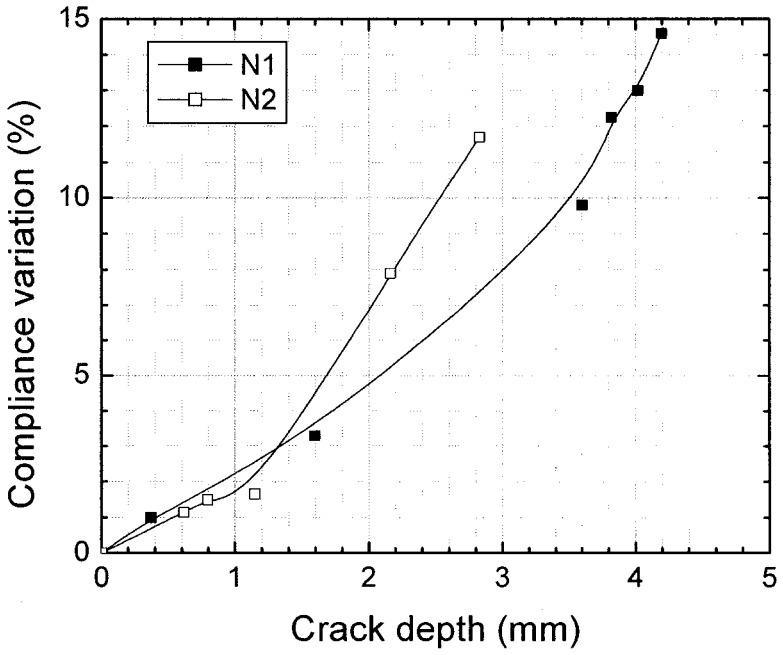

Figure 6.7 Relationship between the compliance variation and the crack depth in the two types of notched specimens under torsional loading.

6.3.1 Axial fatigue

Figure 6.8 shows the total fatigue lives of notched specimens (N1 and N2) and tubular smooth specimens plotted against the amplitude of nominal net stress (being the applied axial stress for tubular specimens). Notched specimens have lower resistance to fatigue compared with smooth specimens. The fatigue notch reduction factor (K_f) in N1 ($\approx$ 3.53) is higher than that in N2 ($\approx$2.44), especially at low stress. The same trend was also observed by Fatemi et al (2002). For notched specimens, specimen N1 has a lower fatigue performance than specimen N2. This is the so-called size effect in notch fatigue, as observed by Verreman and Nie (1996) for welded joints. The nominal stress σ_{net} cannot account for this effect. Figure 6.9 shows fatigue lives of notched specimens

plotted against the mode I stress intensity factor K_I (computed with Eq. 6.1) for a crack with same depth as notch depth. A good correlation is obtained with K_I.

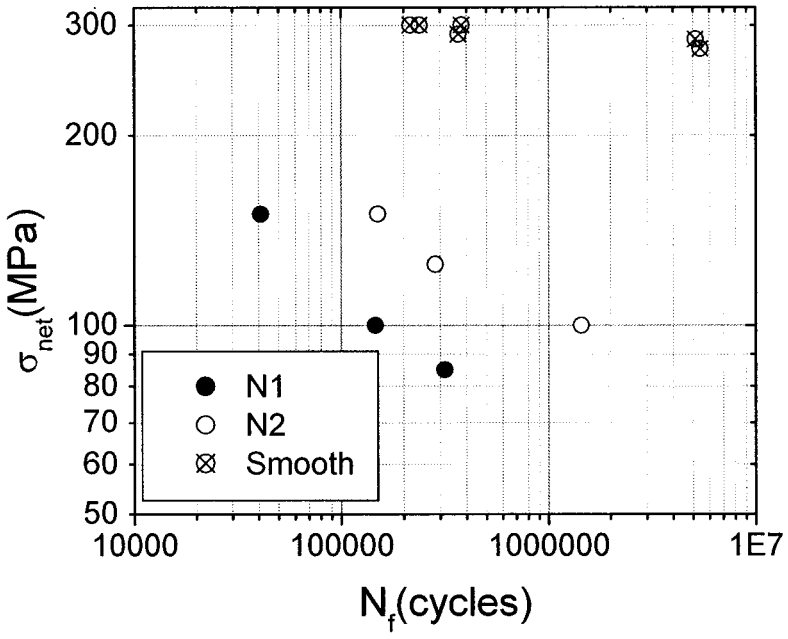

Figure 6.8 Total fatigue lives plotted against nominal net stress σ_{net} for notched specimens (N1 and N2) and for smooth specimen under axial fatigue.

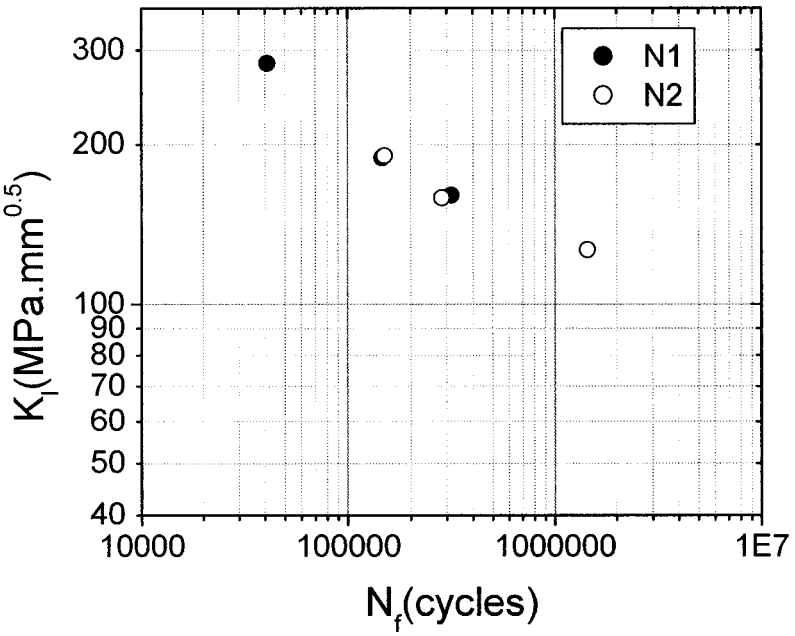

Figure 6.9 Total fatigue lives plotted against crack stress intensity factor (K_I) for notched specimens N1 and N2 under axial fatigue.

6.3.2 Torsional fatigue

Fatigue lives obtained from notched specimens (N1 and N2) and smooth specimens (thin-walled tubes) are plotted against the amplitude of the nominal net shear stress τ_{net} (being the applied shear stress for the tubular specimen) (Figure 6.10). For notched specimens, the fatigue life is the "initiation" life defined by a 1% increase in rotation compliance. For smooth specimen, the total life is used. The notch effect is very small in torsional fatigue in comparison to axial fatigue. This trend was also observed by Nisitani & Kawano (1968, 1970) and by Fatemi et al (2002). Note that fatigue notch factor in torsional fatigue is very much dependent on the definition of initiation life. Specimen N1 still has a lower fatigue performance than specimen N2; however, this difference is not as pronounced as in axial fatigue. It is noticed that the "initiation life" in the V-notched specimens is in fact the short crack propagation life (the very initiation can be very short). Caution should be taken to the lives of notched specimens we compared to those of smooth specimens.

An attempt was also made to use mode III stress intensity factor K_{III} to correlate fatigue life data obtained from the two notched specimens under torsional fatigue, as shown in Figure 6.11. K_{III} is computed using Eq. 6.2, assuming that the notch is equivalent to a crack with the same depth. Contrary to axial fatigue, the stress intensity factor gives a worse correlation than that obtained with the nominal net stress. This implies that the torsional fatigue behavior of a 90^0-sharp notch is different from that of a crack (a 0^0-sharp notch). The assumption of the equivalence of their behavior overestimates the notch effect. Under torsional fatigue, there is an important difference between crack and notch singularities. Further discussion will be made after the notch stress analysis (section 6.5.3).

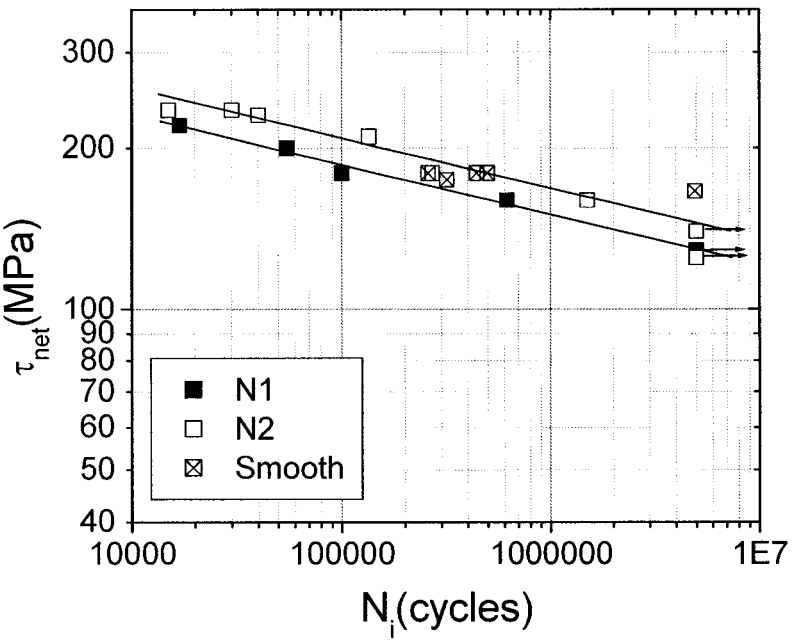

Figure 6.10 Fatigue "initiation" lives plotted against nominal shear stress τ_{net} for notched specimens (N1 and N2) and smooth specimen under torsional fatigue.

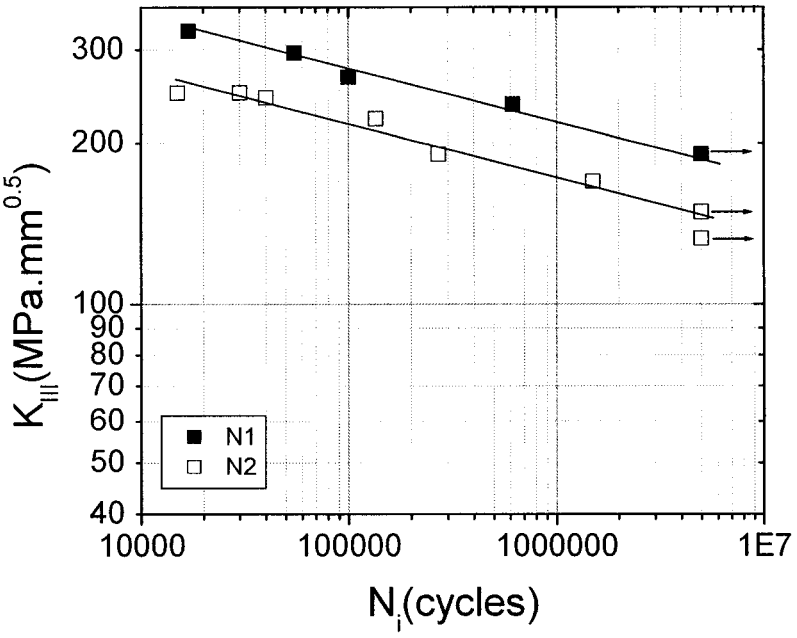

Figure 6.11 Fatigue "initiation" lives plotted against crack stress intensity factor (K_{III}) for notched specimens N1 and N2 under torsional fatigue.

6.4 Fractography

The fracture features of notched specimens under axial and torsional fatigue were observed by SEM.

6.4.1 Axial fatigue

Figures 6.12 and 6.13 show the fracture surfaces of notched specimens N1 and N2, respectively. Under low magnification (Figures 6.12(a) and 6.13(a)), specimens N1 and N2 show the same features. Cracks initiate at the notch tip over the entire circumference, since a V-notch is a severe stress-concentrator. The notch immediately imposes mode I cracking contrary to the smooth surface where cracks initiate at PSBs and propagate to some extent under mode II. In notched specimens, in spite of the roughness induced by crack coalescence at the initial stage of fracture, the overall fracture surfaces are quite flat, and perpendicular to specimen axis. Mode I fracture is the failure mode for notched specimens under axial fatigue.

Under high magnification (Figures 6.11(b) and 6.12(b)), both N1 and N2 specimens show the same microscopic features. These are typical fatigue fractographic features of 1045 steel. Some faint striations are observed (see arrows). Due to the microstructural features, striations observed in 1045 steel are not as well defined as those in aluminum alloy. No obvious crystallographic features are observed. Fracture surfaces of smooth specimens under axial fatigue also have the same microscopic features as those shown in Figures 6.12(b) and 6.13(b). For mode I fracture, there is no intrinsic difference in fracture mechanisms between notched specimens and smooth specimens. Notch size does not affect fractographic features under axial fatigue.

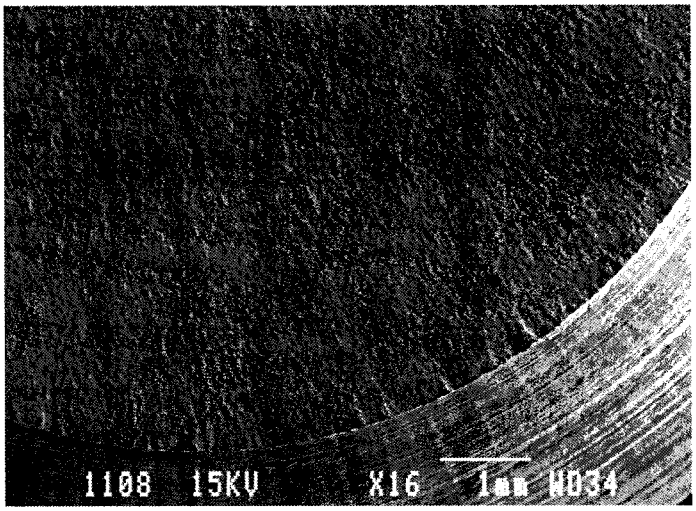

(a)

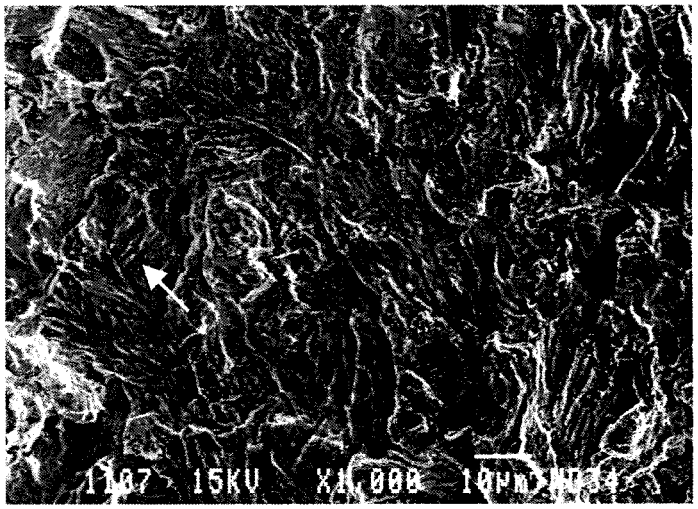

(b)

Figure 6.12 Axial fatigue fracture surfaces of specimen N1 observed under SEM. (a) Under low magnification. (b) Under high magnification; the crack direction is from bottom to top in this photo.

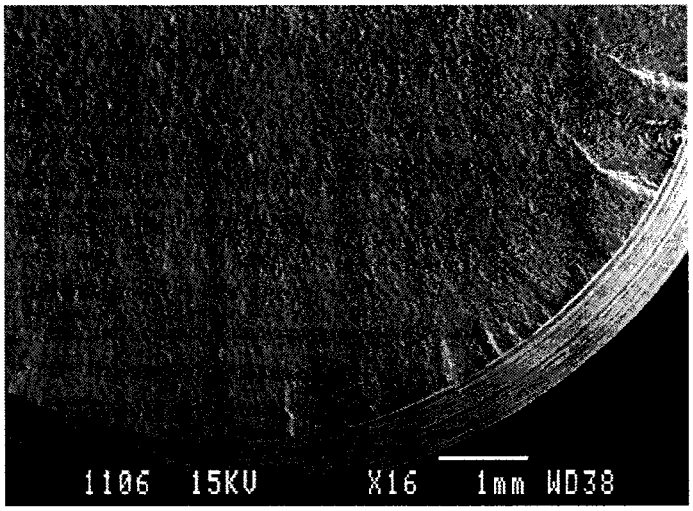

(a)

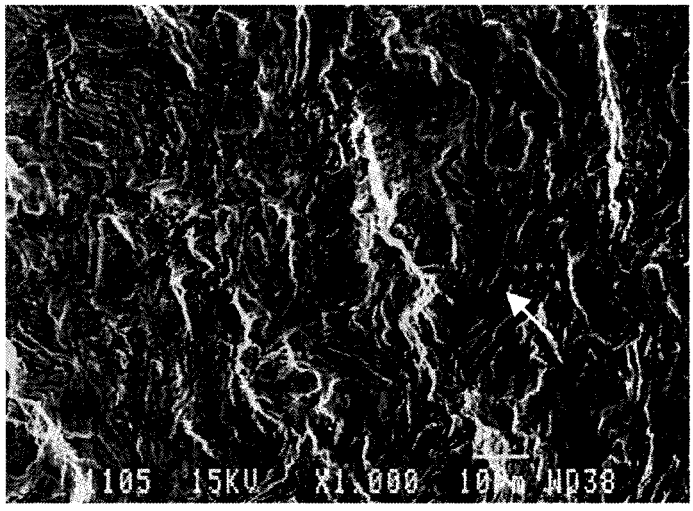

(b)

Figure 6.13 Axial fatigue fracture surfaces of specimen N2 observed under SEM. (a) Under low magnification. (b) Under high magnification; the crack direction is from bottom to top in this photo.

6.4.2 Torsional fatigue

Observations have also been made of the fracture surfaces of notched specimens N1 and N2 subjected to cyclic torsion. Whatever the notch size and the stress level, the so-called "factory-roof" fractographic feature is observed in all specimens (see Figure 6.14). This is a common fracture feature for circumferentially V-notched cylindrical specimen under torsional fatigue, as observed by Tschegg in 4340 steel (1983) and by Brown et al in 1%Cr-Mo-V steel (1985). This kind of fracture surface is formed by mode I crack propagation. Many cracks initiate along all over the circumference at notch tip as in axial fatigue. These cracks could have a small amount of shear propagation, but this is not obvious. They propagate under mode I on planes inclined $\pm 45^0$ with respect to specimen axis (planes of maximum normal stress) into larger section. They encounter more resistance and eventually stop their propagation on these planes. This resistance forces cracks to propagate into specimen thickness from the circumference to the center. Two adjacent main cracks, which propagate on two orthogonal maximum principal planes, coalesce to form the hills and valleys of the factory-roof fracture. Mode I fracture is the basic fracture mode in notched specimens; whereas, in smooth specimen made of 1045 steel, mode II fracture is important under torsional fatigue (Chapter III). Sakane et al (1988) also observed this difference in fracture modes between notched and smooth specimens.

Note that all specimens were finally broken by axial fatigue after the rotation angle amplitude increased by about 20%. The fracture features of torsional fatigue and axial fatigue of these notched specimens are different, macroscopically and microscopically. Macroscopically, the fracture surface of axial fatigue is flat; whereas, the fracture surface produced by torsional fatigue looks like a factory-roof. Microscopically, there is a difference between the local crack propagation directions as shown in Figure 6.15. The photograph shows microscopic fracture features at the boundary between torsional

fracture (right) and axial fracture (left). However, there is no obvious difference in their micro-mechanisms of the mode I fracture caused either by torsional or by axial fatigue.

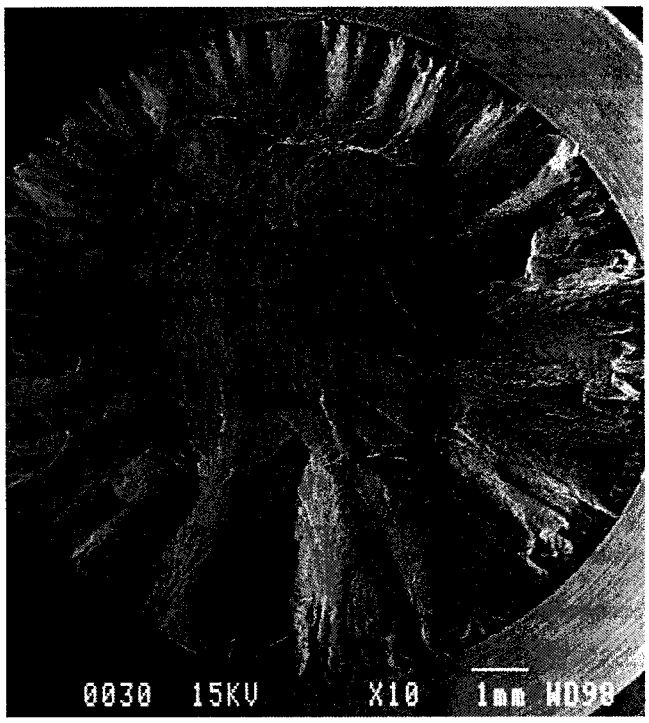

(a)

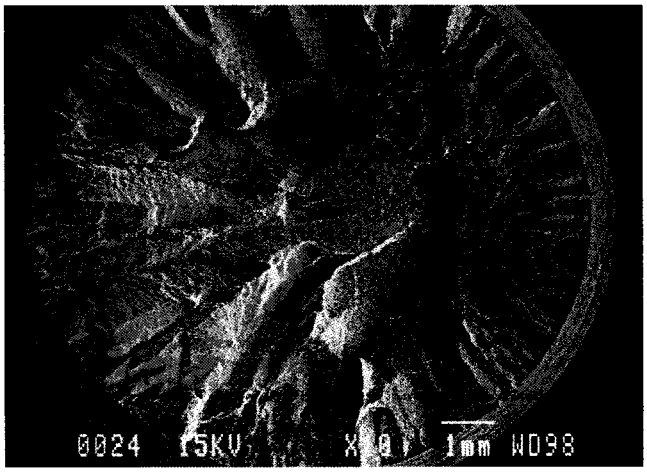

(b)

Figure 6.14 "Factory-roof" fracture surfaces in torsional fatigue.
(a) Notch N1. (b) Notch N2.

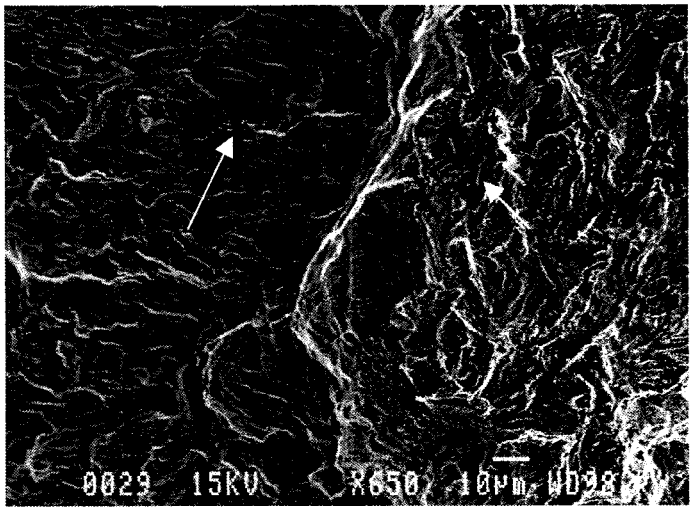

Figure 6.15 Fracture surface caused by torsional fatigue (right), then by and axial fatigue (left). The ridgeline in the middle of the photo is the boundary between torsional fatigue and axial fatigue. Arrows show the crack propagation directions by torsional fatigue and by axial fatigue, and the direction of macro fracture is the same as that of the axial fatigue crack growth (N1T3).

More detailed observations have been made on the fracture features of torsional fatigue. Figure 6.16 shows that initially many cracks propagate. Many small hills are observed, and then coalescence occurs and higher hills form (Figure 6.16). This is why the fracture surface close to the notch tip is flatter. The arrow in Figure 6.16 indicates a secondary mode I crack that propagates on the plane perpendicular to the main crack plane. Intensive friction is observed at the very initial stage of cracking as shown in Figure 6.17. The photograph is taken from the notch tip at the valley. Secondary cracks propagating on the plane perpendicular to the main crack plane are also observed (see dotted arrows in Figure 6.17, while the solid arrow shows the notch tip). Coalescence of 45^0-cracks is observed on a microscopic scale (see the steps and ridges in Figure 6.18). Figure 6.19 shows fractographic features in torsional fatigue which again similar to axial fatigue. There is no intrinsic difference between the micro-mechanisms in mode I fracture of torsional and axial fatigue, even though an obvious difference is observed between the macroscopic features of the two loading cases.

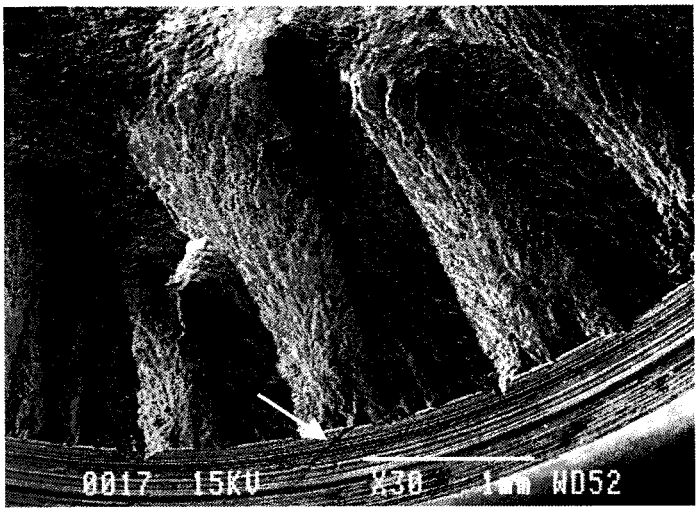

Figure 6.16 Crack coalescence observed on torsional fatigue fracture surface of specimen N2T4 (arrow showing a crack propagating on the plane perpendicular to the main crack front).

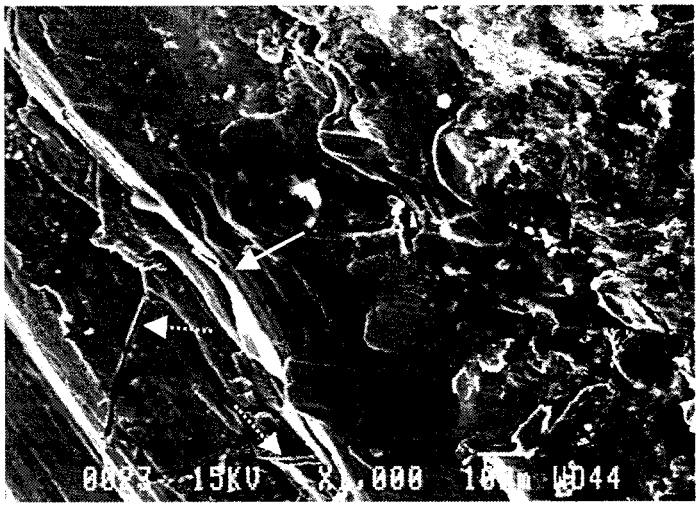

Figure 6.17 Intensive friction observed on the torsional fatigue fracture surface close to the notch tip in specimen N2T4. The solid arrow shows the notch tip, and the dotted arrows show the cracks propagating on the plane perpendicular to the main crack front.

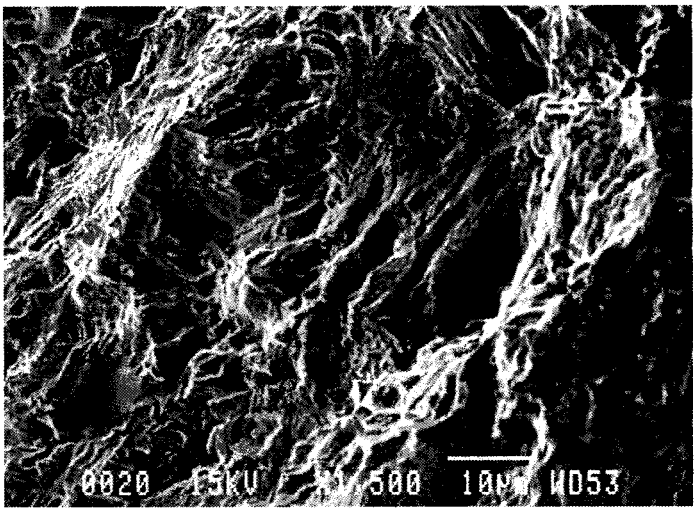

Figure 6.18 Microscopic coalescence on 45^0 crack planes leaves steps and ridges on the torsional fracture surface of specimen N2T4.

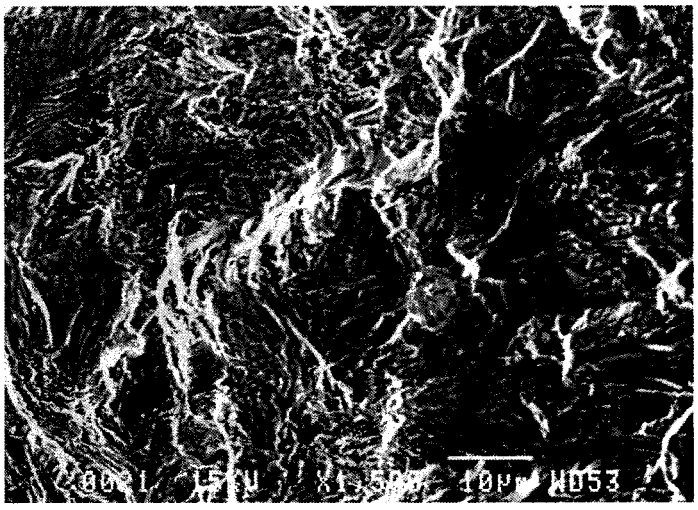

Figure 6.19 Microscopic features observed on the torsional fracture surface of specimen N2T4.

6.5 Correlations between fatigue lives and notch SIFs

6.5.1 Finite element analysis and notch stress intensity factors

Williams (1952) showed that a singular stress field exists in the region surrounding a sharp re-entrant corner (V-notch). By analogy with a crack, the stress field at V-notch tip can be expressed as,

$$\sigma_{ij} = K^N r^{-\alpha} f_{ij}(\theta) \tag{6.3}$$

Here, σ_{ij} is the stress tensor; r and θ are the polar coordinates. K^N is the notch stress intensity factor. The order of stress singularity α is a function of the notch angle. It differs from mode I to mode II or to mode III, except for a crack (0^0 V-notch) where α=0.5 in all modes (Verreman and Nie, 1996; Dunn et al, 1997).

6.5.1.1 Mode I notch stress intensity factors (K_I^{N1} and K_I^{N2})

Under axial loading, the elastic stress field at a V-notched tip presents a singularity. The normal stress σ_{zz} (Figure 6.20) at the notch tip can be expressed as

$$\frac{\sigma_{zz}}{\sigma_{net}} = \lambda_1 \left(\frac{a}{r}\right)^{\alpha} \tag{6.4}$$

λ_1 is a function of the notch angle and the dimensionless geometry. By analogy with crack, the following relation can be obtained

$$\sigma_{zz} = \frac{K_1^N}{r^a} \tag{6.5}$$

Then the mode I notch stress intensity factor is defined as

$$K_1^N = \lambda_1 \sigma_{net} a^{\alpha} \tag{6.6}$$

For a given geometry and a given loading system, the stress distribution $\sigma_{zz}(r)$ can be obtained by finite element analysis. Through linear regression, λ_1 and α can be obtained, hence the expression of K_I^N is obtained.

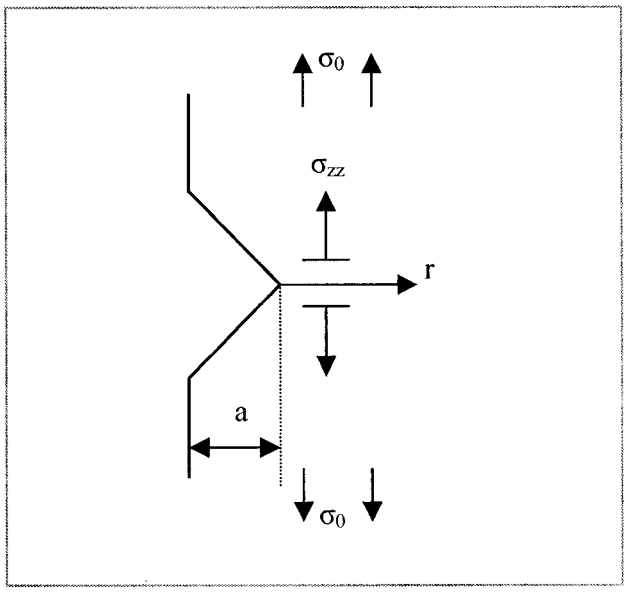

Figure 6.20 Illustration of V-notch under axial loading.

Stress analysis was performed for the two notches N1 and N2 using the linear elastic finite element module available in the Catia 5 code. The mesh size at notch tip is about 0.1mm. All details of the numerical analysis are given in Appendix II. The relations between σ_{zz}/σ_{net} and r obtained for both notches N1 and N2 are shown in Figure 6.21. It can be seen in this log-log plot that both curves have a linear portion. Therefore, in circumferentially V-notched specimens N1 and N2 subjected to axial loading, stress singularities exist within a small zone at the notch tip and their stress fields at the notch tip are characterized by the so-called notch stress intensity factor. Comparing the normal stress in N1 and N2, we can see that notch singularity zone in N1 is larger than that in N2. The depth of the singularity ($\sigma_{zz}/\sigma_{net}\approx 1$) is about 1 mm for N1 and 0.6 mm for N2. Notch N1 is more severe than notch N2. It has a stronger stress concentration within the stress singularity zone. This explains the difference in fatigue performance in terms of net stress σ_{net} between the two specimens (Figure 6.8).

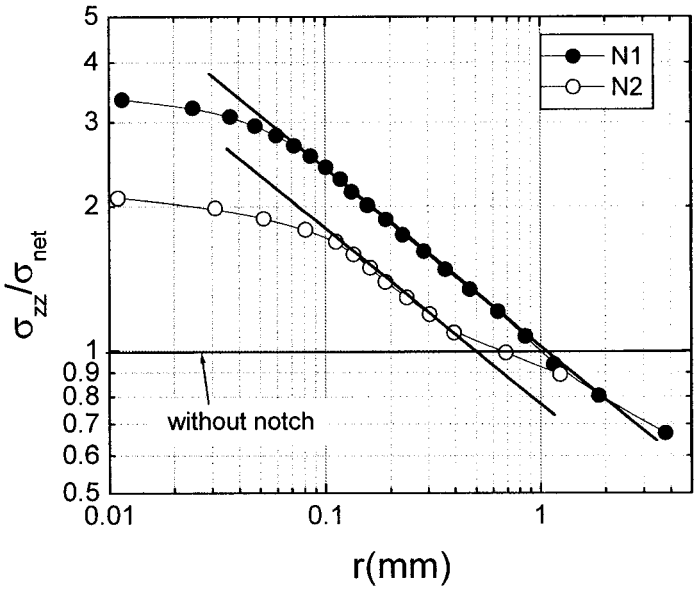

Figure 6.21 Normalized normal stress σ_{zz} as a function of the distance r from the notch tip in specimens N1 and N2 under axial loading.

Linear regression of the straight parts (straight Figure 6.21) determines the notch stress intensity factors for notches N1 and N2 as follows,

$$K_I^{N1} = 0.559\sigma_{net}a^{0.42} \tag{6.7}$$

$$K_I^{N2} = 0.767\sigma_{net}a^{0.42} \tag{6.8}$$

From these FEM solutions, it can be seen that under axial loading, the exponent of singularity α is only a function of the notch angle; whereas, λ_1 is a function of the geometry for a given notch angle. The value of α in the 90^0 V-notch (0.42) is only slightly lower than that in a crack (0.5). It is close to the value obtained from analytical solution

(α=0.455; Dunn et al, 1997). With a=2.8575mm in N1 and a=0.635mm in N2, the mode I notch stress intensity factors in N1 and N2 are,

$$K_I^{N1} = 0.869\sigma_{net}, \tag{6.9}$$

$$K_I^{N2} = 0.634\sigma_{net}. \tag{6.10}$$

The unit of mode I notch stress intensity factor is $MPa.mm^{0.42}$.

6.5.1.2 Mode III notch stress intensity factors (K_{III}^{N1} and K_{III}^{N2})

Under torsional loading, if there is a stress singularity, the shear stress singularity (Figure 6.22) at the V-notch tip can be written as

$$\frac{\tau_{z\theta}}{\tau_{net}} = \lambda_{III}\left(\frac{a}{r}\right)^{\alpha}, \tag{6.11}$$

where λ_{III} is a function of notch angle and geometry.

By analogy with crack, the following relation is obtained

$$\tau_{z\theta} = \frac{K_{III}^{N}}{r^{\alpha}}. \tag{6.12}$$

Then mode III notch stress intensity factor is defined as

$$K_{III}^{N} = \lambda_{III}\tau_{net}a^{\alpha}. \tag{6.13}$$

For a given geometry and a given loading, the stress distribution $\tau_{z\theta}(r)$ can be obtained by finite element analysis. Through linear regression, λ_{III} and α can be obtained, hence the expression of K_{III}^{N} is obtained.

The stress analysis was performed for the two notches N1 and N2 using the Catia 5 code and the same mesh as that used for axial loading. All details are given in Appendix II. The relations between shear stress $\tau_{z\theta}$ and distance r obtained for specimens N1 and N2 are shown in Figure 6.23. This figure uses the same scale as in Figure 6.21.

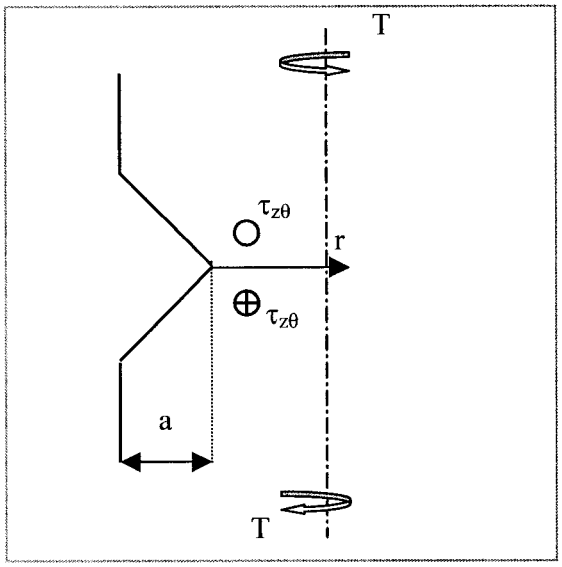

Figure 6.22 Illustration of V-notch under torsional loading.

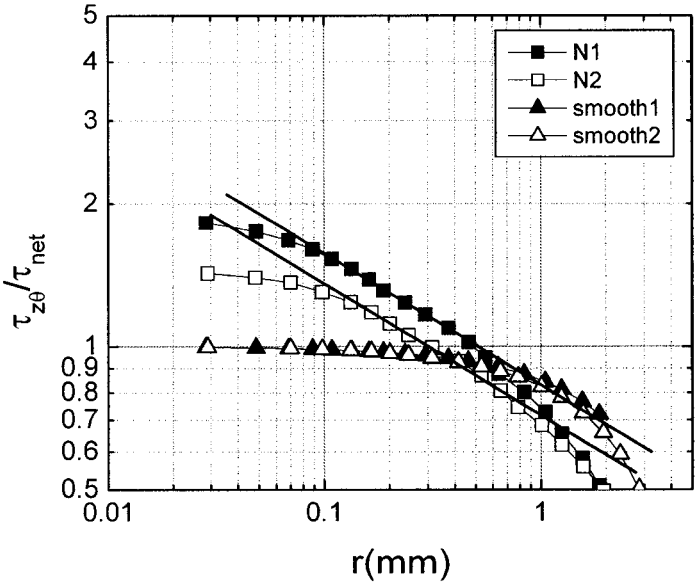

Figure 6.23 Normalized shear stress distributions at notch tip in specimens N1 and N2 under torsional loading (smooth 1 and smooth 2 represent the stress distributions of smooth specimens with the same diameters as the notch specimens N1 and N2, respectively: the straight line represent the regression lines).

Notch stress concentration in torsional loading is lower than that in axial loading, and the difference between the two notches under torsional loading is not as large as that under axial loading. This can explain the lower notch effect on the fatigue performance under torsional loading (Figure 6.10).

Straight portions (solid lines) are also observed on the two curves in Figure 6.23, but they are not as clearly defined as for axial fatigue. A possible reason is that the minimum available meshing size in Catia 5 is not small enough to catch well the immediate region of the notch tip. Errors are introduced for the stress computed at distances very close to notch tip. However, the linear portion of the curve can still be employed for linear regression.

From linear regression of the linear portions (straight lines in Figure 6.23), the following solutions of the mode III notch stress intensity factors are obtained,

$$K_{III}^{N1} = 0.56\tau_{net}a^{0.313} \tag{6.14}$$

$$K_{III}^{N2} = 0.81\tau_{net}a^{0.313} \tag{6.15}$$

With a=2.8575mm in N1 and a=0.635mm in N2, the above solutions become,

$$K_{III}^{N1} = 0.778\tau_{net} \tag{6.16}$$

$$K_{III}^{N2} = 0.703\tau_{net} \tag{6.17}$$

It can be seen that for the mode III notch stress intensity factor, the singularity exponent is equal to 0.313, which is close to analytical solution (α=0.333; Sonsino and Maddox, 2001). The unit of mode III notch stress intensity factor is MPa.mm$^{0.313}$. The depth of the singularity zone ($\tau_{z\theta(r)}/\tau_{net(r)}$=1) is about 0.6 mm in specimens N1 and is about 0.3 mm in N2.

6.5.2 Fatigue life and notch stress intensity factor

The notch stress intensity factor can describe the stress field at the notch tip. For a given loading mode, the same notch stress intensity factor results in the same stress field, and the same fatigue events are expected. The mode I notch stress intensity factor is plotted against the axial notch fatigue life in Figure 6.24 and the mode III notch stress intensity factor against the torsional notch fatigue life in Figure 6.25.

The Mode I notch stress intensity factor K_I^N gives a good correlation of axial fatigue lives from the two notched specimens N1 and N2. Several authors have also shown that K_I^N can correlate fatigue lives obtained from V-notched welded joints of different sizes (Verreman and Nie, 1996; Lazzarin and Livieri, 2001). By comparing Figure 6.24 and Figure 6.9, no significant difference in correlating abilities is observed between K_I and K_I^N. The crack and the notch stress intensity factors have similar singularity exponents (0.5 in K_I and 0.42 in K_I^N). Further, there is not much difference between the ratio of crack stress intensity factors: $K_{I(1)}/K_{I(2)} = 1.5$ and $K_I^{N1}/K_I^{N2} = 1.4$.

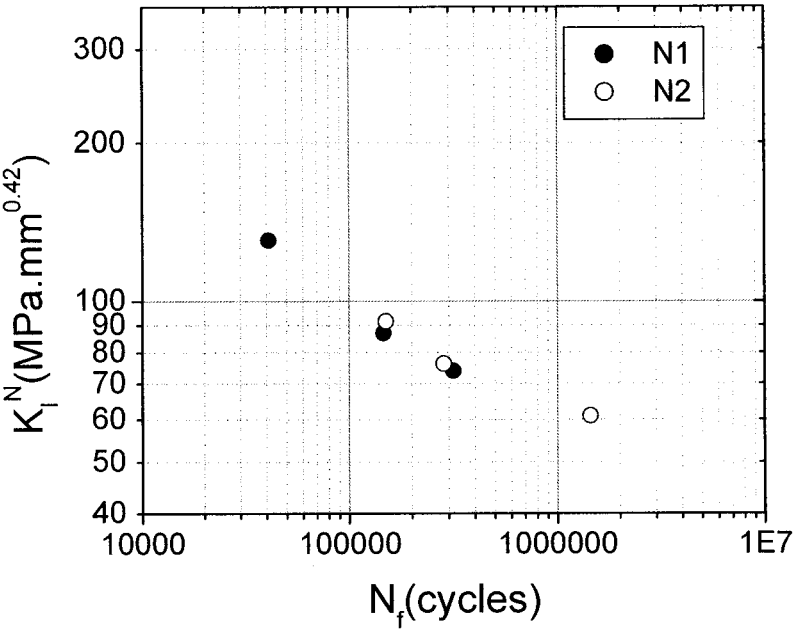

Figure 6.24 Axial total fatigue life plotted against mode I notch stress intensity factor K_I^N.

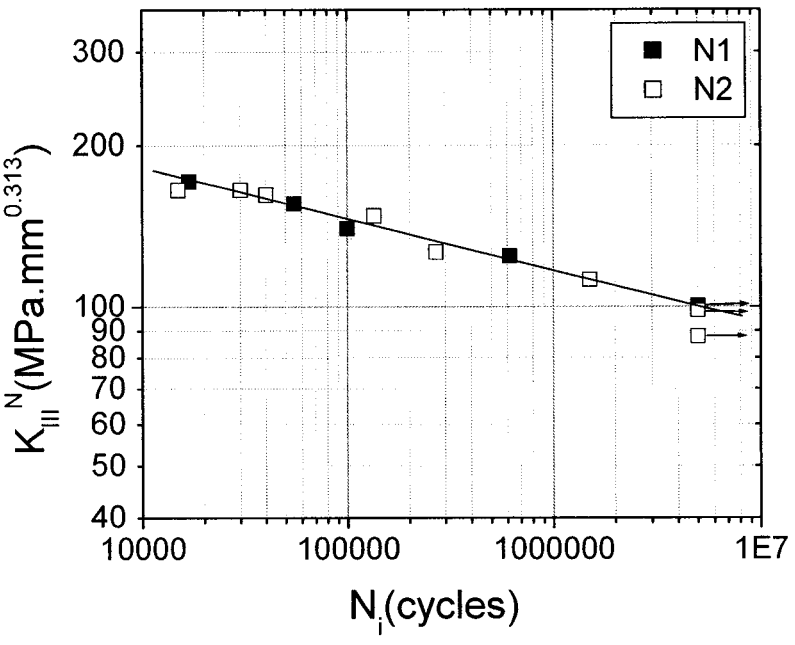

Figure 6.25 Torsional "initiation" fatigue life plotted against mode III notch stress intensity factor K_{III}^{N}.

A good correlation is also obtained when the torsional fatigue lives ("initiation" lives) of the two notched specimen are plotted against the mode III notch stress intensity factor K_{III}^{N} (Figure 6.25). K_{III}^{N} for N1 and N2 are computed according to Eq. 6.16 and Eq. 6.17, respectively. Such a correlation with the mode III notch stress intensity factor was never, to our knowledge, reported yet.

By comparing Figures 6.25 and 6.11, a significant difference in life correlating ability is found between crack stress intensity factor K_{III} and notch stress intensity factor K_{III}^{N}. Note that the singularity exponent obtained for a 90^0 V-notch (α=0.313) is smaller than that for a crack (α=0.5). The ratio between mode III notch stress intensity factors of N1 and N2 ($K_{III}^{N1}/K_{III}^{N2}$=1.106) is smaller than that computed for cracks

($K_{III(1)}/K_{III(2)}$=1.396). Using the crack stress intensity factor overestimates the difference between the two notches under torsional fatigue. K_{III} gives a worse correlation than that obtained with the nominal shear stress τ_{net}. On the other hand, the correlation of fatigue life with K_{III}^{N} is better than that with τ_{net}. This is an experimental confirmation that K_{III}^{N} controls the stress field at the notch tip under torsion.

Mode I and Mode III notch stress intensity factors are good life correlating parameters for 90° V-notches under axial fatigue and torsional fatigue, respectively. For the circumferentially V-notched specimens, the stress field is singular at the notch tip under both mode I loading and mode III loading. The notch stress intensity factors alone describe the stress fields. For a given loading mode, the notch stress intensity factor reflects the same stress field, which results in the same fatigue events, whatever the combination of nominal stress and notch size.

6.6 Notch effects versus loading conditions

By comparing Figure 6.8 and 6.10, two remarks can be made: 1) fatigue notch factor in axial fatigue (2.44 for N2; 3.53 for N1) is higher than in torsional fatigue; 2) the life difference between the two notched specimens (size effect) is larger in axial fatigue than in torsional fatigue. The global conclusion is that the notch effect is more important in axial fatigue than in torsional fatigue. Several researchers have reported similar results (Nisitani and Kawano, 1968 and 1970; Fatemi et al, 2002).

The stress analysis has shown that notch stress concentration is higher in axial fatigue than in torsional fatigue ($\sigma_{zz}/\sigma_{net} > \tau_{z\theta}/\tau_{net}$; Figures 6.21 and 6.23). In axial loading, the stress concentration in notch N1 is higher than that in notch N2; however, for torsional loading, stress concentration in N1 is only slightly higher than that in N2. Higher stress concentration results in lower fatigue performance. This analysis is in good agreement with the different fatigue performances measured in axial fatigue and in torsional fatigue.

The low fatigue notch factor in torsional fatigue can also result from the factory-roof fracture. As compared with the straightforward mode I fracture in axial fatigue, crack propagation resistance is higher when the crack propagates in the zig-zag manner in V-notched specimens under torsion. In torsional fatigue, when a mode I crack propagates into the larger section of specimen along the planes at 45^0 to the specimen axis, it encounters more resistance and finally is forced to propagate into the specimen thickness. A lot of resistance is caused for the crack propagation by the friction due to the large asperities on the crack faces. This high resistance of crack propagation can explain the good torsional fatigue performance of the V-notched specimens. The torsional fatigue "initiation" resistance of V-notched specimens is almost as good as that of smooth specimens if comparison is based on the net stress τ_{net}. This is of engineering interest.

The mode I notch stress intensity factor correlates well the axial fatigue lives of the two 90^0 V-notched specimens. The mode III notch stress intensity factor also gives a good correlation of torsional fatigue lives. Note that these correlations cannot be used to predict fatigue lives for notches with an angle different than 90^0. Different notch angles will result in different values of the singularity exponent, different stress fields and different units in the notch stress intensity factor. Comparison or finding equivalence between these stress fields is complex. This is a limit for the notch stress intensity factor approach. However, configurations with fixed notch angle do exist in real engineering applications. For example, many welded joints contain a 135^0 sharp V-notch at the weld toe. Many machine components contain 90^0 L-notches. For a given notch angle, the notch stress intensity factor approach offers a life prediction method, theoretically founded and conservative.

6.7 Summary

The purpose of this study was to investigate notch effects on axial fatigue performance and on torsional fatigue performance, and to examine the ability of notch stress intensity factors to correlate axial and torsional fatigue lives.

Axial and torsional fatigue tests were performed on two types of circumferentially V-notched cylindrical specimens (with a same notch angle of 90^0, but different notch depths and specimen nominal diameters). Fatigue life results show that in terms of nominal net stress (σ_{net} for axial fatigue and τ_{net} for torsional fatigue), notch effects in axial fatigue are more important than in torsional fatigue. Firstly, the fatigue notch factor is higher in axial fatigue than that in torsional fatigue. Secondly, the notch size influence on fatigue performance is more important in axial fatigue than that in torsional fatigue.

These differences are explained from stress analysis and fatigue mechanisms. Detailed FEM stress analysis shows that the stress concentration due to the notch in axial fatigue (σ_{zz}/σ_{net}) is higher than that in torsional fatigue ($\tau_{z\theta}/\tau_{net}$). The different stress concentration levels can explain the different notch effects in axial fatigue and in torsional fatigue.

Observations on fracture surfaces showed that in both axial and torsional fatigue, mode I is the main failure mode. The fracture surface in axial fatigue is flat. In torsional fatigue, the "factory-roof" fracture in V-notched specimen results in a high crack propagation resistance and hence in good fatigue performance. This is another reason why the fatigue notch factor is low in torsional fatigue.

The FEM stress analysis confirms that the stress fields at the notch tip are singular for both mode I and mode III loadings. These stress fields can be characterized by mode I and mode III notch stress intensity factors. The same stress field should give the same

fatigue events within the stress field. Very good experimental confirmation has been obtained. Both mode I and mode III notch stress intensity factors can well correlate fatigue lives of two specimens of different notch size, under axial and torsional loadings, respectively. These correlations leave the door open to a future study on notch fatigue behavior under combined axial-torsional loadings. Fatigue life is expected to be a function of mode I and mode III components of the notch stress field. Different loading combinations are required to determine this function.

CONCLUSIONS

Axial-torsional high cycle fatigue tests were carried out on smooth tubular specimens made of as-rolled 1045 steel. The effects of two types of non-proportional loadings (90^0 out-of-phase and mean tensile stress) were investigated. Surface fatigue cracking processes were monitored by a replica technique. Fatigue cracking mechanisms were observed in detail by SEM. From the observation of fatigue cracking behavior, the following conclusions are drawn:

- Cracks initiate at PSBs on the specimen surface in well-oriented ferrite grains. Whatever the loading condition, most cracks initiate on planes of maximum shear stress amplitude. Crack initiation is a shear-controlled process. Under non-proportional loadings, more cracks initiate on the maximum shear plane where the normal stress (amplitude or static value) is the highest. Stage I propagation of the fatal crack occurs on this critical plane.

- The two stages of crack propagation have been observed: stage I on maximum shear planes and stage II on maximum normal stress planes. Stage I is a shear-controlled process, while stage II is a tensile-controlled process. The two stages are clearly put into evidence in three loading cases: torsional fatigue, in-phase and 90^0 out-of-phase (λ=2) axial-torsional fatigue. In axial fatigue, the transition from stage I to stage II is not obvious due to the infinity of maximum shear planes. In the special loading case ($\phi=90^0$; λ=0.5), there is no stage II crack branching, since the stage I crack propagates on the maximum normal stress plane.

- Differences in surface crack growth lives and in crack aspect ratios are observed between axial, torsional, in-phase and out-of-phase loadings. However, curves of crack growth against fatigue life ratio are approximately consolidated when crack growth is defined in terms of crack depth. In other words, the relative fraction of total

life spent to initiate a crack of given depth would not depend on the loading condition. In particular, the transition from stage I to stage II occurs at about 30-45% of total life in the region of 10^5-10^6 cycles. While the stage I crack length ranges from 50 μm to 750 μm depending on the loading conditions, their depth is approximately the same of about 20-40 μm. The stage I/stage II transition could correspond to a microstructural barrier in depth.

- A special attention should be paid to the special loading case ($\phi=90^0$; $\lambda=0.5$) for which the shear stress amplitudes on all planes are equal. All grains are well oriented and crack initiation is easier. A much higher crack density is observed compared to the other loading cases. Then crack coalescence occurs and results in faster crack propagation. Faster crack propagation can also result from no stage II crack branching. More damaging mechanisms are involved in crack initiation and crack propagation.

- Fatigue life consumed under shear control (initiation and stage I propagation) represents an important part of total life. Therefore, shear-based parameters are appropriate for the prediction of biaxial high cycle fatigue life in 1045 steel. However, the more damaging mechanisms in the special loading case should be taken into account in life prediction.

The life prediction abilities of eight multiaxial fatigue life parameters have been evaluated for ferritic-pearlitic steels under biaxial high cycle fatigue. There are four stress-based parameters (Tresca, McDiarmid, Dang-Van, and Papadopoulos), three strain-based parameters (KBM, Wang-Brown, Fatemi-Socie) and one energy-based parameter (GWP). Seven of them are based on the critical-plane concept (extensions of the Tresca stress/strain parameter), and one (Papadopoulos) is an extension of von Mises parameter. Two sets of biaxial high cycle fatigue data on ferritic-pearlitic steels (our own data and data from literature) are used for this evaluation. The following conclusions are drawn:

- The Tresca parameter cannot predict biaxial high cycle fatigue life, due to the effects of normal stress (both amplitude and mean) on the fatigue performance. With increasing normal stress amplitude or increasing mean tensile normal stress on the critical plane, the fatigue performance decreases. The Tresca parameter must be modified to account for the normal stress effects.
- The GWP parameter accounts for the normal stress effect but it cannot consolidate pure axial and pure torsional fatigue lives. However, the overall prediction errors are not larger than those of the other parameters.

- The six other parameters can well predict fatigue lives for in-phase and low λ out-of-phase loadings. Fatigue lives for the other loading cases (high λ out-of-phase loading, the special loading case and torsional loading with static tension) are either underestimated or overestimated.

- For high λ out-of-phase loading, the McDiarmid, Fatemi-Socie and KBM parameters underestimate fatigue lives. An attenuation of normal stress/strain amplitude effect due to the large phase angle on the critical plane can explain this underestimation. The Wang-Brown parameter, which considers this phase angle, gives a better life prediction. Both the Dang-Van and Papadopoulos parameters that use the maximum hydrostatic stress, also work well for this loading case.

- The effects of normal stress amplitude and normal mean stress on the critical plane are different a priori. The former is a mode I driving force, and the latter has an opening effect. The maximum normal stress on the critical plane can account for both effects of normal mean stress and in-phase normal stress amplitude on the critical plane. The McDiarmid parameter and the Fatemi-Socie parameter can predict relatively well the fatigue life under cyclic torsion with static tension. Parameters such as KBM and Wang-Brown cannot account for tensile mean stress effects, since

no mean stress/strain terms are used in these parameters. The parameters using the maximum hydrostatic stress (Dang-Van and Papadopoulos) overestimate fatigue life for the torsional loading with static tension. This implies that the static part of the hydrostatic stress has a more important contribution on fatigue damage than the cyclic part.

- The worst fatigue performance in the special loading case is attributed to more damaging mechanisms during crack initiation and crack propagation. This can explain the overestimation of fatigue lives. To obtain a conservative life prediction, the McDiarmid parameter can be modified by introducing an extra damage factor (EDF). It can be calibrated from the ratio between the fatigue strength in torsion and that in the special loading case.

- The above evaluation of multiaxial fatigue parameters has been made in the high cycle fatigue regime, assuming a totally elastic stress-strain response of the material. However, plastic strain can be non-negligible above the fatigue limit. In such conditions, parameters using both strain and stress components (e.g. Fatemi-Socie parameter) can be required to account for different stress-strain response between in-phase and out-of-phase loadings. Better life predictions could be obtained for high λ out-of-phase loadings but the detrimental effect observed in the special loading case ($\phi=90^0$; $\lambda=0.5$) could not be taken into account.

Underaged and overaged 7075 aluminum alloys have been tested in three loading conditions: axial fatigue, torsional fatigue and torsional fatigue with static tension. Based on the observations of the fatigue cracking behavior and on the analysis of the fatigue life results, the following conclusions are drawn:

- Cracks occur on the weakest plane. Two types of weakness exist in fatigue of 7075 aluminum alloy: intrinsic weakness caused by the material anisotropy and extrinsic

weakness caused by the applied loading. The former makes the longitudinal plane weaker, and the latter favors the so-called critical planes as the possible cracking planes. As a result, there are two types of fatigue cracking mechanisms: the anisotropy-enhanced failure mechanism and the critical-plane failure mechanism. These two mechanisms compete and the fastest one determines the fatigue failure.

- Under axial fatigue, anisotropy effects are not observed in both underaged and overaged materials, since the weak plane caused by the material anisotropy is not submitted to a shear stress.

- Under torsional fatigue, anisotropy does have important effects, since the longitudinal maximum shear plane coincides with the weak plane. As a result, longitudinal shear cracking occurs in both materials, especially at high stress level.

- Under torsional fatigue with static tension, the competition between the two mechanisms results in two kinds of fractures: 1) transverse shear cracking in the overaged material once a tensile load is applied; 2) longitudinal shear cracking in the underaged material as long as the applied static tensile load is not high enough.

- Material anisotropy effects are more important in the underaged material. Inclusion fibering plays a role in both materials, but the combination of {111} texture and planar slip enhances the weakness of the underaged material in the longitudinal direction.

- At the same maximum shear stress amplitude, the torsional fatigue life is higher than the axial fatigue life in the overaged material, and the application of static tension decreases the torsional fatigue life. A different trend is observed in the underaged material. The axial fatigue life is higher than the torsional fatigue life, and the

application of static tension does not have much influence on the torsional fatigue life.

- These life differences are attributed to the differences in the fatigue mechanisms. In the overaged material, material anisotropy effect is not important. A conventional fatigue life parameter (e.g., the McDiarmid parameter) can give a good correlation of the fatigue lives under different loading conditions. In the case of the strong anisotropy effects in the underaged material, two stress-life relations are needed to describe the two different mechanisms. Each stress-life relation can be calibrated by different loading cases giving the same mechanism. For a given loading case, the lower life computed from the two relations is taken as the predicted life. However, these conclusions are based on a limited number of tests. Further investigation is required for confirmation.

Axial and torsional fatigue tests were performed on two types of circumferentially V-notched cylindrical specimens (with a same notch angle of 90^0, but different notch depths) made of as-rolled 1045 steel. The study of the fatigue behavior of these notched specimens leads to the following conclusions:

- Notch effects in axial fatigue are more significant than in torsional fatigue. Firstly, the fatigue notch factor is higher in axial fatigue than in torsional fatigue. Secondly, the notch size effect is more pronounced in axial fatigue than that in torsional fatigue.

- Detailed FEM stress analysis shows that in axial fatigue, the notch stress concentration (σ_{zz}/σ_{net}) is higher than that in torsional fatigue ($\tau_{z\theta}/\tau_{net}$). This difference explains the different notch effects observed in axial fatigue and in torsional fatigue.

- The observation of the fracture surfaces in the V-notched specimens shows that mode I fracture prevails in both axial and torsional fatigue. The fracture surface in axial

fatigue is macroscopically flat, while the "factory-roof" fracture is observed under torsional loading. The torsional resistance to crack propagation is almost the same as that to crack initiation in the smooth specimens, if comparison is based on the nominal shear stress.

- The stress analysis also shows that the stress fields at the V-notch tip are singular under both mode I and mode III loadings. These stress fields are characterized by mode I and mode III notch stress intensity factors. The same stress field should give the same fatigue events. Very good experimental confirmation was obtained. Both mode I and mode III notch stress intensity factors can correlate well the fatigue lives from notches of different depth under axial and torsional loadings, respectively. These correlations open the door for a future study on notch fatigue behavior under combined axial-torsional loadings. Fatigue life is expected to be a function of mode I and mode III notch stress intensity factors.

Fatigue life prediction must be based on a good understanding of the fatigue mechanisms. For smooth specimens made of materials dominated by a shear cracking (1045 steel and 7075 aluminum alloy), shear-type critical plane parameters (e.g. McDiarmid, Fatemi-Socie) are appropriate. But modification is necessary to take into account the more damaging mechanisms in the special loading case (same shear stress amplitude on all planes) in order to have conservative life prediction. In the case of strong anisotropy effects (underaged 7075 aluminum alloy), the anisotropy-enhanced cracking mechanism should also be taken into account in fatigue life prediction. For severe notches, fatigue cracking is a propagation-controlled process, and a Fracture Mechanics approach is needed to correlate the notch fatigue lives. The stress fields at a V-notch tip can be characterized by the notch stress intensity factors under both mode I and mode III loadings. The mode I and mode III notch stress intensity factors can correlate well the axial and torsional fatigue lives, respectively, for V-notches with the same angle but different geometries.

STATEMENT OF ORIGINALITY AND CONTRIBUTIONS TO KNOWLEDGE

In this study, several links between fatigue life prediction and fatigue cracking mechanisms have been established. The original contributions of this thesis are the following:

1. An extensive description of axial-torsional high cycle fatigue mechanisms in 1045 steel using replica technique and fractographic observation, wth a special attention paid to cracking mechanisms under non-proportional loadings.
2. An evaluation of the prediction errors of eight multiaxial fatigue life parameters under a variety of proportional and non-proportional loadings; and an analysis of these errors based on cracking mechanisms and stress analysis.
3. A modified critical-plane parameter proposed to account for the extra damage in the special loading case where shear stress amplitude is equal over all plane orientations, and to obtain at least conservative life prediction.
4. A critical evaluation of anisotropy effects in high cycle torsional fatigue behaviors of underaged and overaged 7075 aluminum alloy, including the description of competition of two different cracking mechanisms (critical plane failure mechanism and anisotropy-enhanced failure mechanism).
5. A model based on two stress-life relations proposed to predict biaxial fatigue life for an anisotropic material.
6. An evaluation of axial and torsional stress singularities and high cycle fatigue strengths of circumferential V-notched specimens of different depths.
7. A consolidation of notch size effects on axial and torsional fatigue life using mode I and mode III notch stress intensity factors, respectively.

REFERENCES

AKHURST, K.N., LINDLEY, T.C. and NIX, K.J. (1983). The effect of mode III loading on fatigue crack growth in a rotating shaft. Fatigue of Engineering Materials and Structures, 6, 345-348.

ASME Boiler and Pressure Vessel Code (1974), Section III, Division I, Subsection NA, Appendix XIV, American Society of Mechanical Engineers, New York.

BAIRSTOW, L. (1910). The elastic limits of iron and steel under cyclic variations of stress. Philosophical Transaction of the Royal Society, A210, 35-55.

BANNANTINE, J.A. and SOCIE, D.F. (1985). Observation of cracking behavior in tension and torsion low cycle fatigue. Low Cycle Fatigue, ASTM STP 942, American Society for Testing and Materials, Philadelphia, 899-921.

BARTOLOTTA, P.A., ELLIS, J.R. and ABDUL-AZIZ, A. (1997). A structure test facility for in-plane biaxial testing of advanced materials. Multiaxial Fatigue and Deformation Testing Techniques, ASTM STP 1280, S. Kalluri, P.J. Bonacuse, American Society for Testing and Materials, Philadelphia, 25-42.

BASINKSI, Z.S. and BASINSKI, S.J. (1985). Surface geometry in fatigued cooper crystals. Fundamentals of Deformation and Fracture, B.A. Bilby, K.J. Miller, J.R. Willis, Cambridge University Press, London, 583-894.

BOUKHAROUBA, T., TAMINE, T., NIU, L., CHEHIMI, C. and PLUVINAGE, G. (1995). The use of notch stress intensity factor as a fatigue crack initiation parameter. Engineering Fracture Mechanics, 52, 503-512.

BOWLES, C.Q. and SCHIJVE, J. (1973). The roles of inclusions in fatigue crack initiation in an aluminum alloy. International Journal of Fracture, 9, 171-179.

BRIDGMAN, P.W. (1952). Studies in Large Plastic Flow and Fracture (1st edition). McGraw-Hill, New York.

BROWN, M.W. (1988). Multiaxial fatigue crack propagation behavior. Advances in Fatigue Science and Technology, NATO ASI Series, Series E: Applied Science, vol. 159, C. Moura Branco and L. Guerra Rosa, Kluwer Academic Publishers, 363-386.

BROWN, M.W. (1988). Analysis and design methods in multiaxial fatigue. Advances in Fatigue Science and Technology, NATO ASI Series, Series E: Applied Science, vol. 159, C. Moura Branco and L. Guerra Rosa, Kluwer Academic Publishers, 387-401.

BROWN, M.W., HAY, E. and MILLER, K.J. (1985). Fatigue at notches subjected to reversed torsion and static axial loads. Fatigue and Fracture of Engineering Materials and Structures, 8, 243-258.

BROWN, M.W. and MILLER, K.J. (1973). A theory for fatigue failure under multiaxial stress-strain conditions. Proceeding of Institution of Mechanical Engineers, 187, 745-755.

BROWN, M.W. and MILLER K.J. (1979). Initiation and growth of cracks in biaxial fatigue. Fatigue of Engineering Materials and Structures, 1, 231-246.

BROWN, M.W. and MILLER, K.J. (1985). Mode I fatigue crack growth under biaxial stress under at room and elevated temperature. Multiaxial Fatigue, ASTM STP 853, K.J. Miller, M.W., Brown, American Society for Testing and Materials, Philadelphia, 135-152.

CARTER, R.D., LEE, E.W., STARKE, E.A. JR. and BEEVERS, C.J. (1984). The effects of microstructure and environment on fatigue crack closure of 7475 aluminum alloy. Metallurgica Transactions A, 15A, 555-563.

Cases of the ASME Boiler and Pressure Vessel Code (1978), Code Case N-47-12, American Society of Mechanical Engineers, New York.

CHU, C.C., CONLE, F.A. and BONNEN, J.J.F. (1993). Multiaxial stress-strain modeling and fatigue life prediction of SAE axle shafts. Advances in Multiaxial Fatigue, ASTM STP 1191, D.L.McDowell, R.Ellis, ASTM, Philadelphia, 37-54.

COFFIN, L.F. (1954). A study of the effects of cyclic thermal stresses on a ductile metal. Transaction of the American Society of Mechanical Engineers, 76, 931-950.

COTTRELL, A.H. and HULL, D. (1957). Extrusion and intrusion by cyclic clip in copper. Proceedings of Royal Society, London, A242, 211-213.

CROSSLAND, B. (1956). Effect of large hydrostatic pressure on torsional fatigue strength of an alloy steel. Proceedings of International Conference of Fatigue of Metals, Institution of Mechanical Engineers, London, 138-149.

CUMMINGS, H.N., STULEN, F.B. and SCHULTE, W.C. (1958). Tentative fatigue strength reduction factors for silicate-type inclusions in high strength steels. Proceedings of the American Society for Testing and Materials, 58, 505-512.

DANG-VAN, K. (1993). Macro-micro approach in high-cycle multiaxial fatigue. Advances in Multiaxial Fatigue, ASTM STP 1191, D.L.McDowell, R. Ellis, American Society for Testing and Materials, Philadelphia, 120-130

DANG-VAN, K., GRIEVEAU, B. and MESSAGE, A. (1989). On a new multiaxial fatigue limit criterion: Theory and Application. Biaxial and Multiaxial fatigue, EGF Publication 3, M.W. Brown, K.J. Miller, Mechanical Engineering Publications Limited, London, 479-496.

DOONG, S.H., SOCIE, D.F. and ROBERTSON, I.M. (1990). Dislocation substructures and Nonproportional hardening. Journal of Engineering Materials and Technology, 112, 456-464.

DOUQUET, V. (1997). Crack initiation mechanisms in torsional fatigue. Fatigue and Fracture of Engineering Materials and Structures, 20, 227-235.

DOQUET, V. (1998). A first stage in the development of micromechanical simulations of the crystallographic propagation of fatigue cracks under multiaxial loading. Fatigue and Fracture of Engineering Materials and Structures, 21, 661-672.

DOWNING, S.D. and GILLIART, D.R. (1985). A fatigue test system for a notched shaft in combined bending and torsion. Multiaxial Fatigue, ASTM STP 853, K.J. Miller, M.W. Brown, American Society for Testing and Materials, Philadelphia, 24-32.

DUUN, M., SUWITO, W., CUNNINGHAM, S. and MAY, C.W. (1997). Fracture initiation at sharp nocthes under mode I, mode II, and miled mixed mode loading. International Journal of Fracture, 84, 367-381.

ELBER, W. (1970). Fatigue crack closure under cyclic tension. Engineering Frcature Mechanics, 2, 37-45.

ELBER, W. (1971). The significance of crack closure. Damage Tolerance in Aircraft Structures, ASTM STP 486, American Society for Testing and Materials, Philadelphia, 230-242.

EI-MAGED, E. and MIELKE, S. (1977). Dauerfestikkeit bei uberlangter zweiachsiger statische bearspruchung. Konstruktion, 26, 253-257.

ELLIS, J.R. and BARTOLOTTA, P.A. (1997). Adjustable work coil fixture facilitating the use of induction heating in mechanical testing. Multiaxial Fatigue and Deformation Testing Techniques, ASTM STP 1280, S. Kalluri, P.J. Bonacuse, American Society for Testing and Materials, Philadelphia, 43-62

ELLYIN, F. and KUJAWSKI, D. (1984). Plastic strain energy in fatigue failure. Journal of Engineering Materials and Technology, 106, 342-347.

ELLYIN, F. and KUJAWSKI, D. (1993). A multiaxial fatigue criterion including mean stress effect. Advance in Multiaxial Fatigue, ASTM STP 1191, D.L McDowell, R. Ellis, American Society for Testing and Materials, Philadelphia, 55-66.

ELLYIN, F. AND VALAIRE, B. (1982). High strain multiaxial fatigue. Journal of Engineering Materials and Technology, 104, 165-173.

ERDOGAN, F. and SIH, G.C. (1963). On the crack extension in plates under plane loading and transverse shear. J. Basic Engng., 85, 519-525.

EWING, J.A. and HUMFREY, J.C. (1903). The fracture of metals under repeated alternations of stress. Philosophical Transaction of the Royal Society, 200, 241-250.

EWING, J.A. and ROSENHAIN, W. (1900). Experiments in micro-metallurgy: Effects of strain, preliminary notice. Philosophical Transaction of the Royal Society, 199, 85-90.

FASH, J.W. (1983). An evaluation of damage development during multiaxial fatigue of smooth and notched specimens. PhD Thesis, University of Illinois at Urbana-Champaign.

FASH, J.W., SOCIE, D.F. and MCDOWELL, D.L. (1985). Fatigue life estimates for a simple notched component under biaxial loading. Multiaxial Fatigue, ASTM STP 853, K.J. Miller, M.W. Brown, American Society for Testing and Materials, Philadelphia, 497-513.

FATEMI, A. (1985). PhD thesis. Mechanical Engineering, University of Iowa.

FATEMI, A., FANG, D. AND ZENG, Z. (2002). Notched fatigue behavior under axial and torsional load: experiments and predictions. Proceeding of 8th International Fatigue Congress (Fatigue 2002), A. F. Blom, Stockholm, Sweden, 1905-1914.

FATEMI, A. and KURATH, P. (1988). Multiaxial fatigue life predictions under the influence of mean-stresses. Journal of Engineering Materials and Technology, 110, 380-388.

FATEMI, A. and SOCIE D.F. (1988). Multiaxial fatigue: damage mechanisms and life predictions. Advances in Fatigue Science and Technology, NATO ASI Series, Series E: Applied Science, vol. 159, C. Moura Branco and L. Guerra Rosa, Kluwer Academic Publishers, 877-890.

FATEMI, A. and SOCIE, D.F. (1988). A critical plane approach to multiaxial fatigue damage including out-of-phase loading. Fatigue and Fracture of Engineering Materials and Structures, 11, 149-156.

FATEMI, A. and STEPHENS, R.I. (1987). Biaxial fatigue of 1045 steel under in-phase and out-of-phase loading. Multiaxial Fatigue: Analysis and Experiments, AE-14, Society of Automotive Engineers, 121-137.

FERNANDO, U.S. (1982). A new machine for multiaxial fatigue testing. M. Eng., Thesis, University of Sheffield, UK.

FIGUEROA, J.C. and LAIRD, C. (1983). Crack initiation mechanisms in copper polycrystals cycled under constant strain amplitudes and the in step tests. Materials Science and Engineering, 60, 45-58.

FINDLEY, W.N. (1959). A theory for the effect of mean stress on fatigue of metals under combined torsion and axial load or bending. Journal of Engineering for Industry, 301-306

FINDLEY, W.N., COLEMAN, J.J. and HANLEY, B.C. (1956). Theory for combined Bending and torsion fatigue with data for SAE 4340 steel. The Institution of Mechanical Engineers, Proceedings of International Conference of Fatigue of Metals, London, England, 150.

FINES, M.E. and RITCHIE, R.O. (1979). Fatigue initiation and near threshold growth. Fatigue and Microstructure, ASM, Metal Park, OH, 245.

FROST, N. E. and PHILLIPS, C.E., (1956). Studies in the formation and propagation of cracks in fatigue specimens. Proceedings of the International Conference of Fatigue of Metals, ImechE/ASME, pp.520-526.

FRORSTEY, C., and LASSERRE, S. (1989). Multiaxial fatigue endurance of 30NCD16 steel. International Journal of Fatigue, 11, 169-175.

FORSYTH, P.J.E. (1953). Exudation of material from slip bands at surface of fatigued crystals of an aluminum-copper alloy. Nature, 171, 172-173.

FORSYTH, P.J.E. (1957). Slip bands damage and extrusions. Proceedings of Royal Society, London, A242, 198-202.

FORSYTH, P.J.E. (1961). A two stage process of fatigue crack growth. Crack Propagation: Proceeding of Cranfield Symposium, Her Majesty's Stationary Office, London, 76-94.

FORSYTH, P.J.E. and RYDER D.A. (1960). Fatigue fracture. Aircraft Engineering, 32, 96-99.

FOUND, M. S., FERNANDO, U.S. and MILLER, K. J. (1985). Requirements of a new multiaxial fatigue testing facility. Multiaxial Fatigue, ASTM STP 853, K. J. Miller, M. W. Brown, American Society for Testing and Materials, Philadelphia, 11-23.

GAO, H., BROWN, M.W. and MILLER, K.J. (1982). Mixed mode fatigue crack thresholds. Fatigue of Engineering Materials and Structures, 5, 1-17.

GAO, H., ALAGOK, N., BROWN, M.W. and MILLER, K.J. (1985). Growth of fatigue cracks under combined mode I and mode II loadings. Multiaxial Fatigue, ASTM STP 853, K.J. Miller, M.W. Brown, American Society for Testing and Materials, Philadelphia, 184-202.

GARUD, Y.S. (1981). A new approach to evaluation of fatigue under multiaxial loadings. Journal of Engineering Materials and Technology, 103, 118-125.

GLINKA, G., SHEN, G. and PLUMTREE, A. (1995). A multiaxial strain energy density parameter related to the critical plane. Fatigue and Fracture of Engineering Materials and Structures, 18, 37-46.

GLINKA, G., WANG, G. and PLUMTREE, A. (1995). Mean stress effects on multiaxial fatigue. Fatigue and Fracture of Engineering Materials and Structures, 18, 755-764.

GOODMAN, J. (1899). Mechanics Applied to Engineering. Longmans Green, London.

GOTO, M. (1994). Statistical investigation of the behavior of small cracks and fatigue life in carbon steels with different ferrite grain sizes. Fatigue and Fracture of Engineering Materials and Structures, 17, 635-649.

GONYEA, D.C. (1973). Method for low cycle fatigue design including biaxial stress and notch effects. Fatigue at Elevated Temperature, ASTM STP 520, American Society for Testing and Materials, Philadelphia, 678-687.

GOUGH, H.J. (1933). Crystalline structure in relation to the failure of metals - especially by fatigue. Edgar Marburg Lecture. Porceedings of the Royal Society, A104, 535-565.

GOUGH, H.J., (1949). Engineering steels under combined cyclic and static stresses. Proc. Inst. Mech. Engrs, 160, 472-491.

GOUGH, H.J. and POLLARD, H.V., and CLEASHAW, W.J. (1951). Some experiments on the resistance of metals under combined stresses. Aeronautical Research Council Reports and Memoranda, 2522, HMSO, London.

GRUBISIC, V. and SINBURGER, A. (1976). Fatigue under combine out-of-phase multiaxial stress. Fatigue and Test Design, 2, Proc. S.E.E., Int. Conf. 5, London, 27.1-27.8.

HAIGH, B.P. (1917). Experiments on the fatigue of brasses. Journal of the Institute of Metals, 18, 55-77.

HOBSON, P.D. (1982). The formulation of crack growth equation for short cracks. Fatigue and Fracture of Engineering Materials and Structures, 5, 323-327.

HOFFMAN, M. and SEEGER, T. (1985). Journal of Materials and Technology, 107, 250-258.

HOURLIER, F., MCLEAN, D. and PINEAU, A. (1978). Fatigue crack growth behavior of Ti-5Al-2.5Sn alloy under complex stress (Mode I +static mode III). Metals Technology, 5, 154-158.

HUA, C.T. and SOCIE, D.F. (1984). Fatigue damage in 1045 steel under constant amplitude biaxial loading. Fatigue and Fracture of Engineering Materials and Structures, 7, 165-179.

HUA, C.T. and SOCIE, D.F. (1985). Fatigue damage in 1045 steel under variable amplitude loading. Fatigue and Fracture of Engineering Materials and Structures, 8, 101-114.

IRWIN, G.R. (1957). Analysis of stresses and strains near the end of a crack traversing a plate. Journal of Applied Mechanics, 24, 361-364.

ITOH, T., SAKANE, M., OHANAMI, M. and SOCIE, D.F. (1995). Nonproportional low cycle fatigue criterion for type 304 stainless steel. Journal of Engineering Materials and Technology, 117, 285-292.

JORDAN, E.H., BROWN, M.W. and MILLER, K.J. (1985). Fatigue under severe non-proportional loading. Multiaxial Fatigue, ASTM STP 853, K.J. Miller, M.W. Brown, American Society for Testing and Materials, Philadelphia, 569-585.

KADI, N. AND PLUVINAGE, G. (2002). Analysis of fatigue failure for shafts with key-seats: application of volumetric approach. Fatigue 2002, A.F. Blom, Stockholm, Sweden, EMAS, 1865-1872.

KANAZAWA, K., MILLER, K. J. and BROWN, M.W. (1977). Low cycle fatigue under out-of-phase loading conditions. Journal of Engineering Materials and Technology, 99, 222-228.

KANDIL, F.A., BROWN, M.W. and MILLER, K.J. (1982). Biaxial low cycle fatigue fracture of 316 stainless steel at elevated temperatures. Book 280, The Metal Society, London, 203-210.

KAWANO, K. and NISITANI, H. (1970). Fatigue limits and non-propagating crack and torsional fatigue of notched or shouldered specimens. Thirteen Japan Congress on Materials Research-Metallic Materials, pp.73-76.

KAYNAK, C., ANKARA, A. and BAKER, T.J. (1996). Inclusion induced anisotropy of short fatigue crack growth in steel. Material Science and Technology, 12, 557-562.

KIM, W.H. and LAIRD, C. (1978). Crack nucleation and stage I propagation in high strain fatigue- II. Mechanism. Acta Metallurgica, 26, 789-799.

KITAGAWA, H., TAKAHASHI, S., SUH, C.M. and MIYASHITA, M. (1979). Quantitative analysis of fatigue process-microcracks and slip lines under cyclic strains. ASTM STP 675, American Society for Testing and Materials, Philadelphia, 420-449.

KLAN, D.A., TIPTON, S.M. and CORDES, T.S. (1993). Notch stress and strain estimation considering multiaxial strains. SAE, Jour. Mater. Manuf., 321-331.

KREMPL, E. (1974). Multiaxial fatigue, present and future methods of correction. AGARD conference proceeding, 155, NATO, Advisory Group for R & D, Neuilly Sur Seine, France, 5.1-5.12

LAIRD, C. AND SMITH, G.C. (1962). Crack propagation in high stress fatigue. Philosophical Magazine, 8, 847-857.

LAMBA, H.S. and SIDEBOTTOM, O.M. (1978). Cyclic plasticity for nonproportional Paths, Part 1 & II. Journal of Engineering Materials and Technology, 100, 96-110.

LANGER, B.F. (1971). Pressure Vessel Engineering, R.W. Nichols, Elsevier Publishing Co., Amsterdam, 59-100.

LANKFORD, J. and KUSENBERGER, F.N. (1973). Initiation of fatigue cracks in 4340 steels. Metallurgical Transaction, 4A, 553-559.

LAZZARIN, O. and LIVIERI, P. (2001). Notch stress intensity factors and fatigue strength of aluminum and steel welded joints. International Journal of Fatigue, 23, 225-232.

LAZZARIN, O. and TOVO, R. (1998). A Notch stress intensity factor to the stress analysis of welds. Fatigue and Fracture of Engineering Materials and Structures, 21, 1089-1103.

LEE, S.B. (1985). A criterion for fully reversed out-of-phase torsion and bending. Multiaxial Fatigue, ASTM STP 853, K.J. Miller, M.W. Brown, American Society for Testing and Materials, Philadelphia, 553-568.

LEE, S.B. (1989). Out-of-phase combined bending and torsion fatigue of steels. Biaxial and Multiaxial Fatigue, M.W. Brown, K.J. Miller, Mechanical Engineering Publications, London, 621-634.

LEESE, G.E. and MORROW, J. (1985). Low cycle fatigue properties of 1045 steel in torsion. Multiaxial Fatigue, ASTM STP 853, K.J Miller, M.W. Brown, American Society for Testing and Materials, Philadelphia, 482-496.

LEIS, B.N., AHMAD, J. and KANNINEN, M.F. (1985). Effect of Local Stress State on the Growth of Short Cracks. Multiaxial Fatigue, ASTM STP 853, K.J. Miller, M.W. Brown, American Society for Testing and Materials, Philadelphia, 314-339.

LIN, H. and NAYEB-HASHEMI, H. (1993). Effects of materials anisotropy on cyclic deformation and biaxial fatigue behavior of Al-6061-T6. Advances in Multiaxial Fatigue, ASTM STP 1191, D.L. McDowell, R. Ellis, American Society for Testing and Materials, Philadelphia, 151-182.

LISSENDEN, C.J., LERCH, B.A., ELLIS, J.R. and ROBINSON, D.W. (1997). Experimental determination of yield and flow surfaces under axial-torsional loading. Multiaxial Fatigue and Deformation Testing Techniques, ASTM STP 1280, S. Kalluri, P.J. Bonacuse, American Society for Testing and Materials, Philadelphia,92-112.

LIU, K.C. (1993). A method based on virtual strain energy parameters for multiaxial fatigue life prediction. Advance in Multiaxial Fatigue, ASTM STP 1191, D.L. McDowell, R. Ellis, American Society for Testing and Materials, Philadelphia, 67-84.

LOHR, R. D. and ELLISON, E, G. (1980). A simple theory for low cycle multiaxial fatigue. Fatigue and Fracture of Engineering Materials and Structures, 3, 1-17.

MA, B.T. and LAIRD, C. (1989). Overview of fatigue behavior in copper single crystals – I. Surface morphology and stage I crack initiation sites for tests under constant strain amplitude. Acta Metallurgica, 37, 325-336.

MACHA, E. and SONSINO, C.M. (1999). Energy criteria of multiaxial fatigue failure. Fatigue & Fracture of Engineering Materials and Structures, 22, 1053-1070.

MAKABE, C. AND SOCIE, D.F. (2001). Crack growth mechanism in precracked torsional fatigue specimens. Fatigue & Fracture of Engineering Materials and Structures, 24, 607-615.

MANSON, S.S. (1954). Behavior of materials under conditions of thermal stress. National Advisory Commission on Aeronautics: Report 1170. Cleveland: Lewis Flight Propulsion Laboratory.

MARQUIS, G. and SOCIE, D.F. (2000). Long-life torsion fatigue with normal mean stresses. Fatigue and Fracture of Engineering Materials and Structures, 23, 293-300.

MCCLINTOCK, F.A. (1963). On the plasticity of the growth of fatigue cracks. Fracture of Solids, D.C. Ducker, G.G. Gilman, 20, New York: Wiley, 65-102.

RICE, J.R. (1967). Mechanics of crack deformation and extension by fatigue. Fatigue Crack Propagation, ASTM STP 415, American Society for Testing and Materials, Philadelphia, 247-309.

MCDIARMID, D.L. (1981). A criterion of fatigue failure under out-of-phase multiaxial stresses. Proc. Cam. Cong. App. Mech., 245-246

MCDIARMID, D.L. (1987). Fatigue under out-of-phase bending and torsion. Fatigue and Fracture of Engineering Materials and Structures, 9, 457-475.

MCDIARMID, D.L. (1990). A general criterion for high cycle multiaxial fatigue failure. Fatigue and Fracture of Engineering Materials and Structures, 14, 429-454

MCDIARMID, D.L. (1991). A general criterion for high cycle multiaxial fatigue failure. Fatigue and Fracture of Engineering Materials and Structures, 14, 429-453

MCDIARMID, D.L. (1994). A shear stress based critical-plane criterion of multiaxial fatigue failure for design and life prediction. Fatigue and Fracture of Engineering materials and Structures, 17, 1475-1484.

MCDOWELL, D.L. and BERARD, J.Y. (1990). A ΔJ based approach for biaxial low-cycle fatigue of shear damage materials. Fatigue under Biaxial and Multiaxial Loading, ESIS 10, K. Kussmaul, D. McDiarmid, Socie, 413-431.

MCDOWELL, D.L. and BERARD, J.Y. (1992). A ΔJ based approach to biaxial fatigue. Fatigue and Fracture of Engineering Materials and Structures, 15, 719-741.

MCDOWELL, D.L. and BENNETT, (1995). A macrocrack growth law for multiaxial fatigue. Fatigue and Fracture of Engineering Materials and Structures, 19, 821-837.

MCDOWELL, D.L. and POINDEXTER, V. (1994). Multiaxial fatigue modeling based on the microcrack propagation: stress states and amplitude effects. Proceeding Fourth International Conference on Biaxial/Multiaxial Fatigue, 1, SF2M/ESIS, 115-130.

MCDOWELL, D.L. AND SOCIE, D.F. (1985). Transient and stable deformation behavior under cyclic nonproportional loading. Multiaxial Fatigue, ASTM STP 853, K.J. Miller, M.W. Brown, American Society for Testing and Materials, Philadelphia, 64-87.

MILLER, K.J. (1991). Metal fatigue-past, current and future. Proc. Inst. Mech. Engrs., 205, 1-14.

MILLER, K.J. and CHANDLER, D.C. High strain torsion fatigue of solid and tubular specimens. Proc. Inst. Mech. Engrs., 184, part1, No.25, 433-448.

MILLER, K.J. and BROWN, M.W. (1985). Multiaxial fatigue: a brief review. Advance in Fracture Research, P.R. Rio, J.F. Knott, R. Dunley, Pergamon Press, Oxford, 31-56.

MINER, M.A. (1945). Cumulative damage in fatigue. Journal of Applied Mechanics, 12, 159-164.

MUGHRABI, H., WANG, R. DIFFERT, K. and ESSMANN, U. (1983). Fatigue crack initiation by cyclic irreversibilities in high-cycle fatigue. Quantitative Measurement of Physical Damage, ASTM STP 811, J. Lankford, D.L. Davidson, W.L. Morris, R.P. Wei, ASTM, Philadelphia, 5-45.

NAYEB-HASHEMI, H., MCCLINTOCK, F.A. and RITCHIE, R.O. (1983a). Micromechanically modeling of mode III fatigue crack growth in rotor steels. International Journal of Fracture, 23, 163-185.

NAYEB-HASHEMI, H., MCCLINTOCK, F.A. and RITCHIE, R.O. (1983b). Influence of overloads and block loading on mode III fatigue crack propagation in A469 rotor steel. Engineering Fracture Mechanics, 18, 736-783.

NEUBER, H. (1958). Theory of Notch Stresses, Springer, Berlin.

NEUMANN, P. (1969). Coarse slip model of fatigue. Acta Metallurgica, 17, 1219-1225.

NISITANI, H. and KAWANO, K. (1968). Non-propagating crack and crack strength of shafts with shoulder fillets subjected to rotating bending. Eleventh Japan Congress on Material Research-metallic Materials, 49-51.

NIE, B. and VERREMAN, Y. (1999). An initiation life prediction model for fatigue cracks in weld joints. Proceeding Fatigue'99: Seventh International Fatigue Congress, X.R. Wu, Z.G. Wang, High Education Press, Beijing, China, 1297-1302.

NISHIHARA, T. and KAWAMOTO, M. (1945). The strength of metals under combined alternating bending and torsion with phase difference. Memoirs, college of Engineering, 11, Kyoto Imperial University, 85-112

OHJI, K., OGURA, K., HARADA, S. and HASHIMOTO, T. (1976). Fatigue behavior of anisotropic rolled steel plates under cyclic torsion. Bulletin of JSME, 19, 1236-1244.

OHKAWA, I., TAKAHASHI, H., MORIWAKI, M. and MISUMI, M. (1997). A study on fatigue crack growth under out-of-phase combined loadings. Fatigue and Fracture of Engineering Materials and Structures, 20, 929-940.

OTSUKA, A., MORI, K. and MIYATA, T. (1975). The condition of fatigue crack growth in mixed mode condition. Engineering Fracture Mechanics, 7, 429-439.

OTASUKA, A., MORI, K. and TSUYAMA, S. (1981). Mode II fatigue crack propagation in aluminum alloy and mild steel. Proceeding of 5th International Conference on Fracture, Cannes, Pergamon Press, Oxford, 1851-1859.

OTASUKA, A., TOHGO, K., KIBA, T. and YAMADA, S. (1984). Mode II fatigue crack growth characteristics and mechanism in aluminum alloy 7N01-T4 weldments under mode II loading. Proceeding of the Sixth International Conference of Fracture, New Delhi, India, Pergamon Press, Oxford, 1671-1678.

PALMGREN, A. (1924). Die lebensdauer von kugellagern. Zeitschrift des Vereins Deutscher Ingenieure, 68, 339-341.

PAPADOPOULOS, I.V. (1994). A new criterion of strength for out-of-phase bending and torsion of hard metal. International Journal of Fatigue, 16, 377-384.

PAPADOPOULOS, I.V. (1995). A high-cycle fatigue criterion applied in biaxial and triaxial out-of-phase stress conditions. Fatigue Fract. Engng. Mater. Struct., 18, 79-91.

PAPADOPOULOS, I.V. (2001). Long life fatigue under multiaxial loading. International Journal of Fatigue, 23, 839-849.

PAPADOPOULOS, I.V., DAVOLI, P., GORLA, C., FILIPPINI, M. and BERASCONI, A. (1997). A comparative study of multiaxial high-cycle fatigue criteria for metals. International Journal of Fatigue, 19, 219-235,

PARIS, P.C. and ERDOGAN, F. (1963). A critical analysis of crack propagation laws. Journal of Basic Engineering, 85, 528-534.

PARIS, P.C., GOMEZ, M.P. and ANDERSON, W.P. (1961). A rational analytic theory of fatigue. The Trend in Engineering, 13, 9-14.

PARK J. and NELSON D. (2000). Evaluation of an energy-based approach and a critical plane approach for predicting constant amplitude multiaxial fatigue life. International Journal of Fatigue, 22, 23-29.

PARSONS, M.W. and PASCOE, K.J. (1976). Observation of surface deformation, crack initiation and crack growth in steels under biaxial stress. Materials Science and Engineering, 22, 31-50.

PASCOE, K.J. AND DEVILLIERS, J.W.R. (1967). Low cycle fatigue of steels under biaxial straining. Journal of Strain Analysis, 2, 117-126.

PEARSON, S. (1975). Initiation of fatigue cracks in commercial aluminum alloys and the subsequent propagation of very short cracks. Engineering Fracture Mechanics, 7, 235-247.

PEREZ CATBONELL, E. and BROWN, M.W. (1986). A study of short crack growth in torsional low cycle fatigue for medium carbon steel. Fatigue and Fracture of Engineering Materials and Structures, 9, 15-33.

PETERSON, R.E. (1959). Metal Fatigue, G. Sines and J.L.Waisman, McGraw Hill, New York, 293-306.

PETERSON, R.E. (1974). Stress Concentration Design Factors (2nd Edition). Wiley, New York.

PLUMBRIDGE, W.J. (1972). Review: Fatigue-crack propagation in metallic and polymetric materials. Journal of Materials Science, 7, 939-962.

RADAKRISHANAN, V.M. (1980). An analysis of low cycle fatigue based on hysteresis energy. Fatigue and Fracture of Engineering Materials and Structures, 3, 75-84.

RITCHIE, R.O., SURESH, S. and MOSS, C.M. (1980). Near threshold fatigue crack growth in 2¼Cr-1Mo pressure vessel steel in air and hydrogen. Journal of Engineering Materials and Technology, 102, 293-299.

SAKANE, M., OHNAMI, M. and SAWADA, M. (1987). Fracture modes and low cycle biaxial fatigue life at elevated temperature. Journal of Engineering Materials and Technology, 109, 236-243.

SAKANE, M., OHNAMI, M. and HAMADA, N. (1988). Journal of Engineering Materials and Technology, 110, 48-54.

SHANG D.G. and WANG D.J. (1998). A new multiaxial fatigue damage models based on the critical plane approach. International Journal of Fatigue, 20, 241-245.

SHATIL, G., SMITH, D.J. and ELLISON, E.G. (1994). High strain biaxial fatigue of a structural steel. Fatigue and Fracture of Engineering Materials and Structures, 17, 159-170.

SINES, G. (1955). Failure of materials under combined repeated stresses with superimposed static stresses. NACA TN 3495, National Advisory Committee for Aeronautics, Washington D.C.

SINES, G. and OHGI, G. (1981). Fatigue criterion under combined stresses or strains. Journal of Engineering Materials and Technology, 103, 82-90.

SINES, G. and WASIMAN, J.L. (1959). Metal Fatigue, McGraw-Hill, 145-167.

SMITH, R.A. and MILLER, K.J. (1977). Fatigue cracks at notches. Int. J. Mech. Sci., 19, 11-22.

SMITH, R.A. and MILLER, K.J. (1978). Prediction of fatigue regimes in notched components. Int. J. Mech. Sci., 20, 201-206.

SMITH, M.C. and SMITH, R.A. (1988). Toward an understanding of mode II fatigue crack growth. Basic Question in Fatigue, ASTM STP 942, J.T. Fong, and K.J. Fields, ASTM, Philadelphia, 206-280.

SMITH, R.N, WATSON, P. and TOPPER, T.H. (1970). A stress-strain parameter for the fatigue of metals. Journal of Materials, 5, 767-778.

SOCIE, D.F. (1987). Multiaxial fatigue damage models. Journal of Engineering Materials and Technology, 109, 293-298.

SOCIE, D.F. (1993). Critical plane approaches for multiaxial fatigue damage assessment. Advances in Multiaxial Fatigue, ASTM STP 1191, D.L. McDowell and R. Ellis, ASTM, Philadelphia, 7-36.

SOCIE, D.F., KURATH, P. and KOCH, J.L. (1989). A multiaxial fatigue damage parameter. Biaxial and Multiaxial Fatigue, EGF Publication 3, Mechanical Engineering Publications Limited, London, 535-550.

SOCIE, D.F. and MARQUIS, G. (2000). Multiaxial Fatigue. Society of Automotive Engineers, Warrendal, Pa.

SOCIE, D.F., WAIL, L.A. and DITTER, D.F. (1985). Biaxial fatigue of Inconel 718 including mean stress effects. Multiaxial Fatigue, ASTM STP 853, K.J. Miller, M.W. Brown, ASTM, Philadelphia, 463-481.

SOCIE, D.F. and SHIELD, T.W. (1984). Mean stress effects in biaxial fatigue of Inconel 718. Journal of Engineering Materials and Technology, 106, 227-232.

SONSINO, C.M. and MADDOX, S.S. (2001). Multiaxial fatigue of welded structures-problems and present solution. Proceedings of 6th International Conference on Biaxial/Multiaxial Fatigue & Fracture, M. Moreira de Freitas, Lisboa, 3-15.

STULEN, F.B. and CUMMINGS, H.N. (1954). A failure criterion for multiaxial fatigue stresses. Proceedings of ASTM, 54, ASTM, Philadelphia, 822-830.

SURESH, S. (1998). Fatigue of Materials. Cambridge University Press.

SURESH, S. and RITCHIE, R.O. (1981). On the influence of fatigue underloads on cyclic crack at low stress intensities. Materials Science and Engineering, 51, 61-69.

SURESH, S., VASUDEVAN, A.K. and PERTZ, P.E. (1984). Mechanisms of slow fatigue crack growth in high strength aluminum alloys: role of microstructure and environment. Metallurgical Transaction A, 15A, 369-379.

TAIRA, S., INOUE, J. and TAKASHASHI, M. (1967). Low cycle fatigue under multiaxial stresses (In the cases of combined cyclic tension-compression and cyclic torsion in the same phase at elevated temperature). The 10th Japanese Congress on Testing Materials, 18-23.

TAKAHARA, M., KANESHIRO, M. and ENDO, T. (1972). Assumption for estimating the fatigue strength for notched specimen. Memory Kyushu Inst. Technol. Engng., 2, 55-98.

TANAKA, K. (1983). Engineering formulae for fatigue strength reduction due to crack-like notches. International Journal of Fracture, 22, R39-R45.

TANAKA, K., MATSUOKA, S. and KIMURA, M. (1984). Fatigue strength of 7075-T6 aluminum alloy under combined axial and torsion. Fatigue and Fracture of Engineering Materials and Structures, 7, 195-211.

TANAKA, K. and MURA, T. (1981). A Dislocation model for fatigue crack initiation. Journal of Applied Mechanics, 48, 97-100.

TAYLOR, D. (1999). Geometrical effects in fatigue: a unifying theoretical model. International Journal of Fatigue, 21, 413-420.

TAYLOR, D. and WANG, G. (2000). The validation of some methods of notch fatigue analysis. Fatigue and Fracture of Engineering Materials and Structures, 23, 387-394.

THOMPSON, N., WADSWORTH, N.J. and LOUAT, N. (1956). The origin of fatigue fracture in copper. Philosophical Magazine, 1, 113-126.

TIPTON, S.M. and BANNANTINE, J.A. (1993). Inelastic stress-strain predictions for multiaxial fatigue damage evaluation. Advances in Multiaxial Fatigue, ASTM STP 1191, D.L. McDowell, R. Ellis, ASTM, Philadelphia, 273-297.

TOVO, R. and LAZZARIN, O. (1999). Relationship between local and structural stress in the evaluation of the weld toe stress distribution. International Journal of Fatigue, 21, 1063-1078.

TSCHEGG, E.K. (1983). Mode III and mode I fatigue crack propagation behavior under torsional loading. Journal of Material Science, 18, 1604-1614.

TSCHEGG, E.K. (1983). Sliding mode crack closure and mode III fatigue crack growth behavior in mild steel. Acta Metallugica, 29, 1323-1330.

UMEDA, H., SAKANE, M. and OHMANI, M. (1990). Notch root displacement (NRD) approach to predict crack initiation life of notched specimen in higher temperature multiaxial fatigue. Journal of Engineering Materials and Technology, 112, 429-434.

VARVANI-FARAHANI, A. and TOPPER, T.H. (1999). Closure free biaxial fatigue crack growth rate and life prediction under various biaxiality ratios in SAE 1045 steel. Fatigue and Fracture of Engineering Materials and Structures, 22, 697-710.

VARVANI-FARAHANI, A. (2000). Energy-critical plane parameter for fatigue life assessment of a various metallic materials subjected to in-phase and out-of-phase multiaxial fatigue loading condition. International Journal of Fatigue, 22, 295-305.

VERPOEST, I., NOTOHARDJONO, B.D. and AERNOUDT, E. (1985). Fatigue of steel wire under combined tensile and shear loading conditions. Multiaxial Fatigue, ASTM STP 853, K.J. Miller, M.W. Brown, ASTM, Philadelphia, 361-377.

VERREMAN, Y. ET AL (1986). Fatigue short crack propagation and plasticity –induced crack closure at the toe of a fillet welded joint. The Behavior of Short Fatigue Crack, EGF Publication 1, K.J. Miller and E.R. de Los Rios, Mechanical Engineering Publications, London, 387-404.

VERREMAN, Y. (1987). Closure and propagation behavior of short fatigue cracks at different R-ratios. Fatigue 87, R.O. Ritchie, E.A. Starke Jr., EMAS, 371-380.

VERREMAN Y., BAILON, J.P. and MASOUNAVE, J. (1987). Fatigue of V-notch members: short crack behavior and endurance limit. Engineering Fracture Mechanics, 28, 773-783.

VERREMAN, Y. AND NIE, B. (1991). Short crack growth and coalescence along the toe of a manual fillet weld. Fatigue and Fracture of Engineering Materials and Structures, 14, 337-349.

VERREMAN, Y. and NIE, B. (1996). Early development of fatigue cracking at manual fillet welds. Fatigue and Fracture of Engineering Materials and Structures, 19, 669-681.

VERREMAN, Y. and ESPINOSA, G. (1997). Mechanically short fatigue cracks growth from notches in a mild steel. Fatigue and Fracture of Engineering Materials and Structures, 20, 129-142.

WAILL, L.E. (1983). Crack observation in biaxial fatigue. M.S. Thesis, University of Illinois at Urbana-Champaign.

WANG, C.H. and BROWN, M.W. (1993). A path-independent parameter for fatigue under proportional and non-proportional loading. Fatigue and Fracture of Engineering Materials and Structures, 16, 1285-1298.

WANG, C.H. and MILLER K.J. (1991). The effect of mean shear stress on torsional fatigue behavior. Fatigue and Fracture of Engineering Materials and Structures, 14, 293-307.

WANG, C.H. and MILLER, K.J. (1992). The effect of mean and alternating shear stress on short crack growth rates. Fatigue and Fracture of Engineering Materials and Structures, 15, 1223-1236.

WANG, C.H. and MILLER, K.J. (1993). Short fatigue crack growth under mean stress, uniaxial loading. Fatigue and Fracture of Engineering Materials and Structures, 16, 181-198.

WEIBULL, W. (1939). A statistical theory of the strength of materials. Proceeding 151. Stockholm: Royal Swedish Academy of Engineering Science.

WILLIAMS, R.A., PLACEK, R.J., KLUFAS, O., ADAMS, S.L. and GONYEA, D.C. (1985). Biaxial/torsional fatigue of turbine generator rotor steel. Multiaxial Fatigue, ASTM STP 853, K.J. Miller, M.W. Brown, ASTM, Philadelphia, 440-462.

WILLIAMS, M.L. (1952). Stress singularity resulting from various boundary conditions in angular corner of plates in extension. Journal of Applied Mechanics, 19, 526-528.

WILLIAMS, M.L. (1957). On the stress distribution at the base of a stationary crack. Journal of Applied Mechanics, 24, 109-114.

WÖHLER, A. (1860). Versuche über die festigkeit der eisenbahnwagenachsen. Zeitschrift für Bauwesen, 10.

WOOD, W.A. (1958). Formation of fatigue cracks. Philosophical Magazine, 3, 692-699.

YOKOBORI, T., YAMANOUCHI, H. and YAMMAMOTOM, S. (1965). Low cycle fatigue of thin-walled hollow-cylinder specimens of mild steel under uniaxial and torsional tests at constant strain amplitude. International Journal of Fracture Mechanics, 1, 3-13.

YOU B.R. and LEE S.B. (1996). A critical review on multiaxial fatigue assessments of metals. International Journal of Fatigue, 18, 235-244.

YOU, B.R. and LEE, S.B. (1997). Fatigue crack growth behavior of SM45C steel under cyclic mode I with superimposed static mode II loading. Fatigue and Fracture of Engineering Materials and Structures, 20, 1059-1074.

YOU, B.R. and LEE S.B. (1998). Fatigue crack growth behavior of SM45C steel under mixed-mode I and mode II loading. Fatigue and Fracture of Engineering Materials and Structures, 21, 1037-1048.

ZAMIRIK, S.Y. and FRISHMUTH R.E. (1973). The effects of out-of-phase loading biaxial strain cycling on low cycle fatigue. J. Exp. Mech., 13, 204-208

ZAMIRIK, S.Y., MIRDAMADI, M. and DAVIS, D.C. (1993). A proposed model for biaxial fatigue analysis using triaxiality factor concepts. Advance in Multiaxial Fatigue, ASTM STP1191, D.L. McDowell, R. Ellis, ASTM, Philadelphia, 85-106

ZAPPFE, C.A. and WORDEN, C.O. (1951). Fractographic registrations of fatigue. Transaction of American Society for Metals, 43, 958-969.

ZENNER, H., SIMBURGER, A. and LIU, J. (2000). On the fatigue limit of ductile metals under complex multiaxial loading. International Journal of Fatigue, 22, 137-145.

ZHANG, W. and AKID, R. (1997). Effects of biaxial mean stress on cyclic stress-strain response and behavior of short fatigue cracks in a high strength spring steel. Fatigue and Fracture of Engineering Materials and Structures, 20, 167-177.

ZHANG, W. and AKID, R. (1997). Mechanisms and fatigue performance of two steels in cyclic torsion with axial static tension/compression. Fatigue and Fracture of Engineering Materials and Structures, 20, 547-557.

APPENDIX I - STRESS ANALYSIS OF THE THIN-WALLED TUBULAR SPECIMEN UNDER AXIAL-TORSIONAL LOADING

This stress analysis is available in literature (Ohkawa et al, 1997). We remake it for our understanding and verification.

A tubular specimen is submitted to a combined axial-torsional cyclic loading as shown in Figure I.1. The applied axial and shear stresses (σ and τ) are:

$$\begin{cases} \sigma=\sigma_0 \sin\omega t & \text{(I.1)} \\ \tau=\tau_0 \sin(\omega t-\phi) & \text{(I.2)} \end{cases}$$

Where σ_0 and τ_0 are the applied axial and torsional stress amplitudes, respectively. ω is the angular frequency. ϕ is the phase angle between the applied shear and axial stresses. Stress ratio λ is defined as the ratio between the applied shear and normal stress amplitudes ($=\tau_0/\sigma_0$). The applied axial-torsional stress can be described with stress ratio λ and phase angle ϕ. $\lambda=0$ corresponds to axial fatigue, and $\lambda=\infty$ to torsional fatigue. $\phi=0^0$ corresponds to an in-phase loading and $\phi=90^0$ to a 90^0 out-of-phase loading.

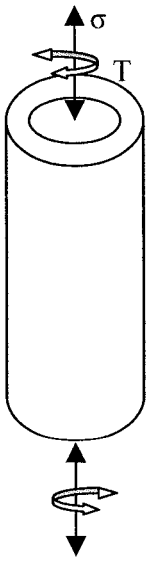

Figure I.1 Schema of a tubular specimen submitted to an axial-torsional loading.

The applied stress tensors for a general axial-torsional loading (stress-controlled high cycle fatigue) are:

$$\begin{pmatrix} \sigma_{zz} & \tau_{zT} & \tau_{zr} \\ \tau_{\theta z} & \sigma_{TT} & \tau_{Tr} \\ \tau_{rz} & \tau_{rT} & \sigma_{rr} \end{pmatrix} = \begin{pmatrix} \sigma_0 \sin\omega t & \tau_0 \sin(\omega t-\phi) & 0 \\ \tau_0 \sin(\omega t-\phi) & 0 & 0 \\ 0 & 0 & 0 \end{pmatrix}$$

Here z corresponds to the specimen axis, T to the circumferential (tangential) direction (the letter "T" is used not to confuse with the plane angle "θ") and r to the radial direction.

The Mohr circle of a general axial-torsional loading is schematized in Figure I.2. The plane of maximum shear (τ_{max}) is perpendicular to the specimen surface plane zT. The normal of the maximum shear plane lies in the surface plane, and the angle between its normal and the specimen axis is determined by the applied stress system (λ and ϕ). Note that in pure axial fatigue, there is also a maximum shear plane perpendicular to the zr plane.

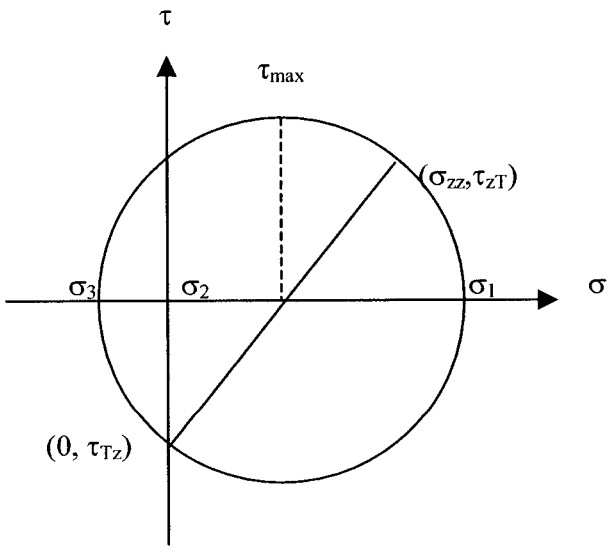

Figure I.2 Mohr circle of a general axial-torsional loading.

Figure I.3 is the 2D schematic of a triangular small element (ABC) on the specimen surface. AC represents a plane perpendicular to the specimen surface and whose normal (n) makes an angle θ with respect to the specimen axis (z). AB and BC represent the longitudinal and transverse planes. The shear and normal stresses on each plane are also illustrated.

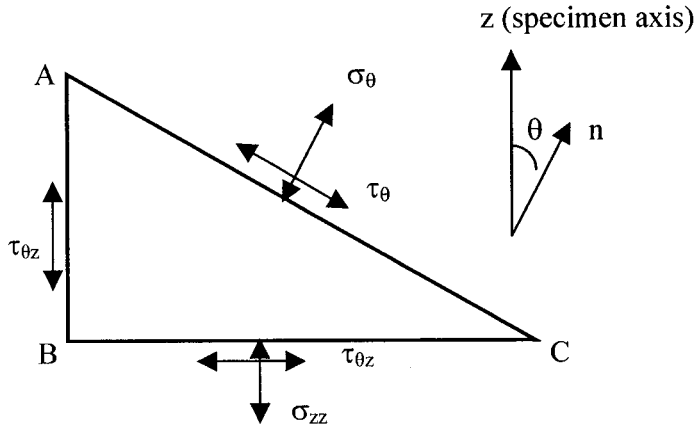

Figure I.3 A small triangle surface element used in stress analysis (σ_θ and τ_θ are the normal and shear stresses on the plane θ).

The normal and shear stresses (σ_θ and τ_θ) on plane AC can be obtained:

$$\begin{cases} \sigma_\theta = \sigma_{zz}\cos^2\theta + 2\tau_{z\theta}\sin\theta\cos\theta & \text{(I.3)} \\ \tau_\theta = \tau_{z\theta}(\cos^2\theta - \sin^2\theta) - \sigma_{zz}\sin\theta\cos\theta & \text{(I.4)} \end{cases}$$

Note that $\sigma_{zz}=\sigma_0\sin\omega t$ and $\tau_{z\theta}=\tau_0\sin(\omega t-\phi)$, then the equations I.3 and I.4 become:

$$\begin{cases} \sigma_\theta = \sigma_0\sin\omega t\cos^2\theta + 2\tau_0\sin(\omega t-\phi)\cos\theta\sin\theta & \text{(I.5)} \\ \tau_\theta = \tau_0\sin(\omega t-\phi)\,(\cos^2\theta - \sin^2\theta) - \sigma_0\sin\omega t\,\cos\theta\sin\theta & \text{(I.6)} \end{cases}$$

Stress ratio $\lambda=\tau_0/\sigma_0$; then the above equations can be expressed as:

$$\begin{cases} \dfrac{\sigma_\theta}{\sigma_0} = \dfrac{1+\cos 2\theta}{2}\sin\omega t + \lambda \sin 2\theta\left(\sin\omega t\cos\phi - \cos\omega t\sin\phi\right) & \text{(I.7)} \\ \dfrac{\tau_\theta}{\sigma_0} = \lambda\cos 2\theta\left(\sin\omega t\cos\phi - \cos\omega t\sin\phi\right) - \dfrac{1}{2}\sin 2\theta\sin\omega t & \text{(I.8)} \end{cases}$$

From the equation I.7, the following relation is obtained:

$$\begin{aligned} \frac{\sigma}{\sigma_0} &= \frac{1+\cos 2\theta + 2\lambda\sin 2\theta\cos\phi}{2}\sin\omega t - \lambda\sin 2\theta\sin\phi\cos\omega t \\ &= \frac{\sqrt{(1+\cos 2\theta + 2\lambda\sin 2\theta\cos\phi)^2 + (2\lambda\sin 2\theta\sin\phi)^2}}{2}\sin(\omega t - x) \end{aligned} \qquad \text{(I.9)}$$

$$\text{Here, } \tan x = \frac{2\lambda\sin 2\theta\sin\phi}{1+\cos 2\theta + 2\lambda\sin 2\theta\cos\phi} \qquad \text{(I.10)}$$

From the equation I.8, the following relation is obtained:

$$\begin{aligned} \frac{\tau_\theta}{\sigma_0} &= \lambda\cos 2\theta\sin\omega t\cos\phi - \lambda\cos 2\theta\cos\omega t\sin\phi - \frac{1}{2}\sin 2\theta\sin\omega t \\ &= \frac{2\lambda\cos 2\theta\cos\phi - \sin 2\theta}{2}\sin\omega t - \lambda\cos 2\theta\sin\phi\cos\omega t \\ &= \frac{\sqrt{(2\lambda\cos 2\theta\cos\phi - \sin 2\theta)^2 + (2\lambda\cos 2\theta\sin\phi)^2}}{2}\sin(\omega t - y) \end{aligned} \qquad \text{(I.11)}$$

$$\text{Here} \quad \tan y = \frac{2\lambda\cos 2\theta\sin\phi}{2\lambda\cos 2\theta\cos\phi - \sin 2\theta} \qquad \text{(I.12)}$$

From the above calculations, the following relations are obtained:

The normal and shear stress amplitudes ($\sigma_{\theta,a}$ and $\tau_{\theta,a}$) on the plane θ :

$$\frac{\sigma_{\theta,a}}{\sigma_0} = \frac{\sqrt{(1+\cos 2\theta + 2\lambda \sin 2\theta \cos\phi)^2 + (2\lambda \sin 2\theta \sin\phi)^2}}{2} \tag{I.13}$$

$$\frac{\tau_{\theta,a}}{\sigma_0} = \frac{\sqrt{(2\lambda \cos 2\theta \cos\phi - \sin 2\theta)^2 + (2\lambda \cos 2\theta \sin\phi)^2}}{2} \tag{I.14}$$

The phase difference δ between the normal and shear stresses on the plane θ:

$$\delta = y - x = \arctan\frac{2\lambda \cos 2\theta \sin\phi}{2\lambda \cos 2\theta \cos\phi - \sin 2\theta} - \arctan\frac{2\lambda \sin 2\theta \sin\phi}{1+\cos 2\theta + 2\lambda \sin 2\theta \cos\phi} \tag{I.15}$$

The maximum shear plane is the plane on which the shear stress amplitude is maximum. Then it can be derived by maximizing the equation I.14 with respect to the angle θ. Such a computation leads to the maximum shear plane (determined by the angle ξ between its normal and the specimen axis) as:

$$\tan 2\xi = \frac{(4\lambda^2 - 1) - \sqrt{(4\lambda^2 - 1)^2 + 16\lambda^2 \cos^2\phi}}{4\lambda \cos\phi} \tag{I.16}$$

The maximum shear stress amplitude (τ_{max}) and the normal stress amplitude acting on this plane (σ_n) are determined by the following relations:

$$\left(\frac{\tau_{max}}{\sigma_0}\right)^2 = \frac{(4\lambda^2 + 1) + \sqrt{(4\lambda^2 - 1)^2 + 16\lambda^2 \cos^2\phi}}{8} \tag{I.17}$$

$$\left(\frac{\sigma_n}{\sigma_0}\right)^2 = \frac{1}{8}\left[(4\lambda^2+3)-\sqrt{(4\lambda^2-1)^2+16\lambda^2\cos^2\phi}+2\sqrt{2}\left\{(4\lambda^2\cos^2\phi+1)+\frac{(4\lambda^2-1)-4\lambda^2(4\lambda^2+3)\cos^2\phi}{\sqrt{(4\lambda^2-1)^2+16\lambda^2\cos^2\phi}}\right\}^{1/2}\right] \quad \text{(I.18)}$$

Substituting the stress ratio λ and the phase angle ϕ by the values of each loading case in the equations I.13 and I.14, the normal and shear stress amplitude variations on different planes are obtained (Figure 3.6, page 99). From this figure, the plane(s) with maximum shear stress amplitude and the plane(s) with maximum normal stress amplitude can be determined for different loading cases. The normal and shear stress variations with time on the critical plane can be also derived (Figure 4.1, page 138) using the equations I.9 and I.11 after the critical plane has been identified.

APPENDIX II - STRESS ANALYSIS OF CIRCUMFERENTIALLY V-NOTCHED CYLINDRICAL SPECIMENS UNDER AXIAL AND TORSIONAL LOADINGS

Two 3-D solid models (Figure II.1) for circumferentially V-notched cylindrical specimens (N1 and N2) are created using "Part Design" in CATIA V5. Before the stress analysis, a material is assigned to these models: 1045 steel, Poisson ratio υ=0.30 and Young's modulus=205GPa. Linear elastic finite element stress analyses of these models under axial and torsional loadings are carried out using "Generative Structural Analysis" in CATIA V5.

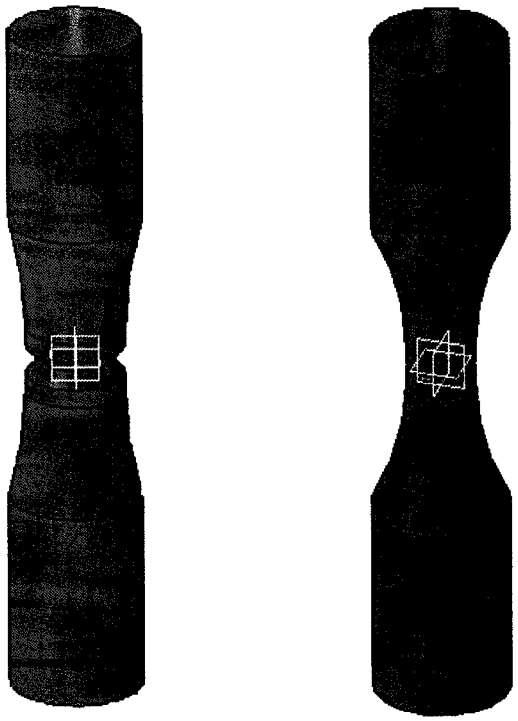

(a) (b)

Figure II.1 The 3-D solid models for the two notched specimens: (a) N1; (b) N2.

1. Stress analysis for axial fatigue

In CATIA 5, first open a model (to which a material has been assigned), and then go to "Generative structural analysis". An analysis workbench is then open. A finite element mesh is defined. The boundary conditions (restraints and loads) are selected. Then the computation is carried out. The results are extracted for post processing.

1.1 Meshing

The meshes in the two models N1 and N2 are shown in Figures II.2 and II.3, respectively. In both meshes, the same linear tetrahedron element is used. In most of volume, the element size is 5mm. Finer elements (0.2mm) are assigned to the notched zone. At the notch tip, the smallest elements (0.1mm) that can be obtained using CATIA V5 are used. In N1, the total number of elements is 172396 and the total number of nodes is 34558. In N2, the total numbers of elements and nodes are 65449 and 12945, respectively.

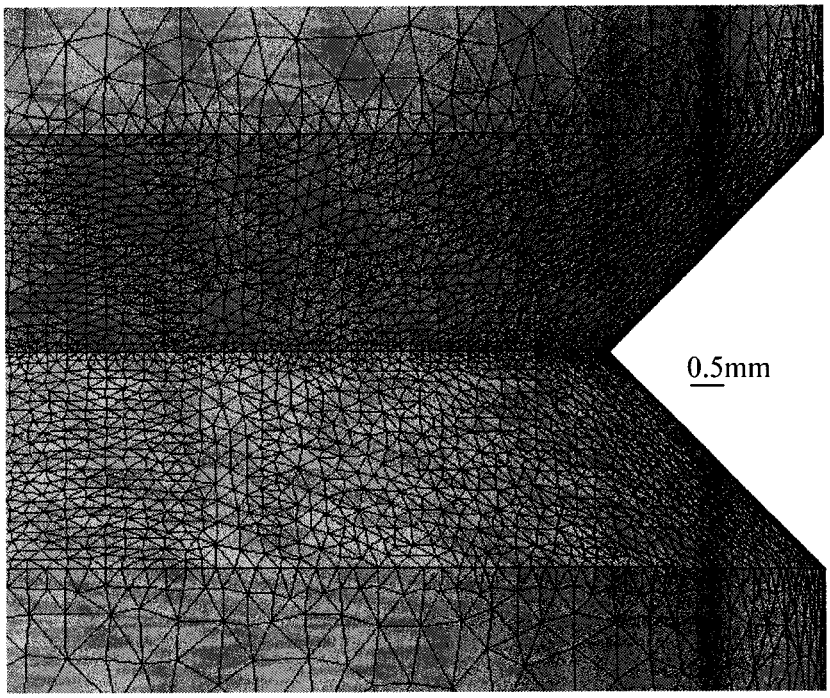

Figure II.2 Mesh of notched specimen N1

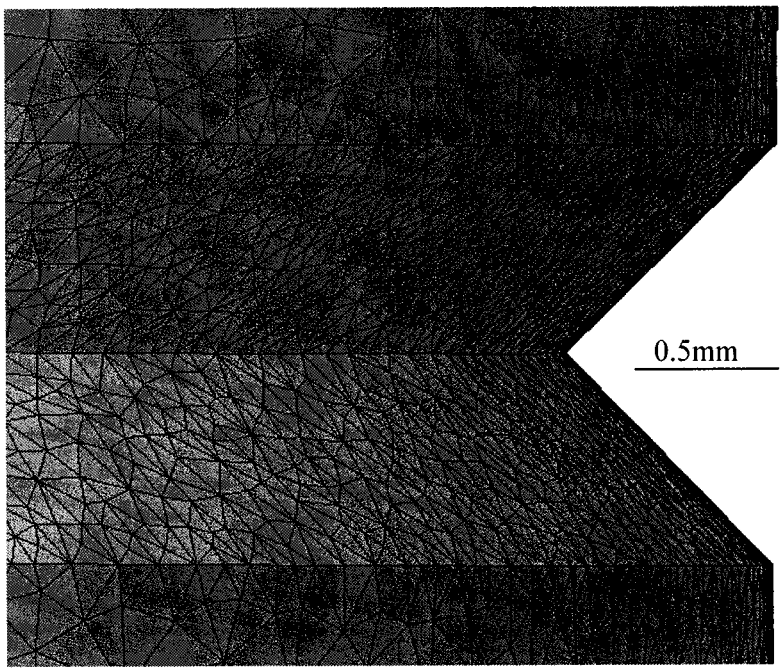

Figure II.3 Mesh of notched specimen N2

1.2 Boundary conditions

The same restraints are applied to the models N1 and N2. A "Clamp" is created on the circumferential surface of one specimen end. This setting fixes all degrees of freedom for this end. It reflects the real testing situation that the specimen end attached to the upper grip of the machine cannot move in any direction. At the other end of the specimen (lower grip), a "Virtual Part" is created on the circumferential surface. Axial loads of 16.959KN for N1 and 12.313KN for N2 (σ_{net}=120MPa for both N1 and N2) are applied to the specimen end where a virtual part has been created.

1.3 Computation

After the "Compute" command is applied, the finite element computation is automatically performed. After the computation, the solutions of displacements and stresses (von Mises stress, principal stresses and stress tensor components) can be either visualized as images or be reported as text documents.

The numerical computation has been verified with the analytical solution for a smooth cylindrical specimen.

1.4 Post-processing

"Cut Plane Analysis" consists in visualizing results in a plane section through the structure. "Cut Plane Analysis" is used to obtain the distribution of the normal stress σ_{zz} in a longitudinal plane that cuts through the specimen axis. An iso-stress contour color map on this plane is then obtained. Figures II.4 and II.5 show the iso-stress contour maps for the two notches N1 and N2, respectively (15 colors in each map).

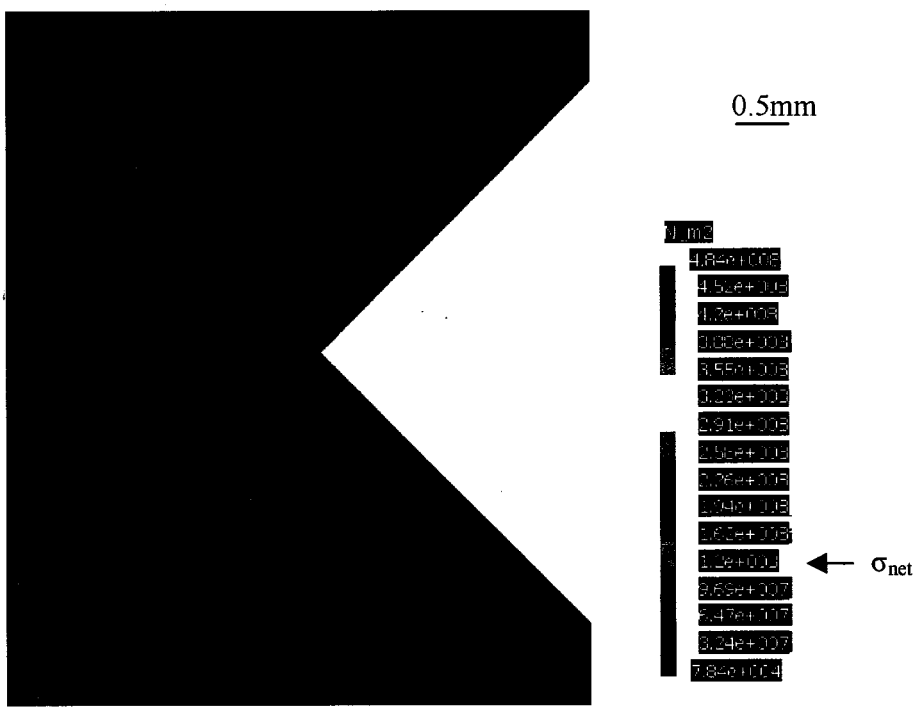

Figure II.4 The iso-stress contour map of σ_{zz} on the longitudinal plane (through the specimen axis) in notched specimen N1.

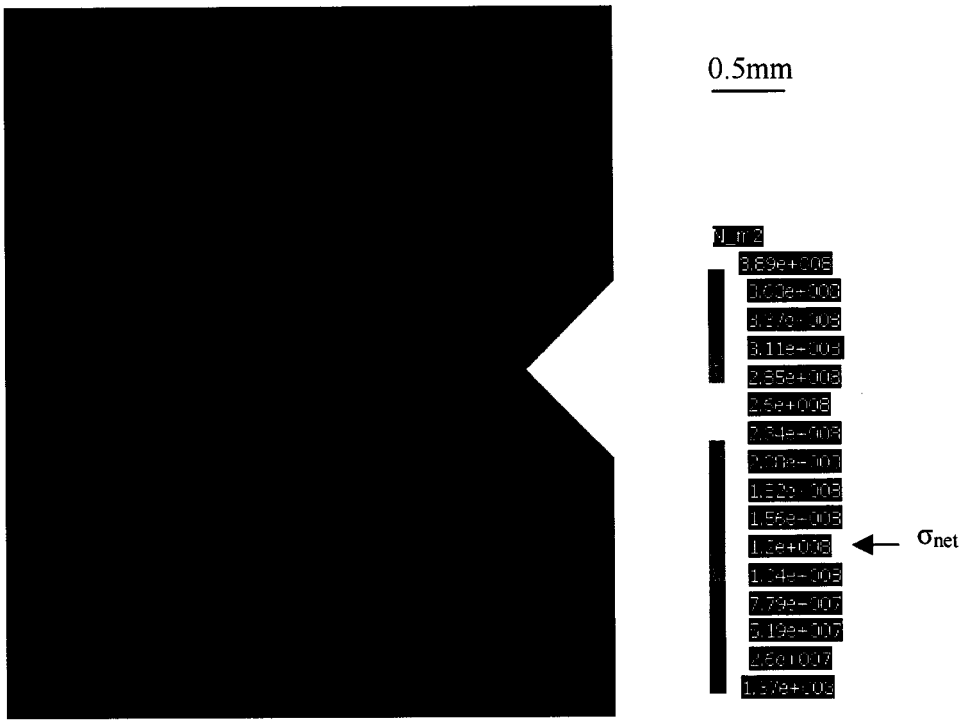

Figure II.5 The iso-stress contour map of σ_{zz} on the longitudinal plane (through the specimen axis) in notched specimen N2.

The stress concentrations at the two notches are readily visualized. A higher stress concentration is found in specimen N1, which is evident by the higher stress values and the larger stress concentration zone.

From the stress contour maps, the stress value and the corresponding coordinates at each boundary of different colors along the diametrical direction on the notch plane (the smallest cross-section of the specimen) can be obtained. The relations between σ_{zz}/σ_{net} and distance r from the notch tip for the two notched specimens N1 and N2 can be obtained as shown in Figure 6.21. The notch stress intensity factors K_I^{N1} and K_I^{N2} are then obtained by linear regression of the linear parts of the two curves in Figure 6.21. Note that the singularity exponents obtained in this analysis is 0.42, which is slightly lower than the analytical solution (0.455). One possible reason is that the meshes used in this analysis are not refined and result in some inaccuracies. A 2-D finite element stress analysis is also conducted on these two notched specimens using another software (Forge 2). With Forge 2, very fine meshes can be defined at the notch tip, and the obtained singularity exponent (0.45) is closer to the analytical solution. However, the curves of σ_{zz}/σ_{net} vs. r obtained with CATIA and with Forge 2 are close to each other when r>0.1mm (beyond one element from notch tip).

2. Stress analysis for torsional loading

The procedure of notch stress analysis for torsional loading is very similar to that for axial loading. For torsional loading, the same meshes and the same restraints are used as those for axial fatigue for both specimens N1 and N2.

Torques of 69.84 N.m for the notch N1 and 43.98 N.m for the notch N2 (τ_{net}=150MPa for both N1 and N2) are applied to the specimen end where a virtual part has been created.

"Cut Plane Analysis" is also used to obtain the iso-stress contour maps for shear stress $\tau_{z\theta}$ on the longitudinal plane that cuts through the specimen axis, for both specimens N1 and N2 (Figure II.6 and Figure II.7).

Notch stress concentration at notch is readily visualized in both specimens N1 and N2. Near the notch tip, the shape of iso-stress contours is more or less circular. Unlike axial loading, a stress gradient still exists at the specimen center. This is understandable from the fact that when a smooth cylinder is submitted to torsional loading, a shear stress gradient exists along the diametrical direction.

The stress value and the corresponding coordinates are known at each boundary of different colors along the diametrical direction on the notch plane. Then the relations between $\tau_{z\theta}/\tau_{net}$ and distance r from notch tip for N1 and N2 are obtained as shown in Figure 6.23. Then, by the linear regression of the straight parts of each curve in Figure 6.23, the mode III notch stress intensity factors K_{III}^{N1} and K_{III}^{N2} are obtained for the specimens N1 and N2, respectively.

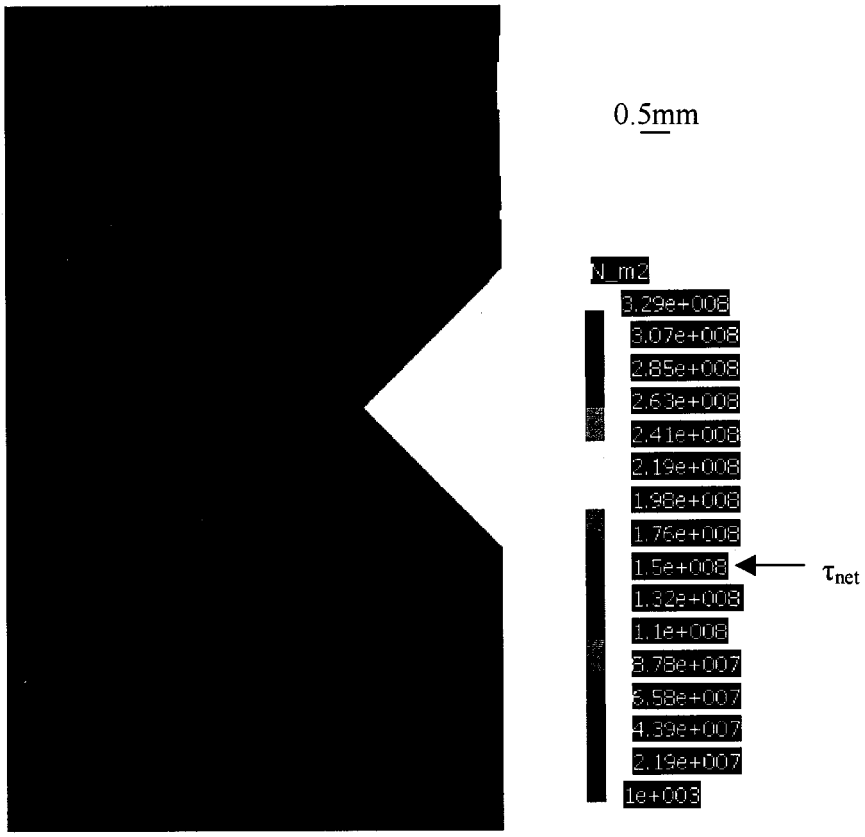

Figure II.6 The iso-stress contour map of $\tau_{z\theta}$ on the longitudinal plane (through the specimen axis) in notched specimen N1.

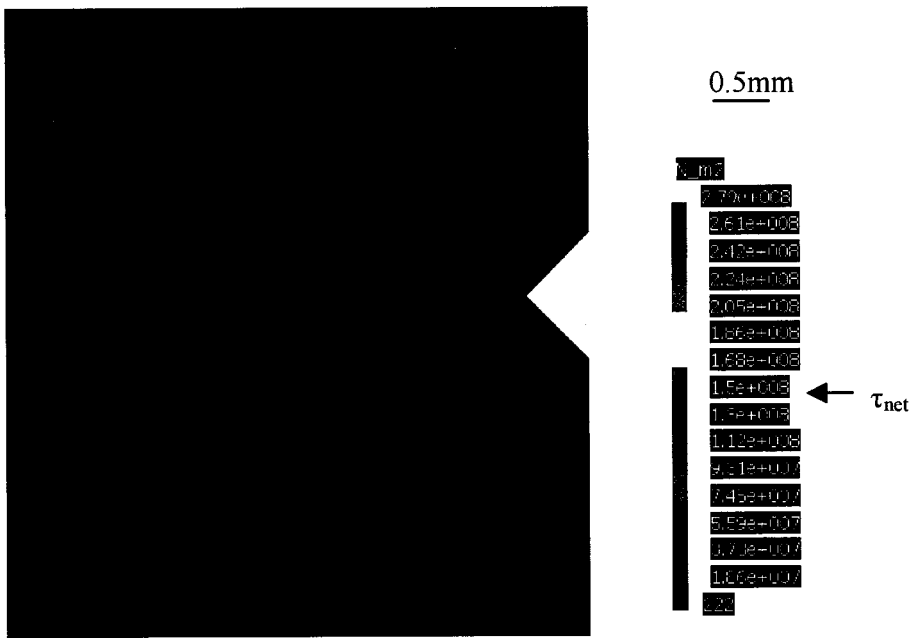

Figure II.7 The iso-stress contour map of $\tau_{z\theta}$ on the longitudinal plane (through the specimen axis) in notched specimen N2.